

GRAVITATIONAL MASS ATTRACTION MEASUREMENT FOR  
DRAG-FREE REFERENCES

A DISSERTATION  
SUBMITTED TO THE DEPARTMENT OF AERONAUTICS AND  
ASTRONAUTICS  
AND THE COMMITTEE ON GRADUATE STUDIES  
OF STANFORD UNIVERSITY  
IN PARTIAL FULFILLMENT OF THE REQUIREMENTS  
FOR THE DEGREE OF  
DOCTOR OF PHILOSOPHY

Aaron J Swank

May 2009

UMI Number: 3364514

Copyright 2009 by  
Swank, Aaron J.

### INFORMATION TO USERS

The quality of this reproduction is dependent upon the quality of the copy submitted. Broken or indistinct print, colored or poor quality illustrations and photographs, print bleed-through, substandard margins, and improper alignment can adversely affect reproduction.

In the unlikely event that the author did not send a complete manuscript and there are missing pages, these will be noted. Also, if unauthorized copyright material had to be removed, a note will indicate the deletion.

**UMI<sup>®</sup>**

---

UMI Microform 3364514  
Copyright 2009 by ProQuest LLC  
All rights reserved. This microform edition is protected against  
unauthorized copying under Title 17, United States Code.

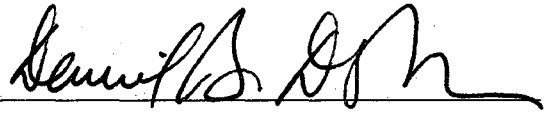
---

ProQuest LLC  
789 East Eisenhower Parkway  
P.O. Box 1346  
Ann Arbor, MI 48106-1346

© Copyright by Aaron J Swank 2009

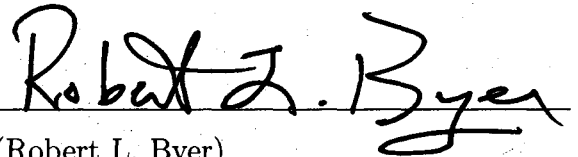
All Rights Reserved

I certify that I have read this dissertation and that, in my opinion, it is fully adequate in scope and quality as a dissertation for the degree of Doctor of Philosophy.



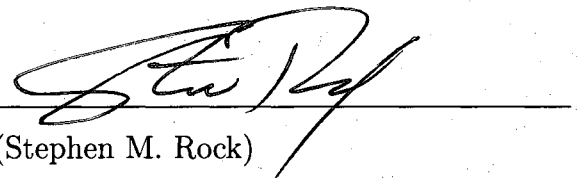
(Daniel B. DeBra) Principal Adviser

I certify that I have read this dissertation and that, in my opinion, it is fully adequate in scope and quality as a dissertation for the degree of Doctor of Philosophy.



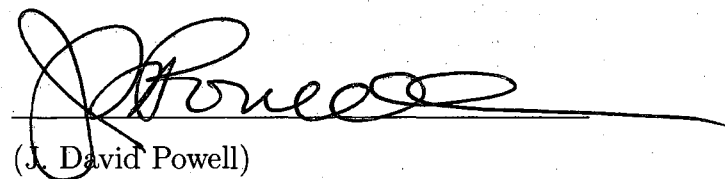
(Robert L. Byer)

I certify that I have read this dissertation and that, in my opinion, it is fully adequate in scope and quality as a dissertation for the degree of Doctor of Philosophy.



(Stephen M. Rock)

I certify that I have read this dissertation and that, in my opinion, it is fully adequate in scope and quality as a dissertation for the degree of Doctor of Philosophy.



(J. David Powell)

Approved for the University Committee on Graduate Studies.

*Pat J. Hargett*

---

# Abstract

Exciting new experiments in gravitational physics are among the proposed future space science missions around the world. Such future space science experiments include gravitational wave observatories, which require extraordinarily precise instruments for gravitational wave detection. In fact, future space-based gravitational wave observatories require the use of a drag free reference sensor, which is several orders of magnitude more precise than any drag free satellite launched to date. With the analysis methods and measurement techniques described in this work, there is one less challenge associated with achieving the high-precision drag-free satellite performance levels required by gravitational wave observatories.

One disturbance critical to the drag-free performance is an acceleration from the mass attraction between the spacecraft and drag-free reference mass. A direct measurement of the gravitational mass attraction force is not easily performed. Historically for drag-free satellite design, the gravitational attraction properties were estimated by using idealized equations between a point mass and objects of regular geometric shape with homogeneous density. Stringent requirements are then placed on the density distribution and fabrication tolerances for the drag-free reference mass and satellite components in order to ensure that the allocated gravitational mass attraction disturbance budget is not exceeded due to the associated uncertainty in geometry and mass properties. Yet, the uncertainty associated with mass properties and geometry generate an unacceptable uncertainty in the mass attraction calculation, which make it difficult to meet the demanding drag-free performance requirements of future gravitational wave observatories. The density homogeneity and geometrical tolerances required to meet the overall drag-free performance can easily force the use

of special materials or manufacturing processes, which are impractical or not feasible.

The focus of this research is therefore to develop the necessary equations for the gravitational mass attraction force and gradients between two general distributed bodies. Assuming the drag-free reference mass to be a single point mass object is no longer necessary for the gravitational attraction calculations. Furthermore, the developed equations are coupled with physical measurements in order to eliminate the mass attraction uncertainty associated with mass properties. The mass attraction formula through a second order expansion consists of the measurable quantities of mass, mass center, and moment of inertia about the mass center. Thus, the gravitational self-attraction force on the drag free reference due to the satellite can be indirectly measured. By incorporating physical measurements into the mass attraction calculation, the uncertainty in the density distribution as well as geometrical variations due to the manufacturing process are included in the analysis.

For indirect gravitational mass attraction measurements, the corresponding properties of mass, mass center, and moment of inertia must be precisely determined for the proof mass and satellite components. This work focuses on the precision measurement of the moment of inertia for the drag-free test mass. Presented here is the design of a new moment of inertia measurement apparatus utilizing a five-wire torsion pendulum design. The torsion pendulum is utilized to measure the moment of inertia tensor for a prospective drag-free test mass geometry. The measurement results presented indicate the prototype five-wire torsion has matched current state of the art precision. With only minimal work to reduce laboratory environmental disturbances, the apparatus has the prospect of exceeding state of the art precision by almost an order of magnitude. In addition, the apparatus is shown to be capable of measuring the mass center offset from the geometric center to a level better than typical measurement devices. Although the pendulum was not originally designed for mass center measurements, preliminary results indicate an apparatus with a similar design may have the potential of achieving state of the art precision.

# Acknowledgments

The life journey known by some as the Ph.D. would not be complete without the help of a number of individuals. It is impossible to list all the people who have become a part of this experience, yet I do wish to acknowledge a few key individuals.

Most importantly I would like to acknowledge Dr. Dan DeBra for his valued guidance and intuition provided over the years. I can only hope that some day I'll have his amazing and well respected intuition in such a wide array of disciplines. I thank Dr. Robert Byer and Dr. Sasha Buchman for their intellect and support. In addition, their primary concern has always been the funding status and well-being of the graduate students. Clearly without their determination, this research would not have been possible. I also thank Dr. Stephen Rock and Dr. David Powell for their time and effort.

I would like to thank all of the individuals comprising the Stanford GRS/LISA team and note a few outstanding individuals. I thank Dr. John Conklin for his contributions to the field, which in many ways has contributed to this work. I wish to acknowledge Dr. Ke-Xun Sun for his work and determination. I am sure that his efforts have either directly or indirectly contributed to all of the graduate student projects in the lab. I would also like to thank Dr. Graham Allen, Brett Allard and Dr. Norna Robertson for many valued discussions and insight. I thank Dr. Scott Williams for his determination in securing funding for the graduate students and his leadership during the ST-7 project. From the LIGO project at Stanford, I would also like to especially note Dr. Brian Lantz for his insights and contributions. Among a number of things, Dr. Lantz was instrumental in providing the insight and equipment necessary for understanding the laboratory vibrational environment.



I thank Dr. Mike Dolphin, Dr. Bree Sharratt, and Dr. Steven Waslander for enlightening discussions, friendship and moral support. Dr. Dolphin also provided a critical eye for numerous proof-readings of this work, for which I am grateful. I thank my friends at Stanford Kenpo Karate, NASA Ames and my family for friendship, fun, stress relief and encouragement. My friends at Kenpo also played an important family role while away from home. From all my friends I am grateful for a number of enjoyable memories during the years at Stanford. Clearly the Ph.D. would not be possible without the contribution from true friends.

Finally, I greatly appreciate the institutions providing financial support, including the Department of Defense and the National Defense Science and Engineering Graduate Fellowship Program (NDSEG), the NASA Beyond Einstein Program, the Stanford Dean's Office of Research and the Swank Family. Without the support from the NDSEG program, I would not have been able to pursue an advanced degree beyond an undergraduate education level. I also acknowledge Dr. Karman Ghia, Dr. Trevor Williams, and Gayle Elliott from the University of Cincinnati, who were instrumental in making my initial graduate education and fellowship support a reality. I thank the individuals at NASA Ames, who ensured an educational experience during my part-time employment in the final years of my Ph.D. research. Not only was the employment essential for funding the final years of my degree, but the skills I learned became a part of my research as well. In particular I would like to thank Stevan Spremo, Dave Mayer, Emmett Quigley and Evan Jackson for their help in making the experimental apparatus design a reality.

# Contents

<b>Abstract</b>	<b>v</b>
<b>Acknowledgments</b>	<b>vii</b>
<b>1 Introduction</b>	<b>1</b>
1.1 Drag-Free References and Applications . . . . .	1
1.2 The Mass Attraction Problem . . . . .	4
1.3 Contributions and Outline . . . . .	8
1.3.1 Gravitational Mass Attraction . . . . .	8
1.3.2 Precision-Mass Property Measurements . . . . .	10
1.3.3 Synthesis of Contributions . . . . .	11
<b>I Gravitational Mass Attraction. In Theory.</b>	<b>14</b>
<b>2 Traditional Solution Methods</b>	<b>15</b>
2.1 Point Mass Summation . . . . .	15
2.2 MacCullagh's Formula . . . . .	17
2.3 Analytical Solution: Block Geometry . . . . .	19
2.3.1 Attraction Force . . . . .	20
2.3.2 Gradient of the Attraction Force . . . . .	28
2.3.3 Simulation Results . . . . .	33
<b>3 The Double Taylor Method</b>	<b>41</b>
3.1 Force Between Distributed Mass and a Point . . . . .	42

3.2	Mass Moment Calculation . . . . .	44
3.2.1	Moment of Inertia Method . . . . .	45
3.2.2	Tetrahedron Decomposition Method . . . . .	47
3.3	MacCullagh's Formula Derivation . . . . .	48
3.4	Force Between Two Distributed Masses . . . . .	54
3.5	Gradients of the Attraction Force . . . . .	57
3.6	Analysis of the Force Equations . . . . .	57
3.7	Force Equation in Matrix Form . . . . .	63
3.8	Application to Computational Methods . . . . .	64
3.8.1	Finite Element Discretization . . . . .	64
3.8.2	Point Mass Summation Limitations . . . . .	66
3.9	Errors Due to Non-Exact Symmetrical Body . . . . .	68
3.10	Observation: A Cube is Similar to a Sphere . . . . .	73
3.11	Variations in Density . . . . .	73
<b>II</b>	<b>The Necessity of Measurements</b>	<b>77</b>
<b>4</b>	<b>Mass Property Measurements</b>	<b>78</b>
4.1	Mass Measurement . . . . .	80
4.2	Mass Center Measurement . . . . .	81
4.3	Moment of Inertia Measurement . . . . .	82
4.3.1	Measurement Techniques . . . . .	84
4.3.2	Determining the Inertia Tensor . . . . .	86
4.4	Measurements Using a Torsion Pendulum . . . . .	88
4.4.1	Torsion Pendulum Dynamics . . . . .	88
4.4.2	Mass Center Measurement Using a Torsion Pendulum . . . . .	90
4.4.3	Inertia Measurement Using a Torsion Pendulum . . . . .	94
<b>5</b>	<b>Inertia Measurement Apparatus Design</b>	<b>97</b>
5.1	Pendulum Platform Design . . . . .	99
5.2	Support Wire and Wire Attachment . . . . .	109

5.2.1	Wire Attachment . . . . .	109
5.2.2	Wire . . . . .	112
5.3	Pendulum Platform Assembly Mounts . . . . .	120
5.4	Measurement Object Fixtures . . . . .	121
5.4.1	Cylindrical Object . . . . .	124
5.4.2	Spherical Object . . . . .	125
5.5	Measurement/Sensing . . . . .	131
5.5.1	Shadow Sensing . . . . .	131
5.5.2	Grating Angular Sensing . . . . .	133
5.6	Grating and Magnet Holder Design . . . . .	134
5.7	Frequency Measurement Procedure . . . . .	137
5.7.1	Damped Sinusoid Curve Fit . . . . .	138
5.7.2	Fourier Transform . . . . .	139
5.7.3	Coherent Demodulation, Sine Drive . . . . .	139
5.7.4	Time Domain Zero Crossing Detection . . . . .	140
<b>6</b>	<b>Experimental Results</b>	<b>144</b>
6.1	Pendulum Calibration . . . . .	144
6.2	Mass Center Measurement . . . . .	148
6.3	Preferred Principal Axis of Inertia Sphere . . . . .	153
<b>7</b>	<b>Measurement Error</b>	<b>168</b>
7.1	Temperature . . . . .	169
7.2	Vibrational Disturbances . . . . .	182
7.3	Air Currents . . . . .	193
7.4	Dynamical Nonlinearity . . . . .	196
<b>8</b>	<b>Future Work</b>	<b>200</b>
8.1	Measurement Apparatus Modifications . . . . .	200
8.1.1	Vacuum Chamber and Temperature Isolation . . . . .	200
8.1.2	Vibration Isolation . . . . .	202
8.1.3	Platform Tilt Reduction and Wire Angle . . . . .	203

8.1.4	Grating Orientation . . . . .	205
8.1.5	Trim Masses . . . . .	206
8.1.6	Object Fixtures . . . . .	206
8.1.7	Continuous Feedback Drive . . . . .	208
8.2	Recommended Future Research . . . . .	209
8.2.1	Mass Center Measurement . . . . .	209
8.2.2	Satellite Design for Mass Attraction . . . . .	210
<b>9</b>	<b>Final Remarks</b>	<b>213</b>
<b>A</b>	<b>Additional Information</b>	<b>216</b>
A.1	Tetrahedron Volume Moments . . . . .	216
A.2	Grating Angular Sensor Calibration . . . . .	217
<b>B</b>	<b>Mechanical</b>	<b>221</b>
B.1	Mechanical Drawings . . . . .	221
B.2	Measurement Apparatus Parameters . . . . .	232
B.3	Bill of Materials . . . . .	233
<b>C</b>	<b>Electrical</b>	<b>237</b>
C.1	Instrumentation . . . . .	237
C.2	Schematics . . . . .	238
<b>D</b>	<b>Software</b>	<b>241</b>
<b>E</b>	<b>Measurement Data</b>	<b>242</b>
	<b>References</b>	<b>250</b>

# List of Tables

2.1	Simulation parameters for force and gradient calculation. . . . .	33
3.1	Sets of $N$ for second order expansion. . . . .	50
3.2	Sets of $N$ and $S$ for double second order expansion. . . . .	57
3.3	Input for non-symmetrical body calculation. . . . .	72
4.1	State of the art mass property measurement capabilities. . . . .	80
4.2	Inertia measurement techniques. . . . .	85
5.1	Design requirement implementation sections. . . . .	103
5.2	Calibration hole distance from rotation center. . . . .	106
5.3	Material properties. . . . .	113
5.4	Wire lengths for five-wire pendulum. . . . .	114
5.5	Wire stiffness configuration. . . . .	116
5.6	Wire and hypodermic tube configuration. . . . .	117
5.7	Data reduction techniques. . . . .	138
6.1	Pendulum calibration results. . . . .	147
6.2	Parameters used for mass center offset calculation. . . . .	150
6.3	Comparison of mass center measurement results. . . . .	152
6.4	Preferred principal axis of inertia sphere design parameters. . . . .	155
6.5	Orientation configurations for sphere measurements. . . . .	159
6.6	Measurement results for preferred principal axis of inertia spheres. . .	161
7.1	Estimated noise source contributions . . . . .	170

7.2	Pendulum properties. . . . .	171
7.3	PID temperature controller hardware. . . . .	178
7.4	PID temperature controller gains. . . . .	179
8.1	Importance of future modifications. . . . .	201
B.1	Estimated machining time for pendulum components. . . . .	222
B.2	Measurement apparatus parameters. . . . .	232
B.3	Bill of Materials: Calibration and Trim Mass Spheres. . . . .	233
B.4	Bill of Materials: Support Wires. . . . .	234
B.5	Bill of Materials: Fasteners. . . . .	235
B.6	Bill of Materials: Optics . . . . .	236
C.1	Experimental apparatus instrumentation. . . . .	237
E.1	Measurement Data for Pendulum Calibration with Sphere Mount. . . . .	243
E.2	Measurement Data for Pendulum Calibration with Object. . . . .	244
E.3	Measurement Data for 2-Part Sphere Number 1. . . . .	245
E.4	Measurement Data for 2-Part Sphere Number 3. . . . .	246
E.5	Measurement Data for 2-Part Sphere Number 4. . . . .	247
E.6	Measurement Data for 2-Part Sphere Number 6. . . . .	248
E.7	Measurement Data for 3-Part Sphere Number 8. . . . .	249

# List of Figures

1.1	LISA Mission. . . . .	2
1.2	Drag-free satellite performance comparison. . . . .	5
1.3	Triad-1/DISCOS . . . . .	6
1.4	Configuration for gravitational mass attraction example. . . . .	12
2.1	Baseline LISA reference mass. . . . .	17
2.2	Attraction at a point due to a brick-shaped body. . . . .	20
2.3	$x$ -Direction mass attraction force for cube, $F^{P/C}$ . . . . .	35
2.4	Delta between point mass and a cubical geometry. . . . .	35
2.5	Delta $F_x^{P/C}$ between point mass and a cubical geometry in $x$ - $y$ plane. . . . .	36
2.6	Gradient $\frac{\partial F_x^{P/C}}{\partial x}$ for a cube in $x$ - $y$ plane. . . . .	37
2.7	Gradient $\frac{\partial F_x^{P/C}}{\partial y}$ for a cube in $x$ - $y$ plane. . . . .	37
2.8	Delta gradient $\frac{\partial F_x^{P/C}}{\partial x}$ between point mass and a cubical geometry. . . . .	38
2.9	Delta gradient $\frac{\partial F_x^{P/C}}{\partial y}$ between point mass and a cubical geometry. . . . .	38
2.10	Delta between point mass and a cubical geometry. . . . .	39
3.1	Distance between point $P$ and a point on the distributed body. . . . .	42
3.2	Tetrahedron defined by three vectors. . . . .	47
3.3	Tetrahedron represented by four sub-tetrahedrons. . . . .	49
3.4	Two distributed bodies with coordinate origins at mass center. . . . .	55
3.5	Common Cartesian grid direction for two bodies. . . . .	66
3.6	Slightly asymmetric central Body C and symmetric Body D. . . . .	70
3.7	Repeated derivative function $h_{3,0,0}^{0,0,0}$ in the $x, y$ plane. . . . .	71



4.1	Torsion pendulum free body diagram. . . . .	88
4.2	Pendulum configuration for mass center measurement. . . . .	91
4.3	Vector addition for mass center location. . . . .	92
4.4	Required frequency resolution for mass center measurements. . . . .	95
5.1	Five-wire torsion pendulum wire geometry. . . . .	98
5.2	Five-wire torsion pendulum solid model. . . . .	100
5.3	Five-wire torsion pendulum. (Actual Hardware, Final Design) . . . .	101
5.4	Five-wire pendulum platform. . . . .	104
5.5	Five-wire platform top view. . . . .	106
5.6	Pendulum configuration for object mass center measurement. . . . .	108
5.7	Five-wire pin vise wire mount. . . . .	110
5.8	Five-wire pendulum platform wire mounts. . . . .	111
5.9	Hardware: five-wire pendulum platform wire mounts. . . . .	111
5.10	Wire mount hole and slot. . . . .	112
5.11	Crimped and soldered wire attachment examples. . . . .	118
5.12	DMC AFM8 wire crimper. . . . .	119
5.13	Five-wire platform assembly mount. . . . .	121
5.14	Five-wire platform on assembly mounts. . . . .	122
5.15	Object orientation fixtures for cylindrical object. . . . .	124
5.16	Mount for spherical object. . . . .	125
5.17	Diagram of polhode paths. . . . .	126
5.18	New Way air bearing used for marking polhode path. . . . .	127
5.19	Apparatus for marking sphere with perpendicular great circles. . . . .	128
5.20	Sphere with polhode paths and great circles. . . . .	129
5.21	Sphere on platform with orientation markings. . . . .	130
5.22	Five-wire pendulum platform with shadow sensing. . . . .	132
5.23	Grating angular sensor. . . . .	133
5.24	Position Sensitive Diode (PSD). . . . .	134
5.25	Five-wire pendulum grating and magnet mount. . . . .	136
5.26	Five-wire pendulum platform with grating holder. . . . .	137

5.27	Time domain zero crossing detection. . . . .	141
5.28	Time domain zero crossing detection results. . . . .	142
6.1	Fixed mass center offset sphere. . . . .	148
6.2	Sphere mass center measurement configuration. . . . .	151
6.3	Preferred principal axis of inertia sphere simplified cross-section. . . . .	154
6.4	Sphere body coordinates. . . . .	157
6.5	Pendulum platform coordinate system. . . . .	157
6.6	Preferred principal axis of inertia sphere. . . . .	159
6.7	Preferred principal axis of inertia sphere on platform. . . . .	160
6.8	Principal axis measurement data for 2-part sphere number 1. . . . .	163
6.9	Principal axis measurement data for 2-part sphere number 3. . . . .	164
6.10	Principal axis measurement data for 2-part sphere number 4. . . . .	165
6.11	Principal axis measurement data for 2-part sphere number 6. . . . .	166
6.12	Principal axis measurement data for 3-part sphere number 8. . . . .	167
7.1	Pendulum temperature calibration prior to compensation. . . . .	172
7.2	Pendulum platform null position change due to temperature. . . . .	174
7.3	Temperature drift for Figure 7.2 . . . . .	175
7.4	Quad sensor top/bottom null position change due to temperature. . . . .	176
7.5	Pendulum frequency vs. null top/bottom position. Symmetric loading. . . . .	176
7.6	Pendulum frequency vs. null top/bottom position. Asymmetric pendulum loading. . . . .	177
7.7	PID temperature controller step input time response. . . . .	180
7.8	Pendulum temperature calibration results using PID controller. . . . .	181
7.9	Observed earthquake in measurement data. . . . .	182
7.10	Observed disturbance in measurement data. . . . .	183
7.11	Vibration noise floor of granite table, horizontal direction. . . . .	185
7.12	Vibration noise floor of granite table, vertical direction. . . . .	186
7.13	Vibration noise spectrum in Astrophysics building, Lab B11. . . . .	188
7.14	Vibration noise spectrum in Astrophysics building, Lab B33. . . . .	189
7.15	Vibration isolation stack. . . . .	190

7.16	Pendulum platform vibration noise spectrum. . . . .	192
7.17	Pendulum response root mean square spectral density. . . . .	194
7.18	Root mean square spectral density with pendulum on assembly mounts. . . . .	195
7.19	Pendulum response, Quad sensor signal. . . . .	197
7.20	Pendulum initial oscillation amplitude. . . . .	199
A.1	Pendulum platform setup for sensor calibration. . . . .	218
A.2	PSD sensor calibration curves. . . . .	219
A.3	Quad sensor calibration curves. . . . .	220
B.1	Mechanical Drawing: Pendulum platform. . . . .	223
B.2	Mechanical Drawing: Pendulum platform, mounting fixture holes. . . . .	224
B.3	Mechanical Drawing: Pendulum platform, calibration holes. . . . .	225
B.4	Mechanical Drawing: Pendulum angled wire mount. . . . .	226
B.5	Mechanical Drawing: Pendulum vertical wire mount. . . . .	227
B.6	Mechanical Drawing: Grating mount top portion. . . . .	228
B.7	Mechanical Drawing: Grating and magnet mount bottom part. . . . .	229
B.8	Mechanical Drawing: Sphere mounting fixture. . . . .	230
B.9	Mechanical Drawing: Pendulum platform assembly mount. . . . .	231
C.1	Schematic: Pendulum coil driver. . . . .	238
C.2	Schematic: Position sensitive diode. . . . .	239
C.3	Schematic: Quadrant photodiode, autocollimator. . . . .	240

# Chapter 1

## Introduction

### 1.1 Drag-Free References and Applications

At the core of a drag-free satellite is a drag-free reference sensor, which is simply a proof mass specifically designed in shape and materials for a particular purpose or application. To be useful, the proof mass must be shielded from all external forces to form an inertial reference. The characteristics of an inertial reference are achieved by surrounding the proof mass with a satellite, coupled with a sophisticated control system. Environmental disturbances are absorbed by the satellite and are counteracted with thrusters to keep the proof mass continuously centered within the cavity at the core of the satellite. In essence, the satellite acts as a shield to protect the proof mass from all environmental disturbances, maintaining a disturbance free environment for the proof mass.

There are a number applications or uses for a drag-free satellite [16]. For instance, the inertial reference can be utilized as part of spacecraft navigation systems for predictable orbit determination, or even as part of satellite formation flight cluster management. In fact, the first drag-free satellite, Triad-1/DISCOS, was used to generate predictable satellite orbits, which could then be used by the US Navy as a navigation system [53]. In addition, there are a number of science experiments in geodesy and experimental gravitation. One application generating a great deal of enthusiasm is

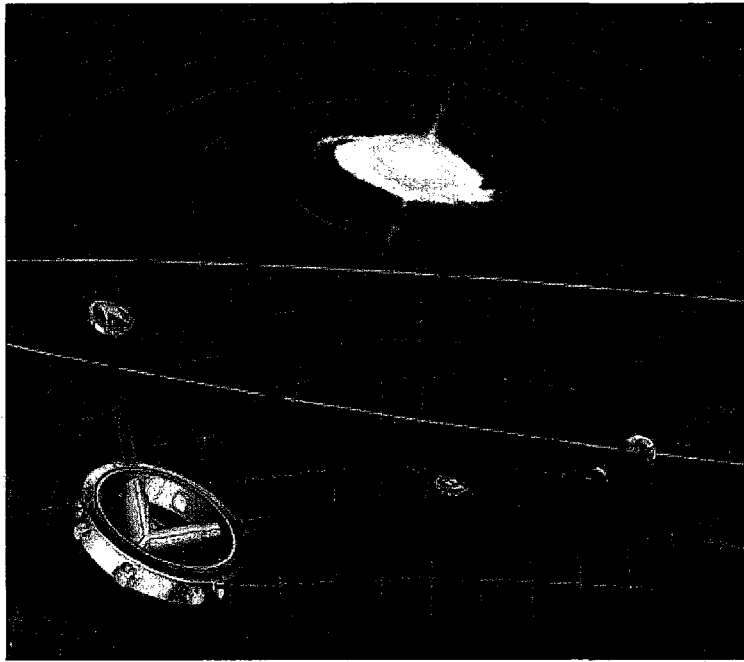


Figure 1.1: Artist's rendition of the Laser Interferometer Space Antenna, (LISA). Future drag-free satellite mission to be used as a gravitational wave observatory.

that of a gravitational wave observatory. Gravity, as described by Einstein is a curvature of space and time. Gravitational waves are ripples in spacetime, created by two super-massive objects moving in space, such as black hole binaries, galactic binaries, and extreme mass ratio inspirals [44]. Although these waves have been predicted to exist by Einstein's theories, gravitational waves have yet to be detected directly and proof of their existence has been limited to indirect observations.

Detection of gravitational waves has become in recent years a top science priority for nations around the world. Not only is it important to verify fundamental physics through the detection of gravitational waves, but a functional gravitational wave observatory can further the discovery of astrophysical objects and also provide insight into the origins of the universe. Figure 1.1 shows for example, an artists rendition of a joint ESA/NASA space-based gravitational wave observatory known as the Laser

Interferometer Space Antenna, (LISA).<sup>1</sup> LISA consists of three drag-free satellites, with the mission to detect gravitational waves and then use the detected signal to look at the universe and its history as a new type of telescope. Clearly the success of LISA will open an exciting new frontier of science. LISA shall provide for the first time a direct observation of gravitational waves and proof of their existence. Furthermore, gravitational wave astronomy will enhance conventional astronomy by providing information about the emitting sources. The gravitational wave sky, as observed by LISA, contains potentially millions of galactic binaries. LISA will target, for example, gravitational wave sources in the frequency band of 0.1 mHz to 0.1 Hz, including sources such as massive black hole binaries and black hole mergers. In addition, fluctuations in the gravitational background radiation will further provide knowledge about the evolution of the early universe.

Gravitational wave detection relies on the underlying drag-free satellite technology to form the science sensor. From gravitational wave physics, a strain in the spacetime curvature occurs when a gravitational wave passes. Thus, if there are two free-floating objects in space, a relative change in displacement will be observed due to the passing of a gravitational wave. Two drag-free references therefore form the essential components for a gravitational detector. The difficulty in detection, however, lies with the magnitude of the gravitational strain and the requirement to ensure that the free-floating proof mass has moved due to the passing of a gravitational wave and not as a result of some other local disturbance. The gravitational strain is similar in definition to a mechanical strain or a change in length divided by the separation distance  $\Delta L/L$ . Since spacetime is extremely stiff, the magnitude of the strain associated with a gravitational wave is on the order of  $10^{-21}$  [44]. Thus, if the separation distance,  $L$ , is on the order of millions of kilometers, the observed change in length,  $\Delta L$ , will be on the order of picometers. The required amount of accuracy over such a long distance is quite a challenging task. Furthermore, it is quite challenging to ensure that the proof mass associated with the science sensor has not moved by a small magnitude due to a force other than by the effects of a gravitational wave.

---

<sup>1</sup>More information on the LISA spacecraft and the mission objectives can be found in Reference [36].

## 1.2 The Mass Attraction Problem

The required drag-free performance to provide a completely inertial reference sensor for gravitational wave detection is not a simple task. Environmental disturbances can be on the order of  $10^{-6}$  g, and gravitational sensor missions often require design accelerations of better than  $10^{-12}$  g [53]. For Triad-1/DISCOS, the Disturbance Compensation System, DISCOS, was designed to provide a disturbance-free environment at the proof mass to an acceleration level of  $10^{-11}$  g ( $10^{-10}$  m/s<sup>2</sup>) [53] [22]. Furthermore, for the LISA gravitational wave observatory, the dynamic stability must be achieved down to 0.1 mHz due to the frequency of the associated gravitational wave science signal. Even the most precise drag-free satellite launched to date, Gravity Probe B (GP-B), would require a substantial increase in the drag-free performance level to achieve the requirements dictated by future space-based gravitational wave observatories. In fact, next generation space-based gravitational wave observatories such as LISA require the use of gravitational reference sensors, which are several orders of magnitude more precise than any drag free satellite launched to date. Figure 1.2 shows for instance the drag-free performance requirement of LISA as compared to GP-B over the target gravitational frequency range for LISA. As shown in the figure on the vertical axis, the residual acceleration on the drag-free reference in the frequency band of interest is the key performance metric for a drag-free satellite.

In order to increase the drag-free performance level for a drag-free satellite, all of the disturbances acting on the proof mass must be determined and characterized. Although the satellite is designed to shield the proof mass from external disturbances, the pure existence of the satellite introduces internal disturbances. Disturbances to the proof mass arise from numerous sources, including for example thermal variations, magnetic fields and gravitational mass attraction gradients. The total drag-free performance is therefore a combination of all these extraneous accelerations. In addition, through engineering design decisions, the magnitude of one disturbance may be traded for another in order to meet the overall drag-free performance requirement. For example, a material chosen to reduce the disturbance due to say magnetic effects may increase the disturbance due to gravitational mass attraction. By proper

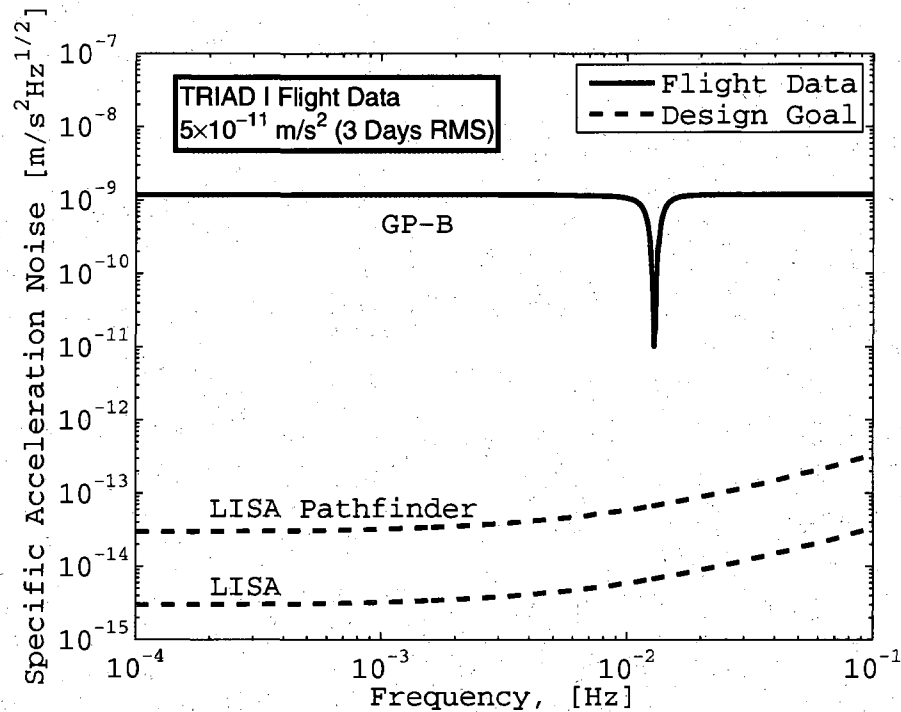


Figure 1.2: Drag-free satellite performance comparison. Design goals for gravitational wave observatories such as LISA require significant improvement over state of the art drag-free performance technology. The frequency range depicted corresponds to the gravitational wave frequency band targeted by LISA.

system-level design, all of the disturbances associated with the satellite must be minimized. A number of individuals have attempted to characterize the expected leading disturbance terms associated with demanding drag-free performance missions such as LISA [47], [56], [29], [28]. Indeed, the gravitational mass attraction force between the satellite and the drag free reference mass has been identified as a contribution to the disturbance budget. For LISA, the required mass attraction acceleration noise level must be reduced to the challenging value of better than  $5 \times 10^{-16} \text{ m/s}^2 \cdot \text{Hz}^{1/2}$  at 0.1 mHz [42]. The static value for the gradient of the mass attraction force is in addition a challenging requirement at  $3 \times 10^{-8} \text{ s}^{-2}$  or less, which is an order of magnitude better than required for Triad-1/DISCOS [56], [53]. Only by designing the satellite as a perfect sphere with a uniform density distribution containing a hollow cavity at



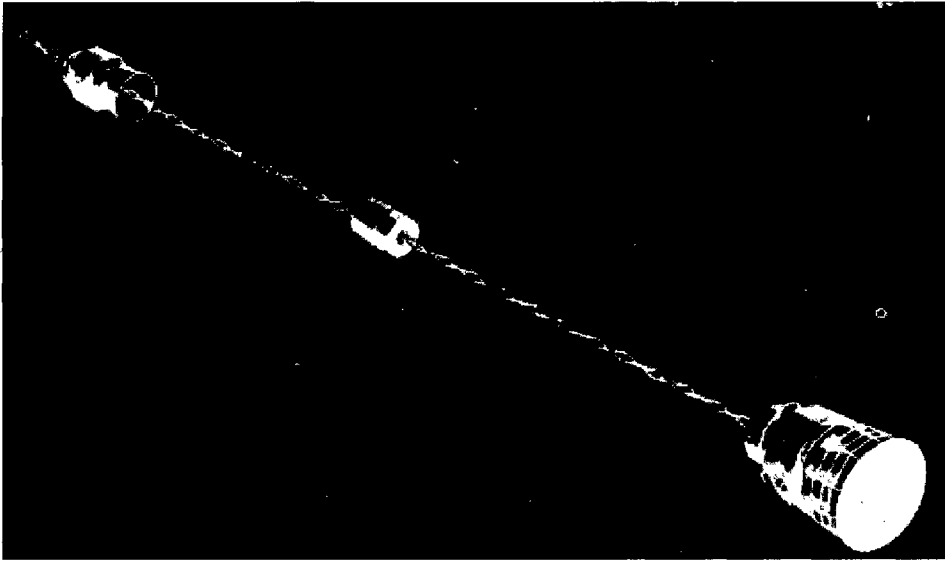


Figure 1.3: Artist's rendition of Triad-1/DISCOS. DISCOS, the Disturbance Compensation System, is at the middle of the satellite near the illustration center. Satellite components not essential to the control system operation were placed at the ends of two booms, as shown at the top left and bottom right of the illustration. Further information on the configuration of Triad-1/DISCOS is found in Reference [13].

the center can the mass attraction force be completely eliminated. Clearly, such a satellite design is impractical and therefore the mass attraction forces and gradients must be determined at the proof mass due to the surrounding satellite.

The gravitational mass attraction between the drag-free reference mass and the surrounding satellite is a dominant disturbance, which limits the overall drag-free performance. Furthermore, the exact gravitational mass attraction properties for the satellite are difficult to determine due to uncertainties in geometric fabrication tolerances, material density distributions and precise component location knowledge. For Triad-1/DISCOS, the mass attraction was the principal potential source of disturbance to the proof mass [16]. The uncertainty associated with the mass attraction disturbance for Triad-1/DISCOS was reduced by moving all the parts of the satellite not essential to the control system to a location far from the drag-free reference as shown in Figure 1.3. The satellite was manufactured in three parts and split between two booms such that the majority of the mass was moved to distances several meters

away from the drag-free satellite proof mass and control system. Three pieces were necessary to maintain symmetry, such that the mass center of the satellite was near the drag-free reference mass. Although the gravitational mass attraction was still the dominant contribution to the disturbance budget for Triad-1/DISCOS, the use of the booms resulted in a satellite design, where the majority of the satellite components could be machined without special fabrication tolerances [53].

Although the design philosophy of separating the drag-free reference mass from the majority of the satellite aids in increasing the drag-free performance, there is a practical limit to such a design. Triad-1/DISCOS, for example, was on the order of 8 m in length with the two 3 m long booms deployed [13]. Increasing the total length of the satellite to meet more stringent drag free performance requirements is therefore impractical. Clearly, when possible it is desired to move components with a large contribution to the mass attraction disturbance budget to locations far from the proof mass. Yet, other contributions in a dynamic sense will exist with the addition of booms, such as oscillatory motion due to differential thermal heating and gravity gradient torques as well as the design trade associated with increased mass and complex mechanisms. For gravitational wave observatories such as LISA, a satellite design utilizing booms is not feasible. As a result, only additional precision knowledge of the satellite component mass, geometry, and orientation/location can further aid in reducing the mass attraction disturbance.

Throughout the history of drag-free satellite design, the theoretical contribution to the mass attraction disturbance budget was determined by assuming idealized values for the density distribution and component geometry. Although Triad-1/DISCOS avoided the requirement of special fabrication tolerances for the majority of the satellite, some critical components did indeed require fabrication tolerances or measurements to the order of 0.0025 mm [53]. Next generation gravitational wave observatories such as LISA dictate an unprecedented drag-free performance level, which in turn generates the requirement for even more strict fabrication tolerances. Satellite components would require special machining processes and/or materials with stringent requirements on the density distribution in order to use the purely theoretical mass attraction computation procedure. In order to enable future drag-free space science

missions such as LISA, one turns to measurements in order to increase the knowledge of the gravitational mass attraction for the satellite. Unfortunately, it is difficult to measure the gravitational attraction directly and any such measurement would be limited to a particular component configuration such as location and orientation. An alternate analysis method is therefore desired and the solution is presented in this work.

### 1.3 Contributions and Outline

This work presents contributions which may be grouped into two primary categories. First, contributions to the area of gravitational mass attraction are presented in Part I. Secondly, contributions in the area of precision mass property measurements are covered in Part II. The contributions in both parts of this work are interconnected. The combination of the contributions in Part I and Part II completes the solution to the mass attraction problem associated with high precision drag-free satellites such as LISA.

#### 1.3.1 Gravitational Mass Attraction

Motivated by the gravitational mass attraction issues associated with precision drag-free satellites, this work presents an alternative calculation approach for the mass attraction disturbance to the drag-free reference. For the first time, a complete closed form solution to the mass attraction force and gradients between any two general shaped objects is presented (Chapter 3). Other solution methods typically require one object to be a point mass in order to carry out the mass attraction calculation. By using the equations presented in this work, neither object needs to be represented as a point mass in order to calculate the mass attraction properties. The mass attraction equations presented utilize a multivariable Taylor Series expansion to achieve the final form. Since Poisson in the 1800's [46], a number of individuals have utilized a Taylor Series expansion to calculate the mass attraction equations. Indeed, this work will utilize a similar approach for solving the gravitational attraction equations. Yet, to

the authors knowledge no solution before has listed the terms beyond a second order expansion for the case of two general shaped bodies and are therefore not complete solutions. The work presented in in Chapter 3 does not limit the analysis to point mass objects and may be represented to the desired expansion order.

Whenever performing mass attraction analyses, the calculation is only as good as the knowledge of the mass properties. The model, which typically assumes ideal mass properties, is therefore only an approximation of the true physical system. The theory presented in Chapter 3 also establishes the insight necessary for incorporating physically measurable quantities into the analysis. It will be shown that through a second order expansion, the gravitational attraction equations consist of the measurable terms of mass, mass center and the moment of inertia tensor. Thus, the method described in this work incorporates physically measurable mass properties into the analysis, such that the calculation is an indirect measurement of the gravitational attraction properties through the second order. Should a higher order expansion be desired, the remaining terms in the expansion are of third order and higher and only require modest geometry and density distribution knowledge compared to a point mass finite element solution. Thus, the density distribution and geometry does not need to be known as accurately as required for common point mass finite element solution methods. By incorporating physical measurements into the calculation, one eliminates uncertainties due to ideal assumptions involving density inhomogeneities and geometrical variations. The mass attraction analysis is no longer a theoretical model of the attraction properties for the system, but rather an indirect measurement of the actual physical system through the second order.

The equations developed in Part I are significant for a number of other reasons which may not be immediately apparent. The developed equations allow for the satellite designer to perform indirect measurements of the mass attraction force and gradients as well as to develop initial multiphysics simulations/models including mass attraction effects. Also developed in Chapter 3 are the necessary equations for incorporating tetrahedron finite elements into mass attraction computations. This developed method therefore allows for an early design using software models and expected idealized mass properties. As the physical hardware becomes available, measured

values for the mass properties can then be used in the analysis to refine the mass attraction properties. Once the measured parameters become available, a full scale finite element analysis need not necessarily be performed again in order to obtain the mass attraction properties. Simply by tabulating mass properties of each component or subsystem, the attraction properties can be re-calculated easily for any redesign resulting in a component location or orientation change.

### 1.3.2 Precision Mass Property Measurements

Part II of this work focuses on the measurement of the necessary mass properties for a mass attraction calculation. The theory for determining mass property measurements by means of a torsion pendulum is detailed in Chapter 4. The design of a novel five-wire torsion pendulum measurement apparatus for precision mass property measurements is then described in Chapter 5.

The five-wire design is vastly different from the common single wire or trifilar torsion pendulum design often used for science experiments. Such pendulum designs are desired to be very sensitive to extraneous forces and as a result have very low damping coefficients with the torsional quality factor,  $Q = 1/2\zeta$ , ranging from  $10^4$  to  $10^6$  or higher [6]. The five-wire design has a much higher stiffness, with the quality factor,  $Q$ , of 3000 or less such that the pendulum is not highly sensitive to external forces. The goal of the five-wire torsion pendulum design is rather to generate a pure rotation about a desired axis with translational degrees of freedom spectrally shifted from the rotation frequency. This new five-wire pendulum design is carried through the initial prototype stage and is described in detail in Chapter 5. The apparatus is then used to measure the mass properties of mass center location and the moment of inertia tensor (Chapter 6). Although the apparatus is still an initial prototype design, the results from the five-wire torsion pendulum match state of the art moment of inertia measurement levels. The pendulum error sources and limitations for the initial design are fully characterized in Chapter 7. With minimal work to suppress laboratory environmental disturbances, the five-wire pendulum is expected to exceed state of the art moment of inertia measurements by almost an order of magnitude.

The five-wire torsion pendulum was primarily designed for measuring moments of inertia. Still, the pendulum performance motivated the application of the pendulum to mass center location measurements. As shown in Chapter 6, the pendulum demonstrates the ability to determine the mass center location to levels better than typical mass center measurement devices. Again, the original pendulum design was not originally intended for mass center measurements. By utilizing the knowledge presented in Chapter 7 to reduce environmental disturbances and the suggestions for future mass center measurement work in Chapter 8, the basic design could potentially be developed for state of the art mass center measurements.

### 1.3.3 Synthesis of Contributions

By combining the theory presented in Part I and the physical mass property measurements presented in Part II, it is possible to show the importance of combining physically measured mass properties into the mass attraction calculation. Consider for example the gravitational mass attraction between two distributed bodies. The difference in the gravitational mass attraction calculation between a simplified point mass attraction and the method developed in Chapter 3 is significant.

For illustrative purposes, consider the gravitational mass attraction between two reference masses as shown in Figure 1.4. A cross sectional view of the objects is depicted. These objects will be further described in Chapter 6 and are referred to as preferred principal axis of inertia spheres. The spheres contain an internal cavity in order to create a spherical shaped object with desired mass properties and are fabricated in either two or three parts. The sphere depicted at the bottom of Figure 1.4 is a three-part sphere and the top sphere is a two-part sphere. Both spheres are of identical radius,  $r_o$ , and the mass centers of the reference masses are separated by  $\bar{R} = 3r_o\hat{z}$ , where  $\hat{z}$  is along the direction for the maximum principal moment of inertia,  $I_3$ , for each reference mass. The configuration in Figure 1.4 provides a mass attraction example for which precision mass property measurements exist for both attracting bodies. The torsion pendulum measurement apparatus, which will be described in detail in Chapter 5, was used to obtain the moment of inertia tensor

for each object to approximately state of the art precision.

For the simplified example in Figure 1.4, the attraction force between two preferred principal axis of inertia spheres is investigated by using a point mass approximation and then by the method described in Chapter 3 of this work. First the attraction force is calculated by assuming each object may be represented by a single point mass, such that the attraction force is given by  $\vec{F}_p = GMm/R^2 \hat{z}$ . The three-part sphere has a measured mass,  $M$ , of 455.1 g and the two-part sphere has a measured mass,  $m$ , of 448.9 g. Next, the attraction force is calculated by utilizing the equations derived using the double Taylor method from Chapter 3, Equation 3.43, and the measured quantities for the moment of inertia as presented in Chapter 6, Table 6.6. The simplified point mass attraction computation results in  $\vec{F}_z = G \cdot 36.319 \text{ N}$ , whereas the double Taylor method results in an attraction force of  $\vec{F}_z = G \cdot 35.204 \text{ N}$ . The difference,  $100\% \times (F_p - F_{DT})/F_{DT}$ , is about 3.2%. The double Taylor method described in this work contains as the first term the simplified point mass attraction result. The additional terms in the expansion therefore account for the geometry and density distribution. Thus, the 3.2% difference noted here is completely due to incorporation of the measured moment of inertia into the calculation. Thus, it is seen that the incorporation of measured mass properties substantially aids in increasing the accuracy of the mass

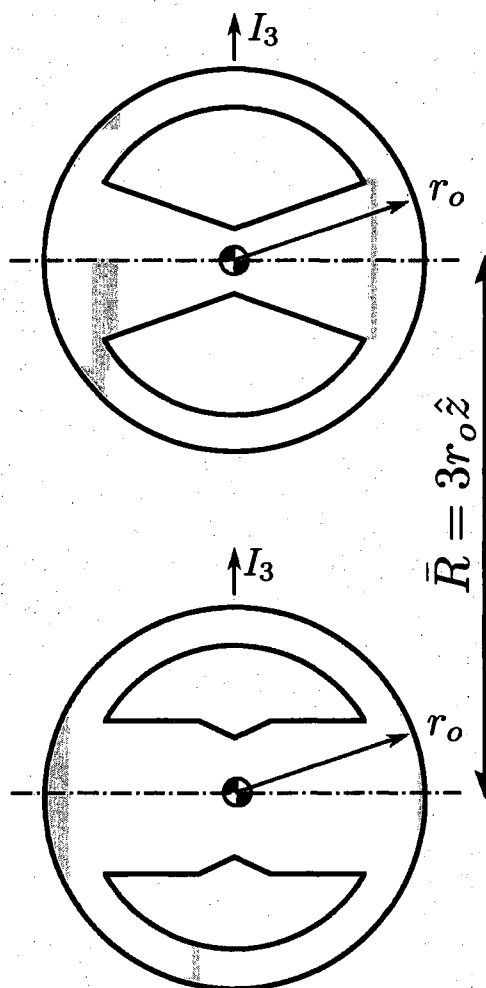


Figure 1.4: Configuration for gravitational mass attraction example.

attraction calculation. In addition, the computation utilizing the measured mass properties incorporates any uncertainty associated with the internal geometry of the spheres and the actual material density distribution. The cross-sectional view depicted in Figure 1.4 is a simplified ideal geometry for the preferred principal axis of inertia spheres. The actual internal geometry, which is not easily measured after fabrication, does not match exactly the depicted idealized geometry due to the fabrication process.



**Part I**

**Gravitational Mass Attraction.**

**In Theory.**

# Chapter 2

## Traditional Solution Methods

### 2.1 Point Mass Summation

For point mass objects<sup>1</sup> and for objects which are separated by great distances, the Newtonian gravitational potential at a point due to an attracting body is defined to be:

$$U = \frac{GM}{r} \quad (2.1)$$

where  $G$  is the gravitational constant,  $M$  is the mass of the attracting body and  $r$  is the distance between the point mass and the body. The gravitational attraction force vector is then given by the gradient of the Newtonian potential. Taking the negative gradient of the potential for a test mass at a point, the Newtonian Force is obtained:

$$\frac{d\vec{F}}{m_1} = -\frac{G dM}{r^2} \hat{r} \quad (2.2)$$

where the force is defined to be along the vector  $\hat{r}$  between the point mass and the body. For two distributed bodies, one could in principle develop a simple routine which repeatedly calculates the force over a very fine grid point representation of the

---

<sup>1</sup>The avid reader should note that a spherical shell exhibits the same properties as a point mass. Thus, a body composed of concentric spherical shells, each of uniform density, also obeys the same properties as a point mass.

mass distribution. However, although it is known that this direct summation method is robust and reasonably accurate, the accuracy depends strongly on the number of point masses which are used to represent the mass distribution. In addition, the required point mass grid density is a function of the separation distance, the object geometry complexity and the desired density distribution. As a result, to obtain a high degree of accuracy, the computational cost is high and scales by the order of the number of total points squared.

The primary limitation of a brute force point mass summation approach is however not the number of points and associated computational cost. Consider for example an initial gravitational mass attraction analysis performed for LISA. Merkowit et. al [42] has applied a brute force point mass summation technique to the LISA spacecraft. The model for the spacecraft was generated from computer solid models to produce a finite element model of all the satellite components, assuming ideal geometry, density distribution and component location. After running the computation repeatedly until a convergence was observed, the initial results using the point mass summation showed that preliminary designs for LISA were only a factor of 4 to 5 times worse than minimum requirements for the gravitational attraction properties of the satellite [42]. At first one might believe that the preliminary results indicate LISA is achievable with a simple point mass representation of the satellite for computing the gravitational attraction force and gradients. Yet the model is merely an approximation of the actual physical system. It would be naive to believe that a point mass attraction model alone would suffice for verifying the mass attraction disturbance requirements. In fact, the results from the point mass model only test how well the satellite is symmetrically distributed, or in a dynamic sense how stable the satellite configuration is expected to be. Clearly, "the models are only as good as our knowledge of the mass distribution" [42]. Thus, the *uncertainty* in how well the model matches the physical system is the primary limitation of the point mass summation approach. In actuality, there is a great deal of uncertainty in the actual mass distribution for the components comprising the satellite. Consider for example the core component, the drag-free reference mass. The current baseline LISA pathfinder proof mass, Figure 2.1, is a faceted geometry similar to a cube, composed of a gold-platinum alloy. By inspection

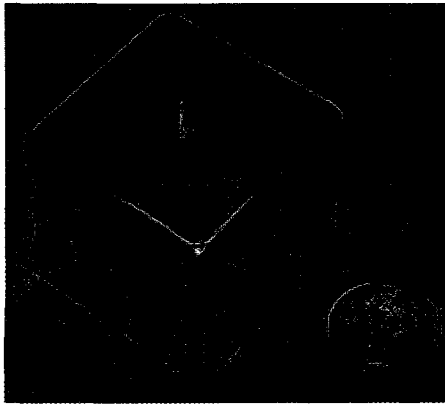


Figure 2.1: Baseline LISA reference mass. The gold-platinum alloy reference mass has geometric features preventing a simple representation as a single point mass or as an ideal cube.

of Figure 2.1, it is clear that the geometry contains features which prevent either a representation as a perfect cubical geometry for analytical solutions or by only a few point masses for a point mass summation approach. In addition, it is not possible to determine the sub-millimeter density distribution of the gold-platinum alloy required for the grid size dictated by the point mass finite element model [41]. The overall accuracy of the model will therefore be limited by the uncertainty in the geometry and density distribution. Therefore, some sort of experimental verification is necessary to validate the models.

## 2.2 MacCullagh's Formula

In the early 1800's Poisson [46] suggested the use of a Taylor Series expansion to represent the Potential. The  $1/r$  term could easily be expanded in a series and then truncated after the 2nd order. MacCullagh [31] then further developed the technique by showing that the equation for the Potential at a point due to a distributed body could be represented by the principal moment of inertia for the distributed body. The formula for the potential at point  $P$  due to an arbitrary distributed body, known as

MacCullagh's formula, is given by:

$$U(P) = \frac{GM}{r} + \frac{G}{2r^3} (I_{xx} + I_{yy} + I_{zz} - 3I) \quad (2.3)$$

MacCullagh assumes that the origin of the coordinate system is located at the center of mass of the distributed body and that principal coordinate axes are used. The value of  $I$  in MacCullagh's formula is the instantaneous moment of inertia about the direction from the origin to point  $P$ . MacCullagh also developed equations for the Force and Moments at a point due to a distributed body. If one eliminates the assumption of principal axes in MacCullagh's formula the equation can be generalized as<sup>2</sup>:

$$U(P) = \frac{GM}{r} + \frac{G}{2r^3} \left( \text{trace}(\bar{I}) - 3\hat{r} \cdot \bar{I} \cdot \hat{r} \right) \quad (2.4)$$

Although it is not explicitly stated, Equation 2.4 forms the foundation for much of the work done by Fleming et. al [22] for the Mass attraction analysis of the Triad-1/DISCOS mission. Fleming develops equations for the attraction force on a point mass due to a number of different common-shaped distributed bodies. Although Fleming no longer requires that principal axes be used, the orientation of the axes used is specified such that the  $\hat{x}_1$  direction in a standard Cartesian coordinate system is along the vector between the point mass and the center of mass of the distributed body. Equation 2.4 is a general form and eliminates requirements on the orientation of the coordinate axes. Still, one limitation in applying the method of MacCullagh and Fleming et. al to gravitational wave observatories such as LISA, is that the calculation requires one object to be represented by a single point mass. As already shown in Figure 2.1, the baseline proof mass for LISA may not be easily represented by a single point mass geometry. It is therefore desired to develop the equations further to include the attraction properties between two general distributed bodies. In Chapter 3, equations will be developed, which overcome the limitation of the single point mass requirement.

---

<sup>2</sup>The generalized MacCullagh's formula is derived in Section 3.3

## 2.3 Analytical Solution: Block Geometry

For a spherical geometry, simple point mass gravitational attraction equations can be used to easily calculate the force and force gradients. For the LISA faceted proof mass design, the point mass attraction equations can only be used to approximate the non-spherical geometry for locations which are far from the proof mass relative to the maximum dimension of the proof mass. For locations which are near to the proof-mass, a more detailed calculation is necessary.

An analytic solution for the gravitational mass attraction force and force gradients due to a right-angled parallelepiped or a brick geometry is desired. The solution over a rectangular region is not a trivial derivation and is not widely published. A few works have been published which work toward developing the gravitational mass attraction force equations for a brick geometry. MacMillan [40] has outlined a method for deriving the equations governing the gravitational potential at a point due to a right-angled parallelepiped with homogeneous density. Nagy [43] presents the vertical component equation for the mass attraction force and the limitations of which are later noted and corrected by Banerjee [2]. Chen and Cook [7] determine an expression for the mass attraction force in the three principal orthogonal directions for a uniform rectangular block by applying the method of MacMillan. However typographical errors in the expression as published by Chen and Cook [7] results in a correct answer for the mass attraction force only along the principal axes. Careful analysis of the published equations by Chen and Cook indicate a region where a repelling force exists, which is clearly in error. Therefore, presented here is what is believed to be the corrected version of the mass attraction force for all regions due to a right-angled parallelepiped with homogeneous density. The expression is then further developed to generate an expression for the gradients of the mass attraction force with respect to the principal directions. Finally, the derived force and gradient equations for a brick geometry are compared to a point mass approximation in an attempt to estimate the accuracy of such an approximation for the brick geometry for applications such as LISA.

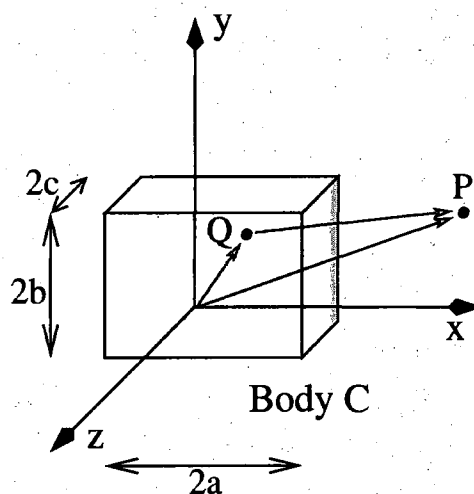


Figure 2.2: Attraction at a point due to a brick-shaped body.

### 2.3.1 Attraction Force

To obtain an expression for the mass attraction force at a point due to a right-angled parallelepiped, it is recognized that by definition the mass attraction force is the gradient of the gravitational potential. Let point  $P = (x, y, z)$  be a point external to the body for which the force shall be computed. The potential at point  $P$  for the coordinate system placed at the center of mass of the distributed mass, body  $C$ , is defined to be:

$$U(P) = G \iiint_V \sigma^c \frac{1}{r} dV \quad (2.5)$$

Where the density of body  $C$  is denoted by  $\sigma^c$  and the integration is performed over the volume  $V$  occupied by the mass. The distance,  $r$ , between point  $P$  and a point  $Q = (u, v, w)$  located within body  $C$  in Cartesian coordinates is:

$$r = \sqrt{\vec{r}^{P/Q} \cdot \vec{r}^{P/Q}} = \sqrt{(x - u)^2 + (y - v)^2 + (z - w)^2} \quad (2.6)$$

The force is the negative gradient of the potential. The component of the force in the Cartesian  $x$ -direction for a test point mass  $m^P$  at point  $P$  due to body  $C$  with

homogeneous density is:

$$-\frac{F_x^{P/C}}{G m^P} = \sigma^c \iiint_V \frac{\partial}{\partial x} \left( \frac{1}{\sqrt{(x-u)^2 + (y-v)^2 + (z-w)^2}} \right) du dv dw \quad (2.7)$$

Recognizing that an increase in the coordinate  $u$  is equivalent to a negative change in the coordinate  $x$ , one obtains:

$$\begin{aligned} -\frac{F_x^{P/C}}{G m^P} &= -\sigma^c \iiint_V \frac{\partial}{\partial u} \left( \frac{1}{\sqrt{(x-u)^2 + (y-v)^2 + (z-w)^2}} \right) du dv dw \quad (2.8) \\ &= -\sigma^c \iint_A \left[ \frac{1}{\sqrt{(x-u)^2 + (y-v)^2 + (z-w)^2}} \right]_{u_1}^{u_2} dv dw \end{aligned}$$

For a right-angled parallelepiped with length  $2a$ ,  $2b$ , and  $2c$  in the  $x$ ,  $y$ ,  $z$  direction, Figure 2.2, the limits of integration are simple and the integral equation for the force becomes:

$$\begin{aligned} \frac{F_x^{P/C}}{G m^P} &= \sigma^c \int_{-c}^c \int_{-b}^b \frac{1}{\sqrt{(x-a)^2 + (y-v)^2 + (z-w)^2}} dv dw - \\ &\quad \sigma^c \int_{-c}^c \int_{-b}^b \frac{1}{\sqrt{(x+a)^2 + (y-v)^2 + (z-w)^2}} dv dw \quad (2.9) \end{aligned}$$

It is seen that in order to evaluate the equation for the force, two double integrals of similar form must be evaluated. Following the style of Chen and Cook [7], the double integral will be simply replaced by a function representation. The double integral will be defined to be:

$$\Psi = \int_{-c}^c \int_{-b}^b \frac{1}{\sqrt{(x-a)^2 + (y-v)^2 + (z-w)^2}} dv dw \quad (2.10)$$

To evaluate the  $\Psi$  integral, the method described in MacMillan [40] is used. First,



multiply the numerator and denominator by the square of the integrand denominator.

$$\Psi = \int_{-c}^c \int_{-b}^b \frac{(x-a)^2 + (y-v)^2 + (z-w)^2}{\left((x-a)^2 + (y-v)^2 + (z-w)^2\right)^{\frac{3}{2}}} dv dw \quad (2.11)$$

By adding and subtracting the quantity  $(x-a)^2$  to the numerator, the integrand can be separated, resulting in three simpler to evaluate integrals:

$$\begin{aligned} \Psi &= \int_{-c}^c \int_{-b}^b \frac{(x-a)^2 + (y-v)^2}{\left((x-a)^2 + (y-v)^2 + (z-w)^2\right)^{\frac{3}{2}}} dv dw + \\ &\quad \int_{-c}^c \int_{-b}^b \frac{(x-a)^2 + (z-w)^2}{\left((x-a)^2 + (y-v)^2 + (z-w)^2\right)^{\frac{3}{2}}} dv dw - \\ &\quad \int_{-c}^c \int_{-b}^b \frac{(x-a)^2}{\left((x-a)^2 + (y-v)^2 + (z-w)^2\right)^{\frac{3}{2}}} dv dw \end{aligned} \quad (2.12)$$

At first it may appear as though the evaluation of one double integral was made more difficult by generating three double integrals. Yet the first two integrals in Equation 2.12 can be rewritten in terms of exact derivatives, namely:

$$\begin{aligned} -\frac{\partial}{\partial w} \left( \frac{(z-w)}{\left((x-a)^2 + (y-v)^2 + (z-w)^2\right)^{\frac{1}{2}}} \right) &= \frac{(x-a)^2 + (y-v)^2}{\left((x-a)^2 + (y-v)^2 + (z-w)^2\right)^{\frac{3}{2}}} \\ -\frac{\partial}{\partial v} \left( \frac{(y-v)}{\left((x-a)^2 + (y-v)^2 + (z-w)^2\right)^{\frac{1}{2}}} \right) &= \frac{(x-a)^2 + (z-w)^2}{\left((x-a)^2 + (y-v)^2 + (z-w)^2\right)^{\frac{3}{2}}} \end{aligned} \quad (2.13)$$

Substituting the exact derivatives of equation 2.13 into the integrand of equation 2.12,

the  $\Psi$  integral takes on the new form:

$$\begin{aligned} \Psi = & - \int_{-c}^c \int_{-b}^b \frac{\partial}{\partial w} \left( \frac{(z-w)}{\left((x-a)^2 + (y-v)^2 + (z-w)^2\right)^{\frac{1}{2}}} \right) dv dw - \\ & \int_{-c}^c \int_{-b}^b \frac{\partial}{\partial v} \left( \frac{(y-v)}{\left((x-a)^2 + (y-v)^2 + (z-w)^2\right)^{\frac{1}{2}}} \right) dv dw - \\ & - \int_{-c}^c \int_{-b}^b \frac{(x-a)^2}{\left((x-a)^2 + (y-v)^2 + (z-w)^2\right)^{\frac{3}{2}}} dv dw \end{aligned} \quad (2.14)$$

The limits of integration are constants, and can thus be easily interchanged to obtain:

$$\begin{aligned} \Psi = & - \int_{-b}^b \left[ \frac{(z-w)}{\left((x-a)^2 + (y-v)^2 + (z-w)^2\right)^{\frac{1}{2}}} \right]_{-c}^c dv - \\ & \int_{-c}^c \left[ \frac{(y-v)}{\left((x-a)^2 + (y-v)^2 + (z-w)^2\right)^{\frac{1}{2}}} \right]_{-b}^b dw - \\ & \int_{-c}^c \int_{-b}^b \frac{(x-a)^2}{\left((x-a)^2 + (y-v)^2 + (z-w)^2\right)^{\frac{3}{2}}} dv dw \end{aligned} \quad (2.15)$$

Evaluating at the limits of integration gives:

$$\begin{aligned} \Psi = & - \int_{-b}^b \frac{(z-c)}{\left((x-a)^2 + (y-v)^2 + (z-c)^2\right)^{\frac{1}{2}}} dv + \\ & \int_{-b}^b \frac{(z+c)}{\left((x-a)^2 + (y-v)^2 + (z+c)^2\right)^{\frac{1}{2}}} dv - \end{aligned}$$

$$\begin{aligned}
& \int_{-c}^c \frac{(y-b)}{\left((x-a)^2 + (y-b)^2 + (z-w)^2\right)^{\frac{1}{2}}} dw + \\
& \int_{-c}^c \frac{(y+b)}{\left((x-a)^2 + (y+b)^2 + (z-w)^2\right)^{\frac{1}{2}}} dw - \\
& \int_{-c}^c \int_{-b}^b \frac{(x-a)^2}{\left((x-a)^2 + (y-v)^2 + (z-w)^2\right)^{\frac{3}{2}}} dv dw \quad (2.16)
\end{aligned}$$

All of the single integrals in Equation 2.16 have a common form, which can be evaluated using a table of integrals:

$$\int \frac{1}{\sqrt{\xi^2 + \alpha^2 + \beta^2}} d\xi = \ln \left( \xi + \sqrt{\xi^2 + \alpha^2 + \beta^2} \right)$$

After evaluating the single integrals in Equation 2.16 the  $\Psi$  integral can be algebraically manipulated to produce:

$$\begin{aligned}
\Psi = & (y-b) \ln \frac{(z-c) + \left((x-a)^2 + (y-b)^2 + (z-c)^2\right)^{\frac{1}{2}}}{(z+c) + \left((x-a)^2 + (y-b)^2 + (z+c)^2\right)^{\frac{1}{2}}} - \\
& (y+b) \ln \frac{(z-c) + \left((x-a)^2 + (y+b)^2 + (z-c)^2\right)^{\frac{1}{2}}}{(z+c) + \left((x-a)^2 + (y+b)^2 + (z+c)^2\right)^{\frac{1}{2}}} + \\
& (z-c) \ln \frac{(y-b) + \left((x-a)^2 + (y-b)^2 + (z-c)^2\right)^{\frac{1}{2}}}{(y+b) + \left((x-a)^2 + (y+b)^2 + (z-c)^2\right)^{\frac{1}{2}}} - \\
& (z+c) \ln \frac{(y-b) + \left((x-a)^2 + (y-b)^2 + (z+c)^2\right)^{\frac{1}{2}}}{(y+b) + \left((x-a)^2 + (y+b)^2 + (z+c)^2\right)^{\frac{1}{2}}} -
\end{aligned}$$

$$\int_{-c}^c \int_{-b}^b \frac{(x-a)^2}{\left((x-a)^2 + (y-v)^2 + (z-w)^2\right)^{\frac{3}{2}}} dv dw \quad (2.17)$$

The double integral term in the  $\Psi$  integral remains to be evaluated. Again the technique of converting the integrand into an exact derivative will be used. The quantities  $x-a$  and  $z-w$  are constants with respect to the variable  $v$ . Thus one can write the exact derivative:

$$\begin{aligned} -\frac{\partial}{\partial v} \left( \frac{(y-v)}{\left((x-a)^2 + (z-w)^2\right) \left((x-a)^2 + (y-v)^2 + (z-w)^2\right)^{\frac{1}{2}}} \right) \\ = \frac{1}{\left((x-a)^2 + (y-v)^2 + (z-w)^2\right)^{\frac{3}{2}}} \end{aligned} \quad (2.18)$$

Replacing the exact derivative for the integrand within the double integral term in the  $\Psi$  integral, the double integral becomes:

$$\begin{aligned} -\int_{-c}^c \int_{-b}^b \frac{(x-a)^2}{\left((x-a)^2 + (y-v)^2 + (z-w)^2\right)^{\frac{3}{2}}} dv dw \quad (2.19) \\ = \int_{-c}^c \int_{-b}^b \frac{\partial}{\partial v} \left( \frac{(x-a)^2 (y-v)}{\left((x-a)^2 + (z-w)^2\right) \left((x-a)^2 + (y-v)^2 + (z-w)^2\right)^{\frac{1}{2}}} \right) dv dw \end{aligned}$$

Evaluating at the limits of integration one has:

$$\begin{aligned} -\int_{-c}^c \int_{-b}^b \frac{(x-a)^2}{\left((x-a)^2 + (y-v)^2 + (z-w)^2\right)^{\frac{3}{2}}} dv dw = \\ \int_{-c}^c \frac{(x-a)^2 (y-b)}{\left((x-a)^2 + (z-w)^2\right) \left((x-a)^2 + (y-b)^2 + (z-w)^2\right)^{\frac{1}{2}}} dw - \end{aligned}$$

$$\int_{-c}^c \frac{(x-a)^2 (y+b)}{\left( (x-a)^2 + (z-w)^2 \right) \left( (x-a)^2 + (y+b)^2 + (z-w)^2 \right)^{\frac{1}{2}}} dw \quad (2.20)$$

The two single integrals in Equation 2.20 have a common form, which can be evaluated using a table of integrals:

$$\int \frac{\alpha^2 \beta}{(\alpha^2 + \xi^2)(\alpha^2 + \beta^2 + \xi^2)^{\frac{1}{2}}} d\xi = \alpha \tan^{-1} \frac{\beta \xi}{\alpha (\alpha^2 + \beta^2 + \xi^2)^{\frac{1}{2}}} \quad (2.21)$$

Evaluating the single integrals in Equation 2.20 the double integral is found to be:

$$\begin{aligned} & - \int_{-c}^c \int_{-b}^b \frac{(x-a)^2}{\left( (x-a)^2 + (y-v)^2 + (z-w)^2 \right)^{\frac{3}{2}}} dv dw = \\ & - (x-a) \tan^{-1} \frac{(y-b)(z-c)}{(x-a) \left( (x-a)^2 + (y-b)^2 + (z-c)^2 \right)^{\frac{1}{2}}} + \\ & (x-a) \tan^{-1} \frac{(y-b)(z+c)}{(x-a) \left( (x-a)^2 + (y-b)^2 + (z+c)^2 \right)^{\frac{1}{2}}} + \\ & (x-a) \tan^{-1} \frac{(y+b)(z-c)}{(x-a) \left( (x-a)^2 + (y+b)^2 + (z-c)^2 \right)^{\frac{1}{2}}} + \\ & - (x-a) \tan^{-1} \frac{(y+b)(z+c)}{(x-a) \left( (x-a)^2 + (y+b)^2 + (z+c)^2 \right)^{\frac{1}{2}}} \end{aligned} \quad (2.22)$$

Using the results of Equation 2.17 and Equation 2.22, the  $\Psi$  Integral can be written in function form to be:

$$\begin{aligned} \Psi(\alpha, \beta, \tilde{\beta}, \gamma, \tilde{\gamma}) = \\ \beta \ln \frac{\gamma + \left( \alpha^2 + \beta^2 + \gamma^2 \right)^{\frac{1}{2}}}{\tilde{\gamma} + \left( \alpha^2 + \beta^2 + \tilde{\gamma}^2 \right)^{\frac{1}{2}}} - \tilde{\beta} \ln \frac{\gamma + \left( \alpha^2 + \tilde{\beta}^2 + \gamma^2 \right)^{\frac{1}{2}}}{\tilde{\gamma} + \left( \alpha^2 + \tilde{\beta}^2 + \tilde{\gamma}^2 \right)^{\frac{1}{2}}} + \end{aligned}$$

$$\begin{aligned}
& +\gamma \ln \frac{\beta + (\alpha^2 + \beta^2 + \gamma^2)^{\frac{1}{2}}}{\tilde{\beta} + (\alpha^2 + \tilde{\beta}^2 + \gamma^2)^{\frac{1}{2}}} - \tilde{\gamma} \ln \frac{\beta + (\alpha^2 + \beta^2 + \tilde{\gamma}^2)^{\frac{1}{2}}}{\tilde{\beta} + (\alpha^2 + \tilde{\beta}^2 + \tilde{\gamma}^2)^{\frac{1}{2}}} + \\
& -\alpha \tan^{-1} \frac{\beta \gamma}{\alpha (\alpha^2 + \beta^2 + \gamma^2)^{\frac{1}{2}}} + \alpha \tan^{-1} \frac{\beta \tilde{\gamma}}{\alpha (\alpha^2 + \beta^2 + \tilde{\gamma}^2)^{\frac{1}{2}}} + \\
& +\alpha \tan^{-1} \frac{\tilde{\beta} \gamma}{\alpha (\alpha^2 + \tilde{\beta}^2 + \gamma^2)^{\frac{1}{2}}} - \alpha \tan^{-1} \frac{\tilde{\beta} \tilde{\gamma}}{\alpha (\alpha^2 + \tilde{\beta}^2 + \tilde{\gamma}^2)^{\frac{1}{2}}} \quad (2.23)
\end{aligned}$$

Equation 2.23 can then be used to evaluate the Equations for the force components at point  $P$  due to body  $C$  for coordinate locations external to the attracting body. The integral equation for the force components at point  $P$  due to body  $C$ , as presented by Chen and Cook [7], can now be represented by:

$$\frac{F_x^{P/C}}{G \sigma^c m^P} = \Psi(\bar{\mathcal{X}}) - \Psi(\bar{\bar{\mathcal{X}}}) \quad (2.24)$$

$$\frac{F_y^{P/C}}{G \sigma^c m^P} = \Psi(\bar{\mathcal{Y}}) - \Psi(\bar{\bar{\mathcal{Y}}}) \quad (2.25)$$

$$\frac{F_z^{P/C}}{G \sigma^c m^P} = \Psi(\bar{\mathcal{Z}}) - \Psi(\bar{\bar{\mathcal{Z}}}) \quad (2.26)$$

where:

$$\bar{\mathcal{X}} = [(x - a), (y - b), (y + b), (z - c), (z + c)]$$

$$\bar{\bar{\mathcal{X}}} = [(x + a), (y - b), (y + b), (z - c), (z + c)]$$

$$\bar{\mathcal{Y}} = [(y - b), (z - c), (z + c), (x - a), (x + a)]$$

$$\bar{\bar{\mathcal{Y}}} = [(y + b), (z - c), (z + c), (x - a), (x + a)]$$

$$\bar{\mathcal{Z}} = [(z - c), (x - a), (x + a), (y - b), (y + b)]$$

$$\bar{\bar{\mathcal{Z}}} = [(z + c), (x - a), (x + a), (y - b), (y + b)]$$

### 2.3.2 Gradient of the Attraction Force

The current LISA mission baseline design incorporates a cubical free-falling proof mass in a drag-free configuration. The drag-free control laws require knowledge of the force gradients to model stiffness terms properly. Having established a representation of the mass attraction force at a single point due to a regular rectangular block, one can proceed to develop the properties of the gravitational mass attraction force gradients. A brute force differentiation of the force equations is possible, since the equations are composed of elementary terms. The process consists of returning to the original integral equations for the potential to take the derivatives instead of starting with integrated form of the force equations. Yet in order to obtain the desired result in a simpler manner, one returns to the suggestion presented by MacMillan [40] to obtain the force equations from the potential:

“It is not necessary to differentiate with respect to the coordinates in so far as these coordinates appear under the log and  $\tan^{-1}$  symbols. It is sufficient to differentiate as though these functions were constants, and a recognition of this fact makes the differentiation a very simple manner.”

By extension, since one can treat the  $\tan^{-1}$  and  $\ln$  terms as constants during the differentiation of the potential to obtain the force, these same terms should also be considered as constants on subsequent differentiations. The proof for making this assumption is presented in MacMillan [40] and is discussed further at the end of Section 2.3.2. Indeed, by noting the constant characteristics of the terms within the force equation, the derivation of the force gradients becomes quite straight-forward. To differentiate the force equations, it is sufficient to differentiate the  $\Psi(\alpha, \beta, \tilde{\beta}, \gamma, \tilde{\gamma})$  function with respect to each of the function arguments, treating the  $\ln$  and  $\tan^{-1}$  terms as constants. Differentiating with respect to  $\alpha$ , one obtains:

$$\frac{\partial \Psi}{\partial \alpha} = \Psi_{\alpha} = -\tan^{-1} \frac{\beta \gamma}{\alpha(\alpha^2 + \beta^2 + \gamma^2)^{\frac{1}{2}}} + \tan^{-1} \frac{\beta \tilde{\gamma}}{\alpha(\alpha^2 + \beta^2 + \tilde{\gamma}^2)^{\frac{1}{2}}} +$$

$$+ \tan^{-1} \frac{\tilde{\beta} \gamma}{\alpha(\alpha^2 + \tilde{\beta}^2 + \gamma^2)^{\frac{1}{2}}} - \tan^{-1} \frac{\tilde{\beta} \tilde{\gamma}}{\alpha(\alpha^2 + \tilde{\beta}^2 + \tilde{\gamma}^2)^{\frac{1}{2}}} \quad (2.27)$$

Differentiating with respect to the remaining variables returns:

$$\frac{\partial \Psi}{\partial \beta} = \Psi_\beta = \ln \frac{\gamma + (\alpha^2 + \beta^2 + \gamma^2)^{\frac{1}{2}}}{\tilde{\gamma} + (\alpha^2 + \beta^2 + \tilde{\gamma}^2)^{\frac{1}{2}}} \quad (2.28)$$

$$\frac{\partial \Psi}{\partial \tilde{\beta}} = \Psi_{\tilde{\beta}} = - \ln \frac{\gamma + (\alpha^2 + \tilde{\beta}^2 + \gamma^2)^{\frac{1}{2}}}{\tilde{\gamma} + (\alpha^2 + \tilde{\beta}^2 + \tilde{\gamma}^2)^{\frac{1}{2}}} \quad (2.29)$$

$$\frac{\partial \Psi}{\partial \gamma} = \Psi_\gamma = \ln \frac{\beta + (\alpha^2 + \beta^2 + \gamma^2)^{\frac{1}{2}}}{\tilde{\beta} + (\alpha^2 + \tilde{\beta}^2 + \gamma^2)^{\frac{1}{2}}} \quad (2.30)$$

$$\frac{\partial \Psi}{\partial \tilde{\gamma}} = \Psi_{\tilde{\gamma}} = - \ln \frac{\beta + (\alpha^2 + \beta^2 + \tilde{\gamma}^2)^{\frac{1}{2}}}{\tilde{\beta} + (\alpha^2 + \tilde{\beta}^2 + \tilde{\gamma}^2)^{\frac{1}{2}}} \quad (2.31)$$

By inspecting Equation 2.24 it is easily seen that the gradient of the force in the  $x$ -direction with respect to  $x$  involves the partial derivative of the  $\Psi$  function with respect to  $\alpha$ . Hence one obtains:

$$\frac{1}{G \sigma^c m^P} \frac{\partial F_x^{P/C}}{\partial x} = \Psi_\alpha(\bar{\mathcal{X}}) - \Psi_\alpha(\tilde{\mathcal{X}}) \quad (2.32)$$

Similarly, according to Equations 2.25 and 2.26 the gradients of the  $y$ - and  $z$ -direction forces with respect to  $y$  and  $z$  respectively are:

$$\frac{1}{G \sigma^c m^P} \frac{\partial F_y^{P/C}}{\partial y} = \Psi_\alpha(\bar{\mathcal{Y}}) - \Psi_\alpha(\tilde{\mathcal{Y}}) \quad (2.33)$$

$$\frac{1}{G \sigma^c m^P} \frac{\partial F_z^{P/C}}{\partial z} = \Psi_\alpha(\bar{\mathcal{Z}}) - \Psi_\alpha(\tilde{\mathcal{Z}}) \quad (2.34)$$



To obtain the gradients of the force in the  $x$ -direction with respect to  $y$ , the partial derivatives of  $\beta$  and  $\tilde{\beta}$  are involved. Since  $\beta$  and  $\tilde{\beta}$  occur linearly outside of the  $\ln$  and  $\tan^{-1}$  functions, a linear combination of  $\Psi_\beta$  and  $\Psi_{\tilde{\beta}}$  is sufficient to represent the gradients of the force in the  $x$ -direction with respect to the variable  $y$ . Denoting the linear combination of the partial derivatives with respect to  $\beta$  and  $\tilde{\beta}$  as:

$$\Psi_\beta(\alpha, \beta, \tilde{\beta}, \gamma, \tilde{\gamma}) + \Psi_{\tilde{\beta}}(\alpha, \beta, \tilde{\beta}, \gamma, \tilde{\gamma}) = [\Psi_\beta + \Psi_{\tilde{\beta}}](\alpha, \beta, \tilde{\beta}, \gamma, \tilde{\gamma}) \quad (2.35)$$

the gradient of the force in the  $x$ -direction with respect to the  $y$  variable can be denoted:

$$\frac{1}{G \sigma^c m^P} \frac{\partial F_x^{P/C}}{\partial y} = [\Psi_\beta + \Psi_{\tilde{\beta}}](\bar{\mathcal{X}}) - [\Psi_\beta + \Psi_{\tilde{\beta}}](\bar{\bar{\mathcal{X}}}) \quad (2.36)$$

Likewise the gradient of the force in the  $x$ -direction with respect to the  $z$  variable can be denoted as:

$$\frac{1}{G \sigma^c m^P} \frac{\partial F_x^{P/C}}{\partial z} = [\Psi_\gamma + \Psi_{\tilde{\gamma}}](\bar{\mathcal{X}}) - [\Psi_\gamma + \Psi_{\tilde{\gamma}}](\bar{\bar{\mathcal{X}}}) \quad (2.37)$$

By following the recipe set forth thus far in calculating the gradients of the force in the  $x$ -direction with respect to the other two Cartesian directions  $y$  &  $z$  and by carefully noting the definitions of the forces in Equations 2.24, 2.25 & 2.26, the expressions for the remaining force gradients can be stated. Furthermore, since the order of the differentiation may be interchanged, it is important to note that the Jacobian matrix is symmetric such that there are only six unique gradients of the force with respect to translation. However, for completeness the expressions for all of the remaining force gradients will be stated.

$$\frac{1}{G \sigma^c m^P} \frac{\partial F_y^{P/C}}{\partial x} = [\Psi_\gamma + \Psi_{\tilde{\gamma}}](\bar{\mathcal{Y}}) - [\Psi_\gamma + \Psi_{\tilde{\gamma}}](\bar{\bar{\mathcal{Y}}}) \quad (2.38)$$

$$\frac{1}{G \sigma^c m^P} \frac{\partial F_y^{P/C}}{\partial z} = [\Psi_\beta + \Psi_{\tilde{\beta}}](\bar{\mathcal{Y}}) - [\Psi_\beta + \Psi_{\tilde{\beta}}](\bar{\bar{\mathcal{Y}}}) \quad (2.39)$$

$$\frac{1}{G \sigma^c m^P} \frac{\partial F_z^{P/C}}{\partial x} = [\Psi_\beta + \Psi_{\tilde{\beta}}](\bar{\mathcal{Z}}) - [\Psi_\beta + \Psi_{\tilde{\beta}}](\bar{\bar{\mathcal{Z}}}) \quad (2.40)$$

$$\frac{1}{G \sigma^c m^P} \frac{\partial F_z^{P/C}}{\partial y} = [\Psi_\gamma + \Psi_{\tilde{\gamma}}] (\vec{z}) - [\Psi_\gamma + \Psi_{\tilde{\gamma}}] (\vec{\tilde{z}}) \quad (2.41)$$

### Observation

In order to prove that the  $\tan^{-1}$  and  $\ln$  terms may be treated as constants during the differentiation of the force to obtain the gradient, one can follow the proof set forth by MacMillan [40] when the force was obtained from the potential using the same method. However, the equations for the gradient of the force presented in section 2.3.2 can be obtained without assuming a constant characteristic for the  $\tan^{-1}$  and  $\ln$  terms. Without presenting a complete derivation, a basic outline for the process is presented here.

Begin with the definition of the potential, Equation 2.5, for the homogeneous density parallelepiped:

$$\frac{U(P)}{G \sigma^c} = \int_{-c}^c \int_{-b}^b \int_{-a}^a \frac{1}{r} du dv dw$$

where the distance,  $r$  between the two points was defined to be:

$$r^2 = (x - u)^2 + (y - v)^2 + (z - w)^2$$

The force is defined to be the negative gradient of the potential and the component of the force in the Cartesian  $x$ -direction is the negative partial derivative of the potential with respect to  $x$ .

$$-\frac{F_x^{P/C}}{G \sigma^c m^P} = \int_{-c}^c \int_{-b}^b \int_{-a}^a \frac{\partial}{\partial x} \left( \frac{1}{r} \right) du dv dw \quad (2.42)$$

Taking the gradient of the force in the  $x$ -direction as an example, one must further

differentiate with respect to  $x$  to obtain:

$$\begin{aligned} -\frac{1}{G \sigma^c m^P} \frac{\partial F_x^{P/C}}{\partial x} &= \int_{-c}^c \int_{-b}^b \int_{-a}^a \frac{\partial}{\partial x} \left( \frac{\partial}{\partial x} \left( \frac{1}{r} \right) \right) du dv dw \\ &= -\int_{-c}^c \int_{-b}^b \int_{-a}^a \frac{\partial}{\partial u} \left( \frac{\partial}{\partial x} \left( \frac{1}{r} \right) \right) du dv dw \end{aligned} \quad (2.43)$$

The innermost partial derivative of  $1/r$  is easily evaluated and the gradient of the force in the  $x$ -direction becomes:

$$\begin{aligned} \frac{1}{G \sigma^c m^P} \frac{\partial F_x^{P/C}}{\partial x} &= -\int_{-c}^c \int_{-b}^b \int_{-a}^a \frac{\partial}{\partial u} \left( \frac{(x-u)}{r^3} \right) du dv dw \\ &= -\int_{-c}^c \int_{-b}^b \left[ \frac{(x-u)}{r^3} \right]_{u_1=-a}^{u_2=a} dv dw \end{aligned} \quad (2.44)$$

To obtain the results presented in Equation 2.32, one must only carry out the integration of Equation 2.44. This is easily achieved with the help of a table of integrals. The following forms of integrals will be encountered in the process:

$$\begin{aligned} \int \frac{\alpha}{(\xi^2 + \alpha^2 + \beta^2)^{\frac{3}{2}}} d\xi &= \frac{\alpha \xi}{(\alpha^2 + \beta^2) \sqrt{\xi^2 + \alpha^2 + \beta^2}} \\ \int \frac{\alpha \beta}{(\alpha^2 + \xi^2) \sqrt{\xi^2 + \alpha^2 + \beta^2}} d\xi &= \tan^{-1} \left( \frac{\beta \xi}{\alpha \sqrt{\xi^2 + \alpha^2 + \beta^2}} \right) \end{aligned}$$

For the gradient of the force with respect to the other variables,  $y$  and  $z$ , the following forms of integrals will be encountered in the process:

$$\begin{aligned} \int \frac{\xi}{(\xi^2 + \alpha^2 + \beta^2)^{\frac{3}{2}}} d\xi &= -\frac{1}{\sqrt{\xi^2 + \alpha^2 + \beta^2}} \\ \int \frac{1}{\sqrt{\xi^2 + \alpha^2 + \beta^2}} d\xi &= \ln \left( \xi + \sqrt{\xi^2 + \alpha^2 + \beta^2} \right) \end{aligned}$$

Identifier	Description	Value	Units
2a	Nominal $x$ -direction length of body $C$	40	[mm]
2b	Nominal $y$ -direction length of body $C$	40	[mm]
2c	Nominal $z$ -direction length of body $C$	40	[mm]
$m^C$	Mass body $C$	1.37	[kg]
$m^P$	Mass point $P$	1.0	[kg]

Table 2.1: Simulation parameters for force and gradient at point due to a homogeneous density cube.

With the knowledge from the table of integrals, the equations presented in section 2.3.2 can be obtained.

### 2.3.3 Simulation Results

Using Equation 2.24 for the force and the equations in Section 2.3.2 for the gradients of the force at a point due to a right-angled parallelepiped with homogeneous density, it is helpful to plot the expressions over a region and to compare the results to that of two point masses. In so doing, it is possible to determine the error produced by approximating a cubical geometry by a single point mass representation. To begin the calculation, the baseline LISA faceted proof mass design is selected for the right-angled parallelepiped (body  $C$ ): a 40 mm cubical proof mass of 1.37 kg with an assumed homogeneous density. A Cartesian coordinate system is placed at the center of mass of body  $C$  and a 1 kg point mass is placed at point  $P$ , consistent with Figure 2.2. The simulation parameters used for the calculation are summarized in Table 2.1. The force,  $F^{P/C}$ , and gradient of the force at point  $P$  due to body  $C$  is then calculated for a region in the  $x$ - $y$  plane. Since the central attracting body is symmetrical, the force in the  $x$ -direction will be of primary concern. For an initial check, the  $x$ -direction force in the vicinity of one quadrant of the cubical proof mass is computed, as shown in Figure 2.3. Contrary to the equations presented by Chen and Cook [7], the plot indicates an attractive force (the  $x$ -direction force at point  $P$  is

in the negative  $x$  direction) for all points within the region. In addition, the presence of mass at the corners, which is non-existent for a spherical or point mass attracting body, generates an increase in the mass attraction force for a constant radial distance relative to the mass center near the cube corners as expected. It is therefore concluded that the minor corrections made herein to the equations presented by Chen and Cook [7] are valid.

By taking the difference between the mass attraction force due to a point mass attracting body of equal mass and the mass attraction force as calculated for the cubical geometry, the error associated with approximating a cubical geometry with a single point mass can be understood. Figure 2.4 depicts the difference in the  $x$ -direction force along the  $x$ -axis between two point masses and a cube and a point mass (force between two point masses minus the force between a cube and point mass). Due to the nature of the gravitational potential, it is well known that only distances close to the attracting body generate a significant deviation in the actual force from a point mass approximation. The slope of the log-log plot in Figure 2.4 indicates that the difference between a point mass approximation and the actual force due to a cubical object along the  $x$ -axis behaves approximately as one over the separation distance raised to the fifth order. Depending on the desired accuracy and location from the mass center of a cubical attracting body, a point mass approximation for a single point mass may or may not be acceptable along the  $x$ -axis. For example, according to Figure 2.3 the force along the  $x$ -axis due to the cubical geometry will be on the order of  $10^{-8}$  N. Returning to the LISA noise budget, a maximum total static self gravity acceleration of  $5 \times 10^{-10}$  m/s<sup>2</sup> is necessary for LISA disturbance requirements [42]. If the knowledge of the mass attraction force is desired to have an uncertainty less than  $10^{-10}$  N, consistent with the LISA requirements, then from Figure 2.4 it is seen that a point mass approximation may only be used for the ratio of  $x/2a$  greater than approximately 2. This estimated boundary is intended only to provide intuition in the gravitational mass attraction analysis, since a more thorough analysis is necessary to establish comprehensive guidelines. In addition, it should be noted that this estimate is valid for the attraction at a single point along the  $x$ -axis only, although the general technique can be applied to any point in space external to

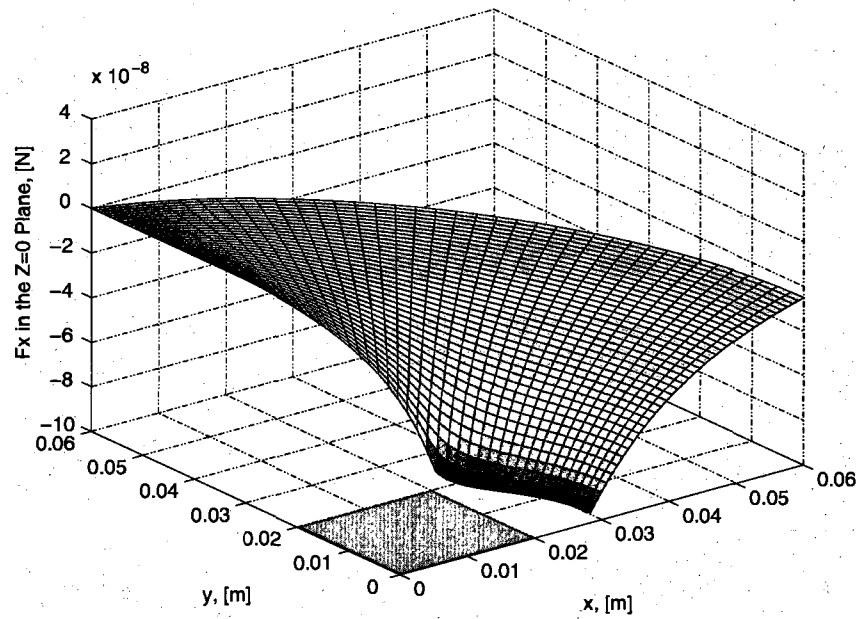


Figure 2.3:  $x$ -Direction mass attraction force for cube,  $F^{P/C}$ .

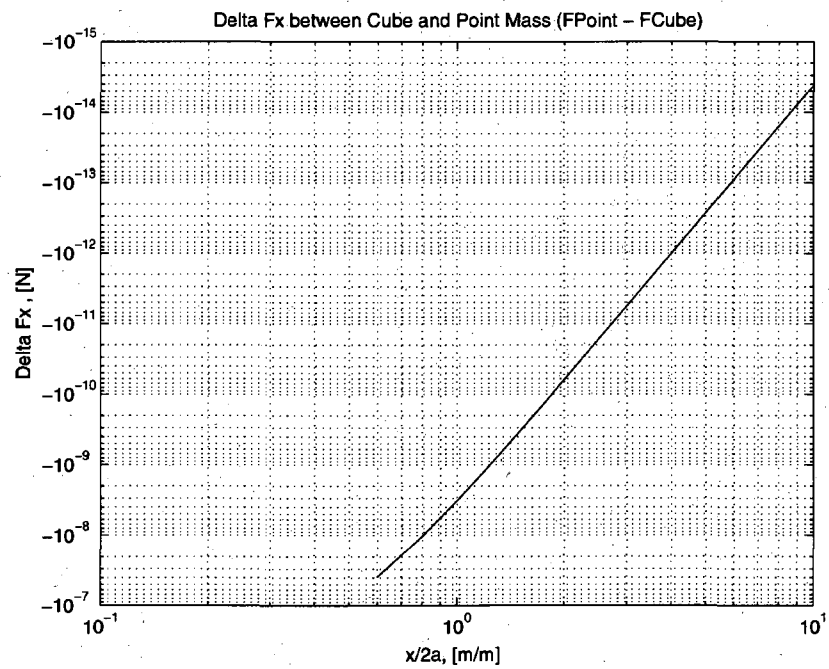


Figure 2.4: Delta between point mass and a cubical geometry  $x$ -direction mass attraction force.

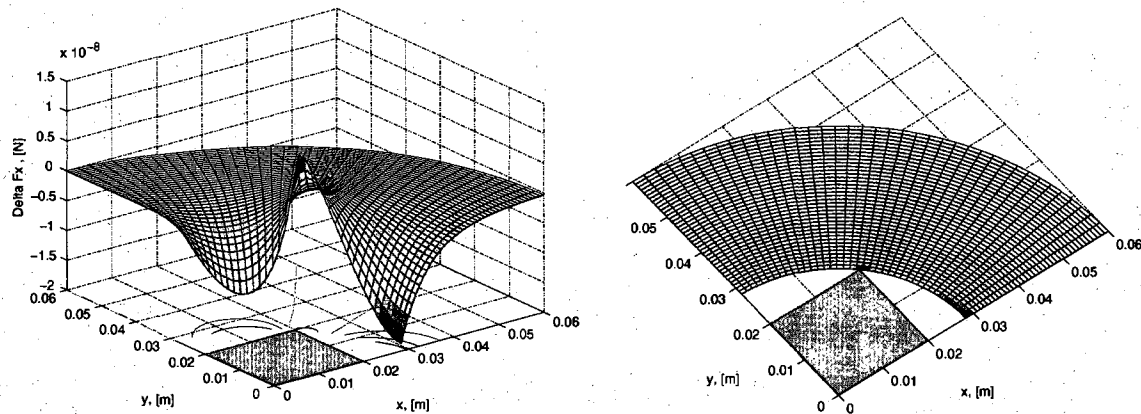


Figure 2.5: Delta  $F_x^{P/C}$  between point mass and a cubical geometry in  $x$ - $y$  plane.

the attracting body.

The difference in the  $x$ -direction force between a point mass approximation and the actual force due to a cube and a point mass for the  $x$ - $y$  plane is plotted in Figure 2.5, with the right sub-figure presenting a projection onto the  $x$ - $y$  plane. By examining the contour plot, it is clearly seen that close to the cube face center along the  $x$ -axis the mass attraction force due to the cube is less than a point mass approximation. That is, if a point mass approximation is used to represent a cubical geometry, the actual force for the cubical geometry would be less than the point mass approximated value along the  $x$ -axis. As the radial distance is kept the same and the location of the point  $P$  approaches the corner of the cube, the point mass approximation becomes an underestimate of the actual force. The equivalent point mass distance to obtain the same force is closer near the corners of the cube and the equivalent distance is further away on radial directions near the faces of the cube. It is also interesting to note that in the contour plot of Figure 2.5 there exists a region for the force in the  $x$ -direction where the difference between a point mass approximation and the true analytical solution for a cube is zero.

The gradients of the  $x$ -direction force with respect to the variables  $x$  and  $y$  were computed for the  $x$ - $y$  plane. The gradients of the mass attraction force in the  $x$ -direction for a cubical central attracting body are depicted in Figure 2.6 & Figure 2.7. Inspection of the gradient contour plots shows the expected similar behavior between

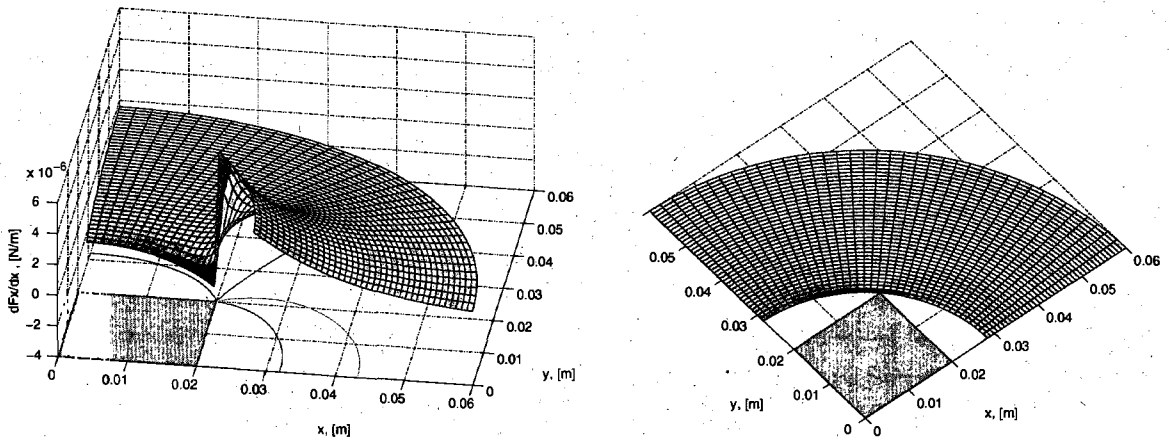


Figure 2.6: Gradient  $\frac{\partial F_x^{P/C}}{\partial x}$  for a cube in  $x$ - $y$  plane.

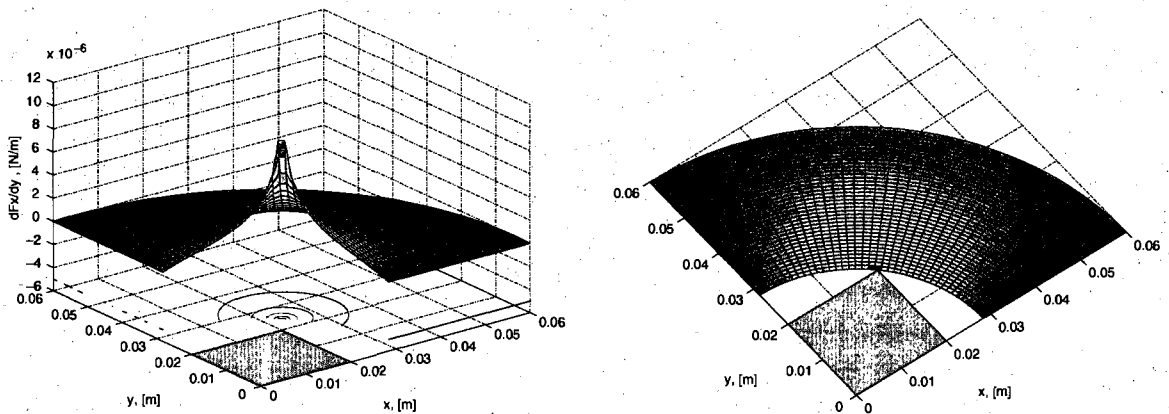


Figure 2.7: Gradient  $\frac{\partial F_x^{P/C}}{\partial y}$  for a cube in  $x$ - $y$  plane.

a cubical and point mass attracting body. For the cubical case, the gradients become more intense close to the cube corners and faces. For the gradient with respect to  $x$  variable, Figure 2.6 shows that the discontinuity has been shifted from the origin to the cube face. Similarly, for the gradient with respect to  $y$  variable, Figure 2.7, the discontinuity has been shifted from the origin to the cube corners, causing a more rapid change in values of the gradient as compared to a point mass attracting body. Again, to more readily see the difference between the force generated by a cubical and point mass attracting body, the gradient of the force from a cubical geometry is subtracted from that of a point mass approximation. Presented in Figure 2.8 and



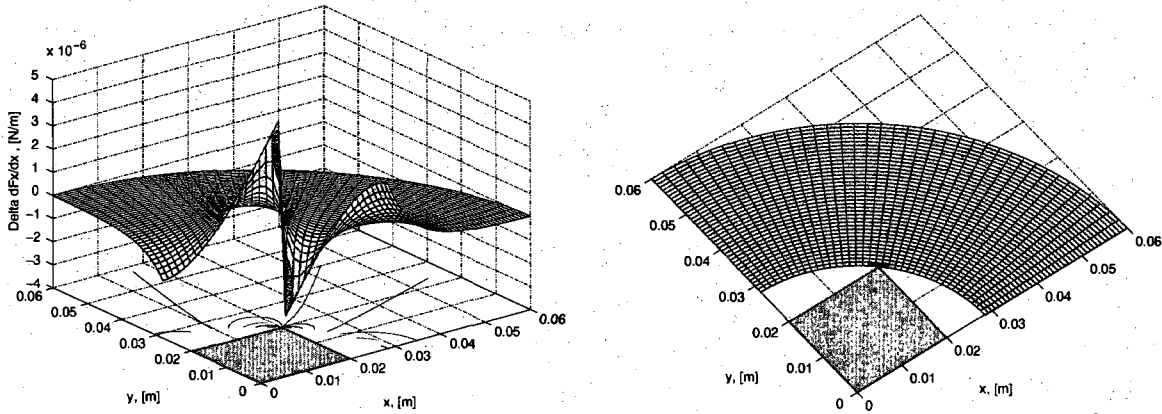


Figure 2.8: Delta gradient  $\frac{\partial F_x^{P/C}}{\partial x}$  between point mass and a cubical geometry.

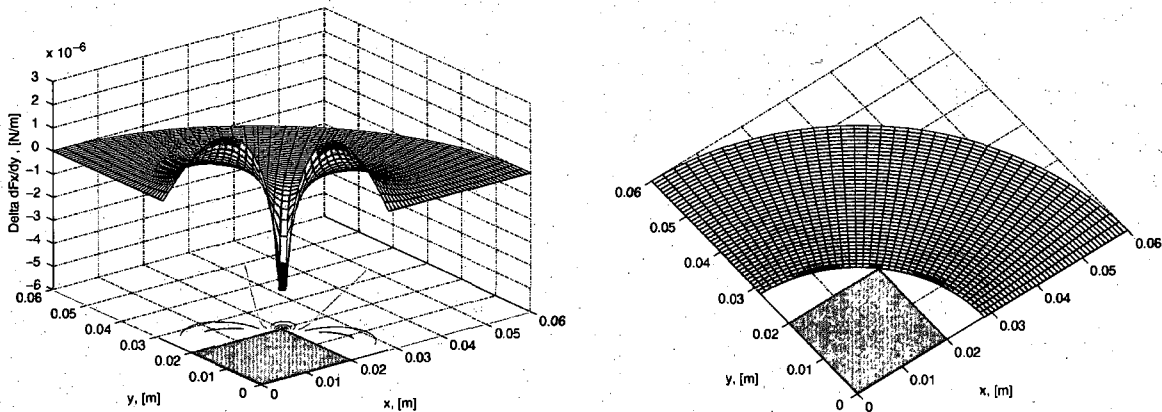


Figure 2.9: Delta gradient  $\frac{\partial F_x^{P/C}}{\partial y}$  between point mass and a cubical geometry.

Figure 2.9, is the difference in the gradient between the two different geometries, where the effect of the cube corners and face is clearly seen. Thus, if a point mass were to be used to approximate the cubical geometry, the largest error for both the gradients  $\frac{\partial F_x^{P/C}}{\partial x}$  and  $\frac{\partial F_x^{P/C}}{\partial y}$  would be in the vicinity of the cube corners. For the gradient with respect to the  $x$ -direction,  $\frac{\partial F_x^{P/C}}{\partial x}$ , a significant error would also exist through the center of the cube face. Similarly, for the gradient with respect to the  $y$ -direction,  $\frac{\partial F_x^{P/C}}{\partial y}$ , a significant error in using a point mass approximation would exist around the  $\pi/8 + n\pi/4$  radials near the cube face.

With the knowledge presented in Figure 2.8 and Figure 2.9, one can return to the

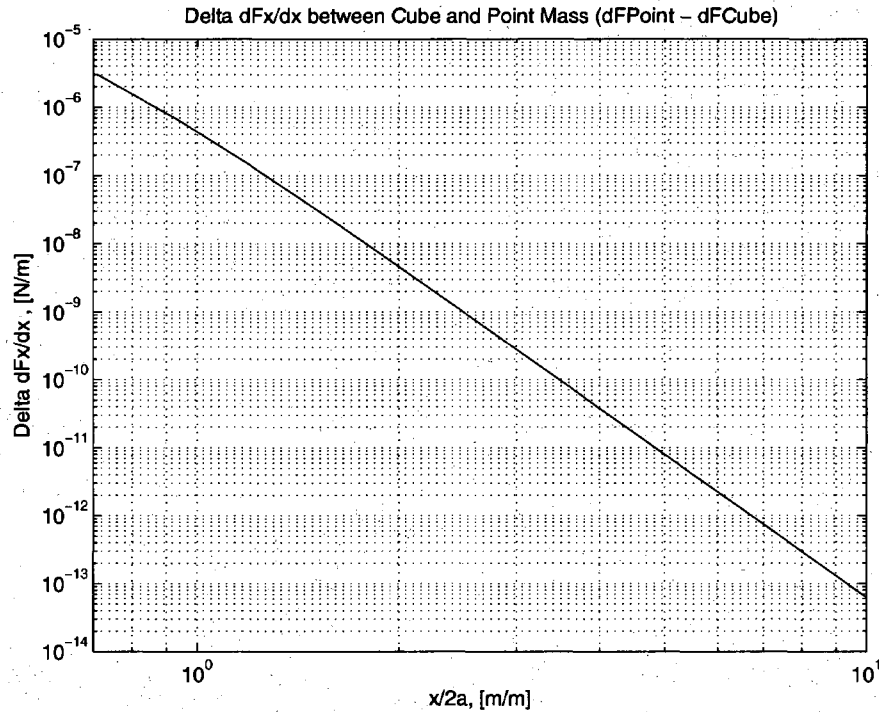


Figure 2.10: Delta between point mass and a cubical geometry  $x$ -direction mass attraction force gradient.

LISA requirements for the uncertainty in the gravitational attraction force gradients to determine when a point mass approximation is acceptable for use. For LISA, a total static self gravity acceleration gradient of  $3 \times 10^{-8} \text{ s}^{-2}$  along the measurement axis is expected to meet the science goals [56]. The largest error for the gradient with respect to the  $x$ -direction,  $\frac{\partial F_x^{P/C}}{\partial x}$ , when using a point mass approximation exists along the  $x$ -axis. The measurement axis for LISA is along the  $x$ -axis, normal to the disturbance free proof mass face. The difference between a point mass approximation and the actual gradient of the mass attraction force due to a cubical object along the  $x$ -axis is presented in Figure 2.10. From Figure 2.10; it is seen that a point mass approximation may only be used for the ratio of  $x/2a$  greater than approximately 2 if the knowledge of the mass attraction force gradient is to have an uncertainty of less than  $10^{-8} \text{ s}^{-2}$  consistent with the LISA requirements. Yet, for LISA this requirement is for the contribution of all the components in the satellite and not just for that

of a single point mass. Thus, this estimated boundary is intended only to provide intuition in the gravitational mass attraction analysis and is valid for the gradient of the mass attraction force at a single point along the  $x$ -axis only.

### **Observation**

Limitations of the manufacturing process prevent the existence of a perfectly homogeneous test mass. Variations in the density distribution of the manufactured test mass will lead to an uncertainty in the mass attraction analysis. In addition, as shown in Figure 2.1, the baseline LISA test mass contains geometric features, causing the actual geometry to deviate from an ideal cubical object. An alternative solution method is presented in Chapter 3, which is extensible to analyses involving density inhomogeneities and the attraction between two general-shaped distributed bodies.

## Chapter 3

# The Double Taylor Method

It has been demonstrated that the gravitational field and the corresponding gradient at the proof mass can be determined by calculating the contribution from every mass element in the satellite. The first drag-free satellite Triad-1/DISCOS [22], for example determined the mass attraction at the proof mass by representing satellite components as a combination of regular geometric shapes for which the attraction force could be easily calculated. By use of the spherical proof mass geometry by the Disturbance Compensation System DISCOS, the mass attraction computation could therefore be treated as a point mass and a distributed body (satellite components). The mass attraction analysis for Triad-1/DISCOS could then utilize and build upon the theory developed by Poisson [46] and MacCullagh [31] in the 1800's. MacCullagh [31] as well as Fleming et. al [22], showed that the gravitational mass attraction at a point due to a distributed body could through a Taylor Series expansion be expressed up to the third order by using moments of inertia for the distributed body. In fact, Fleming et. al notes that the mass attraction formula through a second order expansion consists of the measurable quantities of mass, mass center, and moment of inertia about the mass center. Indeed, the mass attraction analysis for the Triad-1/DISCOS mission was conducted by utilizing these physical quantities. In this work we again follow the technique of expanding the gravitational potential in a Taylor Series expansion to obtain the attraction force and gradient and develop a set of equations for the attraction properties between two general distributed objects.

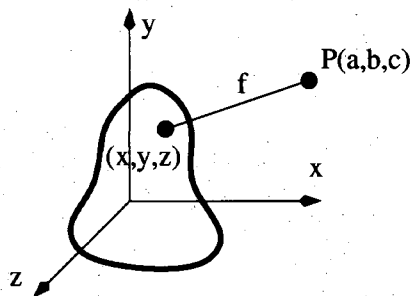


Figure 3.1: Distance between point  $P$  and a point on the distributed body.

In addition the solution is expressed as a full series expansion without truncation for a complete solution. Thus, the solution can be calculated to any desired expansion order and the next higher order term can also be calculated to establish a bound on the magnitude of the neglected terms.

### 3.1 Force Between Distributed Mass and a Point

The previous works of Poisson, MacCullagh and Fleming all used a Taylor Series expansion of the Potential as a foundation for computing the attraction force at a single point due to an attracting body. These works all truncated the series expansion at the second order and were valid for a single point only. If one returns to the notion of using a series expansion for the function representing the distance between two points, one can develop an equation representation for the attraction force between two distributed bodies. Let point  $P = (a, b, c)$  be a point external to the body for which the force shall be computed. We then have for one over the distance between two points in Cartesian coordinates:

$$f(x, y, z) = \frac{1}{\sqrt{(a-x)^2 + (b-y)^2 + (c-z)^2}} \quad (3.1)$$

The Potential at point  $P$  for the coordinate system placed at the center of mass of the distributed mass is therefore:

$$U(P) = G \iiint_V \sigma f(x, y, z) dx dy dz \quad (3.2)$$

Where the density is denoted by  $\sigma$  and the integration is performed over the volume occupied by the mass. The force is the negative gradient of the Potential and the component of the force at point  $P$  in the Cartesian x-direction for a point mass at  $P$ , is:

$$\frac{F_x(P)}{m^P} = -G \iiint_V \sigma f^{1,0,0}(x, y, z) dx dy dz \quad (3.3)$$

For simplicity, when taking gradient of the Potential, a constant density  $\sigma$  throughout the mass was assumed. The comma-delimited superscript notation is used to denote the derivative order with respect to the first, second, and third coordinates (x,y,z). Using the definition of a Taylor Series Expansion [55], one can write an expression for the derivative of  $f$ :

$$f^{1,0,0}(x, y, z) = \sum_{N=0}^{\infty} \left[ \frac{1}{N!} \left( \Delta x \frac{\partial}{\partial x} + \Delta y \frac{\partial}{\partial y} + \Delta z \frac{\partial}{\partial z} \right)^N f^{1,0,0} \Big|_{\substack{x=x_o=0 \\ y=y_o=0 \\ z=z_o=0}} \right] \quad (3.4)$$

If the expansion is taken about the origin ( $x_o = y_o = z_o = 0$ ), then  $\Delta x$  is just  $x$  and similar for  $y$  and  $z$ . The power term can be represented using the multinomial formula [55] such that:

$$\begin{aligned} \left( \Delta x \frac{\partial}{\partial x} + \Delta y \frac{\partial}{\partial y} + \Delta z \frac{\partial}{\partial z} \right)^N = \\ \sum_{\forall N=N_1+N_2+N_3} \frac{N!}{N_1!N_2!N_3!} \left( \Delta x \frac{\partial}{\partial x} \right)^{N_1} \left( \Delta y \frac{\partial}{\partial y} \right)^{N_2} \left( \Delta z \frac{\partial}{\partial z} \right)^{N_3} \end{aligned} \quad (3.5)$$

Where the Summation is taken over the set of all non negative integers  $N_1, N_2, N_3$  such that  $N = N_1 + N_2 + N_3$  (Denoted  $\forall N_n$  here after). Since the power term is also

operating on the powers or rather the order of the derivatives, one can also incorporate the derivatives of  $f$  into the formula using the superscript notation, obtaining a Taylor Series Expansion representation of  $f^{1,0,0}(x, y, z)$ :

$$f^{1,0,0}(x, y, z) = \sum_{N=0}^{\infty} \left[ \frac{1}{N!} \left( \sum_{\forall N_n} \frac{N!}{N_1!N_2!N_3!} (\Delta x)^{N_1} (\Delta y)^{N_2} (\Delta z)^{N_3} f^{N_1+1, N_2, N_3} \Big|_{\substack{x=x_0=0 \\ y=y_0=0 \\ z=z_0=0}} \right) \right] \quad (3.6)$$

The integration over the volume as denoted in Equation 3.3 can be carried out, noting that the only variation with respect to  $x, y, z$  is contained within the  $\Delta$  terms in Equation 3.6. We denote the volume moments using the nomenclature described in Tuzikov [66]:

$$M_{i,j,k}^{C/C_c} = \iiint_V x^i y^j z^k dx dy dz \quad (3.7)$$

and in a similar manner then choose to define the mass moment for Body  $C$  about the center of mass, point  $C_c$  with density  $\sigma^c$  by:

$$m_{i,j,k}^{C/C_c} = \iiint_V \sigma^c x^i y^j z^k dx dy dz \quad (3.8)$$

Then, by taking the representation for the mass moments, Equation 3.8, and substituting the result obtained in Equation 3.6 into Equation 3.3 we obtain a Taylor Series representation for the attraction force in the  $x$ -direction at point  $P$  without having truncated the series representation:

$$\frac{F_x(P)}{m^P} = -G \sum_{N=0}^{\infty} \left[ \frac{1}{N!} \left( \sum_{\forall N_n} \frac{N!}{N_1!N_2!N_3!} m_{N_1, N_2, N_3}^{C/C_c} f^{N_1+1, N_2, N_3} \Big|_{\substack{x=x_0=0 \\ y=y_0=0 \\ z=z_0=0}} \right) \right] \quad (3.9)$$

## 3.2 Mass Moment Calculation

In order to evaluate the expression for the force in an efficient, computational manner, one must determine a method for evaluating Equation 3.8, the mass moment

integrals,  $m_{i,j,k}$ . As shown by MacCullagh [31], if the Taylor Series expansion is taken to the second order, the attraction force can be represented using the moments of inertia for the distributed body. Similarly, as noted by Fleming [22] if regular geometric shapes are used to represent the mass distribution, for which the mass moments can be obtained, the force can be calculated. Thus, we see that there are two simple methods for determining the Mass Moments:

1. Represent mass moments using moments of inertia for the entire body. (Second order expansions)
2. Decompose an object into sub-elements and represent mass moments for the entire body using a summation of easily calculated mass moments. (Higher order expansions)

Each method for determining the mass moments has unique benefits which must be considered for the particular application. For example, the moment of inertia method tends to be favorable for the incorporation of physical measurements into the calculation, whereas the subelement representation tends to be more applicable to a computer modeling approach and higher order expansions.

### 3.2.1 Moment of Inertia Method

After truncating the double Taylor Series expansion at the second order, one can use standard moments of inertia to represent the geometry of the distributed mass, and hence the mass moments required by the two distributed mass force equation. It is convenient to use moments of inertia, since expressions for a variety of geometrical shapes exist. In addition, for those irregular shaped objects, the moment of inertia tensor can be physically measured, which would include unknown variations in density and geometry.

By looking at the integral definition for the moments of inertia, the relationship between the mass moments and moments of inertia is easily established. The moments



of inertia are defined by:

$$\begin{aligned}
 I_{xx}^{C/C_c} &= \iiint_V \sigma^c (y^2 + z^2) dx dy dz & I_{xy}^{C/C_c} &= - \iiint_V \sigma^c x y dx dy dz \\
 I_{yy}^{C/C_c} &= \iiint_V \sigma^c (x^2 + z^2) dx dy dz & I_{yz}^{C/C_c} &= - \iiint_V \sigma^c y z dx dy dz \\
 I_{zz}^{C/C_c} &= \iiint_V \sigma^c (x^2 + y^2) dx dy dz & I_{xz}^{C/C_c} &= - \iiint_V \sigma^c x z dx dy dz
 \end{aligned} \tag{3.10}$$

Using the definition of the mass moments, Equation 3.8, the relationship between the moments of inertia to the second order mass moments is found to be:

$$\begin{aligned}
 I_{xx}^{C/C_c} &= m_{0,2,0}^{C/C_c} + m_{0,0,2}^{C/C_c} & I_{xy}^{C/C_c} &= -m_{1,1,0}^{C/C_c} \\
 I_{yy}^{C/C_c} &= m_{2,0,0}^{C/C_c} + m_{0,0,2}^{C/C_c} & I_{yz}^{C/C_c} &= -m_{0,1,1}^{C/C_c} \\
 I_{zz}^{C/C_c} &= m_{2,0,0}^{C/C_c} + m_{0,0,2}^{C/C_c} & I_{xz}^{C/C_c} &= -m_{1,0,1}^{C/C_c}
 \end{aligned} \tag{3.11}$$

Solving the equations for the second order mass moments in terms of the moments of inertia one finds:

$$\begin{bmatrix} m_{2,0,0}^{C/C_c} \\ m_{0,2,0}^{C/C_c} \\ m_{0,0,2}^{C/C_c} \end{bmatrix} = \frac{1}{2} \begin{bmatrix} -1 & 1 & 1 \\ 1 & -1 & 1 \\ 1 & 1 & -1 \end{bmatrix} \begin{bmatrix} I_{xx}^{C/C_c} \\ I_{yy}^{C/C_c} \\ I_{zz}^{C/C_c} \end{bmatrix} \tag{3.12}$$

$$m_{1,1,0}^{C/C_c} = -I_{xy}^{C/C_c} \quad m_{0,1,1}^{C/C_c} = -I_{yz}^{C/C_c} \quad m_{1,0,1}^{C/C_c} = -I_{xz}^{C/C_c}$$

Having truncated the double Taylor Series expansion at the second order, the only remaining mass moments which need to be defined are the first and zero order mass moments. The zero order mass moment  $m_{0,0,0}^{C/C_c}$  is simply the mass of the distributed mass. If we define the coordinate system to be at the center of mass of the distributed mass, then the first order mass moment  $m_{1,0,0}^{C/C_c}$ ,  $m_{0,1,0}^{C/C_c}$ , and  $m_{0,0,1}^{C/C_c}$  will be equal to zero by definition of the mass center.

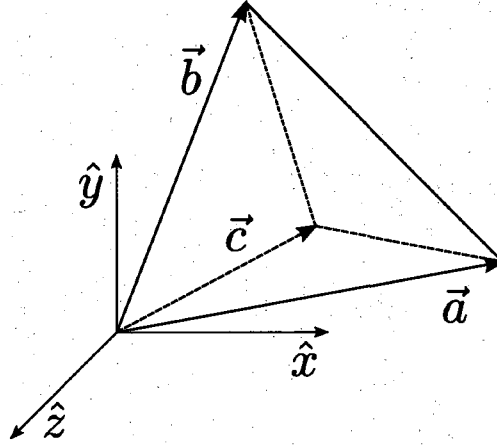


Figure 3.2: Tetrahedron defined by three vectors.

### 3.2.2 Tetrahedron Decomposition Method

Using a finite element approach, we wish to find an expression for the mass moments (including higher order terms) for a regular geometrical shape and then use the solution to construct a representation of a larger distributed mass. A tetrahedron, for example, can be used to decompose a large three-dimensional object into smaller polyhedra. In works by Tuzikov [66] and Sheynin [49] a closed form solution for an expression which generates  $N^{th}$  order volume moments for a tetrahedron is derived. If we define a tetrahedron, which has one vertex at the origin and each of the other three vertexes defined by coordinate points  $\bar{a}$ ,  $\bar{b}$ ,  $\bar{c}$ , Figure 3.2, then Tuzikov and Sheynin define the volume moment of the tetrahedron to be [66], [49]:

$$M_{k_1 k_2 k_3} = \frac{\det(A) k_1! k_2! k_3!}{(k+3)} \sum_{(k_{ij}) \in \mathcal{K}} \left( \frac{\prod_{j=1}^3 ((\sum_{i=1}^3 k_{ij})!)}{\prod_{i,j=1}^3 (k_{ij}!)} \prod_{i,j=1}^3 a_{ij}^{k_{ij}} \right) \quad (3.13)$$

where the matrix  $A$  is composed by the coordinates of the vertexes such that  $A = [\bar{a}, \bar{b}, \bar{c}]$ . The set  $\mathcal{K}$  is a set of 3 x 3 matrices  $(k_{ij})$  for integers  $k_1, k_2, k_3$ , which denote the order of the volume moment, such that  $0 \leq k_{ij} \leq k_i$  and  $\sum_{j=1}^3 k_{ij} = k_i$ ,  $i = 1, 2, 3$ . For the computation of the force equations, it is suggested that the volume moments for a tetrahedron be produced using Equation 3.13, and then placed into function

files for faster computation. The author has found the Matlab symbolic toolbox quite helpful in generating the desired moment order equations. Refer to Tuzikov [66] and Sheynin [49] for a detailed derivation of Equation 3.13. A listing of the volume moments up to the third order can be found in Sheynin [49] and are repeated in Section A.1 up to the second order.

In order to evaluate the attraction force given by Equation 3.9, we require the mass moments to be evaluated about a coordinate system located at the mass center. Although the volume moment expression in Equation 3.13 utilizes a coordinate system with an origin located at one vertex of the tetrahedron, a simple procedure will allow for the volume moment to be calculated at the centroid of the tetrahedron. Given a tetrahedron with one vertex at the origin, Equation 3.13 is used to calculate the zero and first order volume moments:  $M_{0,0,0}$ ,  $M_{1,0,0}$ ,  $M_{0,1,0}$ ,  $M_{0,0,1}$ . The location of the centroid by definition is then:  $[x_{cm}, y_{cm}, z_{cm}] = \left[ \frac{M_{1,0,0}}{M_{0,0,0}}, \frac{M_{0,1,0}}{M_{0,0,0}}, \frac{M_{0,0,1}}{M_{0,0,0}} \right]$ . The coordinate axes can now be translated to the centroid. Furthermore, by using the location of the centroid as a new vertex, the original tetrahedron can now be represented by four sub-tetrahedrons consisting each of the centroid as one vertex and each side of the original tetrahedron. Refer to Figure 3.3 for a geometric depiction. Equation 3.13 can then be used to find the volume moments of each of the sub-tetrahedrons and added together to find the volume moment of the original whole tetrahedron about the centroid. By assuming a constant density across the tetrahedron element, the mass moment is then obtained by simply multiplying the volume moment by the constant element density.

### 3.3 MacCullagh's Formula Derivation

The Taylor Series representation for the attraction force at a point due to a distributed body, Equation 3.9, can be algebraically manipulated to obtain the general form of MacCullagh's Formula, Equation 2.4. We begin by ignoring the derivative order in the  $x$ -direction in Equation 3.9 (which was produced by taking the negative

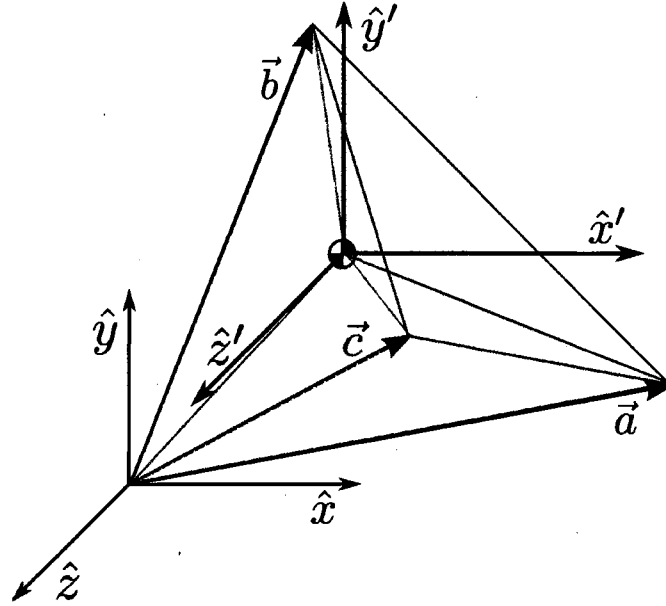


Figure 3.3: Tetrahedron represented by four sub-tetrahedrons.

gradient of the potential) to obtain the Potential at Point  $P$ :

$$\frac{U(P)}{G} = \sum_{N=0}^{\infty} \left[ \frac{1}{N!} \left( \sum_{\forall N_n} \frac{N!}{N_1!N_2!N_3!} m_{N_1, N_2, N_3}^{C/C_c} f^{N_1, N_2, N_3} \Big|_{\substack{x=x_0=0 \\ y=y_0=0 \\ z=z_0=0}} \right) \right] \quad (3.14)$$

According to the formula, one is to take the summation over the set of all non negative integers  $N_1, N_2, N_3$  such that  $N = N_1 + N_2 + N_3$  (Denoted  $\forall N_n$ ). MacCullagh's formula only incorporates mass moments up to the second order. Thus, for an expansion up to  $N = 2$  one expands the summations for the sets of  $N$  listed in Table 3.1. After expanding for the sets of  $N$  up to order two, one obtains:

$$\begin{aligned} \frac{U(P)}{G} &= m_{0,0,0}^{C/C_c} f^{0,0,0} \\ &+ m_{1,0,0}^{C/C_c} f^{1,0,0} + m_{0,1,0}^{C/C_c} f^{0,1,0} + m_{0,0,1}^{C/C_c} f^{0,0,1} \\ &+ \frac{1}{2} \left( m_{2,0,0}^{C/C_c} f^{2,0,0} + m_{0,2,0}^{C/C_c} f^{0,2,0} + m_{0,0,2}^{C/C_c} f^{0,0,2} \right. \\ &\quad \left. + 2m_{1,1,0}^{C/C_c} f^{1,1,0} + 2m_{0,1,1}^{C/C_c} f^{0,1,1} + 2m_{1,0,1}^{C/C_c} f^{1,0,1} \right) \end{aligned} \quad (3.15)$$

Order: N	N <sub>1</sub>	N <sub>2</sub>	N <sub>3</sub>
0	0	0	0
1	1	0	0
	0	1	0
	0	0	1
2	2	0	0
	0	2	0
	0	0	2
	1	1	0
	0	1	1
	1	0	1

Table 3.1: Sets of  $N$  for second order expansion.

By choosing the mass center as the origin of the coordinate system, the first order mass moments about the mass center are all identically zero for Body  $C$  ( $m_{1,0,0}^{C/C_c} = m_{0,1,0}^{C/C_c} = m_{0,0,1}^{C/C_c} = 0$ ). Simplifying by using the mass center definition, one obtains:

$$\begin{aligned}
\frac{U(P)}{G} &= m_{0,0,0}^{C/C_c} f^{0,0,0} \\
&+ \frac{1}{2} \left( m_{2,0,0}^{C/C_c} f^{2,0,0} + m_{0,2,0}^{C/C_c} f^{0,2,0} + m_{0,0,2}^{C/C_c} f^{0,0,2} \right. \\
&\quad \left. + 2m_{1,1,0}^{C/C_c} f^{1,1,0} + 2m_{0,1,1}^{C/C_c} f^{0,1,1} + 2m_{1,0,1}^{C/C_c} f^{1,0,1} \right) \quad (3.16)
\end{aligned}$$

We further proceed by calculating the derivatives of  $f$ , where the distance between the mass center and point  $P$  is denoted by:

$$r = \sqrt{x^2 + y^2 + z^2} \quad (3.17)$$

The calculated derivatives are then:

$$\begin{aligned}
 f^{0,0,0} &= \frac{1}{r} \\
 f^{2,0,0} &= \frac{3x^2}{r^5} - \frac{1}{r^3} \\
 f^{0,2,0} &= \frac{3y^2}{r^5} - \frac{1}{r^3} \\
 f^{0,0,2} &= \frac{3z^2}{r^5} - \frac{1}{r^3} \\
 f^{1,1,0} &= \frac{3xy}{r^5} \\
 f^{0,1,1} &= \frac{3yz}{r^5} \\
 f^{1,0,1} &= \frac{3xz}{r^5}
 \end{aligned} \tag{3.18}$$

Substituting into Equation 3.16 to obtain:

$$\begin{aligned}
 \frac{U(P)}{G} &= m_{0,0,0}^{C/C_c} \frac{1}{r} \\
 &+ \frac{1}{2} \left( m_{2,0,0}^{C/C_c} \left( \frac{3x^2}{r^5} - \frac{1}{r^3} \right) + m_{0,2,0}^{C/C_c} \left( \frac{3y^2}{r^5} - \frac{1}{r^3} \right) + m_{0,0,2}^{C/C_c} \left( \frac{3z^2}{r^5} - \frac{1}{r^3} \right) \right. \\
 &\quad \left. + 2m_{1,1,0}^{C/C_c} \frac{3xy}{r^5} + 2m_{0,1,1}^{C/C_c} \frac{3yz}{r^5} + 2m_{1,0,1}^{C/C_c} \frac{3xz}{r^5} \right)
 \end{aligned} \tag{3.19}$$

which further rearranges to:

$$\begin{aligned}
 \frac{U(P)}{G} &= m_{0,0,0}^{C/C_c} \frac{1}{r} \\
 &+ \frac{1}{2r^3} \left( - (m_{2,0,0}^{C/C_c} + m_{0,2,0}^{C/C_c} + m_{0,0,2}^{C/C_c}) \right. \\
 &\quad \left. + m_{2,0,0}^{C/C_c} \frac{3x^2}{r^2} + m_{0,2,0}^{C/C_c} \frac{3y^2}{r^2} + m_{0,0,2}^{C/C_c} \frac{3z^2}{r^2} \right. \\
 &\quad \left. + 2m_{1,1,0}^{C/C_c} \frac{3xy}{r^2} + 2m_{0,1,1}^{C/C_c} \frac{3yz}{r^2} + 2m_{1,0,1}^{C/C_c} \frac{3xz}{r^2} \right)
 \end{aligned} \tag{3.20}$$

In order to obtain the generalized MacCullagh's formula, one must transform the mass moment representation into moments of inertia. This is achieved by adding and

subtracting mass moment terms for a net change of zero to the equation.

$$\begin{aligned}
\frac{U(P)}{G} &= m_{0,0,0}^{C/C_c} \frac{1}{r} \\
&+ \frac{1}{2r^3} \left( 2(m_{2,0,0}^{C/C_c} + m_{0,2,0}^{C/C_c} + m_{0,0,2}^{C/C_c}) - 3(m_{2,0,0}^{C/C_c} + m_{0,2,0}^{C/C_c} + m_{0,0,2}^{C/C_c}) \right. \\
&\quad + m_{2,0,0}^{C/C_c} \frac{3x^2}{r^2} + m_{0,2,0}^{C/C_c} \frac{3y^2}{r^2} + m_{0,0,2}^{C/C_c} \frac{3z^2}{r^2} \\
&\quad \left. + 2m_{1,1,0}^{C/C_c} \frac{3xy}{r^2} + 2m_{0,1,1}^{C/C_c} \frac{3yz}{r^2} + 2m_{1,0,1}^{C/C_c} \frac{3xz}{r^2} \right) \quad (3.21)
\end{aligned}$$

Collecting terms with the common factor of three:

$$\begin{aligned}
\frac{U(P)}{G} &= m_{0,0,0}^{C/C_c} \frac{1}{r} \\
&+ \frac{1}{2r^3} \left( 2(m_{2,0,0}^{C/C_c} + m_{0,2,0}^{C/C_c} + m_{0,0,2}^{C/C_c}) - \right. \\
&\quad 3 \left( m_{2,0,0}^{C/C_c} - m_{2,0,0}^{C/C_c} \frac{x^2}{r^2} + m_{0,2,0}^{C/C_c} - m_{0,2,0}^{C/C_c} \frac{y^2}{r^2} + m_{0,0,2}^{C/C_c} - m_{0,0,2}^{C/C_c} \frac{z^2}{r^2} + \right. \\
&\quad \left. \left. - 2m_{1,1,0}^{C/C_c} \frac{xy}{r^2} - 2m_{0,1,1}^{C/C_c} \frac{yz}{r^2} - 2m_{1,0,1}^{C/C_c} \frac{xz}{r^2} \right) \right) \quad (3.22)
\end{aligned}$$

Creating a common denominator for the terms multiplied by the common factor of three:

$$\begin{aligned}
\frac{U(P)}{G} &= m_{0,0,0}^{C/C_c} \frac{1}{r} \\
&+ \frac{1}{2r^3} \left( 2(m_{2,0,0}^{C/C_c} + m_{0,2,0}^{C/C_c} + m_{0,0,2}^{C/C_c}) \right. \\
&\quad - 3 \left( m_{2,0,0}^{C/C_c} \frac{x^2 + y^2 + z^2}{r^2} - m_{2,0,0}^{C/C_c} \frac{x^2}{r^2} + \right. \\
&\quad \quad m_{0,2,0}^{C/C_c} \frac{x^2 + y^2 + z^2}{r^2} - m_{0,2,0}^{C/C_c} \frac{y^2}{r^2} + \\
&\quad \quad \left. m_{0,0,2}^{C/C_c} \frac{x^2 + y^2 + z^2}{r^2} - m_{0,0,2}^{C/C_c} \frac{z^2}{r^2} + \right.
\end{aligned}$$

$$\left. - 2m_{1,1,0}^{C/C_c} \frac{xy}{r^2} - 2m_{0,1,1}^{C/C_c} \frac{yz}{r^2} - 2m_{1,0,1}^{C/C_c} \frac{xz}{r^2} \right) \quad (3.23)$$

Collecting like terms:

$$\begin{aligned} \frac{U(P)}{G} &= m_{0,0,0}^{C/C_c} \frac{1}{r} \\ &+ \frac{1}{2r^3} \left( 2(m_{2,0,0}^{C/C_c} + m_{0,2,0}^{C/C_c} + m_{0,0,2}^{C/C_c}) \right. \\ &\quad - 3 \left( \frac{x^2}{r^2} (m_{0,2,0}^{C/C_c} + m_{0,0,2}^{C/C_c}) + \right. \\ &\quad \quad \frac{y^2}{r^2} (m_{2,0,0}^{C/C_c} + m_{0,0,2}^{C/C_c}) + \\ &\quad \quad \left. \frac{z^2}{r^2} (m_{2,0,0}^{C/C_c} + m_{0,2,0}^{C/C_c}) + \right. \\ &\quad \left. \left. - 2m_{1,1,0}^{C/C_c} \frac{xy}{r^2} - 2m_{0,1,1}^{C/C_c} \frac{yz}{r^2} - 2m_{1,0,1}^{C/C_c} \frac{xz}{r^2} \right) \right) \quad (3.24) \end{aligned}$$

The mass moments can now be replaced with the moments of inertia, using the relationships listed in Equation 3.11.

$$\begin{aligned} \frac{U(P)}{G} &= m_{0,0,0}^{C/C_c} \frac{1}{r} \\ &+ \frac{1}{2r^3} \left( I_{xx}^{C/C_c} + I_{yy}^{C/C_c} + I_{zz}^{C/C_c} \right. \\ &\quad - 3 \left( \frac{x^2}{r^2} I_{xx}^{C/C_c} + \frac{y^2}{r^2} I_{yy}^{C/C_c} + \frac{z^2}{r^2} I_{zz}^{C/C_c} \right. \\ &\quad \left. \left. + 2 \frac{xy}{r^2} I_{xy}^{C/C_c} + 2 \frac{yz}{r^2} I_{yz}^{C/C_c} + 2 \frac{xz}{r^2} I_{xz}^{C/C_c} \right) \right) \quad (3.25) \end{aligned}$$

Finally, by replacing the moment of inertia components with tensor notation, and noting that the zero order mass moment is simply the mass, the generalized version of MacCullagh's formula, Equation 2.4, is obtained.

$$U(P) = \frac{GM}{r} + \frac{G}{2r^3} \left( \text{trace}(\bar{I}) - 3\hat{r} \cdot \bar{I} \cdot \hat{r} \right) \quad (3.26)$$



### 3.4 Force Between Two Distributed Masses

Having established a representation of the attraction Force at a single point due to a distributed body in a non-truncated Taylor Series, we can proceed to develop a solution for two distributed bodies. Looking closer at Equation 3.9, one should notice that all of the information concerning the location of point  $P$  is contained within the  $f^{N_1+1, N_2, N_3}$  term, which was evaluated at the origin. By integrating the solution over a second volume with homogeneous density ( $dm = \sigma dV$ ), for all possible points  $P$  with incremental mass  $dm$ , we can obtain the desired solution for two distributed bodies. Since all the information regarding point  $P$  is contained within the  $f^{N_1+1, N_2, N_3}$  term, evaluating the volume integral over the force reduces to determining the triple integral over  $f^{N_1+1, N_2, N_3}$  for all points  $P$  within the volume:

$$F_x = -G \sum_{N=0}^{\infty} \left[ \frac{1}{N!} \left( \sum_{\forall N_n} \frac{N!}{N_1! N_2! N_3!} m_{N_1, N_2, N_3}^{C/C_c} \iiint_V \sigma^d f^{N_1+1, N_2, N_3} \Big|_{\substack{x=x_o=0 \\ y=y_o=0 \\ z=z_o=0}} da db dc \right) \right] \quad (3.27)$$

Again using the Taylor Series expansion and multinomial formula technique described in Section 3.1 a representation for the volume integral is found to be:

$$\begin{aligned} & \iiint_V \sigma^d f^{N_1+1, N_2, N_3} \Big|_{\substack{x=x_o=0 \\ y=y_o=0 \\ z=z_o=0}} da db dc \\ &= \sum_{S=0}^{\infty} \left[ \frac{1}{S!} \left( \sum_{\forall S_s} \frac{S!}{S_1! S_2! S_3!} m_{S_1, S_2, S_3}^{D/D_c} h_{N_1+1, N_2, N_3}^{S_1, S_2, S_3} \Big|_{\substack{a_o=x_{cm} \\ b_o=y_{cm} \\ c_o=z_{cm}}} \right) \right] \end{aligned} \quad (3.28)$$

The sub- & super-scripted function  $h$  represents the repeated derivative of  $f(x, y, z)$ , such that the first derivative  $f^{N_1+1, N_2, N_3} \Big|_{\substack{x=x_o=0 \\ y=y_o=0 \\ z=z_o=0}}$  evaluated at the origin is represented by the subscript and the superscript represents the continued derivative with respect to the point  $(a, b, c)$ , which is then evaluated at the center of mass of the second body. The order of the subscripts for the repeated derivative function  $h$  will match the order of the corresponding mass moment multiplier for Body  $M_c$  plus one due to taking the derivative of the gravitational potential function to obtain the force in the

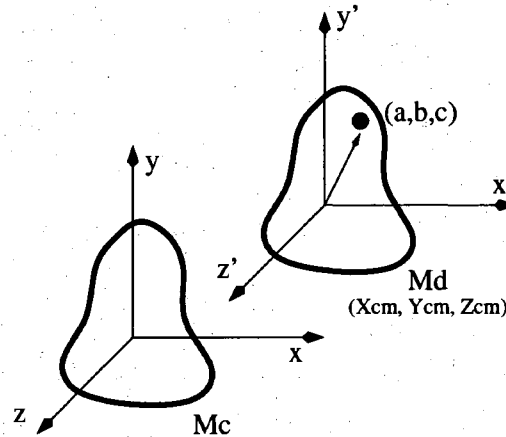


Figure 3.4: Two distributed bodies with coordinate origins at mass center.

$x$  direction. The order of the superscripts will match the order of the corresponding mass moment multiplier for second body  $M_d$ .

The repeated derivative function is applied to Equation 3.1, the distance between two points in Cartesian coordinates. To generate the repeated derivative function  $h_{i,j,k}^{p,q,r}$ , first the derivative with respect to  $x, y, z$  is taken to the order  $i, j, k$ , the resulting function is then evaluated at  $(x, y, z) = (0, 0, 0)$ . The result now contains only the variables  $a, b, c$ . Next the derivative is taken with respect to  $a, b, c$  to the order  $p, q, r$  and then evaluated at the point  $(a, b, c) = (x_{cm}, y_{cm}, z_{cm})$ .

Although it is suspected that a series could be used to represent the repeated derivative, it was found to be simpler to manually calculate the derivatives and place the results into software function files. The Matlab symbolic toolbox and the differentiate command was used to automatically generate the derivatives. These functions can be calculated in a loop and by creatively writing the Matlab code to actually generate Matlab function files containing the resulting derivatives, the repeated derivatives functions are easily calculated for predetermined orders.

For the Taylor Series expansion of the second volume, the expansion is performed about the center of mass of the body,  $(x_{cm}, y_{cm}, z_{cm})$ . The displacements from the

point of evaluation for the Taylor Series expansion are therefore represented by:

$$\Delta x = (a - x_{cm}) \quad \Delta y = (b - y_{cm}) \quad \Delta z = (c - z_{cm})$$

As a result, the mass moment is calculated about the center of mass of the body. If a primed coordinate system is a simple translation to the center of mass of the second body, then the mass moments of the second distributed body can be represented by:

$$\begin{aligned} m_{p,q,r}^{D/Dc} &= \iiint_V \sigma^d (a - x_{cm})^p (b - y_{cm})^q (c - z_{cm})^r da db dc \\ &= \iiint_V \sigma^d (x')^p (y')^q (z')^r dx' dy' dz' \end{aligned} \quad (3.29)$$

Finally, collecting the results of Equation 3.29 and Equation 3.28, we have an expression for the attraction force in the  $x$ -direction. It should be noted that the negative sign is dropped to obtain the force on the central body due to the second distributed body. The expression is in coordinates with an origin located at the center of mass of  $M_c$ .

$$\begin{aligned} F_x &= G \sum_{N=0}^{\infty} \left\{ \frac{1}{N!} \left[ \sum_{\forall N_n} \left( \frac{N!}{N_1! N_2! N_3!} m_{N_1, N_2, N_3}^{C/Cc} \right. \right. \right. \\ &\quad \left. \left. \left. \sum_{S=0}^{\infty} \left[ \frac{1}{S!} \left( \sum_{\forall S_s} \frac{S!}{S_1! S_2! S_3!} m_{S_1, S_2, S_3}^{D/Dc} h_{N_1+1, N_2, N_3}^{S_1, S_2, S_3} \Big|_{\substack{a_0=x_{cm} \\ b_0=y_{cm} \\ c_0=z_{cm}}} \right) \right] \right] \right\} \end{aligned} \quad (3.30)$$

By noting that in the derivation of the force in the  $x$ -direction, the partial of the Potential function with respect to  $x$  gave rise to the  $N_1 + 1$  term, an expression for the Force in the  $y$  and  $z$  directions can be quickly determined. This is achieved by modifying the subscripts on the repeated derivative function  $h$ . For the  $y$  direction, the proper subscripts are  $(N_1, N_2 + 1, N_3)$  and for the  $z$  direction the proper subscripts are  $(N_1, N_2, N_3 + 1)$ . The increase in the derivative order as such, results directly from the fact that the Force is the gradient of the gravitational potential function.

Order: X	X <sub>1</sub>	X <sub>2</sub>	X <sub>3</sub>
0	0	0	0
1	1	0	0
	0	1	0
	0	0	1
2	2	0	0
	0	2	0
	0	0	2
	1	1	0
	0	1	1
	1	0	1

Table 3.2: Sets of  $N$  and  $S$  for double second order expansion.

### 3.5 Gradients of the Attraction Force

An expression for gradients of the attraction force in each of the principal directions can also be quickly derived from Equation 3.30. This is achieved by once again manipulating the derivative order in the repeated derivative function  $h$ . Suppose for example we wish to calculate the rate of change in the  $x$ -component of the force as a displacement in the  $y$ -direction of the first distributed mass is observed. That is we wish to determine  $\frac{\partial F_x}{\partial y}$ . By manipulating the subscript notation on the repeated derivative function  $h$  to  $(N_1 + 1, N_2 + 1, N_3)$  we have an expression for  $\frac{\partial F_x}{\partial y}$ . By manipulating the superscript notation of the repeated derivative function  $h$  we can obtain an expression for the gradient. For example, if we wish to find the rate of change in the  $x$  component of the force due to a change or uncertainty in the  $z$  location of the second distributed mass, we would alter the superscript notation of Equation 3.30 to read  $S_1, S_2, S_3 + 1$ .

### 3.6 Analysis of the Force Equations

In order to gain some insight into the attraction force between two distributed bodies, one begins by expanding the force between two distributed masses, Equation 3.30, up to the second order mass moments to include all the terms involving the moments

of inertia for the two bodies. According to the formula, one is to take the summation over the set of all non negative integers  $N_1, N_2, N_3$  such that  $N = N_1 + N_2 + N_3$  (Denoted  $\forall N_n$ ). For an expansion up to  $N = 2$  and for  $S = 2$ , one expands the summations for the sets of  $N$  and  $S$  listed in Table 3.2. After expanding for the sets of  $N$  and  $S$  up to order 2, and noting that the first order mass moments about the mass center are all identically zero for Body  $C$  and Body  $D$  ( $m_{1,0,0}^{C/C_c} = m_{0,1,0}^{C/C_c} = m_{0,0,1}^{C/C_c} = 0$ ) one obtains the second order expanded form of Equation 3.30:

$$\begin{aligned}
\frac{F_x^{C/D}}{G} = & m_{0,0,0}^{C/C_c} \left( m_{0,0,0}^{D/D_c} h_{1,0,0}^{0,0,0} + \frac{1}{2} m_{2,0,0}^{D/D_c} h_{1,0,0}^{2,0,0} + \frac{1}{2} m_{0,2,0}^{D/D_c} h_{1,0,0}^{0,2,0} \right. \\
& \left. + \frac{1}{2} m_{0,0,2}^{D/D_c} h_{1,0,0}^{0,0,2} + m_{1,1,0}^{D/D_c} h_{1,0,0}^{1,1,0} + m_{0,1,1}^{D/D_c} h_{1,0,0}^{0,1,1} + m_{1,0,1}^{D/D_c} h_{1,0,0}^{1,0,1} \right) + \\
& \frac{1}{2} m_{2,0,0}^{C/C_c} \left( m_{0,0,0}^{D/D_c} h_{3,0,0}^{0,0,0} + \frac{1}{2} m_{2,0,0}^{D/D_c} h_{3,0,0}^{2,0,0} + \frac{1}{2} m_{0,2,0}^{D/D_c} h_{3,0,0}^{0,2,0} \right. \\
& \left. + \frac{1}{2} m_{0,0,2}^{D/D_c} h_{3,0,0}^{0,0,2} + m_{1,1,0}^{D/D_c} h_{3,0,0}^{1,1,0} + m_{0,1,1}^{D/D_c} h_{3,0,0}^{0,1,1} + m_{1,0,1}^{D/D_c} h_{3,0,0}^{1,0,1} \right) + \\
& \frac{1}{2} m_{0,2,0}^{C/C_c} \left( m_{0,0,0}^{D/D_c} h_{1,2,0}^{0,0,0} + \frac{1}{2} m_{2,0,0}^{D/D_c} h_{1,2,0}^{2,0,0} + \frac{1}{2} m_{0,2,0}^{D/D_c} h_{1,2,0}^{0,2,0} \right. \\
& \left. + \frac{1}{2} m_{0,0,2}^{D/D_c} h_{1,2,0}^{0,0,2} + m_{1,1,0}^{D/D_c} h_{1,2,0}^{1,1,0} + m_{0,1,1}^{D/D_c} h_{1,2,0}^{0,1,1} + m_{1,0,1}^{D/D_c} h_{1,2,0}^{1,0,1} \right) + \\
& \frac{1}{2} m_{0,0,2}^{C/C_c} \left( m_{0,0,0}^{D/D_c} h_{1,0,2}^{0,0,0} + \frac{1}{2} m_{2,0,0}^{D/D_c} h_{1,0,2}^{2,0,0} + \frac{1}{2} m_{0,2,0}^{D/D_c} h_{1,0,2}^{0,2,0} \right. \\
& \left. + \frac{1}{2} m_{0,0,2}^{D/D_c} h_{1,0,2}^{0,0,2} + m_{1,1,0}^{D/D_c} h_{1,0,2}^{1,1,0} + m_{0,1,1}^{D/D_c} h_{1,0,2}^{0,1,1} + m_{1,0,1}^{D/D_c} h_{1,0,2}^{1,0,1} \right) + \\
& m_{1,1,0}^{C/C_c} \left( m_{0,0,0}^{D/D_c} h_{2,1,0}^{0,0,0} + \frac{1}{2} m_{2,0,0}^{D/D_c} h_{2,1,0}^{2,0,0} + \frac{1}{2} m_{0,2,0}^{D/D_c} h_{2,1,0}^{0,2,0} \right. \\
& \left. + \frac{1}{2} m_{0,0,2}^{D/D_c} h_{2,1,0}^{0,0,2} + m_{1,1,0}^{D/D_c} h_{2,1,0}^{1,1,0} + m_{0,1,1}^{D/D_c} h_{2,1,0}^{0,1,1} + m_{1,0,1}^{D/D_c} h_{2,1,0}^{1,0,1} \right) + \\
& m_{0,1,1}^{C/C_c} \left( m_{0,0,0}^{D/D_c} h_{1,1,1}^{0,0,0} + \frac{1}{2} m_{2,0,0}^{D/D_c} h_{1,1,1}^{2,0,0} + \frac{1}{2} m_{0,2,0}^{D/D_c} h_{1,1,1}^{0,2,0} \right. \\
& \left. + \frac{1}{2} m_{0,0,2}^{D/D_c} h_{1,1,1}^{0,0,2} + m_{1,1,0}^{D/D_c} h_{1,1,1}^{1,1,0} + m_{0,1,1}^{D/D_c} h_{1,1,1}^{0,1,1} + m_{1,0,1}^{D/D_c} h_{1,1,1}^{1,0,1} \right) + \\
& m_{1,0,1}^{C/C_c} \left( m_{0,0,0}^{D/D_c} h_{2,0,1}^{0,0,0} + \frac{1}{2} m_{2,0,0}^{D/D_c} h_{2,0,1}^{2,0,0} + \frac{1}{2} m_{0,2,0}^{D/D_c} h_{2,0,1}^{0,2,0} \right.
\end{aligned} \tag{3.31}$$

$$+\frac{1}{2}m_{0,0,2}^{D/D_c}h_{2,0,1}^{0,0,2} + m_{1,1,0}^{D/D_c}h_{2,0,1}^{1,1,0} + m_{0,1,1}^{D/D_c}h_{2,0,1}^{0,1,1} + m_{1,0,1}^{D/D_c}h_{2,0,1}^{1,0,1} \Big)$$

Suppose further for simplicity that principal axes can be chosen and both Body  $C$  and Body  $D$  can be oriented to align the principal axes in a parallel set of orthogonal coordinates. Due to the choice of principal axes, the cross products of inertia are identically zero for both Body  $C$  and Body  $D$  ( $m_{1,1,0}^{C/C_c} = m_{0,1,1}^{C/C_c} = m_{1,0,1}^{C/C_c} = 0$ ). The second order expanded form of Equation 3.30 further reduces to:

$$\begin{aligned} \frac{F_x^{C/D}}{G} = & \frac{1}{2}m_{0,0,0}^{C/C_c} \left( 2m_{0,0,0}^{D/D_c}h_{1,0,0}^{0,0,0} + m_{2,0,0}^{D/D_c}h_{1,0,0}^{2,0,0} + m_{0,2,0}^{D/D_c}h_{1,0,0}^{0,2,0} + m_{0,0,2}^{D/D_c}h_{1,0,0}^{0,0,2} \right) \\ & + \frac{1}{4}m_{2,0,0}^{C/C_c} \left( 2m_{0,0,0}^{D/D_c}h_{3,0,0}^{0,0,0} + m_{2,0,0}^{D/D_c}h_{3,0,0}^{2,0,0} + m_{0,2,0}^{D/D_c}h_{3,0,0}^{0,2,0} + m_{0,0,2}^{D/D_c}h_{3,0,0}^{0,0,2} \right) \\ & + \frac{1}{4}m_{0,2,0}^{C/C_c} \left( 2m_{0,0,0}^{D/D_c}h_{1,2,0}^{0,0,0} + m_{2,0,0}^{D/D_c}h_{1,2,0}^{2,0,0} + m_{0,2,0}^{D/D_c}h_{1,2,0}^{0,2,0} + m_{0,0,2}^{D/D_c}h_{1,2,0}^{0,0,2} \right) \\ & + \frac{1}{4}m_{0,0,2}^{C/C_c} \left( 2m_{0,0,0}^{D/D_c}h_{1,0,2}^{0,0,0} + m_{2,0,0}^{D/D_c}h_{1,0,2}^{2,0,0} + m_{0,2,0}^{D/D_c}h_{1,0,2}^{0,2,0} + m_{0,0,2}^{D/D_c}h_{1,0,2}^{0,0,2} \right) \end{aligned} \quad (3.32)$$

Equation 3.32 provides us with the ability to analyze the accuracy of the Newtonian gravitational attraction force between two bodies. By looking closely at the information presented in Equation 3.32, the first term is precisely the classical Newtonian attraction formula for two bodies located at a large separation distance compared to the size of the body:

$$\frac{F_x^{C/D}}{G} = m_{0,0,0}^{C/C_c}m_{0,0,0}^{D/D_c}h_{1,0,0}^{0,0,0} + \dots = m^C m^D \frac{x_{cm}}{(x_{cm}^2 + y_{cm}^2 + z_{cm}^2)^{3/2}} + \dots = \frac{m^C m^D}{r^2} \hat{x}$$

Thus, the remaining terms are correction terms to the classical Newtonian gravitational force, which are neglected due to the assumption of a large separation distance relative to the size of the attracting body.

From physics and a little calculus, it is known that the mass attraction force between two spheres is equivalent to the attraction force between two point masses. Thus, the correction terms in Equation 3.32 must sum to zero for two spherical

bodies. From symmetry, a spherical body has identical moments of inertia in each principal direction and similarly, the second order mass moments are all equal. Body  $C$  and Body  $D$  are represented as symmetrical bodies by defining second order mass moments to be equal, such that:

$$\begin{aligned} m_{2,0,0}^{C/C_c} &= m_{0,2,0}^{C/C_c} = m_{0,0,2}^{C/C_c} = m_2^{C/C_c} \\ m_{2,0,0}^{D/D_c} &= m_{0,2,0}^{D/D_c} = m_{0,0,2}^{D/D_c} = m_2^{D/D_c} \end{aligned} \quad (3.33)$$

and then substitute into Equation 3.32 to obtain:

$$\begin{aligned} \frac{F_x^{C/D}}{G} &= m_{0,0,0}^{C/C_c} m_{0,0,0}^{D/D_c} h_{1,0,0}^{0,0,0} \\ &+ \frac{1}{2} m_{0,0,0}^{C/C_c} m_2^{D/D_c} (h_{1,0,0}^{2,0,0} + h_{1,0,0}^{0,2,0} + h_{1,0,0}^{0,0,2}) \\ &+ \frac{1}{2} m_2^{C/C_c} m_{0,0,0}^{D/D_c} (h_{3,0,0}^{0,0,0} + h_{1,2,0}^{0,0,0} + h_{1,0,2}^{0,0,0}) \\ &+ \frac{1}{4} m_2^{C/C_c} m_2^{D/D_c} \left( (h_{3,0,0}^{2,0,0} + h_{3,0,0}^{0,2,0} + h_{3,0,0}^{0,0,2}) \right. \\ &\quad \left. + (h_{1,2,0}^{2,0,0} + h_{1,2,0}^{0,2,0} + h_{1,2,0}^{0,0,2}) \right. \\ &\quad \left. + (h_{1,0,2}^{2,0,0} + h_{1,0,2}^{0,2,0} + h_{1,0,2}^{0,0,2}) \right) \end{aligned} \quad (3.34)$$

Since the mass moments of each Body are non-zero, the repeated derivatives must sum to zero. In order to unlock the information contained within the repeated derivatives contained within the correction terms in Equation 3.32 and Equation 3.34, return to the definition of the sub- and super-scripted repeated derivative function  $h$  for the distance between two points. The definition of the repeated derivative function was defined during the double Taylor series expansion of the function representing the distance between a point on the body and a point  $P$ . The distance between a point  $P = (a, b, c)$  and a point on the body in Cartesian coordinates, Figure 3.1, is given by Equation 3.1. The subscripts on the repeated derivative function  $h$  represent derivatives of the distance between two points, Equation 3.1, with respect to  $x, y, z$  and then evaluated at the origin,  $(x = 0, y = 0, z = 0)$ . The order of the subscripts will match the order of the corresponding mass moment multiplier for Body  $C$  plus one. For a Force in the  $x$  direction, the order  $(1, 0, 0)$  is added to the subscript of the

repeated derivative function  $h$  and  $(0, 1, 0)$  and  $(0, 0, 1)$  are added for a Force in the  $y$ , and  $z$  directions respectively. The increase in the derivative order as such, results directly from the fact that the Force is the gradient of the gravitational potential function. The superscripts represent the derivative with respect to the point  $a, b, c$  and then evaluated at the center of mass  $(x_{cm}, y_{cm}, z_{cm})$  of the second body, Body  $D$ . The order of the superscripts will thus match the order of the corresponding mass moment multiplier for Body  $D$ . To simplify the procedure for calculating the derivatives, point  $P$  is chosen to be the center of mass of the second distributed Body. We thus have an alternative representation of the repeated derivative function:

$$h_{i,j,k}^{p,q,r} = (-1)^{((i+j+k)(p+q+r))} f^{(i+p),(j+q),(k+r)} \quad (3.35)$$

and the superscripts on  $f$  are the orders of the derivatives with respect to  $x, y, z$ . Although this representation hides more of the information, such that the subscript on the multiplying mass moments no longer matches the superscript of derivative function  $f$ , the representation aids in computation of the derivative terms. Using Equation 3.35, the required repeated derivatives for the double second order expansion are calculated. The origin of the coordinate system is placed at the center of mass of Body  $C$  and the center of mass of Body  $D$  is located at  $(x, y, z) = (x_{cm}, y_{cm}, z_{cm})$ . The distance between the mass centers of Body  $C$  and  $D$  is therefore simply:

$$r = \sqrt{x_{cm}^2 + y_{cm}^2 + z_{cm}^2} \quad (3.36)$$

The calculated repeated derivatives are then:

$$\begin{aligned} h_{1,0,0}^{0,0,0} &= f^{1,0,0} = \frac{x_{cm}}{r^3} \\ h_{1,0,0}^{2,0,0} = h_{3,0,0}^{0,0,0} &= f^{3,0,0} = 15 \frac{x_{cm}^3}{r^7} - 9 \frac{x_{cm}}{r^5} \\ h_{1,0,0}^{0,2,0} = h_{1,2,0}^{0,0,0} &= f^{1,2,0} = 15 \frac{x_{cm} y_{cm}^2}{r^7} - 3 \frac{x_{cm}}{r^5} \\ h_{1,0,0}^{0,0,2} = h_{1,0,2}^{0,0,0} &= f^{1,0,2} = 15 \frac{x_{cm} z_{cm}^2}{r^7} - 3 \frac{x_{cm}}{r^5} \end{aligned}$$



$$\begin{aligned}
h_{3,0,0}^{2,0,0} &= f^{5,0,0} = 945 \frac{x_{cm}^5}{r^{11}} - 1050 \frac{x_{cm}^3}{r^9} + 225 \frac{x_{cm}}{r^7} \\
h_{3,0,0}^{0,2,0} = h_{1,2,0}^{2,0,0} &= f^{3,2,0} = 945 \frac{x_{cm}^3 y_{cm}^2}{r^{11}} - 105 \frac{x_{cm}^3}{r^9} - 315 \frac{x_{cm} y_{cm}^2}{r^9} + 45 \frac{x_{cm}}{r^7} \\
h_{3,0,0}^{0,0,2} = h_{1,0,2}^{2,0,0} &= f^{3,0,2} = 945 \frac{x_{cm}^3 z_{cm}^2}{r^{11}} - 105 \frac{x_{cm}^3}{r^9} - 315 \frac{x_{cm} z_{cm}^2}{r^9} + 45 \frac{x_{cm}}{r^7} \\
h_{1,2,0}^{0,2,0} &= f^{1,4,0} = 945 \frac{x_{cm} y_{cm}^4}{r^{11}} - 630 \frac{x_{cm} y_{cm}^2}{r^9} + 45 \frac{x_{cm}}{r^7} \\
h_{1,2,0}^{0,0,2} = h_{1,0,2}^{0,2,0} &= f^{1,2,2} = 945 \frac{x_{cm} y_{cm}^2 z_{cm}^2}{r^{11}} - 105 \frac{x_{cm} y_{cm}^2}{r^9} - 105 \frac{x_{cm} z_{cm}^2}{r^9} + 15 \frac{x_{cm}}{r^7} \\
h_{1,0,2}^{0,0,2} &= f^{1,0,4} = 945 \frac{x_{cm} z_{cm}^4}{r^{11}} - 630 \frac{x_{cm} z_{cm}^2}{r^9} + 45 \frac{x_{cm}}{r^7}
\end{aligned} \tag{3.37}$$

Using the calculated repeated derivative functions, we return to the correction terms in Equation 3.34. The first two correction term repeated derivatives are identical:

$$\begin{aligned}
(h_{1,0,0}^{2,0,0} + h_{1,0,0}^{0,2,0} + h_{1,0,0}^{0,0,2}) &= (h_{3,0,0}^{0,0,0} + h_{1,2,0}^{0,0,0} + h_{1,0,2}^{0,0,0}) \\
&= 15 \frac{x_{cm}^3}{r^7} - 9 \frac{x_{cm}}{r^5} + 15 \frac{x_{cm} y_{cm}^2}{r^7} - 3 \frac{x_{cm}}{r^5} + 15 \frac{x_{cm} z_{cm}^2}{r^7} - 3 \frac{x_{cm}}{r^5}
\end{aligned}$$

Collecting terms with the same power of  $r$ , one can simplify to find the leading repeated derivative terms sum to zero for the case when each body has equal second order mass moments (moments of inertia) in each direction.

$$\begin{aligned}
(h_{1,0,0}^{2,0,0} + h_{1,0,0}^{0,2,0} + h_{1,0,0}^{0,0,2}) &= (h_{3,0,0}^{0,0,0} + h_{1,2,0}^{0,0,0} + h_{1,0,2}^{0,0,0}) \tag{3.38} \\
&= 15 \frac{x_{cm}^3 + x_{cm} y_{cm}^2 + x_{cm} z_{cm}^2}{r^7} - 15 \frac{x_{cm}}{r^5} \\
&= 15 \frac{x_{cm} (x_{cm}^2 + y_{cm}^2 + z_{cm}^2)}{r^7} - 15 \frac{x_{cm}}{r^5} \\
&= 15 \frac{x_{cm}}{r^5} - 15 \frac{x_{cm}}{r^5} \\
&= 0
\end{aligned}$$

Similarly, one can algebraically show that the remaining derivative terms sum to zero for the case when each body has equal second order mass moments (moments of inertia) in each direction:

$$(h_{3,0,0}^{2,0,0} + h_{3,0,0}^{0,2,0} + h_{3,0,0}^{0,0,2}) = 0 \tag{3.39}$$

$$(h_{1,2,0}^{2,0,0} + h_{1,2,0}^{0,2,0} + h_{1,2,0}^{0,0,2}) = 0$$

$$(h_{1,0,2}^{2,0,0} + h_{1,0,2}^{0,2,0} + h_{1,0,2}^{0,0,2}) = 0$$

As expected, the correction terms sum to zero yielding the classical Newtonian attraction force between two spheres, when each attracting Body has equal second order mass moments in each direction about parallel coordinate systems located at the mass centers.

### 3.7 Force Equation in Matrix Form

For purposes of computational efficiency, it is often favorable to represent a system of multiplications and additions in matrix form. By using a linear algebra representation, optimized linear algebra packages can be used to increase computational efficiency. To rewrite the equation for the force on Body  $C$  due to Body  $D$  in matrix form, begin with the equation for the force, Equation 3.32, which has assumed that the cross products of inertia for Body  $C$  and Body  $D$  are zero. Using Equation 3.35 one rewrites Equation 3.32 to obtain:

$$\begin{aligned} \frac{F_x^{C/D}}{G} = & \frac{1}{2} m_{0,0,0}^{C/C_c} \left( 2m_{0,0,0}^{D/D_c} f^{1,0,0} + m_{2,0,0}^{D/D_c} f^{3,0,0} + m_{0,2,0}^{D/D_c} f^{1,2,0} + m_{0,0,2}^{D/D_c} f^{1,0,2} \right) \\ & + \frac{1}{4} m_{2,0,0}^{C/C_c} \left( 2m_{0,0,0}^{D/D_c} f^{3,0,0} + m_{2,0,0}^{D/D_c} f^{5,0,0} + m_{0,2,0}^{D/D_c} f^{3,2,0} + m_{0,0,2}^{D/D_c} f^{3,0,2} \right) \\ & + \frac{1}{4} m_{0,2,0}^{C/C_c} \left( 2m_{0,0,0}^{D/D_c} f^{1,2,0} + m_{2,0,0}^{D/D_c} f^{3,2,0} + m_{0,2,0}^{D/D_c} f^{1,4,0} + m_{0,0,2}^{D/D_c} f^{1,2,2} \right) \\ & + \frac{1}{4} m_{0,0,2}^{C/C_c} \left( 2m_{0,0,0}^{D/D_c} f^{1,0,2} + m_{2,0,0}^{D/D_c} f^{3,0,2} + m_{0,2,0}^{D/D_c} f^{1,2,2} + m_{0,0,2}^{D/D_c} f^{1,0,4} \right) \end{aligned} \quad (3.40)$$

Rearranging the terms into a matrix, the Force on Body  $C$  due to Body  $D$  with the cross products of inertia identically equal to zero can be written as:

$$\frac{F_x^{C/D}}{G} = \begin{bmatrix} \frac{1}{2}m_{0,0,0}^{C/C_c} \\ \frac{1}{4}m_{2,0,0}^{C/C_c} \\ \frac{1}{4}m_{0,2,0}^{C/C_c} \\ \frac{1}{4}m_{0,0,2}^{C/C_c} \end{bmatrix}^T \begin{bmatrix} 2f^{1,0,0} & f^{3,0,0} & f^{1,2,0} & f^{1,0,2} \\ 2f^{3,0,0} & f^{5,0,0} & f^{3,2,0} & f^{3,0,2} \\ 2f^{1,2,0} & f^{3,2,0} & f^{1,4,0} & f^{1,2,2} \\ 2f^{1,0,2} & f^{3,0,2} & f^{1,2,2} & f^{1,0,4} \end{bmatrix} \begin{bmatrix} m_{0,0,0}^{D/D_c} \\ m_{2,0,0}^{D/D_c} \\ m_{0,2,0}^{D/D_c} \\ m_{0,0,2}^{D/D_c} \end{bmatrix} \quad (3.41)$$

$$\frac{F_y^{C/D}}{G} = \begin{bmatrix} \frac{1}{2}m_{0,0,0}^{C/C_c} \\ \frac{1}{4}m_{2,0,0}^{C/C_c} \\ \frac{1}{4}m_{0,2,0}^{C/C_c} \\ \frac{1}{4}m_{0,0,2}^{C/C_c} \end{bmatrix}^T \begin{bmatrix} 2f^{0,1,0} & f^{2,1,0} & f^{0,3,0} & f^{0,1,2} \\ 2f^{2,1,0} & f^{4,1,0} & f^{2,3,0} & f^{2,1,2} \\ 2f^{0,3,0} & f^{2,3,0} & f^{0,5,0} & f^{0,3,2} \\ 2f^{0,1,2} & f^{2,1,2} & f^{0,3,2} & f^{0,1,4} \end{bmatrix} \begin{bmatrix} m_{0,0,0}^{D/D_c} \\ m_{2,0,0}^{D/D_c} \\ m_{0,2,0}^{D/D_c} \\ m_{0,0,2}^{D/D_c} \end{bmatrix} \quad (3.42)$$

$$\frac{F_z^{C/D}}{G} = \begin{bmatrix} \frac{1}{2}m_{0,0,0}^{C/C_c} \\ \frac{1}{4}m_{2,0,0}^{C/C_c} \\ \frac{1}{4}m_{0,2,0}^{C/C_c} \\ \frac{1}{4}m_{0,0,2}^{C/C_c} \end{bmatrix}^T \begin{bmatrix} 2f^{0,0,1} & f^{2,0,1} & f^{0,2,1} & f^{0,0,3} \\ 2f^{2,0,1} & f^{4,0,1} & f^{2,2,1} & f^{2,0,3} \\ 2f^{0,2,1} & f^{2,2,1} & f^{0,4,1} & f^{0,2,3} \\ 2f^{0,0,3} & f^{2,0,3} & f^{0,2,3} & f^{0,0,5} \end{bmatrix} \begin{bmatrix} m_{0,0,0}^{D/D_c} \\ m_{2,0,0}^{D/D_c} \\ m_{0,2,0}^{D/D_c} \\ m_{0,0,2}^{D/D_c} \end{bmatrix} \quad (3.43)$$

## 3.8 Application to Computational Methods

### 3.8.1 Finite Element Discretization

Proceed now to consider the situation where one wishes to discretize a large distributed body into a finite element representation. By using the information contained within Equations 3.31, 3.32 & 3.34, one can quickly deduce criteria for which a finite element representation will yield valid results. It is common practice to represent a distributed body with several point masses and to then sum up the contribution due to each element to obtain the gravitational attraction force for the entire distributed body. These point masses are essentially approximating the finite elements of the distributed body. For example, if the point masses are placed on equally spaced grid

points parallel to the axes of a Cartesian coordinate system, the point masses will be approximating a block-shaped finite element. It is already well known that by increasing the number of point masses representing a body, a more accurate approximation to the actual gravitational attraction force can be calculated. By increasing the number of points representing a body, the moments of inertia for the finite element which the point mass is approximating will approach zero in the limit. It is clearly seen by Equations 3.31, 3.32 & 3.34, that as one reduces the magnitude of the finite element moments of inertia, the correction terms to the classical Newtonian gravitational attraction force will approach zero. Thus, for a point mass summation approach, where the correction terms consisting of the moment of inertia have been neglected, the grid size must be small compared to the separation distance to reduce the magnitude of the neglected correction terms. Furthermore, Equations 3.32 & 3.34, indicate that one can eliminate correction terms by intelligently choosing the geometric shape and orientation of the finite elements. Suppose an element is chosen such that the moments of inertia are equal in all three principal directions and the cross products of inertia are zero. This is the case for example, when a sphere or a perfect cube is chosen. In the case of the sphere, as already shown, all of the correction terms collapse to zero. For the cube it will be shown in Section 3.10 that a cube is similar to a sphere to the fourth order. For a point mass summation approach, by choosing symmetric equal spacing of a Cartesian grid, the point masses are representing cubical finite elements. Hence cubical finite elements are nearly equivalent to using a point mass summation approach as long as both grids for each attracting body are aligned along the directions of a common Cartesian coordinate system. Thus, in order to calculate accurately the gravitational attraction force between two distributed bodies using a point mass summation approach, the points must be placed equidistant apart in the coordinate axis directions. This can become problematic when the distributed body has one dimension that is much larger than the smallest dimension. In addition, the principal directions of the grid used for each object must be the same. This can become restrictive if one desires to rotate the grid directions of one body to maximize the number of equally spaced grid points that are within a surface that is not parallel to a principal direction. To use a point mass summation approach for objects which

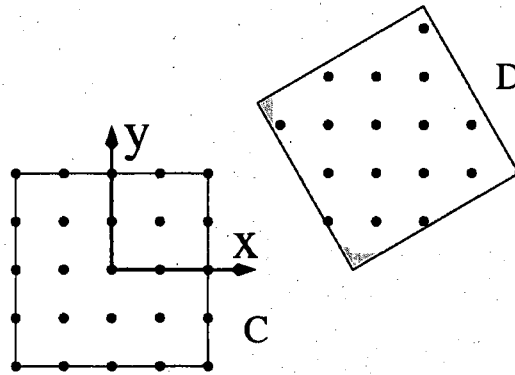


Figure 3.5: Common Cartesian grid direction for two bodies.

would require grids aligned in different directions for each body, a higher density of points would be required. For example, Figure 3.5, indicates a situation where the limitation of retaining common grid directions in each body would require additional points to obtain a valid result using a point mass summation approach. It can be clearly seen that Body *C* is well represented in the discretization, whereas Body *D* is not.

### 3.8.2 Point Mass Summation Limitations

There are four criteria that must be considered when using a point mass summation approach to calculate the gravitational attraction force between two distributed bodies:

1. Assumptions of ideal geometry and density distribution will lead to an uncertainty between the point mass model and the physical system.
2. Large number of points required to reduce moments of inertia and hence magnitude of correction terms.
3. Point mass locations must be equally spaced in all three dimensions. (Cubical finite element representation.)
4. Grid principal directions must be common for all the distributed bodies.

For simple geometric test cases, these criteria are often not problematic. However, these requirements can become restrictive for instances involving:

- Materials with unknown variations in the density distribution.
- Components not manufactured with tight fabrication tolerances.
- Large aspect ratio bodies. (Unable to increase the grid size in one direction, while keeping grid spacing in other directions fixed.)
- Large distributed bodies requiring lots of points for accuracy.
- Irregular shaped bodies.
- Simulations using non-cubical finite elements.

In such cases, where the restrictions of the point mass summation are limiting, it is useful to utilize the double Taylor method presented in Equation 3.30 or Equation 3.31. Although the restrictions may not at first appear problematic, there are several situations which arise in common practice that become problematic for accurate results using a point mass summation approach. Consider for example, a high precision sensor on a satellite, for which a gravitational mass attraction analysis must be performed. Large aspect ratio bodies can be quite common, which include satellite wiring and plumbing. For wires and pipes, it is difficult to increase the number of points in all directions equally while discretizing the object into finite elements. Typically, one would want to increase the number of points in the direction along the wire, while keeping the number of points in the cross sectional directions fixed. Yet, this procedure violates the criteria outlined for which a point mass summation technique will yield valid results. A satellite is also composed of many complex-shaped components. If a gravitational mass attraction analysis is to be performed to a high degree of accuracy, then a large number of points could be required. By using the double Taylor method, it is possible to reduce the overall number of points. If the double Taylor method is applied through a second order expansion, the object may be represented by the mass and moments of inertia, eliminating the need for discretization. In addition, uncertainties associated with material properties and fabrication could be

included by utilized measured parameters for the mass properties. If a discretization method is used to represent the satellite using finite elements for multiphysics simulations, it is often desirable to use one common grid for all the simulations. However, solid objects are usually discretized using tetrahedrons or block elements rather than cubical elements. If a tetrahedron mesh is used, then the criteria of equally spaced grid points in all directions will be violated, requiring the use of the double Taylor method to achieve accurate results.

### 3.9 Errors Due to Non-Exact Symmetrical Body

In Section 3.6 after assuming that the second order mass moments were identically equal, Equation 3.33, it was shown that the correction terms to the classical Newtonian attraction force sum to zero. This resulted in a collapse of the double Taylor equations to the equivalent of computing the attraction force between two point masses. However, in practice it is often difficult to manufacture an object with identical mass moments (moments of Inertia) in each principal direction. It is therefore of interest to determine the error associated with using a point mass attraction formula if the attracting body is not perfectly symmetrical. Consider the case where the second order mass moment in the  $x$  direction is slightly larger than the other two principal direction second order mass moments:

$$m_{2,0,0}^{C/C_c} - \delta m_{2,0,0}^{C/C_c} = m_{0,2,2}^{C/C_c} = m_{0,0,2}^{C/C_c} = m_2^{C/C_c} \quad (3.44)$$

For simplicity, further assume that the second distributed body, Body  $D$ , is a perfectly symmetrical body, such that second order mass moments are identical.

$$m_{2,0,0}^{D/D_c} = m_{0,2,0}^{D/D_c} = m_{0,0,2}^{D/D_c} = m_2^{D/D_c}$$

Begin with the double Taylor equation for the attraction force in the  $x$  direction, Equation 3.32, where the cross products of inertia are zero for both attracting bodies.

Plugging in the chosen geometry into Equation 3.31, one obtains:

$$\begin{aligned}
 \frac{F_x^{C/D}}{G} &= m_{0,0,0}^{C/C_c} m_{0,0,0}^{D/D_c} h_{1,0,0}^{0,0,0} \\
 &+ \frac{1}{2} m_{0,0,0}^{D/D_c} \left( (m_2^{C/C_c} + \delta m_{2,0,0}^{C/C_c}) h_{3,0,0}^{0,0,0} + m_2^{C/C_c} h_{1,2,0}^{0,0,0} + m_2^{C/C_c} h_{1,0,2}^{0,0,0} \right) \\
 &= m_{0,0,0}^{C/C_c} m_{0,0,0}^{D/D_c} h_{1,0,0}^{0,0,0} + \frac{1}{2} m_{0,0,0}^{D/D_c} \delta m_{2,0,0}^{C/C_c} h_{3,0,0}^{0,0,0}
 \end{aligned} \tag{3.45}$$

Again, the last term can be viewed as a correction term to the classical Newtonian gravitational attraction force between two point masses. If the second order mass moment is larger in either the  $y$  or  $z$  direction for the chosen slightly asymmetric geometry, a similar expression can be obtained. To summarize, for the three different cases where each mass moment in the  $x$ ,  $y$ , or  $z$  direction is slightly larger, the attraction force is:

$$\begin{aligned}
 \frac{F_x^{C/D}}{G} &= m_{0,0,0}^{C/C_c} m_{0,0,0}^{D/D_c} h_{1,0,0}^{0,0,0} + \\
 &\begin{cases} \frac{1}{2} m_{0,0,0}^{D/D_c} \delta m_{2,0,0}^{C/C_c} h_{3,0,0}^{0,0,0} & \text{if } m_{2,0,0}^{C/C_c} - \delta m_{2,0,0}^{C/C_c} = m_2^{C/C_c} \\ \frac{1}{2} m_{0,0,0}^{D/D_c} \delta m_{0,2,0}^{C/C_c} h_{1,2,0}^{0,0,0} & \text{if } m_{0,2,0}^{C/C_c} - \delta m_{0,2,0}^{C/C_c} = m_2^{C/C_c} \\ \frac{1}{2} m_{0,0,0}^{D/D_c} \delta m_{0,0,2}^{C/C_c} h_{1,0,2}^{0,0,0} & \text{if } m_{0,0,2}^{C/C_c} - \delta m_{0,0,2}^{C/C_c} = m_2^{C/C_c} \end{cases}
 \end{aligned} \tag{3.46}$$

Using the information presented in Equation 3.46, one can easily determine the sensitivity to the magnitude of the attraction force due to a slight asymmetry of a symmetrical body.

To calculate the magnitude of the correction terms, a simple test case is chosen consisting of two nominally cubical masses. One side of the central attracting mass, Body  $C$ , is manufactured to be slightly different in length than the other two dimensions. Let the side in the  $x$  direction to be slightly larger by  $\epsilon$  as presented in Figure 3.6, resulting in a change of the mass moment. For a simple brick-shaped object, the mass moment terms can be easily calculated by hand. If a constant density



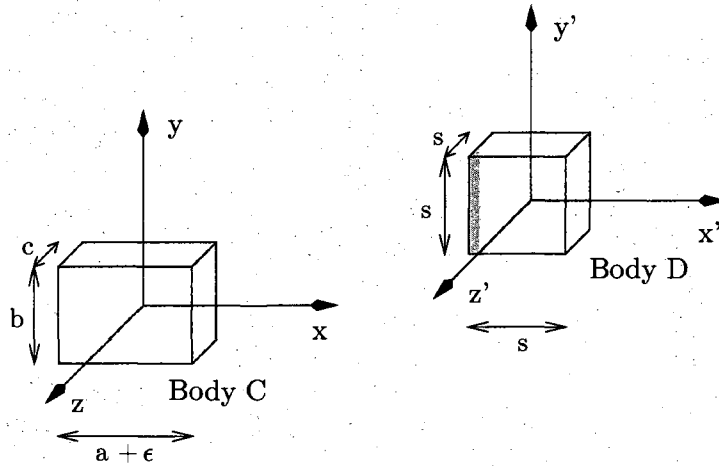


Figure 3.6: Slightly asymmetric central Body C and symmetric Body D.

rectangular brick of dimension  $a, b, c$  in the  $x, y, z$  directions respectively is considered, the mass moments are found to be:

$$m_{i,j,k}^{C/C_c} = \int_{-\frac{c}{2}}^{\frac{c}{2}} \int_{-\frac{b}{2}}^{\frac{b}{2}} \int_{-\frac{a}{2}}^{\frac{a}{2}} \sigma^c x^i y^j z^k dx dy dz$$

$$m_{i,j,k}^{C/C_c} = \begin{cases} 0 & \text{if } i \text{ or } j \text{ or } k \text{ is odd,} \\ \sigma^c \frac{8(\frac{a}{2})^{i+1}(\frac{b}{2})^{j+1}(\frac{c}{2})^{k+1}}{(i+1)(j+1)(k+1)} & \text{otherwise} \end{cases} \quad (3.47)$$

Recognizing that  $m_{0,0,0}^{C/C_c}$  is the mass of Body C, Equation 3.47 can be rewritten to remove the density term  $\sigma^c$  to produce:

$$m_{i,j,k}^{C/C_c} = \begin{cases} 0 & \text{if } i \text{ or } j \text{ or } k \text{ is odd,} \\ \frac{(\frac{a}{2})^i (\frac{b}{2})^j (\frac{c}{2})^k}{(i+1)(j+1)(k+1)} m_{0,0,0}^{C/C_c} & \text{otherwise} \end{cases} \quad (3.48)$$

Using Equation 3.48 and the repeated derivative functions listed in Equation 3.37, the correction term magnitudes in Equation 3.46 can be computed. However, before actually computing a value for the correction term, it is useful to gain some intuition on how the results should behave for various locations of Body D. By looking closely

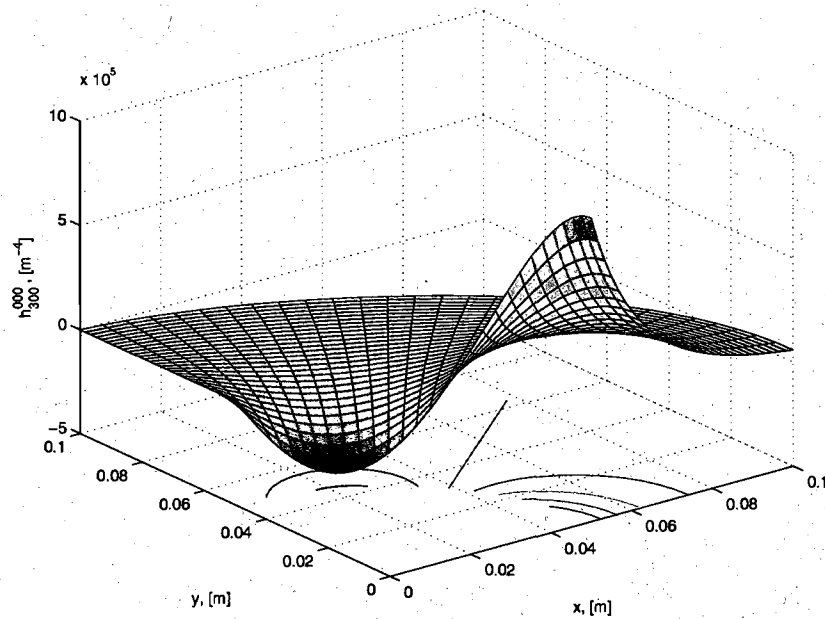


Figure 3.7: Repeated derivative function  $h_{3,0,0}^{0,0,0}$  in the  $x, y$  plane.

at the correction terms in Equation 3.46, one should observe that the location dependency information is all contained within the repeated derivative function. For an object, the mass and the variation of the second order mass moment can be considered fixed. The remaining term is only the repeated derivative function, which depends on location. Thus, the behavior of the correction term magnitude will behave like the repeated derivative function. Figure 3.7 is a plot of the repeated derivative function  $h_{3,0,0}^{0,0,0}$  in the  $x, y$  plane.

By observing the information provided in Figure 3.7, it is seen that the largest positive value of the correction term due to the additional length in the  $x$ -direction will occur when the radial distance is aligned along the  $x$ -axis. Selecting a location for the Body  $D$  to be along the  $x$ -axis, the point mass attraction force in the  $x$ -direction and corresponding correction term were calculated. The value used for each variable in the calculation is found in Table 3.3. In the calculation the mass was assumed constant, such that an increase in the  $x$ -direction length of Body  $C$  and hence a change in the volume, would alter the density. Using the values presented in Table 3.3, the

Identifier	Description	Value	Units
a	Nominal $x$ -direction length of Body $C$	40	[mm]
b	Nominal $y$ -direction length of Body $C$	40	[mm]
c	Nominal $z$ -direction length of Body $C$	40	[mm]
$\epsilon$	Error in $x$ -direction length of Body $C$	0.1	[mm]
s	Nominal cube side length for Body $D$	40	[mm]
$x, y, z$	Body $D$ mass center location relative to Body $C$	(60, 0, 0)	[mm]
$m_{0,0,0}^{C/C_c}$	Body $C$ mass	1.37	[kg]
$m_{0,0,0}^{D/D_c}$	Body $D$ mass	1.37	[kg]
$\delta m_{2,0,0}^{C/C_c}$	Change in Body $C$ 2 <sup>nd</sup> order mass moment due to $\epsilon$	0.9145	[kg mm <sup>2</sup> ]

Table 3.3: Input for non-symmetrical body calculation.

point mass attraction force on Body  $C$  due to Body  $D$  in the  $x$ -direction was found to be  $F_x^{C/D} = 3.4788 \times 10^{-8}$  N with a correction term of  $\delta F_x^{C/D} = 1.9351 \times 10^{-11}$  N. This results in a total force of  $F_x^{C/D} = 3.4808 \times 10^{-8}$  N. The correction term magnitude is small compared to the point mass force, but in situations where a precise value is required, the contribution can become significant. Consider for example the LISA mission, where the static value of the gravitational attraction force must be kept below  $5 \times 10^{-10}$  m/s<sup>2</sup> for the entire satellite [42]. If there are approximately 25 components within the entire satellite which exhibited a similar geometrical error, the mass attraction disturbance budget would be exceeded if the correction terms were neglected. This could easily be the case where perhaps 25 fasteners were slightly longer than expected, but still within manufacturers specifications. The error associated with neglecting the correction terms is especially problematic if the mass attraction analysis had assumed the ideal geometry and the actual deviation from the geometry was unknown or assumed to be ideal. For this calculation it is important to note that the chosen geometry results in the attraction force between a slightly asymmetric body in a single direction and a purely symmetrical body. If an additional asymmetry is added to the Body  $D$  or additional asymmetries are added in other directions, additional correction terms will be generated. In addition, if a body is discretized using a slightly asymmetric grid, the neglected correction terms for each element can sum

to a significant error if a point mass summation were used. In cases, where precision is required, the magnitude of the correction term can be further reduced by placing more strict requirements on the allowed dimensional variation  $\epsilon$ , or by intelligently choosing the location of Body  $D$ .

### 3.10 Observation: A Cube is Similar to a Sphere

Using the information presented thus far, it is interesting to note that a sphere and a cube exhibit similar gravitational attraction properties. In fact, a cube of homogeneous density and a sphere of homogeneous density exhibit identical gravitational attraction properties through a third order expansion. To show this, recall Equation 3.48 for the mass moments of a rectangular brick-shaped object, where it was found that the mass moments  $m_{i,j,k}^{C/C_c}$  are identically equal to zero if  $i$  or  $j$  or  $k$  is odd. Thus, the third order mass moments for a brick-shaped object are identically equal to zero. For a cube, each side of the brick-shaped object are identical in length. As a result, the moment of inertia in each principal direction and similarly the second order mass moments are all equal. In Section 3.6 it was shown that when such a condition exists, namely all the moments of inertia are identical, then the attraction equations simplify to that of the classical Newtonian attraction equations. Thus, for a homogeneous cubical shaped geometry, the attraction force through the third order expansion is identical to the classical Newtonian attraction equation.

### 3.11 Variations in Density

Although during the derivation of the attraction force between two distributed bodies, a constant density distribution was assumed, a variation in density throughout the body can still be accounted for when using Equation 3.30. By looking closely at the force equation due to two distributed bodies, it is noted that information regarding the mass distribution is all contained within the mass moment representations. Thus, the solution to incorporating variations in density into the attraction force calculation lies within the determination of the mass moments. As described in Section 3.2, two

basic approaches exist: a physical measurement approach and a modeling approach.

The first solution utilizes physical measurements of the moments of inertia to account for the unknown density variation. By computing the attraction force using measured moments of inertia of the component in question, variations in density as well as geometric variations will be included in the attraction calculation. As a result, the exact density distribution within an object need not necessarily be known in order to determine the actual gravitational attraction force. In fact, by using measured quantities in a Taylor Series representation of the gravitational mass attraction, the only unknown uncertainty in the calculated attraction force lies within the neglected higher order terms.

The second solution involves a modeling approach, where either the density distribution throughout an object is known or can be described using a polynomial representation. Knowledge of a variation in density within the body can be included in two ways. The first is on a finite element level during the computation of the mass moments for each individual tetrahedron. When the distributed mass is broken into individual tetrahedrons to calculate the volume moment, the density of the tetrahedron being computed can be multiplied by the volume moment, before the result is summed to determine the volume moments for the entire body. This method allows for single point variations within the density, since single tetrahedrons can be selected to have a different density than the rest of the volume. Although single point variations within the density may not be a likely occurrence, the method allows for voids or stress hardened areas near machined surfaces/holes within the structure to be included.

The second method for incorporating a variation in density within the mass involves a polynomial representation for the density. First we return to the fundamental derivation of the attraction force, where the negative gradient of the gravitational Potential was applied. The Potential at point  $P$ , Equation 3.2, modified to explicitly denote a non-constant density throughout the volume occupied by the distributed

body is:

$$U(P) = G \iiint_V \sigma(x, y, z) f(x, y, z) dx dy dz \quad (3.49)$$

Again, one takes the negative partial derivative of the Potential with respect to the variable  $x$  to obtain the attraction force in the  $x$ -direction. By applying the chain rule due to the non-constant density term, a modified form of Equation 3.3 for the attraction force is obtained.

$$\begin{aligned} -\frac{F_x(P)}{G m^P} &= \iiint_V \sigma^c(x, y, z) f^{1,0,0}(x, y, z) dx dy dz + \\ &\quad \iiint_V \sigma^{c^{1,0,0}}(x, y, z) f(x, y, z) dx dy dz \end{aligned} \quad (3.50)$$

The comma-delimited superscript notation on the density is again used to denote the derivative order with respect to the first, second, and third coordinates (x,y,z). By using our insight of the resulting force equation due to two distributed bodies with constant density, it is again noted that information regarding the mass distribution is all contained within the mass moment representations. Knowledge of a variation in density within the body can then be included in the mass moment terms. Assuming a polynomial representation for the density can be determined, the modified mass moments can be calculated. Recall the definition of the volume moment and mass moment, Equation 3.7, and Equation 3.8, again modified to explicitly indicate a non-constant density:

$$\begin{aligned} M_{i,j,k}^{C/C_c} &= \iiint_V x^i y^j z^k dx dy dz \\ m_{i,j,k}^{C/C_c} &= \iiint_V \sigma^c(x, y, z) x^i y^j z^k dx dy dz \end{aligned}$$

For a simple example, suppose that the density can be defined as:

$$\sigma^c(x, y, z) = \mu x + \nu y + \xi z + \sigma_o \quad (3.51)$$

After substituting the expression for the density as a function of spatial coordinates, we see that the mass moment due to the density variation becomes:

$$\begin{aligned} \tilde{m}_{i,j,k}^{C/C_c} &= \iiint_V \sigma^c(x, y, z) x^i y^j z^k dx dy dz \\ &= \iiint_V \mu x x^i y^j z^k dx dy dz + \iiint_V \nu y x^i y^j z^k dx dy dz + \\ &\quad \iiint_V \xi z x^i y^j z^k dx dy dz + \iiint_V \sigma_o x^i y^j z^k dx dy dz \\ &= \mu M_{i+1,j,k}^{C/C_c} + \nu M_{i,j+1,k}^{C/C_c} + \xi M_{i,j,k+1}^{C/C_c} + m_{i,j,k}^{C/C_c} \end{aligned} \quad (3.52)$$

Thus, depending on the representation of the density as a function of position, the mass moment representation in Equation 3.30, can be substituted by a weighted summation of higher order volume moments and the constant density mass moment. For the second term in Equation 3.50, which contains the derivative of the density function, we apply a similar technique for the mass moment representation, where the derivative of the density is used.

## **Part II**

# **The Necessity of Measurements**



## Chapter 4

# Mass Property Measurements for Mass Attraction Calculations

Due to material property limitations and machining technology, it is not feasible to manufacture something which is perfectly homogeneous in density or geometrically exact as designed. Geometrical imperfections can be minimized by tedious measurements and with modern machining methods, but there will always exist a deviation from the desired ideal final product. Material density variations can be reduced by choosing appropriate materials, but the density distribution within an object will never match an ideal homogeneous distribution. It is not practical nor feasible to manufacture a part which has a completely homogeneous density. For example, typical inhomogeneities for steel can be on the order of a part in  $10^3$ . In addition, there may be density variations due to the machining process, such as localized stress hardening. Brass and BeCu typically have a density inhomogeneity within the range of a part in  $10^4$  to a part in  $10^5$ . Some ceramics can even have a density inhomogeneity as high as several percent.

These real-world variations in geometry and the density distribution create an uncertainty, which may lead to an unacceptable error in gravitational mass attraction calculations. Consider for example the Disturbance Compensation System, DISCOS, for the first drag free satellite. For DISCOS, the beryllium oxide proof mass housing was expected to have better than 0.1% density uniformity [15], such that the total

contribution to the drag-free disturbance budget due to mass attraction effects was on the order of 20%. Yet, the manufacturer could only guarantee the material to be manufactured with a 0.3% density uniformity [16]. The result was an increase in the mass attraction budget for the proof mass housing to over 40% of the total drag-free disturbance budget [17], [53].

For drag-free satellites, the associated uncertainty in the mass properties and geometry create an uncertainty in the mass attraction calculations, which may lead to an unacceptable contribution to the disturbance budget and hence a reduction in the drag-free performance. One method to proceed in the satellite design process is to place stringent requirements on the density distribution within a component to ensure that the mass attraction noise budget allocation will not be exceeded due to the associated uncertainty. For high-precision drag-free references, the requirements of an ideal geometry or homogeneous density distribution can easily force the use of special materials or manufacturing processes.

In order to reduce the uncertainty in the mass attraction calculations associated with idealized geometry and density assumptions, it is desired to physically measure the attraction force. The gravitational mass attraction force between the drag-free reference mass and the surrounding satellite can not be easily measured directly. Yet, as shown in Chapter 3, the mass attraction formula through a second order expansion consists of the measurable quantities of mass, mass center, and moment of inertia about the mass center. Thus, the gravitational mass attraction force on the drag free reference due to the satellite can be indirectly measured to the third order, which includes the unknown density inhomogeneities and geometry variations. The only unknown uncertainty in the calculated attraction force then lies within the neglected higher order terms. The geometrical and density variation errors do not contribute significantly to the remaining higher order terms and may be modeled, requiring only  $\sim 10\%$  accuracy to achieve better than  $\sim 1e-5$  overall accuracy. As a result, the exact density distribution within an object and the geometry need not necessarily be known or measured in order to determine the actual gravitational attraction force. Variations in density as well as geometric variations will be automatically included in the calculation by utilizing the measured mass properties.

Mass Property	Measurement Precision	Notes
Mass	1 part in $10^9$	For 1 kg object. Reference: [14]
Mass Center	$\sim 100$ nm	Reference: [9], [12]
Moment of Inertia	$\sim 1$ part in $10^4$	For 2.25 kg object. Reference: [54]

Table 4.1: State of the art mass property measurement capabilities.

In order to predict the satellite system gravitational mass attraction force and force gradients, physical mass property measurements are necessary. The corresponding properties of mass, mass center, and moment of inertia must be precisely determined for the proof mass and satellite components. The remainder of this chapter will therefore provide an overview of mass property measurement techniques. Table 4.1 provides an initial overview of current state of the art mass property measurement abilities, which are discussed in the following sections.

## 4.1 Mass Measurement

The physical property of mass is a fundamental property associated with all objects and the measurement or quantity of mass is required for a number of every day applications, including international commerce. As such, the unit of mass is defined by international treaty to establish a consistent set of measurement units. The unit of mass in the International System of Units is the kilogram and the value is defined with reference to an object known as the International Prototype Kilogram (IPK). A variety of measurement techniques exist for mass measurement and the ability to measure mass is at an unprecedented precision. In fact, the National Institute of Standards and Technology (NIST) offers mass calibration measurement services [45] with an uncertainty of  $50 \times 10^{-9}$  kg at 1 kg and replicas of the IPK have been measured to nearly  $1 \times 10^{-9}$  kg using the best balances [14]. Thus, the use of an object's

mass for an indirect measurement of gravitational attraction force will not hinder the overall precision of the attraction force measurement.

### Required Precision

Whenever performing measurements, it is often helpful to know the answer to the question "how good does the measurement need to be?". One can not justify the additional expense or complexity to measure an item to state of the art precision if an approximate value is "good enough". For mass measurements it is however not difficult to achieve a high precision with regular laboratory grade equipment. The mass of an object is in the first term of the gravitational potential Taylor series expansion, which is the standard Newtonian point mass attraction force,  $F = GMm/r^2$ . In order to utilize measured values for the mass in the gravitational attraction analysis, the error associated with the mass measurement is directly proportional to the error in the attraction properties. The actual required precision for the mass measurement will depend on the separation distance between the two objects as well as the relative magnitude of the mass for each object. In addition, if the system is composed of a number of objects, the required precision on each object will need to be increased in order to achieve the overall desired precision on the gravitational mass attraction properties for the complete system. For gravitational wave observatories such as LISA, the dynamic stability of the system is also of importance. Stebbins et. al [56] estimates a combination of 0.03 kg mass error at a 0.05 m separation distance with a displacement stability of  $3 \times 10^{-9}$  m/Hz<sup>1/2</sup> is necessary to meet science requirements for LISA.

## 4.2 Mass Center Measurement

Since the mass center location of an object is not a fundamental SI unit, the ability to measure the mass center is less understood than the fundamental measure of mass. Still, the location of an object's mass center is a fundamental mass property. The mass center for example is the key reference point for an object when analyzing the statics/dynamics of an object. In theory, the mass center for a homogeneous density

object of perfect geometry can be calculated and suffices for typical calculations in statics/dynamics. For a three-dimensional object, a pendulous technique is typically used to determine the mass center offset. Such a measurement technique is capable of determining the mass center location to levels greater than approximately  $1\ \mu\text{m}$ . Conklin [9] has shown that a velocity modulation technique can be used to measure the mass center location of spheres to state of art precision on the order of  $\sim 100\ \text{nm}$ .

### Required Precision

For an indirect measurement of the gravitational attraction force, the equations require position location for the object. In addition the equations are simplified by choosing the coordinate axes coincident with the object's mass center such that the moment of inertia for the object is about the mass center, consistent with standard definitions. For the purposes of this work, it is assumed that the position location for an object is that of the object's mass center and the current state of the art precision is sufficient. Consider for example the simplified point mass attraction force between two objects each of mass  $1\ \text{kg}$ , separated by  $0.1\ \text{m}$ . The gravitational attraction force is on the order of  $6.67 \times 10^{-9}\ \text{N}$ . An uncertainty of  $100\ \text{nm}$  in the location results in an associated uncertainty in the attraction force on the order of  $1.3 \times 10^{-15}\ \text{N}$  for better than 2 parts in  $10^7$  order of accuracy on the point mass attraction force. For Triad-1/DISCOS, a position uncertainty of  $0.5\ \text{mm}$  was allowed for a part with mass of about  $1\ \text{g}$  located within the DISCOS electronics [22]. For LISA, Stebbins et. al [56] utilized an estimated displacement sensitivity of  $3 \times 10^{-9}\ \text{m/Hz}^{1/2}$  to establish the requirements on the mass attraction disturbance levels.

## 4.3 Moment of Inertia Measurement

The moment of inertia is also a fundamental mass property parameter associated with an object. The moment of inertia is typically important for rigid body rotational dynamics. Rotational motion is present in a number of every-day industries from automotive to aerospace to information technology. Still, the moment of inertia

measurement as compared to the other mass property measurements is the least understood. Often a rough approximation for the moment of inertia is sufficient for a number of applications. Typical moment of inertia measurement devices are capable of 1 part in  $10^3$  accuracy and current state of the art techniques are approaching capabilities of a few parts in  $10^4$ . Space Electronics LLC provides current state of the art moment of inertia measurement devices [54], which are capable of an accuracy of 1 part in  $10^4$  for objects on the order of 2.25 kg to 20 kg. These instruments are the most accurate commercially available instruments in the world today and are two to three times more expensive than the same instrument with a 1 part in  $10^3$  accuracy.

### Required Precision

For gravitational mass attraction measurements utilizing measured values for the moment of inertia tensor, it is difficult to provide a direct answer to the question of "how good does the measurement need to be?". Although the moment of inertia tensor is the least understood of the mass properties, one would like to know if the state of the art precision is good enough. In Chapter 3 it was noted that the first term in the series expansion is simply the point mass attraction term and the higher order terms were therefore corrections due to non-symmetrical shaped objects. The terms involving the moment of inertia tensor are the first terms to include the effects of a non point mass object. In fact, it was shown in Section 3.6 that the second order terms sum to zero for the case when the object has identical principal moments of inertia. Thus, the required precision on the inertia will be highly dependent on the ratio of the minimum to maximum principal moment of inertia. In general, the more symmetrical an object is in terms of the moment of inertia ellipsoid, the more relaxed the accuracy requirement may be for the moment of inertia tensor measurements.

To gain some insight into the required precision on the moment of inertia measurements, recall the previous example in Section 1.3.3 between two spherical shaped objects (Figure 1.4). The spherical shaped objects in the example contained internal voids, which is comparable to an object with an irregular density distribution or where the object has the maximum principal moment of inertia about 10% larger than the minimum principal moment of inertia. For the example in Section 1.3.3,

the second attracting body was located along the direction of the maximum principal moment of inertia,  $\bar{R} = 3r_o\hat{z}$ . By incorporating the inertia values into the mass attraction calculation, the result was a difference of about 3.2% from the point mass solution. Now consider the case where the second attracting object is positioned along a different principal moment of inertia direction. For the two objects in this example, the intermediate and minimum principal moments of inertia are about the same magnitude. For the case where the second object is located along the minimum principal moment of inertia,  $\bar{R} = 3r_o\hat{x}$ , the difference between the point mass attraction and the double Taylor method,  $100\% \times (F_P - F_{DT}) / F_{DT}$ , is about 1.6%. Thus, the actual orientation of each object determines the magnitude of the contribution to the mass attraction calculation. Intuitively this makes sense, as the moment of inertia is defined by the mass distribution. As a result, the required precision on the moment of inertia tensor will also be a function of the actual orientation. Now consider an actual uncertainty in the moment of inertia tensor measurement. If the two-part sphere in the example has a maximum moment of inertia that is 1 part in  $10^4$  larger, one finds a change in acceleration of  $1.5 \times 10^{-13} \text{ m/s}^2$ , or about a 2.8 in  $10^5$  accuracy. If the LISA static mass attraction disturbance requirement for the entire spacecraft is  $5 \times 10^{-10} \text{ m/s}^2$  [56], then for this example a part in  $10^4$  accuracy for the moment of inertia will result in about 3 parts in  $10^4$  accuracy on the acceleration.

### 4.3.1 Measurement Techniques

A moment of inertia measurement apparatus typically attempts to produce a pure rotation about one degree of freedom. The measurements of rotation can have uncertainties when there are significant other degrees of freedom. A number of measurement techniques exist for producing the rotation about a single degree of freedom in order to obtain the moment of inertia. Devices include for example wire supported torsion pendulums, torsion rod platforms and air bearing platforms. A comparison of various measurement techniques is presented in Table 4.2. The current state of the art measurement apparatus manufactured by Space Electronics LLC utilizes an air bearing technology for generating the pure rotation necessary for the measurement.

Methods	Advantages	Challenges
Three-Wire Pendulum	Simple	Unconstrained swinging modes
Three-Wire Pendulum with Pin Bearing	Simple	Damping/Friction
Five-Wire Pendulum	Constrained swinging modes	New technique
Torsion Rod and Platform	Less expensive than air bearing platforms	
Air Bearing Platform	Current state of the art accuracy	Requires restoring force. Expensive
Air Bearing and Torsion Rod	Torsion rod provides stability	Expensive

Table 4.2: Inertia measurement techniques.



### 4.3.2 Determining the Inertia Tensor

As already mentioned, measuring the moment of inertia involves producing a pure rotation about one degree of freedom. The moment of inertia for an object is however a second order tensor quantity. An apparatus producing a pure rotation can therefore only determine the radius of gyration, or rather the instantaneous moment of inertia about the rotation axis. Thus, in order to obtain the full inertia tensor ellipsoid, measurements must be made about multiple axes of rotation.

The complete inertia tensor for an object,  $\bar{I}$ , has nine components  $I_{ij}$  six of which are independent. Consider an object which is rotating about the unit vector  $\hat{a}$ . The instantaneous inertia about the direction of  $\hat{a}$  is a scalar and is given by:

$$I = \hat{a} \cdot \bar{I} \cdot \hat{a} \quad (4.1)$$

Thus, with  $n$  measurements of  $^{(n)}I$  along  $n$  unique directions,  $^{(n)}\hat{a}$ , the system of  $n$  equations is formulated:

$$\begin{bmatrix} ^{(1)}I \\ ^{(2)}I \\ ^{(3)}I \\ \vdots \\ ^{(n)}I \end{bmatrix} = \begin{bmatrix} ^{(1)}a_1^2 & 2^{(1)}a_1^{(1)}a_2 & 2^{(1)}a_1^{(1)}a_3 & ^{(1)}a_2^2 & 2^{(1)}a_2^{(1)}a_3 & ^{(1)}a_3^2 \\ ^{(2)}a_1^2 & 2^{(2)}a_1^{(2)}a_2 & 2^{(2)}a_1^{(2)}a_3 & ^{(2)}a_2^2 & 2^{(2)}a_2^{(2)}a_3 & ^{(2)}a_3^2 \\ ^{(3)}a_1^2 & 2^{(3)}a_1^{(3)}a_2 & 2^{(3)}a_1^{(3)}a_3 & ^{(3)}a_2^2 & 2^{(3)}a_2^{(3)}a_3 & ^{(3)}a_3^2 \\ \vdots & \vdots & \vdots & \vdots & \vdots & \vdots \\ ^{(n)}a_1^2 & 2^{(n)}a_1^{(n)}a_2 & 2^{(n)}a_1^{(n)}a_3 & ^{(n)}a_2^2 & 2^{(n)}a_2^{(n)}a_3 & ^{(n)}a_3^2 \end{bmatrix} \begin{bmatrix} I_{xx} \\ I_{xy} \\ I_{xz} \\ I_{yy} \\ I_{yz} \\ I_{zz} \end{bmatrix} \quad (4.2)$$

where  $x, y, z$  represent the body fixed axis directions. Rewriting Equation 4.2 more compactly as  $^{(n)}\bar{I} = A\bar{I}_{ij}$ , the solution to these  $n$  equations in the six unknown inertia components can be solved by least squares formulation so long as there are six or more independent directions of rotation:

$$\bar{I}_{ij} = (A^T A)^{-1} A^T ^{(n)}\bar{I} \quad (4.3)$$

The inertia tensor  $\bar{I}$  is completed by noting that the tensor is symmetric. Furthermore,

the covariance matrix for the least squares estimate is given by [57]:

$$P_{LSE} = (A^T A)^{-1} MSE \quad (4.4)$$

where the mean square error of the estimate,  $MSE$ , is a function of the residuals from the least squares estimate:

$$MSE = \frac{{}^{(n)}\bar{I}^T \left( {}^{(n)}\bar{I} - A\bar{I}_{ij} \right)}{m - n} \quad (4.5)$$

where  $m$  and  $n$  are the number of measurements and the number of unknowns respectively. The matrix diagonal,  $\text{diag}(P_{LSE})$ , produces the covariance elements  $\sigma_{ij}^2$ , corresponding to the inertia tensor components,  $\bar{I}_{ij}$ . The standard deviation is then the square-root of the elements. The resulting standard deviation tensor is denoted by  $\bar{\Sigma}_{LSE}$ , or in matrix form:

$$[\Sigma_{LSE}] = \begin{bmatrix} \sigma_{xx} & \sigma_{xy} & \sigma_{xz} \\ \sigma_{yx} & \sigma_{yy} & \sigma_{yz} \\ \sigma_{zx} & \sigma_{zy} & \sigma_{zz} \end{bmatrix} \quad (4.6)$$

Once the inertia tensor is determined for the object in the body fixed coordinate frame, which potentially may have been arbitrarily defined, the principal moment of inertia values,  $I_{p11}$ ,  $I_{p22}$ ,  $I_{p33}$ , are determined through an eigenvalue problem. The eigenvalues are the principal moment of inertia values and the eigenvectors,  $\hat{e}_1$ ,  $\hat{e}_2$ ,  $\hat{e}_3$ , define the directions for the principal moment of inertia, such that:

$$I_{p11} = \hat{e}_1 \cdot \bar{I} \cdot \hat{e}_1 \quad (4.7)$$

$$I_{p22} = \hat{e}_2 \cdot \bar{I} \cdot \hat{e}_2 \quad (4.8)$$

$$I_{p33} = \hat{e}_3 \cdot \bar{I} \cdot \hat{e}_3 \quad (4.9)$$

Additionally, the eigenvectors create the columns of the required transformation matrix from the body frame to the principal axis frame,  $T^{P/B} = [\hat{e}_1 \ \hat{e}_2 \ \hat{e}_3]$ , such

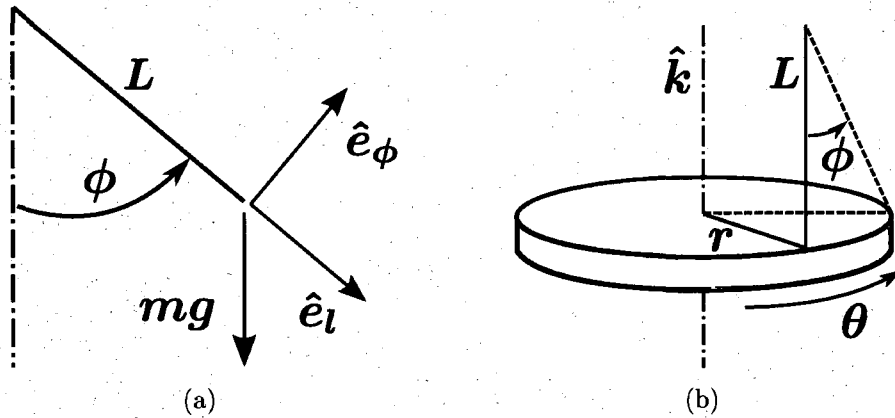


Figure 4.1: Torsion pendulum free body diagram.

that:

$$[I_p] = [T^{P/B}]^T [I] T^{P/B} \quad (4.10)$$

The rotation matrix is then used to transform the standard deviation matrix to the principal axis frame:

$$[\Sigma_p] = [T^{P/B}]^T [\Sigma_{LSE}] T^{P/B} \quad (4.11)$$

## 4.4 Measurements Using a Torsion Pendulum

### 4.4.1 Torsion Pendulum Dynamics

Consider a torsion pendulum with a constraint to rotate about a vertical axis. The dynamics follow the simple relationship between the torque,  $\tau$ , the angular acceleration,  $\ddot{\theta}$ , and the instantaneous moment of inertia,  $I$ , about the axis of rotation for a rotation through an angle  $\theta$ :

$$\tau = I\ddot{\theta} \quad (4.12)$$

Three wires may be used for instance to generate the necessary constraint for the

torsion pendulum to rotate about a vertical axis. From the free body diagram of a trifilar torsion pendulum shown in Figure 4.1(a), a rotation of the pendulum platform through an angle of  $\theta$ , results in the restoring force of  $-mg \sin \phi$ , where  $m$  is the mass of the pendulum,  $\phi$  the angular change in the wire position and  $g$  the gravitational constant. The restoring torque, assuming small angles such that  $\sin \phi \simeq \phi$ , is therefore:

$$\tau = -mg\phi r \quad (4.13)$$

where  $r$  is the distance from the rotation center to the wire attach point. Equating Equation 4.12 with Equation 4.13 one obtains:

$$I\ddot{\theta} = -mg\phi r \quad (4.14)$$

From the geometry shown in Figure 4.1(b) it is seen that the relationship between  $\theta$  and  $\phi$  is given by equating the arc lengths, such that  $r\theta = L\phi$ , where  $L$  is the length of the wire. Substituting in the relationship for  $\phi$  and rearranging terms, one obtains the ordinary differential equation for the motion of the pendulum platform in terms of the rotation angle  $\theta$ :

$$\ddot{\theta} + \frac{m gr^2}{I L} \theta = 0 \quad (4.15)$$

Therefore, the equation of motion is a simple harmonic oscillator where the natural frequency of oscillation is:

$$\omega^2 = \frac{m gr^2}{I L} \quad (4.16)$$

Clearly, the physical system will exhibit some damping and the system response will be that of a damped harmonic oscillator. The damped natural frequency,  $\omega_d$ , is a quadratic function of the damping coefficient,  $\zeta$ , given by:

$$\omega_d = \omega \sqrt{1 - \zeta^2} \quad (4.17)$$

Thus, the natural frequency of a lightly damped pendulum is not strongly dependent on the system damping, and  $\omega_d \approx \omega$ . Since the radius of gyration,  $R_g$ , is defined as  $R_g^2 = I/m$ , the relationship between the pendulum radius of gyration and the frequency of oscillation is given by:

$$R_g^2 = \frac{I}{m} = \frac{k}{\omega^2} \quad (4.18)$$

where the torsion stiffness coefficient  $k$  is defined by:

$$k = \frac{gr^2}{L} \quad (4.19)$$

The torsion pendulum oscillatory frequency therefore characterizes the pendulum radius of gyration, or indirectly the instantaneous moment of inertia about the rotation axis.

#### 4.4.2 Mass Center Measurement Using a Torsion Pendulum

Although a number of techniques exist for measuring an object's mass center offset from the geometric center, it is worth recognizing that a torsion pendulum is also capable of such a measurement. Recall Equation 4.18 for the relationship between the torsion pendulum rotational frequency and the radius of gyration:

$$R_g^2 = \frac{I}{m} = \frac{k}{\omega^2}$$

By measuring the natural frequency of rotation, the mass center offset from the geometric center of an object is also obtained. To see this, first replace the instantaneous moment of inertia,  $I$ , about the rotation axis in Equation 4.18 with the separate contributions to the total instantaneous inertia due to the torsion pendulum platform,  $I_{ozz}$  and the measurement object,  $I_o$ . Furthermore, note that the moment of inertia for the object consists of the linear sum of the moment of inertia about the objects mass center,  $I_o$ , plus the parallel axis theorem components of the objects mass,  $m_o$ , times the square of the distance from the rotation center to the mass center,  $r^2$ . In

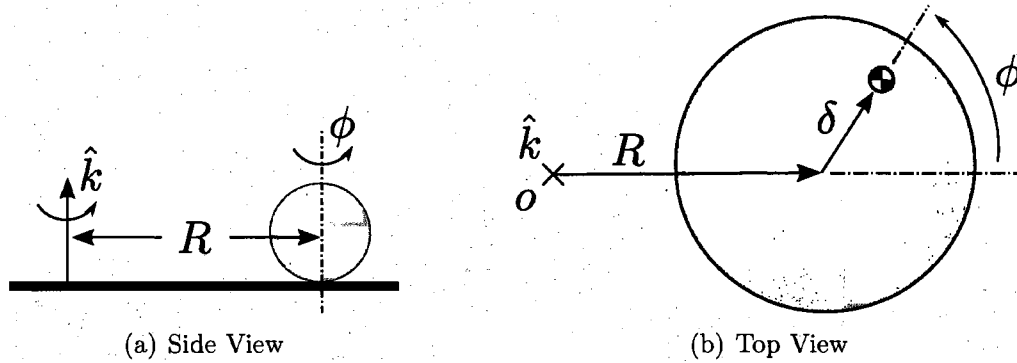


Figure 4.2: Pendulum configuration for mass center measurement.

addition, the total mass is replaced by the mass of the object,  $m_o$ , plus the mass of the pendulum platform,  $m_p$  to obtain:

$$R_g^2 = \frac{I_{ozz} + (I_o + m_o r^2)}{m_o + m_p} = \frac{k}{\omega^2} \quad (4.20)$$

Placing the object on the pendulum far from the rotation axis amplifies the contribution due to the mass center offset from the geometric center, due to the quadratic dependence on  $r$ . By changing the orientation of the object with a fixed geometric location relative to the pendulum rotation center, the mass center offset is determined by measuring the change in the natural frequency,  $\omega$ .

Consider for example an object with a mass center offset from the geometric center of magnitude  $\delta$ . The object's geometric center is placed on the pendulum at a location of  $R$  from the pendulum rotation axis,  $\hat{k}$ . Refer to Figure 4.2 for a graphical depiction. The mass center offset within a plane can be determined by rotating the object about an axis parallel to the pendulum rotation axis. The offset is determined by measuring the pendulum oscillation frequency for different rotation angles of  $\phi$ . The angle  $\phi$  is the angular location of the mass center relative to the vector from the rotation axis to the object's geometric center. For each rotation angle  $\phi$ , a corresponding change in the pendulum oscillation frequency will be observed. For instance, if the mass center location is at an angle of  $\phi = 0$  and then rotated to  $\phi = \pi$ , the maximum change in the radial distance to the mass center will occur. The maximum change in the

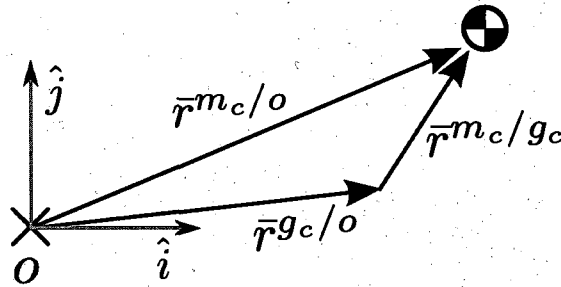


Figure 4.3: Vector addition for mass center location.

measured pendulum frequency will also result.

The required frequency resolution, or rather the ratio between the maximum and minimum pendulum oscillation frequency for the range of  $\phi$ , is a function of the radial offset location,  $R$ , and the magnitude of the mass center offset,  $\delta$ . Consider the simple vector addition scenario depicted in Figure 4.3, for the addition of the vectors from the rotation axis to the geometric center,  $\bar{r}^{g_c/o}$ , and the vector from the rotation axis to the mass center location,  $\bar{r}^{m_c/o}$ . The vector from the rotation axis to the mass center location is given by the vector sum:

$$\bar{r}^{m_c/o} = \bar{r}^{g_c/o} + \bar{r}^{m_c/g_c} \quad (4.21)$$

and the magnitude of the distance to the mass center,  $r^2$  in Equation 4.20, is given by the scalar product:

$$r^2 = \bar{r}^{m_c/o} \cdot \bar{r}^{m_c/o} \quad (4.22)$$

For this example, assume the location of the geometric center is given by:

$$\bar{r}^{g_c/o} = R\hat{i} \quad (4.23)$$

The magnitude of the mass center offset from the geometric center,  $\delta$ , as shown in

Figure 4.3 is defined by the scalar product:

$$\delta = (\bar{r}^{m_c/g_c} \cdot \bar{r}^{m_c/g_c})^{\frac{1}{2}} \quad (4.24)$$

such that the vector from the geometric center to the mass center is given by:

$$\bar{r}^{m_c/g_c} = \delta \cos \phi \hat{i} + \delta \sin \phi \hat{j} \quad (4.25)$$

Using the vector addition as described in Equation 4.21, one obtains the vector to the mass center location from the rotation axis as a function of the rotation angle  $\phi$ :

$$\bar{r}^{m_c/o} = (R + \delta \cos \phi) \hat{i} + \delta \sin \phi \hat{j} \quad (4.26)$$

The magnitude of the distance to the mass center from the pendulum rotation center,  $r^2$ , for Equation 4.20 is therefore:

$$\begin{aligned} r^2 &= \bar{r}^{m_c/o} \cdot \bar{r}^{m_c/o} \\ &= R^2 + 2R\delta \cos \phi + \delta^2 \end{aligned} \quad (4.27)$$

Substituting in the expression for  $r^2$  into Equation 4.20, one obtains an expression for the pendulum oscillation frequency as a function of the rotation angle  $\phi$ :

$$\frac{I_{ozz} + I_o + m_o (R^2 + 2R\delta \cos \phi + \delta^2)}{m_o + m_p} = \frac{k}{\omega^2} \quad (4.28)$$

For the required range on the frequency resolution, consider the two extreme conditions, where the mass center is at either  $\phi_1 = 0$  or  $\phi_2 = \pi$ . Taking the ratio of Equation 4.20 for each case, one obtains:

$$\left( \frac{\omega_2}{\omega_1} \right)^2 = \frac{I_{ozz} + I_o + m_o (R^2 + 2R\delta \cos \phi_1 + \delta^2)}{I_{ozz} + I_o + m_o (R^2 + 2R\delta \cos \phi_2 + \delta^2)} \quad (4.29)$$

Simple algebraic manipulation results in a relationship for the change in oscillation



frequency due to a mass center offset,  $\delta$ :

$$\frac{\omega_2 - \omega_1}{\omega_1} = \frac{\Delta\omega}{\omega} = \left( \frac{I_{ozz} + I_o + m_o (R^2 + 2R\delta \cos \phi_1 + \delta^2)}{I_{ozz} + I_o + m_o (R^2 + 2R\delta \cos \phi_2 + \delta^2)} \right)^{\frac{1}{2}} - 1 \quad (4.30)$$

Equation 4.30 is plotted in Figure 4.4. for a representative value of the pendulum platform inertia. The measurement object values utilized are for a 25 mm radius brass sphere. From Figure 4.4 it is seen that for our representative example, a frequency resolution of approximately 1 part in  $10^4$  is necessary to measure a mass center offset of  $8 \mu\text{m}$ . Thus, it is possible to measure the mass center offset to values comparable to the traditional pendulous technique with only a modest frequency resolution. Depending on the pendulum parameters and the measurement object, it is theoretically possible to surpass the  $1 \mu\text{m}$  level for mass center determination using a torsion pendulum.

### 4.4.3 Inertia Measurement Using a Torsion Pendulum

In order to determine the moment of inertia tensor using a torsion pendulum, recall Equation 4.1 for the instantaneous moment of inertia about an axis of rotation  $\hat{a}$ :

$$I = \hat{a} \cdot \bar{\bar{I}} \cdot \hat{a}$$

Substituting in the relationship for the instantaneous moment of inertia as described by the torsion pendulum dynamics, Equation 4.18, one obtains the inertia tensor, characterized by the torsion pendulum properties:

$$\frac{mk}{\omega^2} = \hat{a} \cdot \bar{\bar{I}} \cdot \hat{a} \quad (4.31)$$

Equation 4.31 however does not completely indicate how one obtains the inertia tensor of an unknown object using a torsion pendulum and the procedure outlined in Section 4.3.2. When an object is placed onto a torsion pendulum platform, the apparatus is only capable of determining the radius of gyration for the complete system, namely the pendulum plus the measurement object. Thus, the quantities

Parameter	Value
$I_{ozz}$	400 kg·mm <sup>2</sup>
$m_o$	0.55 kg
$I_o$	125 kg·mm <sup>2</sup>
$R$	75 mm

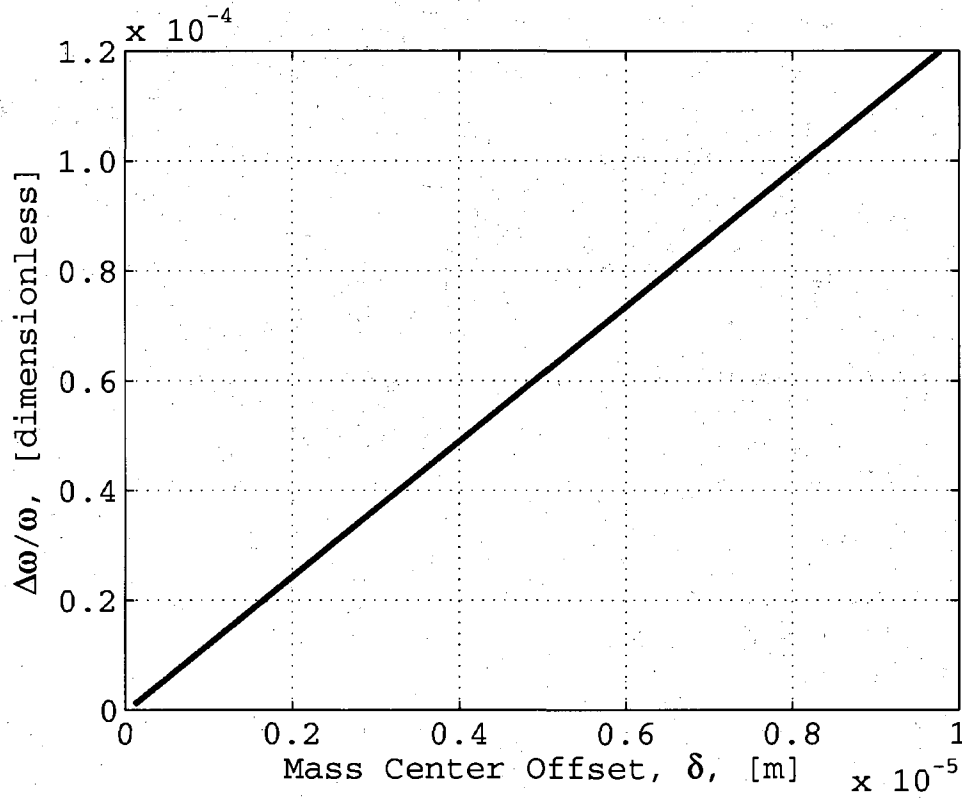


Figure 4.4: Required frequency resolution for mass center measurement using a torsion pendulum.

in Equation 4.31 must be modified to include the total system mass,  $m_T$ , and total moment of inertia. The total moment of inertia consists of the inertia tensor for the measurement object,  $\bar{\bar{I}}_m$ , and the pendulum platform inertia,  $\bar{\bar{I}}_o$ , or the initial offset inertia before the measurement object is added to the system. As described in Section 4.3.2, the inertia tensor determination requires measurements of the object with unknown inertia along  $n$  unique directions  ${}^{(n)}\hat{a}$ . The axis of rotation for the pendulum platform is however constant for each measurement by nature of the torsion pendulum dynamics. Consistent with Figure 4.1(b), the fixed rotation axis of the torsion pendulum is  $\hat{k}$ . Equation 4.31 thus becomes:

$$\frac{m_T k}{\omega^2} = \hat{a} \cdot \bar{\bar{I}}_m \cdot \hat{a} + \hat{k} \cdot \bar{\bar{I}}_o \cdot \hat{k} \quad (4.32)$$

Furthermore, define the pendulum inertia about the fixed rotation axis by:

$$I_{ozz} = \hat{k} \cdot \bar{\bar{I}}_o \cdot \hat{k} \quad (4.33)$$

$I_{ozz}$  is a constant for each measurement direction  ${}^{(n)}\hat{a}$  and therefore represents a constant offset to the magnitude of the measured inertia tensor. Rearranging Equation 4.32 and substituting in the representation for the initial inertia offset due to the pendulum platform, one obtains an equation for the inertia of the measurement object as a function of the torsion pendulum natural frequency:

$$\frac{m_T k}{\omega^2} - I_{ozz} = \hat{a} \cdot \bar{\bar{I}}_m \cdot \hat{a} \quad (4.34)$$

Equation 4.34 is then used to formulate Equation 4.2 for the system of equations relating the inertia tensor to the instantaneous moment of inertia about a rotation axis.

## Chapter 5

# Apparatus Design: Moment of Inertia Measurement

When designing an apparatus to measure the moment of inertia to a high precision, care must be taken to minimize the extra degrees of freedom in the system. Introduced here is a new method for measuring the moment of inertia using a novel five-wire torsion pendulum design [18], which shows the prospect of exceeding current state of the art by almost an order of magnitude. Bifilar and trifilar pendulums do not constrain the swinging or lateral translation modes. To improve the accuracy of a standard trifilar pendulum, the lateral pendulum modes need to be constrained. Five support wires are sufficient to constrain all but one degree of freedom. In a five-wire pendulum, two additional wires are arranged as shown in Figure 5.1 to minimize rotations about the other two rotational axes. The design reduces errors due to tilt and horizontal translational degrees of freedom. The three attach points on the platform supporting the inertia to be measured are positioned equidistant from the center of rotation. At one attach point, a single vertical wire is used and the other two attach points consist of two wires. The wire geometry is symmetrical about a plane formed with the vertical wire and a line emanating from the rotation center to the vertical wire attach point. The horizontal components of the wires which are splayed out from a single attach point provide horizontal stiffness to prevent pendulum platform swinging motion. The translational stiffness is provided in two ways. First,

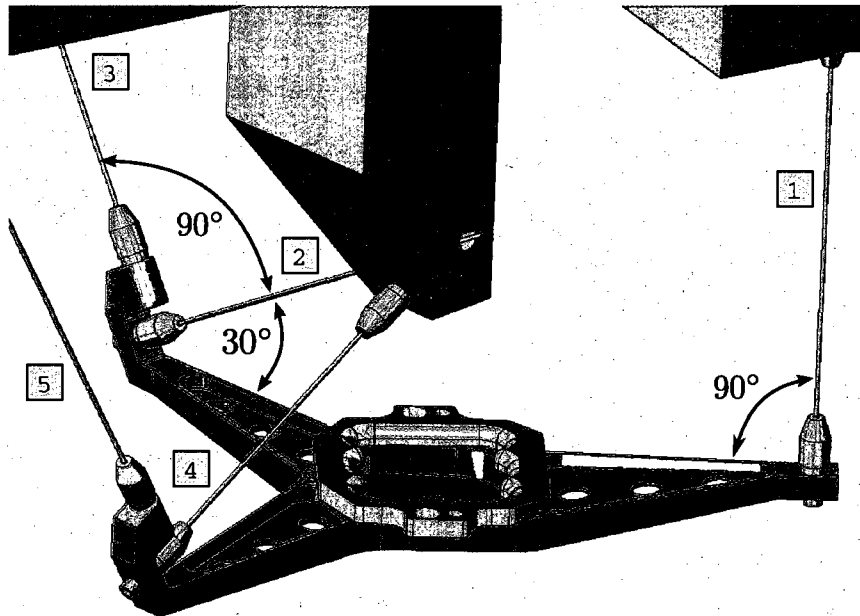


Figure 5.1: Five-wire torsion pendulum wire geometry. Initial platform design version. The wire geometry is identical for subsequent platform versions.

the attachment locations for the two-wire attach point are separated by  $90^\circ$  within the plane of the pendulum platform. In addition, the two wires at the single attach point are splayed out at  $90^\circ$ . The wires are attached to the supporting frame along a line emanating from the rotation center at a point in the plane containing the mass center of the object to be measured. The choice of the attach point locations on the supporting frame ensures a constant curvature at the platform wire mount points from each wire, which coincides with the curvature of the pendulum rotation. The constant curvature constraint is necessary to ensure proper rotation about the vertical axis.

It is important to note that friction is eliminated by the five-wire design. The pure rotation could be achieved by other means, such as the use of an air bearing or jewel bearing. Yet by adding a bearing into the system, frictional uncertainty must be considered. The wires are attached to ensure constant curvature at each platform wire attach point, which forces the pendulum platform to rotate about a

specific vertical line. Thus, the rotation center of the platform is dictated by the wire geometry and the uncertainty due to friction is eliminated.

## 5.1 Pendulum Platform Design

The pendulum platform is the key component to the five-wire torsion pendulum. The platform is responsible for connecting the wires in such a fashion to enable the proper rotational motion. In addition the platform provides a foundation on which to fixture measurement objects. To begin the design of the pendulum platform the following key design requirements exist:

- Low inertia relative to the test article.
- Low mass relative to the test article.
- Easily machined.

The inertia of the platform must be low compared to the object to be measured, such that the measurement object inertia is a relatively large contribution to the overall pendulum plus object combination. If the measurement object inertia were small compared to the pendulum platform for example, then say a 1 part in  $10^4$  measurement precision of the combined platform plus object would not yield a 1 part in  $10^4$  precision for the object in question. Similarly, the mass of the pendulum platform needs to be low compared to the measurement object such that a shift in the mass center of the measurement object can be easily identified. In addition to the requirements set upon the mass properties of the pendulum platform, there exists the ease of manufacturability requirement. A part which is easily machined allows not only for reduced cost, but allows for a yield of a higher quality machined part/tolerances, as well as a faster turn around of future revisions.

During the design process, two revisions were carried through the manufacture and testing phase. First, an initial proof of concept version was generated as a student project [18], which was further modified by the author to overcome design limitations. The initial student project platform design geometry is shown in Figure 5.1. The final

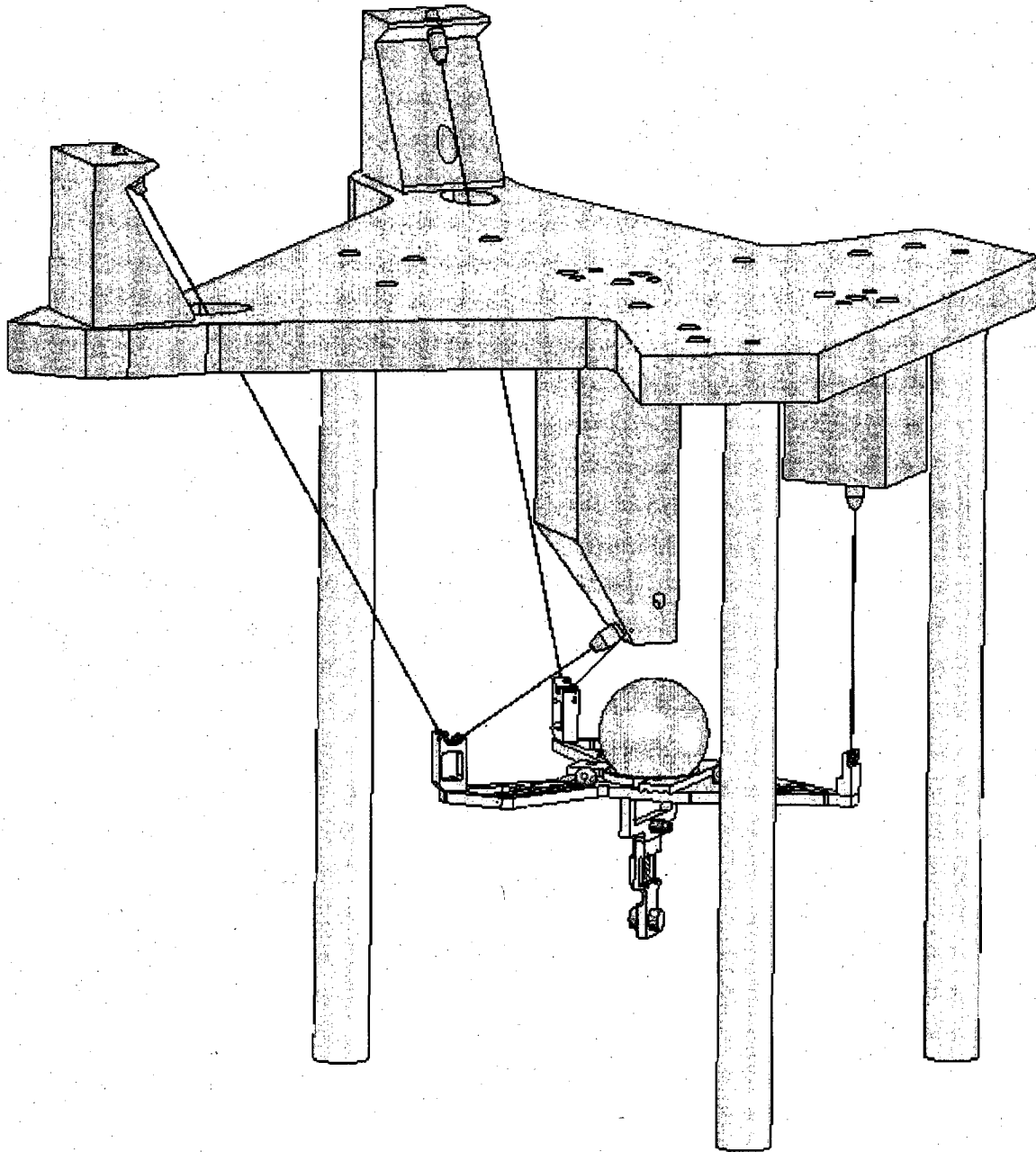


Figure 5.2: Five-wire torsion pendulum solid model.

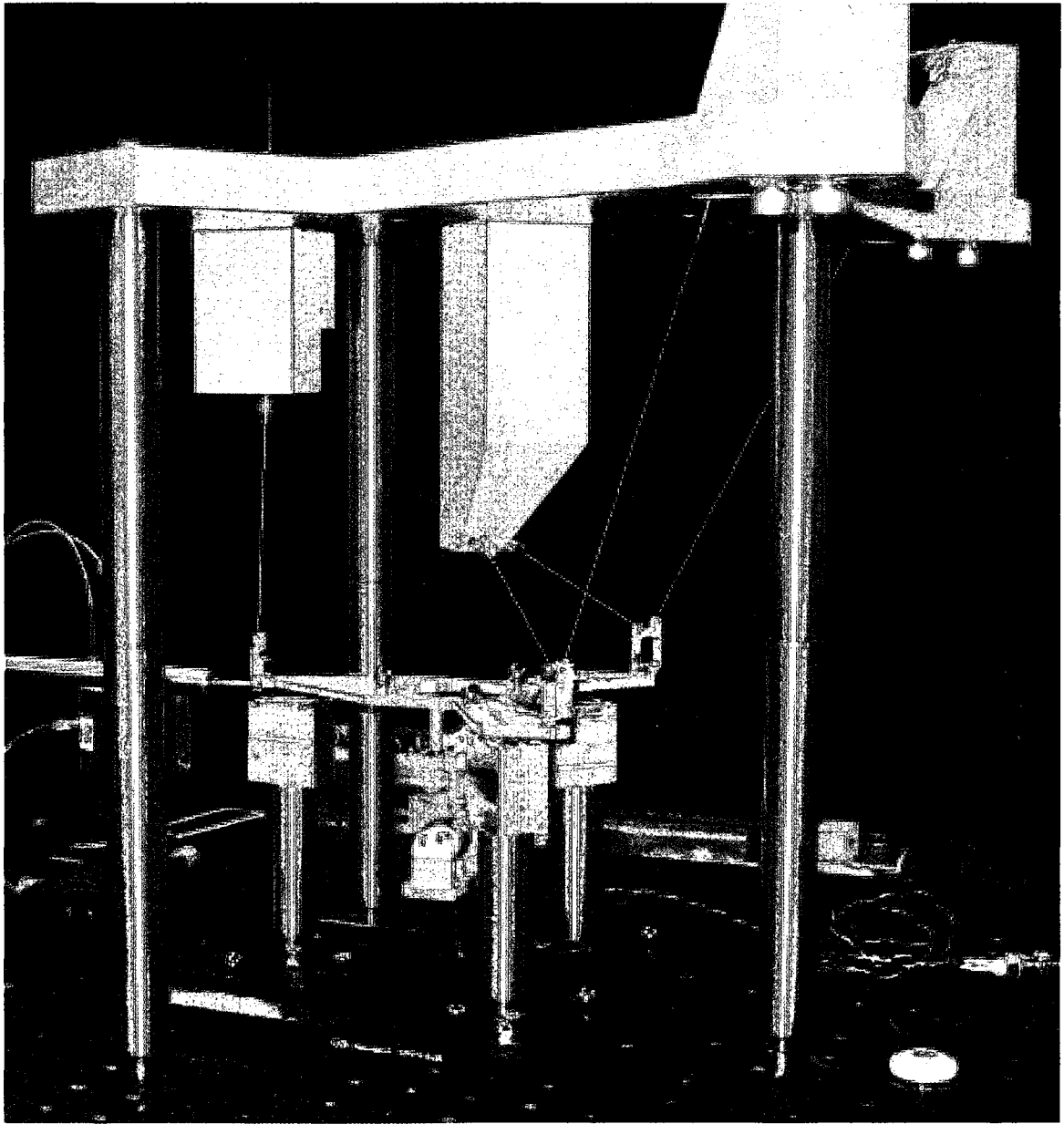


Figure 5.3: Five-wire torsion pendulum. (Actual Hardware, Final Design)



version which is discussed in this work was then designed and constructed by the author based on information gained during testing the initial design. The pendulum design history is summarized as follows:

- Design 1:** Original student course project design with shadow sensing.
- Design 2:** Student project design modified for optical sensing (Section 5.5.2). Only the mechanical hardware was reused. New software, instrumentation and optical sensing.
- Design 3:** Symmetrical five-wire design. All wires were of same length, symmetrically distributed about the rotation center. The design did not properly constrain the translational modes and was not carried beyond initial CAD modeling.
- Design 4:** The final design described in this work. The design utilized the same wire geometry as produced in Design 1. The mechanical hardware was redesigned to overcome limitations observed during testing of Design 2.

Through testing of Design 2, a number of secondary requirements were discovered, including:

- Platform Symmetry
- Non-Contact Sensor and Actuator
- Repeatable Wire Attachment and Assembly
- Symmetric Kinematic Fixturing System
- Mass Center Near Rotation Center
- Repeatable Calibration Method
- Automated Measurement Instrumentation
- Thermal Insensitivity

<b>Requirement</b>	<b>Section</b>
Non-Contact Sensor	5.6, 5.5.2
Non-Contact Actuator	5.6
Wire Attachment	5.2
Kinematic Fixtures	5.4
Calibration	6.1
Thermal	7.1
Vacuum	8.1.1

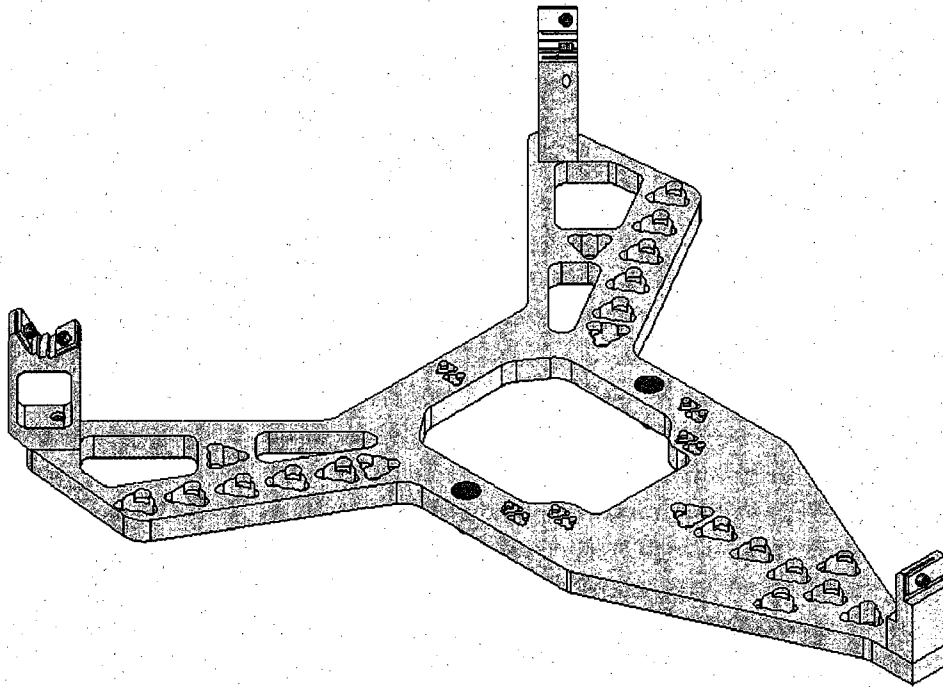
Table 5.1: Design requirement implementation sections.

- Vacuum Compatible, (desired but not required)

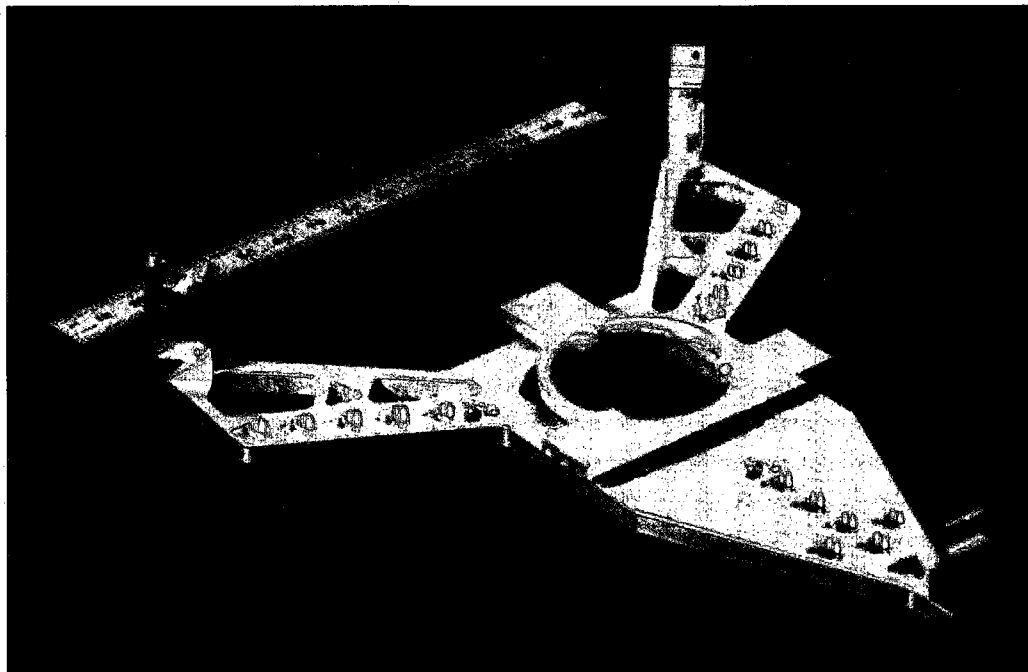
The corresponding design which addresses each of these requirements are further discussed in the following sections, yet the impact on the actual pendulum platform design is discussed here. Table 5.1 summarizes the sections for further information on each of the secondary design requirements which are not fully discussed here.

For the pendulum platform, a great deal of care was taken to ensure a symmetrical geometry. Due to the required five-wire geometry and requirement for a low moment of inertia, the platform was designed to be symmetrical about a vertical plane passing through the vertical wire and the rotation center. Figure 5.4 depicts the SolidWorks model and the final machined platform hardware. Simplified mechanical drawings for the final pendulum platform are also found in Appendix B.1.

In standard dynamics theory, an object with no constraints will rotate about the mass center. For the five-wire design, the platform is constrained by the wires to rotate about a fixed axis, which may not necessarily pass through the mass center. Thus, in order to help the platform generate a pure rotation without fighting nature, the mass center of the complete pendulum platform is carefully designed to coincide with the desired rotation center. From the model designed in SolidWorks, the designed mass center of the complete system, assuming a homogeneous density, was within 0.02 mm of the expected rotation center. The triangular platform geometry leading to the vertical wire at the right in Figure 5.4 is chosen such that the mass required to offset the opposite end of the platform is close to the rotation center, reducing



(a) Solid model



(b) Actual hardware

Figure 5.4: Five-wire pendulum platform.

the total moment of inertia for the system. During the solid model design, a trade was constantly made between the platform thickness and the size of the triangular geometry leading to the vertical wire mount (right side of Figure 5.4). At the opposite end of the platform (left side of Figure 5.4), slots are machined to remove extra mass far from the rotation center to reduce the platform moment of inertia. The large center hole allows the measurement object to fit with limited clearance above the platform resulting from the five-wire design geometry and the required wire attach points. In addition, the large center hole ensures that the mass center of the measurement object can be shifted close to the vertical location of the wire attach points above the platform. This ensures any inverted pendulum-like tilting frequencies of the combined object/platform system are above the measurement frequency band. Geometry details for the large center hole are found in Mechanical Drawing B.2.

The pendulum calibration process, which is further discussed in Section 6.1, requires the addition of spheres to the pendulum platform. The spheres are repeatably located on the platform through a number of calibration holes, as shown in Figure 5.5. Each set of three calibration holes are located equidistant from the pendulum rotation center, as listed in Table 5.2. The calibration hole locations are positioned in a symmetric fashion along  $120^\circ$  radial lines emanating from the platform mass center to ensure the mass center is not shifted by a change in calibration sphere location. Each calibration hole has three equally distributed small stress relief holes drilled around the calibration hole circumference. The relief holes ensure a three contact point interface between the hole and the calibration sphere for a repeatable placement. Refer to Mechanical Drawing B.1 and Mechanical Drawing B.3 for further details on the calibration hole location and design.

The pendulum platform needs the ability to hold a variety of measurement object geometries. The fixturing philosophy is to utilize a common interface for a number of different measurement object fixtures. The measurement object fixtures are further discussed in Section 5.4. On the pendulum platform, the interface to the fixtures is provided via holes drilled again along  $120^\circ$  radial lines from the mass center. The  $120^\circ$  geometry is chosen for the same reasons as discussed for the calibration holes. Each hole will accept a small sphere for a kinematic interface to the object fixtures.

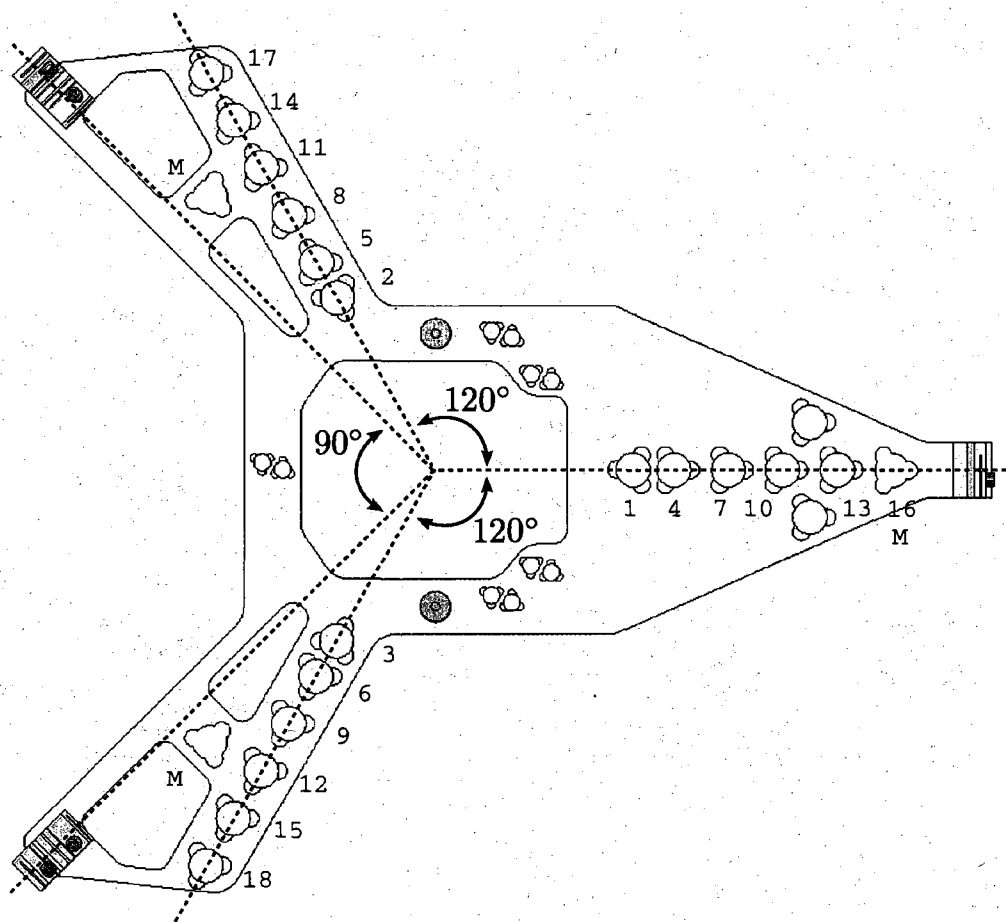


Figure 5.5: Five-wire platform top view. The holes for calibration sphere placement are depicted along the  $120^\circ$  lines. Note also that the wire attach points are separated by  $90^\circ$  for translational stiffness.

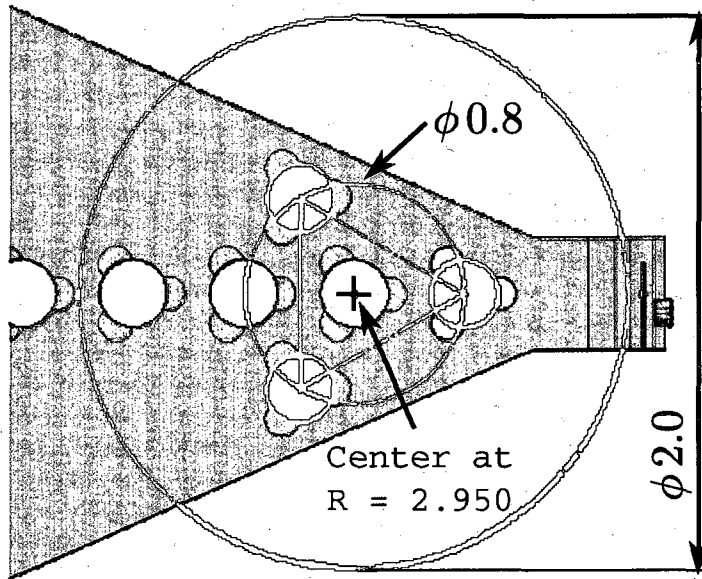
Identifier	Numbers	Radial Distance	
		inches	(mm)
Hole Set 1	1,2,3	1.450	36.8
Hole Set 2	4,5,6	1.750	44.5
Hole Set 3	7,8,9	2.150	54.6
Hole Set 4	10,11,12	2.550	64.8
Hole Set 5	13,14,15	2.950	74.9
Hole Set 6	16,17,18	3.350	85.1

Table 5.2: Calibration hole distance from rotation center.

As such, each hole is again drilled with three equally spaced relief holes for a three contact point interface between the sphere and the platform. Refer to Mechanical Drawing B.2 for details on the interface fixture mounting holes.

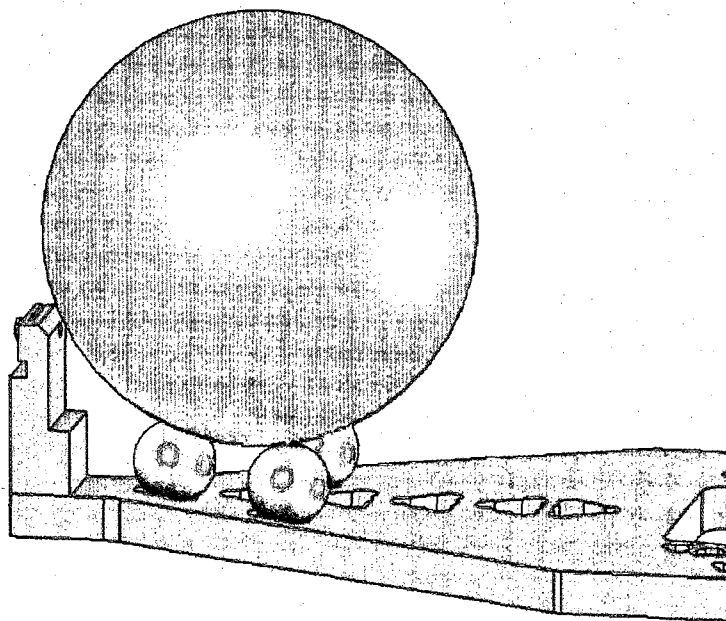
As shown in Section 4.4.2, a torsion pendulum may also be used to measure the mass center offset for an object. Mass center measurements require that the measurement object be placed far from the rotation center, contrary to moment of inertia measurements. Although the pendulum platform is designed primarily as a moment of inertia measurement apparatus, mounting holes are also placed onto the pendulum for use in mass center measurements. For mounting an object, three holes separated by  $120^\circ$  angles are drilled with identical design as the calibration holes. The three mounting holes are centered around the calibration hole set number five, located along the direction of the vertical wire attach point. For a spherical shaped object, three small spheres are placed into each mounting hole, creating a symmetrical three-point mount. The geometric center of the sphere is then positioned at a radial distance from the rotation center equal to that of calibration hole set number five. The location of the mounting holes will allow a 2 inch sphere to fit onto the platform without interfering with the vertical pendulum support wire. Refer to Figure 5.6 for the geometry of the mounting holes for mass center measurements using the torsion pendulum and a depiction of the configuration for the mass center measurement of a spherical shaped object.

The pendulum platform is designed with a simple flat surface for the top and bottom of the platform. Although it is desired to reduce the total pendulum platform mass and moment of inertia, the thin, lightweight web and stiffener design utilized in the first pendulum platform version shown in Figure 5.1, proved to be problematic. The web and truss structure limited the size and number of calibration spheres due to interference with the web stiffeners, as well as limited the position of measurement objects due to interference with fixtures. In addition the platform top surface on the first version exhibited a slight upward slope to reduce the platform total mass. This upward slope made it difficult to assemble the platform to the attach wires at the desired wire length, as it was difficult to make sure the platform was level and in a repeatable position relative to the supporting foundation. The flat top and bottom



All dimensions in inches

(a) Mounting Holes for Mass Center Measurement



(b) With Measurement Sphere

Figure 5.6: Pendulum configuration for object mass center measurement.

surface not only avoids interference issues, but also allows for a more repeatable assembly to the attach wires. The flat bottom surface provides a clean, level surface for assembly fixtures, which are further discussed in Section 5.3.

## 5.2 Support Wire and Wire Attachment

The natural frequency of rotation for a torsion pendulum, Equation 4.16, is a function of the wire length and the distance from the rotation center to the wire attach point. A change in the wire length or the configuration of the wire attach point will therefore change the pendulum natural frequency.<sup>1</sup> Thus, in designing the torsion pendulum, a great deal of consideration must be devoted to the pendulum wires and wire attach method.

### 5.2.1 Wire Attachment

For attaching the wires to the pendulum, a low mass, strong, reliable, repeatable placement is required. In the first wire mount design iteration, Figure 5.7, a three-jaw pin vise was used for attaching the wires to the pendulum platform and supporting structure. Although the pin vise attach method is easily implemented and provides ample clamping force for a variety of wire diameters, the design proved to be problematic. The issues with the pin vise setup were:

- Non-repeatable wire positioning
- Total mass

The three-jaw pin vise does not reliably position or center the wires within the three-jaw pin vise teeth, which is further complicated as the wire diameter is reduced. The total mass of the three-jaw pin vise is also a concern. The pin vises are made of steel and hence are of relatively large mass compared to the pendulum platform. Thus, use of the pin vises results in a relatively large amount of mass placed at the pendulum

---

<sup>1</sup>Section 7.1 in the measurement error chapter further addresses the error associated with a change in wire length.



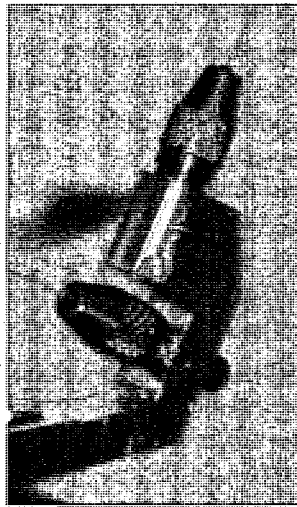


Figure 5.7: Five-wire pin vise wire mount.

platform extremities. The mass at a large distance from the rotation center results in an increase in the total inertia of the platform.

The solution to the issues encountered with the pin vise attachment method are solved via an alternate flexure mount design shown in Figures 5.8 and 5.9. The designed aluminum mount consists of a 0.014 inch (0.356 mm) radius hole and an electrical discharge machined 0.015 inch (0.381 mm) slot through the hole to create a flexure clamp as shown in Figure 5.10. The wire is inserted into the hole and clamping force on the wire is provided to the flexure via a #0-80 hex screw. The flexure mount ensures a repeatable placement of wire within the mount. A ledge is machined at the end of the wire attach hole to allow insertion of the wire up to a specified depth. Combined with an additional groove for visual inspection, the ledge ensures a consistent insertion depth of the wire into the flexure clamp. Refer to Mechanical Drawings B.4 and B.5 for further information regarding the pendulum wire mount geometry.

The mount is attached to the pendulum platform using 1/32 inch stainless steel dowel pins and a corresponding hole/slot mate for repeatable alignment. A single #4-40 cap screw is used to provide the mating force between the wire attach mount and the pendulum platform. The height of the wire mount is chosen such that the

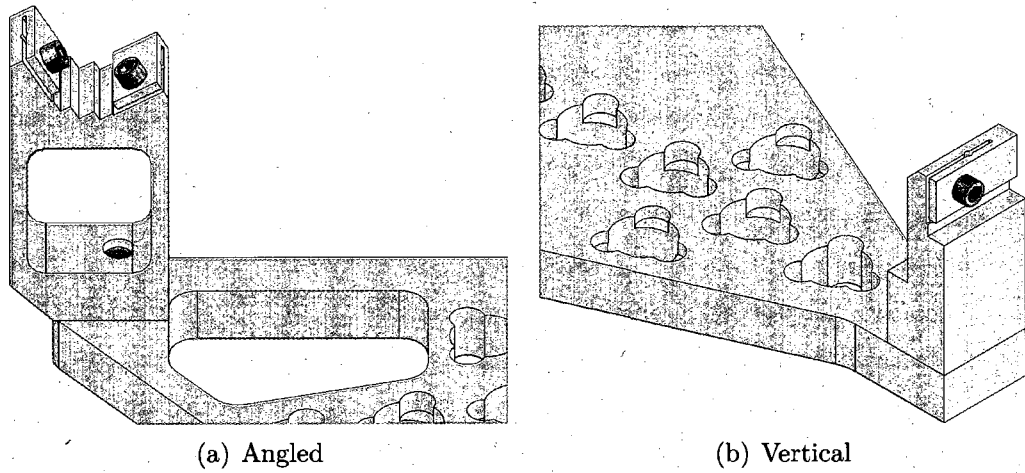


Figure 5.8: Five-wire pendulum platform wire mounts.

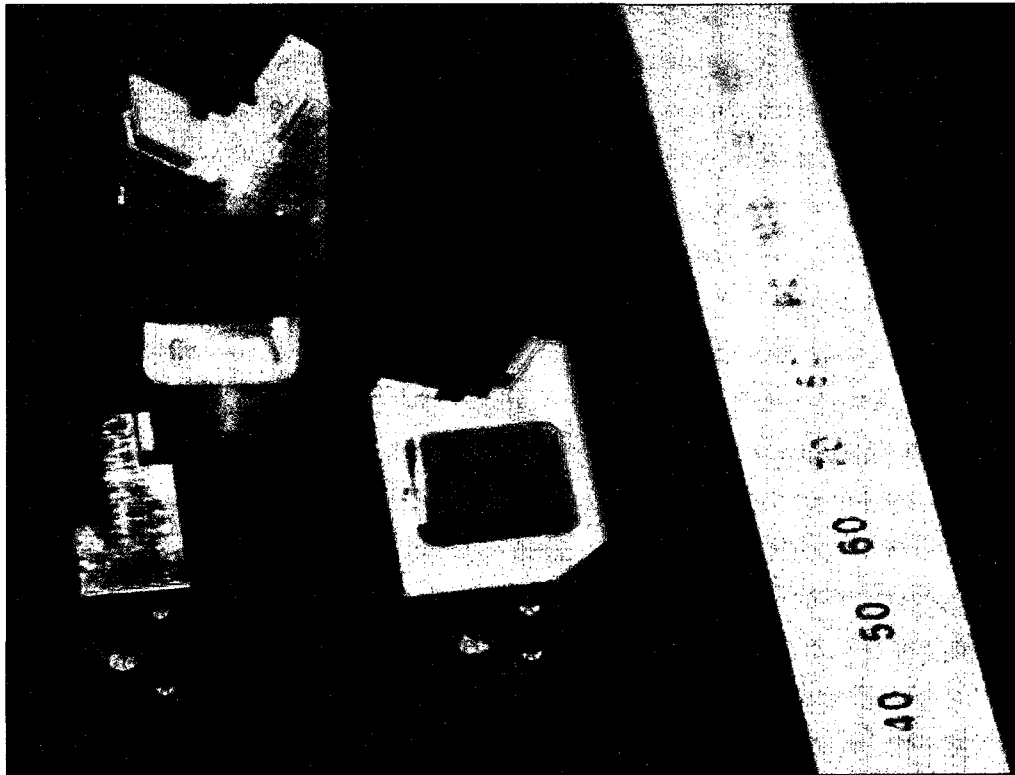


Figure 5.9: Hardware: five-wire pendulum platform wire mounts.

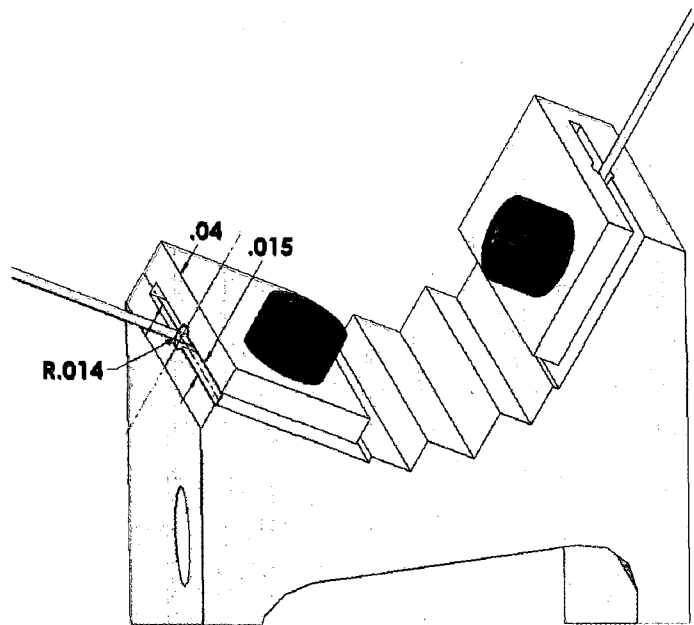


Figure 5.10: Wire mount hole and slot. Dimensions in inches.

intersection point of the two wires matches the height of the measurement object mass center above the pendulum platform. In so doing, any swinging modes of the wire supported structure are spectrally shifted to frequencies above the measurement oscillation frequency. To meet the design requirements of a light-weight design and the required height to match the object mass center, the structure is light-weighted by material removal in the center of the mount as depicted in Figure 5.8(a). The light-weighted aluminum structure wire mount design produces a mount that is less mass than the steel pin vise mount method.

### 5.2.2 Wire

The desired mechanical performance of the wire is established by first selecting the material properties for the wire. For the torsion pendulum attach wires the following properties are desired:

- High modulus of elasticity

Material	E GPa	$\alpha$ at 298 K $\times 10^{-6} \text{ K}^{-1}$
Tungsten, Pure	345	4.5
Spring Steel, 1085	200	14.7
Brass, C260	117	19

Table 5.3: Material properties.

- Low coefficient of thermal expansion
- Ductile, non-brittle
- Flexible, such that a slight bend will not retain shape
- Non-corrosive properties
- Low magnetic susceptibility
- Material is readily available
- Vacuum compatible, desired but not required

The modulus of elasticity and the thermal expansion coefficients are of primary interest, as these parameters dictate the static length of the supporting wires. Again, since the natural frequency of rotation for a torsion pendulum is a function of the wire length, it is crucial that the length of the wire remain constant under various loads and environmental conditions.

Before selecting the material for the wire, the available form factors must first be considered. The attach wires must be readily available in various diameters and lengths. In addition, there exists the requirement that the wire be available in a straightened form to avoid any natural spring force associated with typical coiled wire. Straightened wire is readily available in various metals such as aluminum, brass, titanium, steel, and tungsten. Tungsten, stainless steel and spring steel offer a high modulus of elasticity. Compared to steel, tungsten has a higher modulus of elasticity, and a lower coefficient of thermal expansion. Refer to Table 5.3 for a

Wire	Length	
	inches	(mm)
short wire	3.0	(76.2)
vertical wire	4.5	(114.3)
long wire	12.0	(304.8)

Table 5.4: Wire lengths for five-wire pendulum.

comparison of the modulus of elasticity,  $E$ , and thermal expansion coefficient,  $\alpha$ , for different materials. The higher modulus of elasticity is desired to reduce the stretch of the wire under a load. The lower thermal expansion coefficient equates to a lower change in wire length from temperature fluctuations and hence a reduced dependency of the pendulum natural frequency due to temperature. For primarily the modulus of elasticity and thermal expansion coefficient values for tungsten, straightened tungsten wire was selected for the torsion pendulum. It should be noted that carbon fiber yarn is an excellent choice for high modulus of elasticity, low coefficient of thermal expansion and is flexible at small diameters. Although carbon fiber is widely available in fabric form, carbon fiber yarn is not readily available in small quantities and can be difficult to handle. Future research may justify using carbon fiber yarn, but the expense could not be justified during the initial design stages.

Having selected the material for the wire, the wire stiffness, or rather the appropriate wire diameter is the next design decision. Wire diameter selection is further complicated by the fact that the wires on the five-wire are of different lengths and support different tension loads to meet the proper dynamic constraints. Refer to Table 5.4 for a listing of the pendulum wire lengths. If the wires were all of the same length and supported the same load, then an applied load to the pendulum would result in an equal change in length of the wires. Consider for example the case of a simple three-wire pendulum, consisting of three identical vertical wires attached equidistant from the rotation center. As a load is applied to the pendulum platform, each wire will support the same load and hence exhibit the same change in length.

For the five-wire pendulum, It is desired to match the stretch in each of the wires, such that a change in load of the platform results in a vertical only change in position

with no tilt/translation. This further ensures a constant direction for the axis of rotation between a loaded and unloaded platform. In order to match the stretch in each of the wires, we begin by modeling the wires as simple springs for the relationship between the applied load,  $F$ , and change in wire length  $\Delta L$ :

$$F = k\Delta L \quad (5.1)$$

where  $k$  is the stiffness associated with the wire. For each of the three wire lengths, we require the stretch of the wires due to an applied load to be consistent.

$$\Delta L = \frac{F_1}{k_1} = \frac{F_2}{k_2} = \frac{F_3}{k_3} \quad (5.2)$$

where the stiffness,  $k$ , of the wires is given by

$$k_i = \frac{A_i E_i}{L_i} \quad (5.3)$$

By choosing the cross sectional-area,  $A$ , and modulus of elasticity,  $E$ , of one wire, the properties required of the other length wires are established:

$$A_1 E_1 = A_2 E_2 \frac{F_1 L_1}{F_2 L_2} \quad (5.4)$$

$$A_3 E_3 = A_2 E_2 \frac{F_3 L_3}{F_2 L_2} \quad (5.5)$$

In order to match the same change in length of the different length wires, we therefore have the option of either maintaining a constant wire modulus of elasticity among the wires and varying the cross-sectional area, or retaining the same cross-sectional area for the wires and changing the material. It was chosen to use various wire cross-sectional areas (via wire diameter) to match the change in length of each wire. By selecting the same material the wires will exhibit similar responses to environmental disturbances such as for example thermal (coefficient of thermal expansion  $\alpha$ ).

From the standpoint of varying the wire cross-sectional area, a thick wire will bend and tend to retain shape. The pendulum stiffness increases with wire thickness and the natural frequency raises due to a shorter equivalent wire length. As such,

Wire No.	Wire Diameter		Required $AE$	Actual $AE$	% Diff.
	inches	(mm)	$\times 10^4$ N	$\times 10^4$ N	
Tungsten:					
1	0.010	(0.254)	1.75	1.75	0%
2	0.005	(0.127)	0.452	0.437	-3.3%
3	0.013	(0.330)	2.92	2.95	1.0%
Steel:					
1	0.008	(0.203)	0.649	0.649	0%
2	0.004	(0.102)	0.168	0.162	-3.6%
3	0.010	(0.254)	1.09	1.01	-7.3%

Table 5.5: Wire stiffness configuration.

it is desired to use as small of a cross-sectional area for the wires as feasible. Yet, extremely thin wire is difficult to attach, fragile to work with and needs to exhibit enough strength to support the load. In addition, wire diameters less than 0.004 inches (0.102 mm) are not readily available. In order to determine the appropriate cross-sectional area for the wires, the required supporting load in each wire is determined. From statics, the tension in each wire due to a 1 kg load is found to be:

$$T_1 = 4.5 \text{ N} \quad (\text{vertical wire})$$

$$T_2 = 1.6 \text{ N} \quad (\text{short wire})$$

$$T_3 = 2.7 \text{ N} \quad (\text{long wire})$$

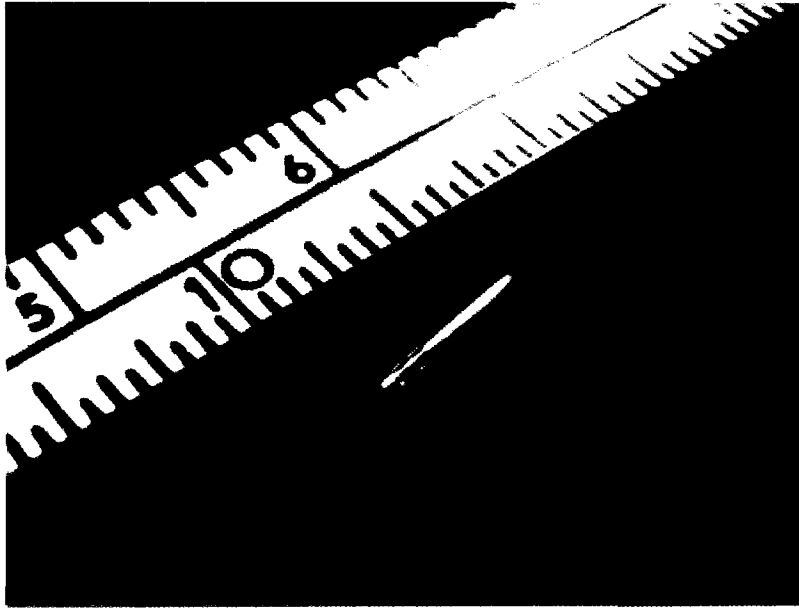
The lowest stiffness required is therefore in the shortest wire. As such the stiffness of the shortest wire (wire 2) is defined based on the smallest available wire diameter. From Equation 5.4 and the various wire material and geometry pairs which are readily available, a set of suitable wire combinations for the five-wire apparatus is determined. Table 5.5 lists the desired wire combinations to match the change in wire length due to an applied 1 kg load of the platform and Table B.4 in the Appendix lists the part numbers for the supporting wires utilized in the apparatus.

Wire Diameter		Tube ID		Tube OD		Notes
inches	(mm)	inches	(mm)	inches	(mm)	
0.005	(0.127)	0.006	(0.152)	0.012	(0.305)	short wire
		0.013	(0.330)	0.025	(0.635)	
0.010	(0.254)	0.013	(0.330)	0.025	(0.635)	vertical wire
0.013	(0.330)	0.013	(0.330)	0.025	(0.635)	long wire

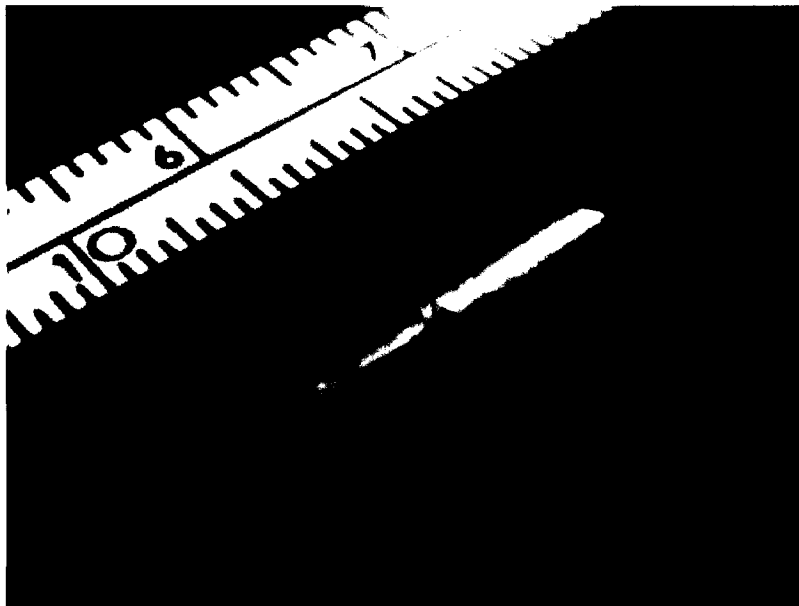
Table 5.6: Wire and hypodermic tube configuration.

Since the supporting wires are of a different cross-sectional area in order to match the same wire stretch of the loaded platform, the wire attach method is slightly complicated. In addition, it is desired to use wires on the order of 0.004 inches (0.102 mm) in order to reduce the total stiffness of the system. In order to simplify the design and to reduce manufacturing complexity of the flexure wire mount hardware design, (Figure 5.9), the flexure mounts are designed for a common size wire. Since it is difficult to drill a long hole at 0.004 inches (0.102 mm) in diameter, a larger hole size of 0.028 inch (0.711 mm) diameter is designed into the flexure wire mounts to accommodate the largest expected wire diameter. By designing the flexure wire mounts to handle the largest expected wire diameter, not only is the manufacturability of the wire mounts increased, but there also exists the flexibility in interchanging the wire diameters to achieve the desired stiffness and performance. The resulting issue is how to attach a wire of diameter 0.005 inches (0.127 mm) into the flexure clamp hole diameter of 0.028 inches (0.711 mm) designed for a wire of 0.013 inches (0.330 mm) in diameter. It is not possible to provide adequate clamping force to a small wire with such a mis-match in the wire diameter to the hole size. The solution is to place the attach wire into a set of concentric tubing, which increases the equivalent wire diameter at the attach point. Stainless steel hypodermic tubing is readily available in a number of diameters with tight tolerances on the internal and external diameters to allow a tight concentric fit. Table B.4 lists the part numbers and mechanical specifications for the hypodermic tubing tested for the wire attachment fittings. Table 5.6 lists the final combination of hypodermic tubing used for each wire diameter.





(a) Crimp Attachment



(b) Solder Attachment

Figure 5.11: Crimped and soldered wire attachment examples.

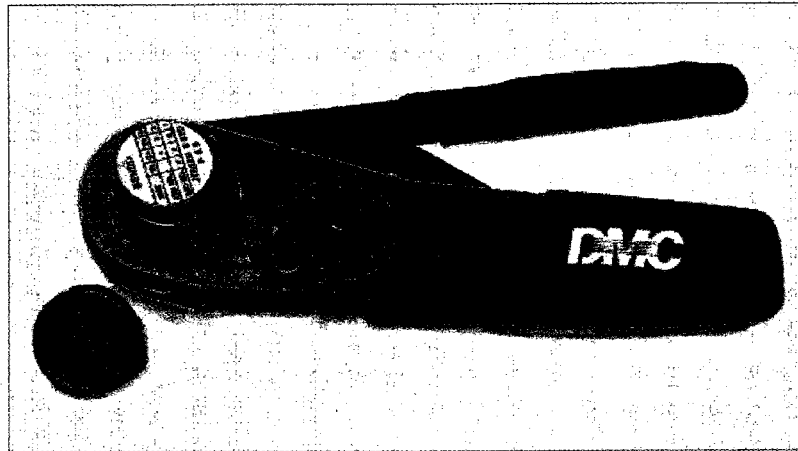


Figure 5.12: DMC AFM8 wire crimper.

In order to attach the wires to the hypodermic tubes, the two methods of soldering and crimping was attempted. Figure 5.11 shows two representative examples of the crimping and soldering wire attach methods. Figure 5.11(a) shows a radially crimped set of two concentric stainless steel hypodermic tubes with a tungsten wire in the center. The solder method, Figure 5.11(b), is a set of two concentric brass telescoping tubing, which are soldered together with a tungsten wire in the center. Through experimentation, the crimp method was preferred for a number of reasons related to a clean, reliable and repeatable attach method. For example, the solder method requires the addition of solder to the assembly through the addition of heat. It is difficult to obtain the right amount of solder and flux to obtain a clean connection. Extra solder protruding from the end of the hypodermic tubes tends to create an equivalently stiffer wire beyond the section with the concentric tubes. In addition, it is difficult to provide the proper amount of heat for a good consistent bond to the tungsten or stainless steel wire. In comparison, crimping is a clean connection and the crimp doesn't harden the wire beyond the concentric tube section like the soldering method. All of the test cases for the crimp method survived a successful pull test, yet several of the solder method tests did not due to inconsistent bonding between the solder and the wire. For crimping the wires to the set of concentric hypodermic tubes, a DMC AFM8 wire crimper, (shown in Figure 5.12), designed

for miniature and sub-miniature electrical connections of 20 AWG through 32 AWG (0.008 inch diameter) wire was utilized. The crimper is a mil-standard 8 impressing crimp for maximum tensile strength, and the radial crimp centers the wire well inside the hypodermic tubes. The maximum crimp depth is dialed in on the AFM8 crimper selector knob to ensure consistent crimps between the wires.

### 5.3 Pendulum Platform Assembly Mounts

Since the platform rotation center is fixed by the geometry of the wires, there is no single mechanical constraint device to properly locate the pendulum platform with respect to the foundation. During assembly, it is important to properly locate the pendulum platform before attaching the wires. If for example, the platform is located offset from the rotation center imposed by the wire constraints when the wires are attached, then the pendulum platform will shift after the wires are attached. The resulting configuration of the pendulum will not be level and the wires will have inconsistent tension. In fact, it is possible that one or more of the wires may not be loaded at all, and the proper constraints to force the desired rotation center will not be imposed. Thus, in order to attach the wires between the pendulum platform and the supporting foundation in a consistent manner, an assembly mount is required. Prior to wire attachment, the designed assembly mount locates the pendulum platform to a position consistent with the desired rotation center relative to the pendulum foundation. This is achieved by making use of the optics plate and the standard 1 inch hole pattern on which the entire pendulum structure is constructed. The pendulum foundation is constructed such that the desired rotation center is coincident with one of the threaded holes on the optics plate. The pendulum platform is then designed with three corresponding mounting interface holes on a 1 inch hole pattern relative to the rotation center. These mounting holes are labeled with a "M" in Figure 5.5. Each mount hole has three equally distributed small stress relief holes drilled around the mount hole circumference. The relief holes ensure a three contact point interface between the hole and a mounting sphere, which is used as the interface to the assembly mount structure. The kinematic design ensures a repeatable placement of the

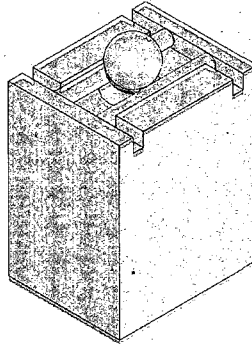


Figure 5.13: Five-wire platform assembly mount.

pendulum platform onto the assembly mounts.

The assembly mounts, Figure 5.13 and Mechanical Drawing B.9, consist of an aluminum machined block with a pair of stainless steel dowel pins to form a set of parallel rails. The assembly mount contains a counter sunk 1/4-20 screw below the parallel rails for attaching the mount onto the optics plate. A stainless steel sphere is then placed onto the parallel rails for a single degree of freedom interface to the pendulum platform. The pendulum platform is then placed onto the spheres at the 1 inch hole pattern mounting holes. A solid model depiction of the pendulum platform on the assembly mounts is depicted in Figure 5.14. The location of the pendulum platform can be adjusted slightly by rotating each of the assembly mounts and hence changing the direction of the degree of freedom provided by the parallel rails. During the assembly of the five-wire pendulum, the assembly mount rails were oriented parallel to the side of the pendulum platform. A heavy weight was placed on top of the pendulum platform to aid in stretching the wires to the desired tension.

## 5.4 Measurement Object Fixtures

In order to measure the moment of inertia for an object in question, the object must be attached or fixtured to the pendulum platform. The fixtures provide two important functions:

- Repeatable object location.

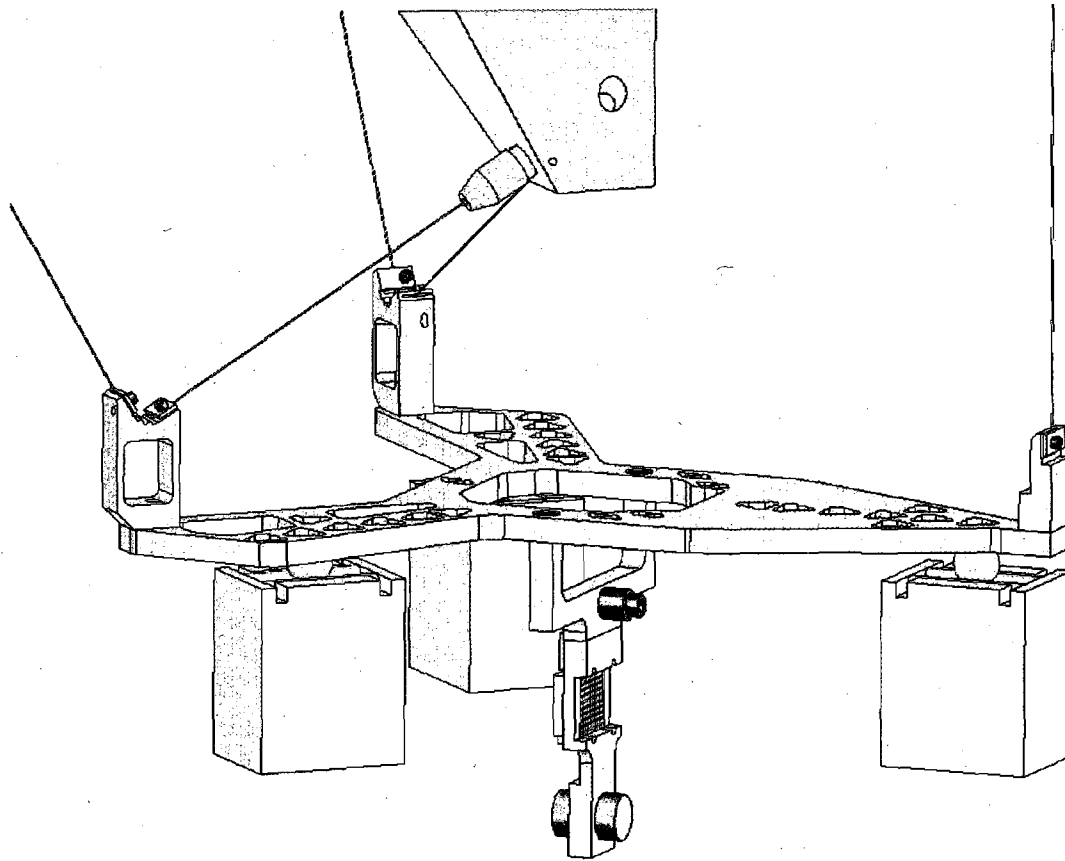


Figure 5.14: Five-wire platform on assembly mounts.

- Repeatable object orientation.

As the object is positioned onto the platform, the location of the mass center relative to the rotation center is of concern. Any offset from the rotation center must be accounted for when determining the inertia for the object by applying the parallel axis theorem. Thus, by having a repeatable placement of the measurement object onto the pendulum platform, a consistent contribution to the radius of gyration due to the offset from the rotation center will occur.

Similar to the requirement for a repeatable placement of the object with respect to the pendulum rotation center, the orientation of the object must also be consistent. In addition, as explained in Section 4.3.2, a moment of inertia measurement device must be capable of determining the instantaneous moment of inertia about at least six different axes of rotation, which span the complete moment of inertia ellipsoid, in order to determine the full moment of inertia tensor. A torsion pendulum design is capable of measuring the radius of gyration about one axis. As such, the apparatus requires the capability of positioning the measurement object in at least six different orientations. The object fixturing method must therefore incorporate the capability for both a repeatable object placement and orientation.

In order to accommodate a wide variety of geometries, the object fixturing philosophy for the five-wire pendulum is to create a standard interface on which specialized fixturing devices can be attached. As discussed in Section 5.1 during the pendulum platform design description, a set of holes are drilled along  $120^\circ$  radial lines to interface with the orientation fixtures. In Figure 5.5, the interface holes are the smaller holes drilled near the center of the platform. The holes accept a small  $3/16$  inch, (4.8 mm), diameter sphere, which are then designed to interface with a set of v-grooves on the mounting fixture. The sphere and v-groove interface provides a simple kinematic two-point contact for repeatable positioning. A set of three spheres in the holes drilled along the  $120^\circ$  lines completes a three-point mount to the mounting fixture.

For each mounting fixture design, a set of parallel v-grooves are machined to allow shifting the object location in steps of known, repeatable amounts. In addition, the pendulum platform contains an identical set of three mounting holes offset by a fixed

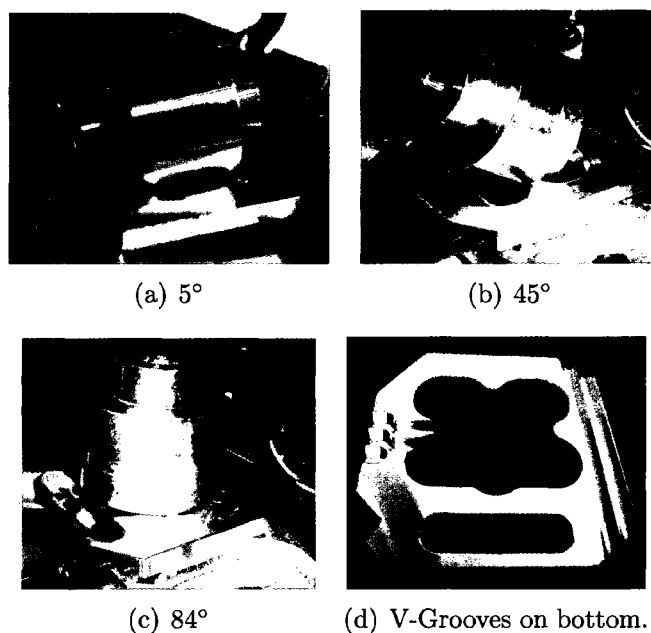


Figure 5.15: Object orientation fixtures for cylindrical object.

amount to provide an additional number of object location configurations. The ability to shift the location of the measurement object relative to the pendulum platform, and hence the rotation center provides the ability to determine the approximate location of the measurement object's mass center relative to the rotation center. For example, by measuring the pendulum frequency of oscillation and then repeating the measurement after shifting the object by a known amount, a change in the oscillation frequency will be observed due to the parallel axis theorem.

For the five-wire pendulum, orientation fixtures for two different geometries were created: spherical and cylindrical. These fixtures are kinematic in design to ensure a repeatable fixturing method for the object position. Where possible, a kinematic design is also utilized for establishing a repeatable object orientation.

### 5.4.1 Cylindrical Object

For the cylindrical-shaped object, a set of sleds to generate both a repeatable object placement and different orientations were constructed as part of a student

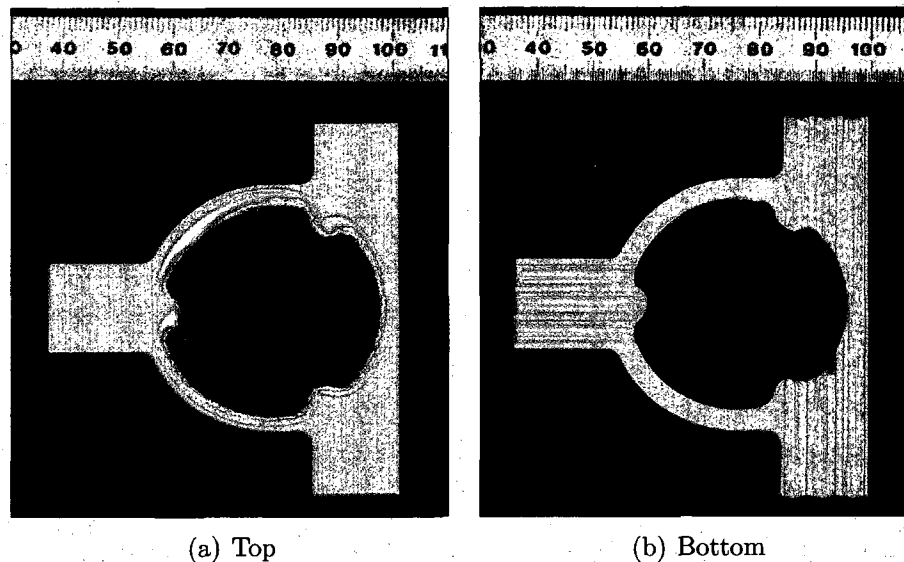


Figure 5.16: Mount for spherical object.

project in the Precision Engineering course taught at Stanford University by Professors Dan DeBra and Dave Beach [18]. For repeatable placement, the fixtures are mounted to the pendulum platform using a set of v-grooves and ball bearings. For orientation, a set of kinematic fixtures, one for each orientation, were constructed. Refer to Figure 5.15. Each fixture permits changing the orientation of the cylindrical object with high repeatability and are measured to be repeatable in orientation to within  $0.02^\circ$ . Note that there are only three different orientations required for the cylindrical-shaped object. By utilizing the symmetry of the object, different orientations can be achieved with the same fixture by simply rotating the object about the axis of symmetry.

### 5.4.2 Spherical Object

A single fixture mount was constructed for an object with a spherical geometry. Refer to Figure 5.16 and Mechanical Drawing B.8. Since a sphere is of a simple geometry with no features for orientation positioning, the mount can only position a spherical object with respect to translation. Clearly a kinematic mount design as used



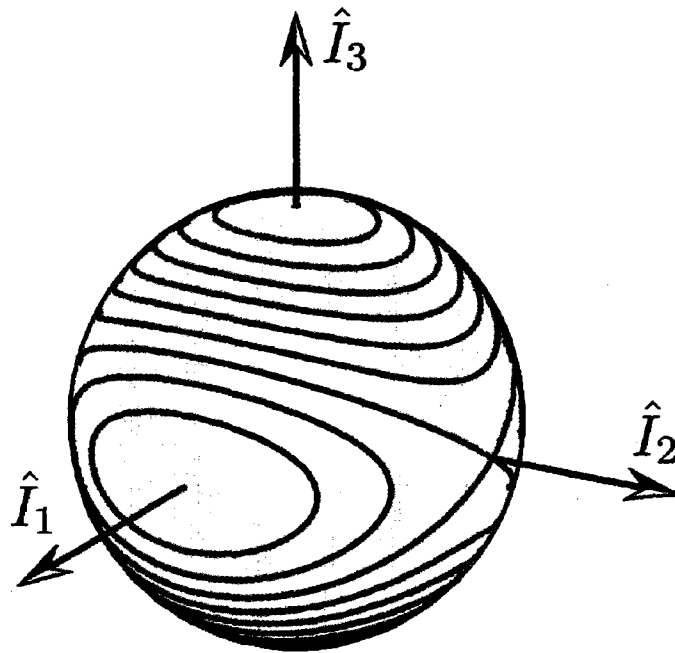


Figure 5.17: Polhode paths for different energy levels and a given angular momentum.

for the cylindrical shaped object is preferred for both translational and orientation positioning; but the lack of geometrical features on the sphere prevent such a design. For a repeatable placement in the plane of the pendulum platform, the same kinematic interface consisting of v-grooves and ball bearings is used. The mount is further designed with a three-point contact interface to the sphere at the proper radius to position the mass center of a 50 mm diameter sphere in the plane of the wire attach points. For establishing the actual orientation of the sphere in a repeatable fashion, an alternate method must be used. The philosophy for the spherical object is to place a set of markings on the object to use for establishing the orientation.

First, in order to place a coordinate system on the sphere in a logical position and orientation, it is desired to determine the approximate directions for the principal moments of inertia. From rigid body dynamics, a rotating object free of external torques will have constant energy and constant angular momentum. The angular momentum is fixed in inertial space and the spin axis will move within the coordinate frame of the rotating body. The path traced by the spin axis within the body frame

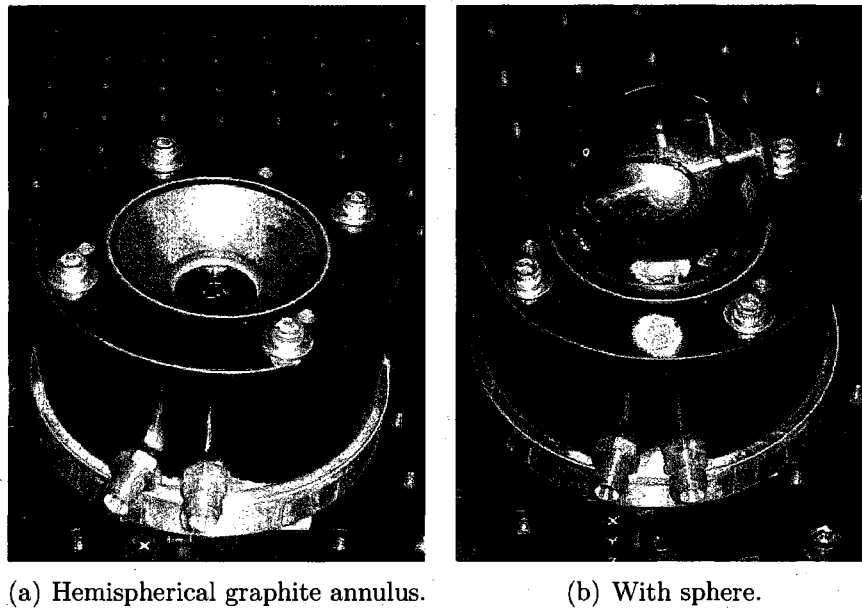


Figure 5.18: New Way air bearing used for marking polhode path.

is known as the polhode path and is described by the locus of all points of constant rotational kinetic energy and constant angular momentum [19]. Thus, the intersection of the angular momentum ellipsoid and the rotational kinetic energy ellipsoid is the polhode path. This elliptical intersection, and hence the polhode path, is centered around the minimum or maximum principal moment of inertia. Figure 5.17 shows for example a set of polhode paths for different energy levels. The figure shows the elliptical polhode paths are centered around the direction for the maximum and minimum moment of inertia. Therefore, in order to determine the direction of the principal axes, one needs only to trace a set of polhode paths onto the surface of the sphere.

In order to achieve torque free motion, the sphere is placed into a specially designed air bearing, which was graciously donated by New Way Air Bearings. The air bearing consists of a sintered graphite hemispherical annulus with a diameter slightly larger than that of the sphere. Refer to Figure 5.18. The sphere is then placed inside of the hemispherical shell to create the air bearing. As pressurized air passes through the porous graphite in the hemispherical shell, an equally distributed cushion of air is



Figure 5.19: Apparatus for marking sphere with perpendicular great circles.

generated at the surface of the sphere. This uniform, continuous flow of air creates a low friction interface between the surface of the sphere and the air bearing, allowing the sphere to rotate freely with negligible external torques. Once the sphere is placed into torque free rotational motion using the air bearing housing, the polhode path is traced by periodically placing a mark at the rotation center with a permanent marker. If kinetic energy is dissipated, the spin axis migrates toward the direction of the principal axis of maximum inertia. Thus, by changing the color of the marks over time, the direction of the polhode motion is additionally identified, allowing for distinction between the directions for the axes of maximum and minimum moment of inertia.

Next, a set of perpendicular great circles are drawn on the surface of the sphere. A specially designed apparatus [24], as shown in Figure 5.19, is used to mark the



Figure 5.20: Sphere with polhode paths and great circles.

spheres.<sup>2</sup> The crossing point of the two great circles is then positioned to be located near the center of the polhode paths previously drawn on the sphere surface. Figure 5.20 shows a sphere with polhode paths marked around the maximum and minimum principal directions. Two perpendicular great circles are drawn with the intersection at the center of the elliptical polhode path. These great circles are then used as a reference when the sphere is placed onto the fixture and the pendulum platform. One great circle is oriented in a vertical fashion and oriented with a set of vertical references: the pendulum vertical wire and the sharp edge of the wire attach fixture of the pendulum foundation. A simple laser pointer, which was modified to produce an elongated elliptical spot, was then aligned with the horizontal great circle, and positioned at the intersection of the two great circles. The laser spot allows for the sphere to be removed and to reposition the great circle intersection at the same location. Figure 5.21 shows the pendulum platform with a sphere on the mounting fixture. The polhode paths are clearly marked on the sphere and the positioning laser spot is visible at the center of the elliptical polhode path.

---

<sup>2</sup>The apparatus was built as a student project in the Precision Engineering course taught at Stanford by professors Dave Beach and Dan DeBra with John Conklin as the customer.

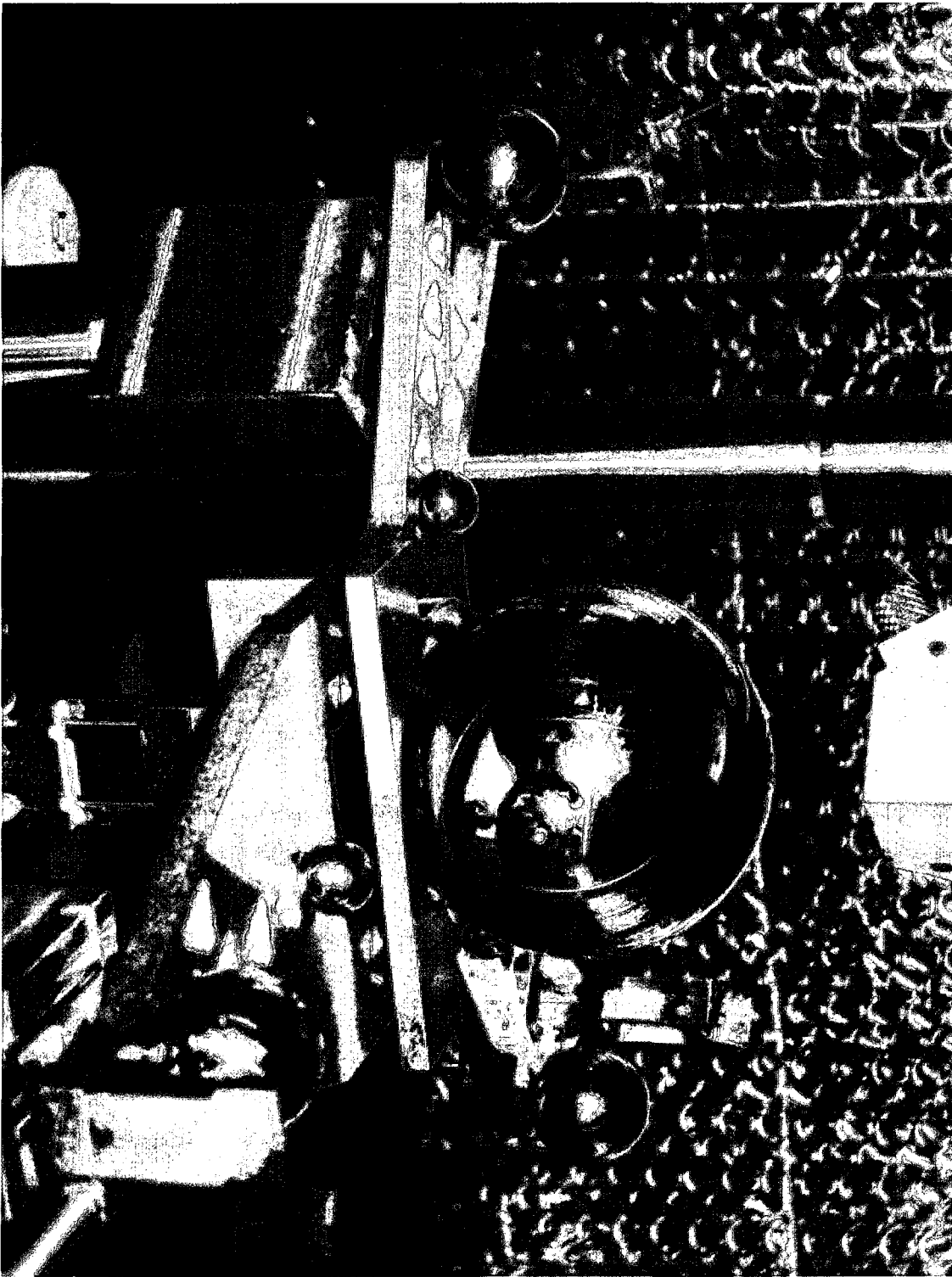


Figure 5.21: Sphere on platform with orientation markings.

## 5.5 Measurement/Sensing

The five-wire pendulum requires a non-contact angular position sensor and actuator. Recall from Equation 4.18, that the oscillatory motion of a torsion pendulum is described by the relationship between the radius of gyration  $R_g$ , or the instantaneous moment of inertia about the axis of rotation  $I_p$ , and the angular frequency  $\omega$ :

$$R_g^2 = \frac{I_p}{m_p} = \frac{k}{\omega^2}$$

where  $k$  is the torsion coefficient or stiffness constant of the pendulum and  $m_p$  is the total mass of the pendulum. The moment of inertia for the system is therefore determined by measuring the angular frequency  $\omega$  and the pendulum mass. The angular displacement of the five-wire pendulum can be measured by a number of different methods. The angular frequency is then extracted from the time history of the angular displacement.

### 5.5.1 Shadow Sensing

Shadow sensing is a straight-forward method for measuring the angular displacement of the pendulum platform. A split photo-diode coupled with a wiper and thin slit, Figure 5.22, will record a translational change in position. The wiper blocks the illumination of the photo-diode from a diode emitter. As the wiper moves across the sensor, the area of illumination is changed. The wiper is attached to the pendulum through the rotation center. Using a small angle assumption, a rotation of the platform is converted to a translation, which is measured by the split photo-diode. Increased sensitivity is achieved by increasing the length of the wiper to locate the slit far from the rotation center. Using a small angle assumption, a larger displacement is produced for the same amount of angular rotation. Yet, by increasing the length of the wiper, the total moment of inertia for the platform plus the sensor is increased. It is desired to reduce the total moment of inertia for the platform to allow precision radius of gyration measurements.

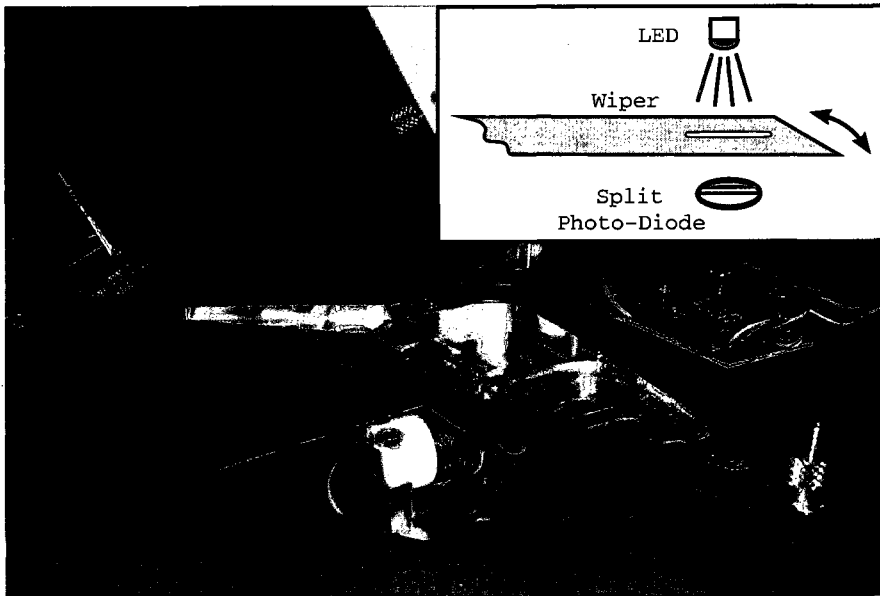


Figure 5.22: Five-wire pendulum platform with shadow sensing.

A shadow sensing method of determining the pendulum platform angular displacement was determined not to be suitable for the five-wire pendulum. Horizontal as well as vertical translations of the platform are also recorded as an observed rotation. Using the metal wiper depicted in Figure 5.22, it was observed that a vertical displacement of the wiper and slit would generate an artificial observed rotation at the sensor. As the slit moves farther away from the split photo-diode sensor, the size of the illuminated area generated by the slit increases. Translational contributions to the angular measurement are further complicated by vibrations which create a vertical displacement of the slit and the wiper. Since the shadow sensing method with a split photo-diode for angular measurement is coupled to translational motion of the pendulum platform, the method was abandoned in favor of grating angular sensing using optics.

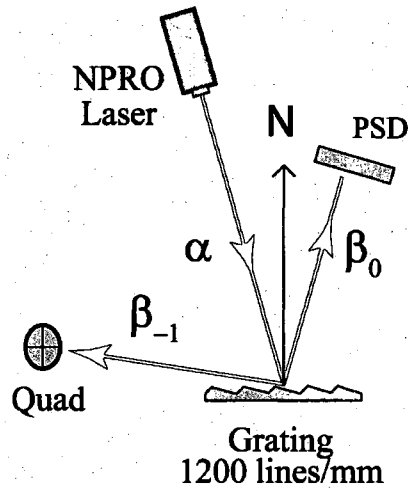


Figure 5.23: Grating angular sensor.

### 5.5.2 Grating Angular Sensing

The angular displacement of the five-wire pendulum is measured by application of optical angular sensing. A grating angular sensor [62] and diffraction grating angular magnification is used to provide a sensor with both a large dynamic range and high resolution. Optical sensing decouples any vertical motion from the detection sensor signal and the associated angular magnification allows for a high sensitivity measurement. A diffraction grating is attached to the pendulum platform at the center of rotation. Using a laser as a light source, the grating diffraction orders are used for angular sensing as depicted in Figure 5.23. As the pendulum platform rotates, the diffracted beams rotate similar to a plane mirror reflection but are additionally magnified by the diffraction order angle. Any minor translational motion of the pendulum will not be magnified and vertical motion of the pendulum will not affect the diffracted beam. If the pendulum rotates (and hence the attached grating) by an angle of  $\delta\alpha$ , the resulting incremental rotation angle  $\delta\beta_n$  of the diffracted beam for diffraction order  $n$  is given by [62]:

$$\delta\beta_n = \frac{\cos(\alpha)}{\cos(\beta_n)} \delta\alpha \quad (5.6)$$



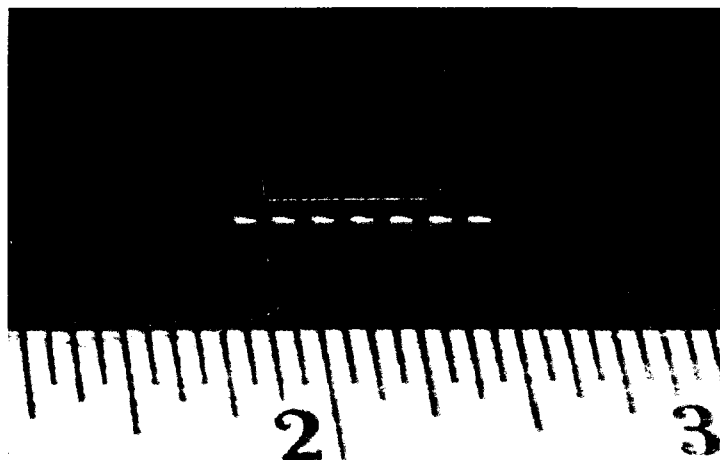


Figure 5.24: Position Sensitive Diode (PSD).

where  $\alpha$  and  $\beta_n$  are the angles from the grating norm for the incident beam and the diffraction angle respectively. This grating angle magnification enhances the measurement sensitivity. The grating angular sensor magnifies the angular displacement of the pendulum but does not magnify any translation.

The diffracted beams are captured by a position sensitive diode (PSD), Figure 5.24, at the 0 diffraction order and a quad photo diode at the  $-1$  diffraction order. The diffraction order angles of  $81^\circ$  and  $16.8^\circ$  were chosen to combine the advantages of a high dynamic range sensor with high precision. The electrical signal conditioning schematics for the PSD and the quad photo diode are found in Appendix C.2, Figures C.2 and C.3 respectively. The sensors are arranged such that a positive signal on the quad sensor (full right signal) and PSD are positive for a negative rotation of the pendulum platform about the vertical axis.

## 5.6 Grating and Magnet Holder Design

The non-contact optical sensing scheme for the five-wire pendulum is provided by the grating angular sensor described in Section 5.5.2. An optical grating must be rigidly attached to the pendulum platform with the grating surface located at the

rotation center to utilize the sensor. The non-contact actuator is provided by fixing a permanent magnet on the pendulum at the rotation center. The magnet is surrounded by two wire coils, which when energized produces a magnetic field and hence a torque on the platform. Since both the actuator and sensor require components to be located at the pendulum rotation center, a common fixture is used to mount both the grating and the magnet to the pendulum platform. The manufactured grating and magnet holder shown in Figure 5.25 is attached to the bottom of the pendulum platform. The entire holder is carefully designed to reduce the contributed moment of inertia to the pendulum platform and to maintain the mass center of the platform at the rotation center. A stainless steel bushing and screw are used to offset the mass of the grating to retain the mass center location. The holder is machined into two parts: a top u-shape attach fitting and a bottom mount for the grating and magnet. The two pieces are held together by two 1/16 inch diameter stainless steel spring pins. The u-shaped top to the holder provides adequate clearance for the measurement object and spans the large middle hole in the pendulum platform. The bottom portion of the mount provides a simple interface for holding the magnet and grating. Two magnets are placed into counter sunk holes on opposite sides of the mount and held in place by the magnetic attraction force. A single stainless steel #2-56 set screw is used to clamp the grating into place. The grating is positioned such that the surface is at the rotation center of the platform. The grating surface is also flush to the surface of the mount to prevent obstruction to the diffracted laser beam on either side of the grating surface. The grating center is located at a height of 4 inches (10.16 cm) above the optics plate to match the optics mirror mounts. Refer to Mechanical Drawings B.6 and B.7 for further information regarding the geometry of the two-piece grating and magnet mount parts. A solid model showing the grating/magnet mount attached to the pendulum platform is shown in Figure 5.26.

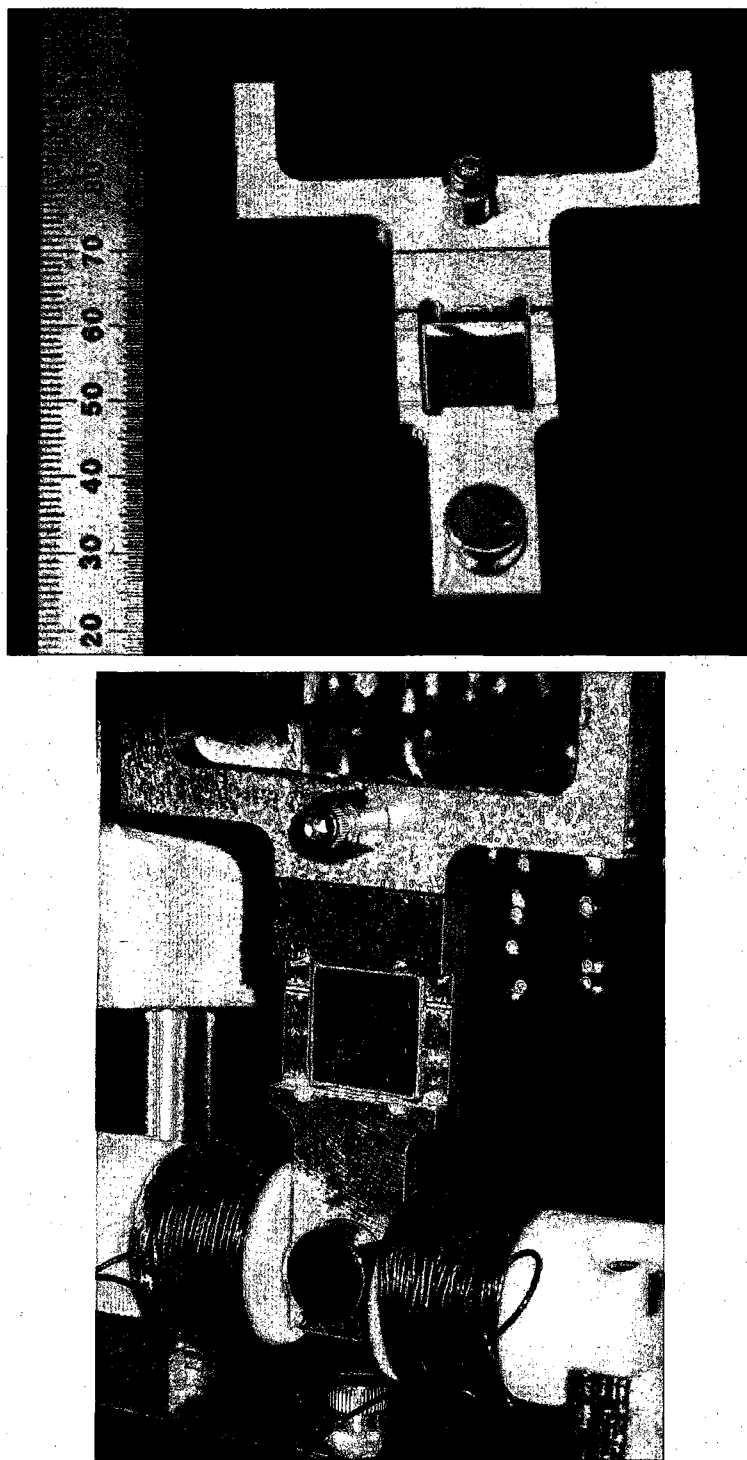


Figure 5.25: Five-wire pendulum grating and magnet mount.

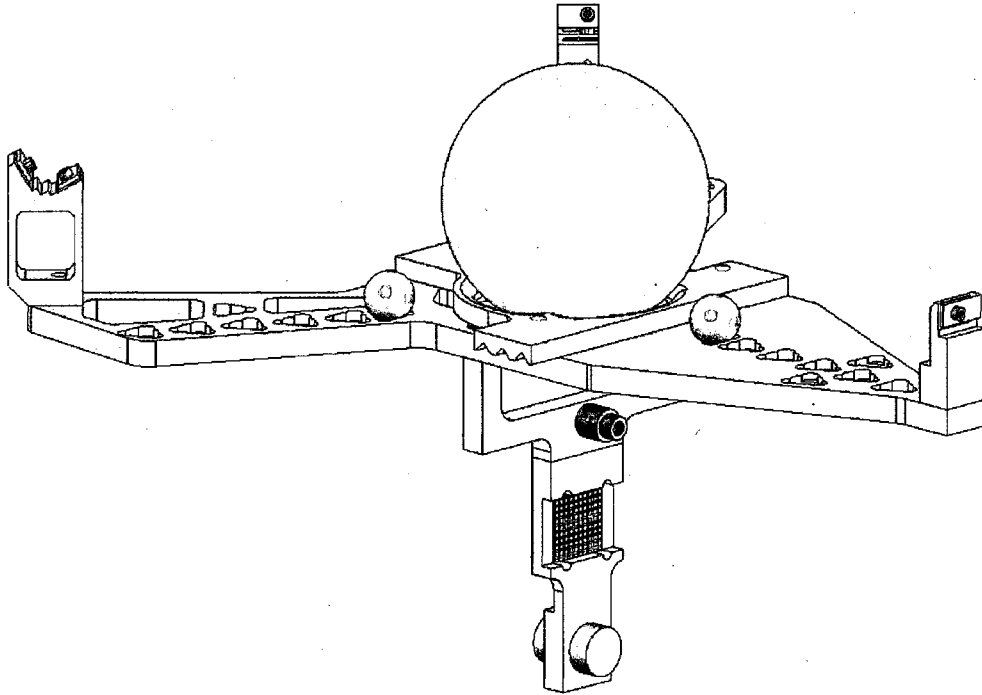


Figure 5.26: Five-wire pendulum platform with grating holder.

## 5.7 Frequency Measurement Procedure

As mentioned in Section 5.6, the pendulum platform contains a small permanent magnet and a corresponding set of coils to pulse the pendulum. A repeatable pendulum response for each measurement run is ensured by using a function generator connected to a coil driver circuit (Figure C.1) which sends a pulse to the coils. A repeatable response is necessary, as the pendulum natural frequency of oscillation is also a slight function of the pendulum oscillation amplitude. The time history angular position of the platform is recorded from the PSD and Quad photo diode signal using the grating angular sensor described in Section 5.5.2. A number of data reduction techniques exist to extract the natural frequency of rotation for the pendulum platform. The following paragraphs will describe and compare the various data reduction techniques which were considered. A summary of the data reduction techniques is depicted in Table 5.7.

Technique	Complications/Issues
Fourier Transform	Resolution limited by data length. Requires long-term noise suppression and environmental stability.
Coherent Demodulation	Excessive measurements required
Zero Crossing Detection	Limited repeatability for noisy data
Damped Sinusoid Curve Fit	Susceptible to vibrations and variation in response amplitude.

Table 5.7: Data reduction techniques.

### 5.7.1 Damped Sinusoid Curve Fit

The pendulum oscillatory frequency is easily extracted by data reduction in the time domain. The pendulum response to a single disturbance is known to be governed by the equations for damped harmonic motion:

$$\theta(t) = A_o e^{-\zeta \omega_n t} \cos(\omega_d t + \phi) + dc \quad (5.7)$$

$$\omega_d = \omega_n \sqrt{1 - \zeta^2} \quad (5.8)$$

where  $A_o$  is the initial amplitude of oscillation,  $\zeta$  the damping coefficient,  $\omega_d$  the damped natural frequency,  $\omega_n$  the natural frequency,  $\phi$  the phase, and  $dc$  the offset from zero in the raw voltage signal. A nonlinear curve fit is then applied to the data to experimentally determine the parameters of the pendulum response, including the natural frequency  $\omega_n$  and damping coefficient. In practice, the damped sinusoid curve fit of the data for a particular pendulum configuration typically resulted in a repeatability on frequency determination,  $f = \omega_n/2\pi$ , to be within the standard deviation range of  $\sigma = 2 \times 10^{-6}$  to  $9 \times 10^{-6}$  Hz for a frequency of around 2.0 to 3.0 Hz.

### 5.7.2 Fourier Transform

Analysis in the frequency domain consists of performing a Fourier transform of the recorded oscillatory motion to calculate the amplitude spectral density of the signal. The peak in the amplitude spectral density data will indicate a bin width limited estimate of the measured damped natural frequency. In order to increase the frequency resolution of the Fourier transform estimate, the data length needs to be increased. By periodically pulsing the pendulum to keep the pendulum oscillating, long data lengths can be achieved. A repeated pulse drive is however not entirely desirable, as the FFT will contain harmonics from the pulse period and will affect the higher natural frequency of the pendulum to be measured. Since the measured damping coefficient is on the order of  $10^{-4}$ , the damped natural frequency is within approximately  $10^{-8}$  of the natural frequency for the system. The measured natural frequency is therefore essentially the same as the natural frequency for the system.

### 5.7.3 Coherent Demodulation, Sine Drive

By using the frequency response for a damped driven harmonic oscillator the natural frequency of a system can be determined. The system frequency response is obtained by applying a sinusoidal driving force to the system and measuring the phase offset of the response from the drive force. A Bode plot of the system response can then be generated by repeating the procedure at various sinusoidal drive frequencies around the expected natural frequency of the system.

The phase offset of the response from drive frequency will pass through  $\pi/2$  at the natural frequency of the system regardless of the damping ratio for the system. Thus, by curve fitting the phase offset as a function of frequency, the  $\pi/2$  crossing will establish the natural frequency of the system. What remains is a method for determining the phase offset of the response from the sinusoidal drive force. The phase offset can be determined by using the technique of coherent demodulation. Assume a drive force of the form:

$$F(t) = \cos(\omega t) \tag{5.9}$$

and assume a sinusoidal response of the form:

$$x(t) = \cos(\omega t + \phi) \quad (5.10)$$

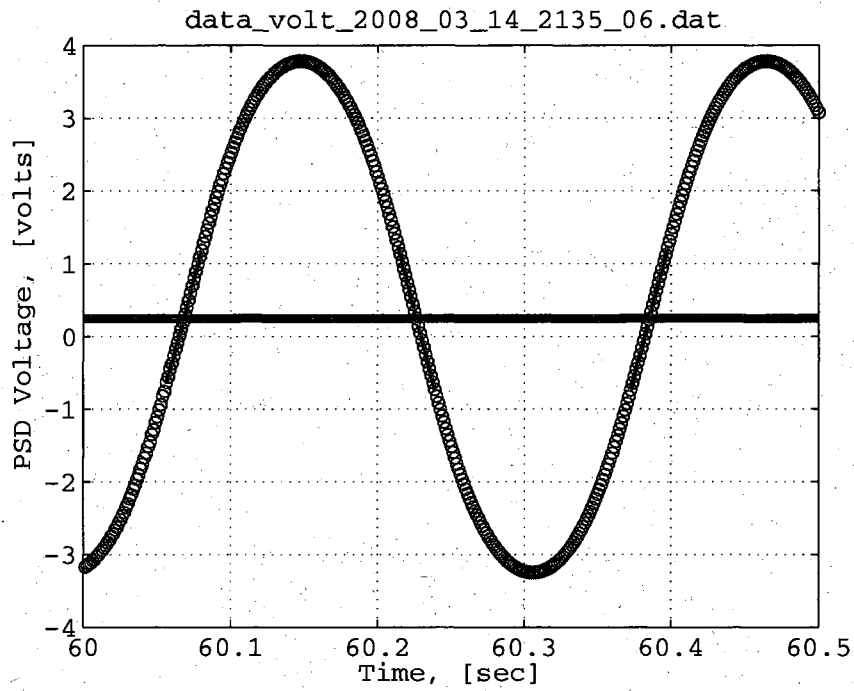
If the response signal is modulated with a cosine signal of the same drive frequency,  $\omega$ , one obtains:

$$M = \cos(\omega t + \tilde{\phi}) \cos(\omega t + \phi) \quad (5.11)$$

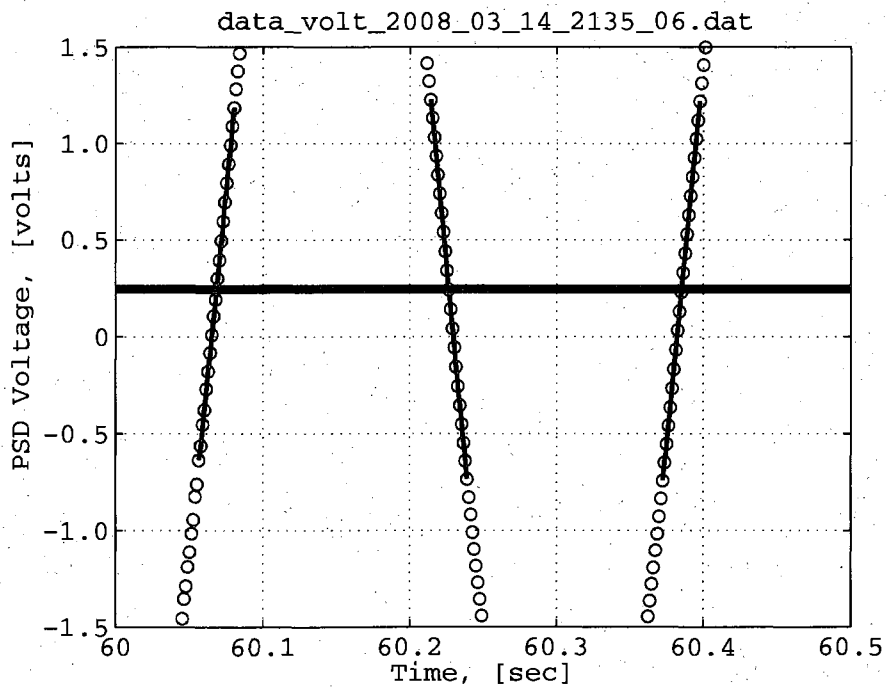
The phase offset between the drive and response signal is easily obtained, since the max of  $M$  occurs when  $\tilde{\phi} = \phi$  and  $M = \cos^2(\omega t + \phi)$ . For the physical system, it is necessary to measure both the drive signal and the system response since the zero phase definition for the drive signal is arbitrary. The coherent demodulation procedure was not applied to the five-wire data for determining the oscillation frequency since excessive measurements would be required to determine the  $\pi/2$  phase offset crossing.

#### 5.7.4 Time Domain Zero Crossing Detection

To determine the pendulum frequency, the period is measured by detecting and measuring the difference between successive zero crossings of the sinusoidal signal. To find the zero crossing, a straight line is fit to the data in the proximity of the signal mean value. Using the best fit line for each data segment, the time value corresponding to the mean value crossing is determined for successive crossings. Then by subtraction the signal period and thus the frequency is determined. Although the technique works very well for a pure theoretical system response, as tested with a measured signal produced by a signal generator, the technique does not perform well in the physical world in the presence of disturbances and higher order system response modes. Figure 5.27, for example, shows the raw five-wire quad photo diode sensor data acquired at a sample frequency of 800 Hz with the time domain zero crossing detection algorithm applied. Although the zero crossing detection algorithm shows a clear fit to the data across the mean signal value crossing, the calculated signal frequency was inconsistent. Figure 5.28 shows the results after several successive



(a) Full Wave



(b) Zero Crossing Details

Figure 5.27: Time domain zero crossing detection.



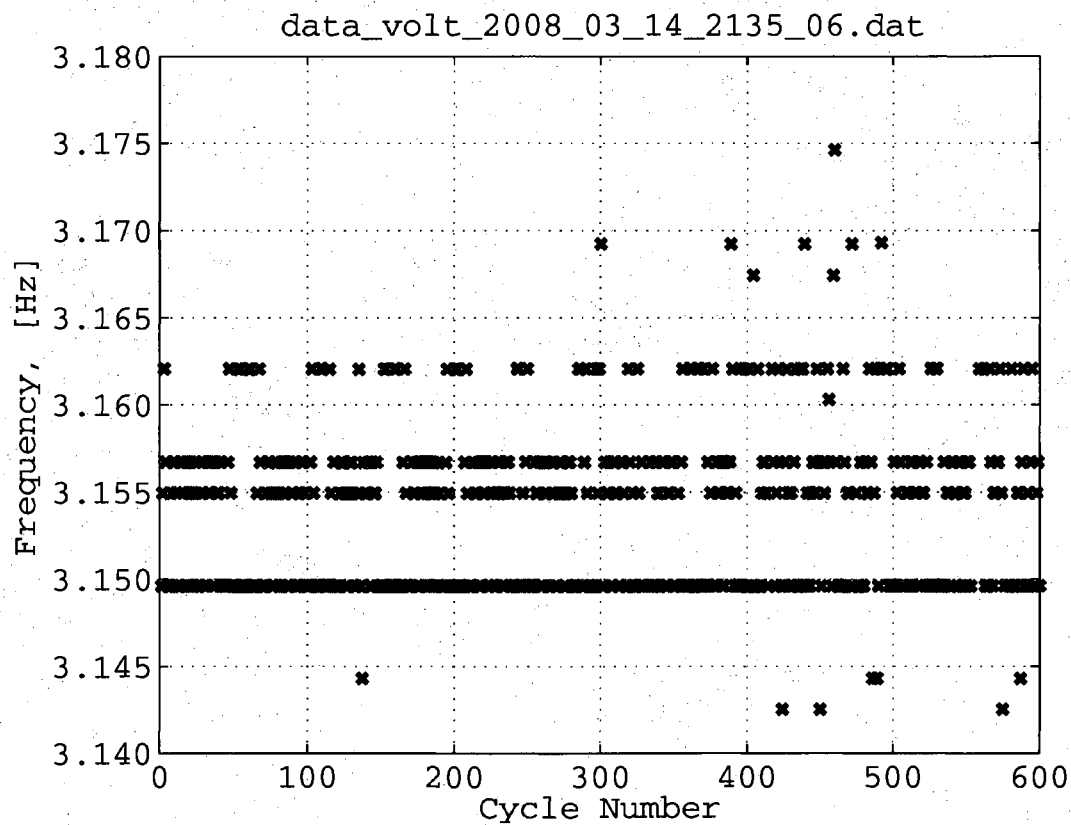


Figure 5.28: Time domain zero crossing detection results. The mean frequency for the data is 3.1539 Hz with a standard of  $\sigma = 4.7 \times 10^{-3}$  Hz.

frequency calculations using the zero crossing detection technique. The results clearly indicated a bound determination of the frequency. At first the banded results observed in Figure 5.28 were thought to be due to measurement instrumentation digitization error. Yet as the data measurement sample frequency was increased, the results were unchanged. The variation in the determined frequencies is a result of disturbances and higher frequencies within the sinusoidal signal. The high frequency oscillation generated by disturbances and other oscillation modes cause a fluctuation of the zero crossing. As a result, the zero crossing detecting technique could not be applied to the five-wire pendulum data for extracting the frequency of oscillation to better than  $10^{-2}$  Hz.

# Chapter 6

## Experimental Results

In order to perform measurements with any measurement apparatus, there exists a number of steps which must be performed before the actual desired quantity is determined. The five-wire pendulum is no exception. Regardless of the final desired physical mass property, whether it be the mass center location or the moment of inertia, the pendulum platform must be set up properly and calibrated. The pendulum calibration is therefore the first step prior to measurements. After an adequate calibration, the measurements for the desired mass property are conducted. As described in Section 4.4.2 for the mass center determination, and Section 4.3.2 for the moment of inertia measurement, a number of measurements must be performed for various configurations of the object in question. First, Section 6.1 describes the calibration procedure and corresponding measurement results. The remaining sections describe the measurement process and corresponding results for the desired physical mass property.

### 6.1 Pendulum Calibration

As with any measurement device, the apparatus must first be calibrated before measurements can be made. For the five-wire torsion pendulum, the moment of inertia for the pendulum platform must be determined. The oscillatory motion of a torsion pendulum is described by the relationship in Equation 4.18. For the torsion

pendulum the moment of inertia,  $I_{ozz}$ , torsion coefficient,  $k$ , and actual rotation center are unknown. The unknown parameters are determined by adding a known moment of inertia to the system. This is achieved by the addition of  $n$  calibration spheres to the platform with a known moment of inertia  $I_c$ , such that the relationship in Equation 4.18 becomes:

$$I_{ozz} + \sum_{i=1}^n I_{c_i} = \left( m_p + \sum_{i=1}^n m_i \right) \frac{k}{\omega^2} \quad (6.1)$$

Each calibration sphere mass  $m_i$  with radius  $a_i$ , is placed in holes at locations  $R_i$ , as discussed in Section 5.1. The use of fixed holes for locating the calibration spheres ensures a high repeatability for positioning and hence a consistent addition to the total system moment of inertia. Since the calibration spheres are not placed at the rotation center of the pendulum platform, the parallel axis theorem is applied and Equation 6.1 becomes:

$$I_{ozz} + \sum_{i=1}^n m_i R_i^2 + \frac{2}{5} m_i a_i = \left( m_p + \sum_{i=1}^n m_i \right) \frac{k}{\omega^2} \quad (6.2)$$

The calibration measurement is repeated for various combinations of calibration sphere positions and a least squares fit of the measured data is then performed to obtain the unknown parameters.

During the calibration process, the same number of calibration spheres are used for each calibration configuration and the calibration spheres will remain on the pendulum platform for any further measurements. In addition, the calibration process is performed with any required object mounting fixtures in place, such that the only addition to the system after calibration is the object for which the moment of inertia is to be determined. The goal is to minimize the change in system mass between the calibration measurements and the object identification measurements. The requirement to avoid a change in the system mass between measurements stems from the fact that a change in pendulum platform load results in a stretch of the attach wires.

As explained in Section 5.2.2, the wire properties were chosen such that the compliance in each wire would be matched as a load is applied to the pendulum platform. Matching of the wire compliance reduces the change in the pendulum orientation and translation within the plane of the platform due to the additional load to the platform. Yet, the vertical position of the pendulum platform will translate with the additional stretch of the wires. This additional stretch will affect the calibration parameters determined for the pendulum. Recall for example Equation 4.19 for the torsion pendulum stiffness parameter. The stiffness parameter is inversely proportional to the nominal pendulum wire length. Due to a stretch of the wires from the applied load, the wire length will be different for various loading configurations. Care must be therefore taken to reduce the amount of mass change to the pendulum platform for each configuration in order to avoid a change in the torsion coefficient for the system. Similarly, by maintaining a constant system mass, the platform rotation axis direction is unchanged during the measurement process.

The calibration procedure must be repeated if the total mass supported by the attach wires changes. This includes the addition of the measurement object to the torsion pendulum platform. After the measurement object is in place on the pendulum platform, the calibration procedure is then repeated to determine the new torsion pendulum stiffness parameter. The calibration procedure is summarized as follows:

1. Measure frequency for various calibration sphere locations for the pendulum platform with the mounting fixtures in place. Both symmetric and asymmetric loading of the pendulum platform with the calibration spheres is required to determine the pendulum rotation center location. Parameters determined:
  - Pendulum instantaneous moment of inertia about rotation axis,  $I_{OZZ}$ .
  - Pendulum stiffness coefficient,  $k$ .
  - Pendulum rotation center location relative to design value,  $x_r, y_r$ .
2. Repeat previous step with measurement object on the pendulum platform. The pendulum stiffness coefficient will have a new value due to the stretch of the wires. In addition, the pendulum rotation center may have changed. Parameters determined:

Parameter	Unloaded Pendulum		Loaded Pendulum		Units
$I_{ozz}$	432.3	$\sigma = 0.7$	—	—	$\text{kg}\cdot\text{mm}^2$
$k$	1.1764	$\sigma = 6.7 \times 10^{-4}$	1.0652	$\sigma = 8.7 \times 10^{-4}$	$\text{m}^2/\text{s}^2$
$x_r$	2.21	$\sigma = 0.07$	-1.97	$\sigma = 0.09$	mm
$y_r$	3.16	$\sigma = 0.07$	0.12	$\sigma = 0.09$	mm

Table 6.1: Pendulum calibration results. The unloaded pendulum was calibrated with the sphere mounting fixture at the nominal center location. Three 3/4 inch spheres were also positioned in the outer calibration hole set for use as trim masses. The value for  $I_{ozz}$  includes the sphere mounting fixture but not the 3/4 inch spheres. The loaded pendulum contained the addition of a 448.9 g sphere placed in the sphere mount. The measurement object is described in Section 6.3 and was sphere number six, in configuration number nine.

- Pendulum stiffness coefficient,  $k$ .
- Pendulum rotation center location relative to design value,  $x_r$ ,  $y_r$ .

The results for the parameters determined in the calibration process are summarized in Table 6.1. Three 3/8 inch diameter calibration spheres were used for the calibration.<sup>1</sup> The pendulum platform was calibrated with the sphere mounting fixture in the nominal center location and then with a spherical measurement object on the sphere mounting fixture. The value for the pendulum instantaneous moment of inertia,  $I_{ozz}$ , as listed in Table 6.1 includes the sphere mounting fixture. For the platform without the measurement object in place, the frequency measurements were on the order of 2.53 Hz with a standard deviation below  $3.7 \times 10^{-5}$  Hz. The calibration results with the measurement object in place had frequency measurements on the order of 3.9 Hz with a standard deviation on the order of  $2 \times 10^{-5}$  Hz or better. The raw frequency measurements and the calibration sphere location configurations are found in Appendix E, Table E.1 and Table E.2. For comparison purposes, the SolidWorks estimate for  $I_{ozz}$  is  $1055.3 \text{ kg}\cdot\text{mm}^2$ , which includes the platform, sphere mount, the 3/8 inch calibration spheres in hole set one and the 3/4 inch spheres in hole set six. The measured value of  $I_{ozz}$  as listed in Table 6.1 corresponds to a value of  $1058.0 \text{ kg}\cdot\text{mm}^2$  for the same configuration.

<sup>1</sup>For more information on the calibration spheres, refer to Table B.3 in the Appendix, Section B.3.

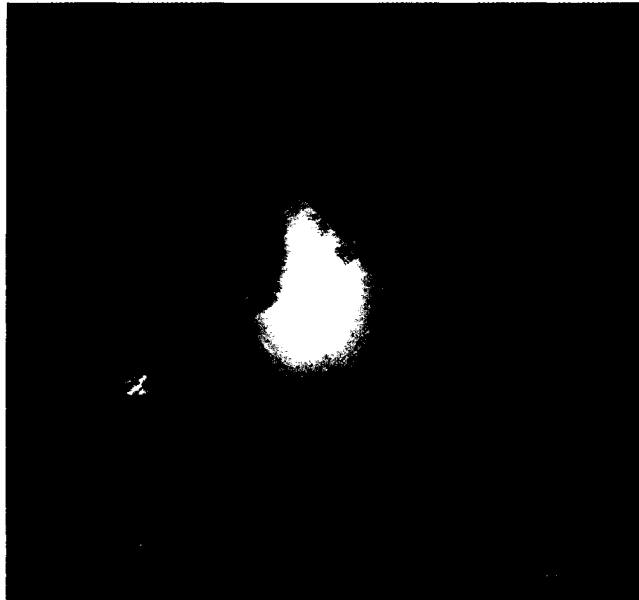


Figure 6.1: BeCu fixed mass center offset sphere. One of the holes drilled to form the mass center offset is visible in the lower left of the image. The location of the mass center offset is marked on the surface of the sphere in the upper right of the image. The great circles drawn on the sphere form the  $x - y$  coordinate axes.

## 6.2 Mass Center Measurement

Although the five-wire pendulum was primarily designed to perform moment of inertia measurements, the apparatus was also utilized to demonstrate the feasibility of mass center measurements using a torsion pendulum. As described in Section 4.4.2, the mass center location relative to the geometric center can be determined by placing the object far from the pendulum rotation center and then rotating the object to be measured. In order to demonstrate the ability to perform mass center measurements with the five-wire pendulum, a sphere with a fixed mass center offset was measured. This specially designed sphere was generated as a portion of a student project in the Precision Engineering course taught at Stanford University [5]. As part of the student course project, a 2 inch (50.8 mm) diameter BeCu sphere was machined with a specific geometry to generate a fixed mass center offset. The sphere was drilled with two holes forming a "V" to produce a mass center offset with respect to the geometric center.

Figure 6.1 shows the fixed mass center offset sphere with one of the holes forming the "V" visible. The sphere was designed to have a theoretical mass center offset of approximately  $\delta = 40 \mu\text{m}$  [5]. One advantage to using this sphere as a mass center measurement object is that during John Conklin's PhD. work at Stanford, the mass center location was measured using the velocity modulation technique. Based on the ability to measure the hole location and geometry of the actual fabricated sphere, the expected mass center location was estimated by Conklin to be  $\delta = 44 \mu\text{m}$  with an error of approximately  $10 \mu\text{m}$  [9]. By applying the velocity modulation technique for mass center measurements, Conklin has measured the mass center offset of this fixed mass center offset sphere to be [10], [9]:

$$\vec{r}^{m_c/g_c} = 3.17\hat{x} - 20.61\hat{y} - 35.56\hat{z} \mu\text{m} \quad (6.3)$$

for a total mass center offset magnitude of  $\delta = 41.17 \mu\text{m}$  with a standard deviation of  $1.5 \mu\text{m}$ . In addition, the fixed mass center offset sphere has visible markings drawn on the outside surface to locate the approximate position of the measured mass center. By knowing the approximate location of the mass center prior to measurements, it is not necessary to perform a complete set of measurements at various orientations in order to demonstrate the ability to measure the mass center location using the torsion pendulum. Thus, the fixed mass center offset sphere can be positioned on the pendulum such that the mass center is located at the minimum and maximum distance from the pendulum rotation center (using  $\phi = \pi$  and  $\phi = 2\pi$  in Equation 4.28). As a result, only measurements for two orientation configurations are required to obtain the mass center offset location. In order to solve for the mass center offset using measured values of the pendulum oscillation frequency, one can algebraically manipulate Equation 4.29 to obtain a polynomial in  $\delta$ :

$$0 = m_o \left( \left( \frac{\omega_2}{\omega_1} \right)^2 - 1 \right) \delta^2 + 2m_o R \left( \left( \frac{\omega_2}{\omega_1} \right)^2 \cos \phi_2 - \cos \phi_1 \right) \delta + I_o \left( \left( \frac{\omega_2}{\omega_1} \right)^2 - 1 \right) \quad (6.4)$$



Parameter	Value	Notes
$I_{ozz}$	422.8 kg·mm <sup>2</sup>	Measured, $I_{ozz} = \frac{m_T k}{\omega_0^2}$ Includes mounting fixtures.
$m_o$	569.3 g	
$a$	25.4 mm	Nominal sphere radius.
$I_o$	121.11 kg·mm <sup>2</sup>	Theoretical value: $\frac{2}{5}m_o a^2$
$R$	76.89 mm	Design value: 2.950 inch, (74.93 mm)
$\omega_1/2\pi$	2.192462 Hz	25 Measurements, $\sigma = 1.2 \times 10^{-5}$ Hz
$\omega_2/2\pi$	2.190501 Hz	25 Measurements, $\sigma = 0.7 \times 10^{-5}$ Hz
$\phi_1$	$\pi$ rad	Theoretical
$\phi_2$	$2\pi$ rad	Theoretical

Table 6.2: Parameters used for mass center offset calculation.

With frequency measurements for  $\phi = \pi$  and  $\phi = 2\pi$ , Equation 6.4 can then be used to find the mass center location within a desired plane. It should be noted, that in order to determine an unknown mass center location within a three-dimensional space, repeated measurements are necessary. That is, the object must be rotated by a fixed amount for multiple configurations within a single plane and then repeated for other planes of rotation.

The BeCu fixed mass center offset sphere was placed onto the pendulum as shown in Figure 6.2. First, the sphere was placed with the mass center marking visible toward the pendulum vertical wire. The great circles marked on the sphere were aligned with the vertical wire and a visible laser beam was used for a repeatable sphere orientation. The measurement instrumentation was setup to allow data acquisition overnight at a constant 26.5 °C temperature. The process was then repeated for the sphere rotated by  $\pi$ , such that the marking for the mass center was away from the pendulum vertical wire. Finally, the frequency was obtained for each configuration using the damped sinusoid curve fitting routine as described in Section 5.7. The frequency measurements had a standard deviation below  $\sigma = 1.2 \times 10^{-5}$  Hz for a frequency on the order of 2.5 Hz. Equation 6.4 and the parameters listed in Table 6.2 were then used to calculate the mass center offset magnitude  $\delta$ . The measured mass center offset from the geometric center for the fixed mass center offset sphere was

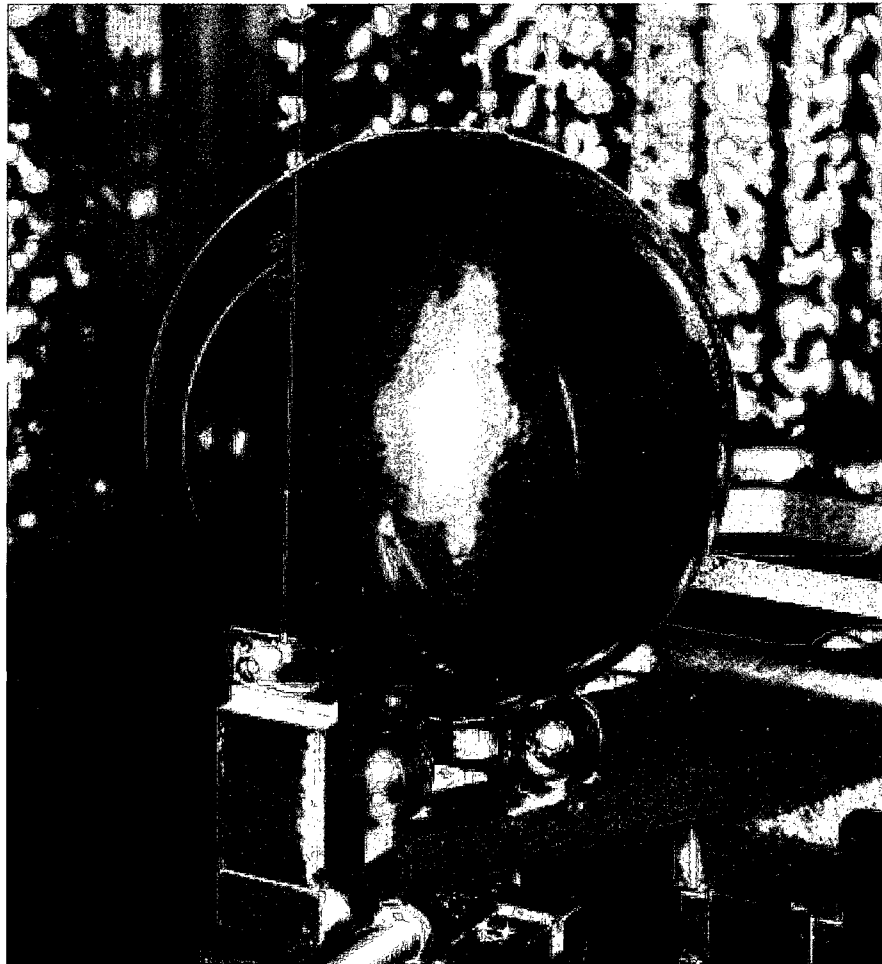


Figure 6.2: BeCu fixed mass center offset sphere on the pendulum in the configuration for mass center measurement. Three  $3/8$  inch spheres are used to create a three point mount. The geometric center of the sphere is located at a radial distance from the rotation center equivalent to calibration hole set number five.

Source	MC Offset	Notes
Design Value	40.0 $\mu\text{m}$	Theoretical, [5]
Estimate from Geometry	44.0 $\mu\text{m}$	$\sigma = 10 \mu\text{m}$ , [9]
Velocity Modulation, Measured	41.17 $\mu\text{m}$	$\sigma = 1.5 \mu\text{m}$ , [10], [9]
Torsion Pendulum, Measured	40.23 $\mu\text{m}$	Error Estimate: 1 $\mu\text{m}$

Table 6.3: Comparison of mass center measurement results.

found to be  $\delta = 40.23 \mu\text{m}$ . Although a full error budget on the measurements was not performed, it is estimated that the mass center offset measurement has an error within about 1  $\mu\text{m}$ . The results are consistent with and within the standard deviation of the measured results as presented by Conklin [9]. Table 6.3 summarizes the various estimates for the mass center offset of the fixed mass center offset sphere. The measured results indicate that the pendulum can indeed be used for accurate mass center measurements.

Currently, the limitation on the accuracy of the mass center measurement is that of the pendulum calibration process and the value for the unloaded pendulum radius of gyration,  $I_{ozz}/m_T$ . It should be noted, that the measured results presented here assume the rotation center of the pendulum is equivalent to the value determined in the calibration process with a sphere of 448.9 g placed at the center of the pendulum. The actual fixed mass center offset sphere measured has a mass of 569.3 g. The difference in over 100 g will generate a change in the torsion pendulum stiffness coefficient,  $k$ , and hence the estimated unloaded pendulum radius of gyration,  $I_{ozz}/m_T$ . The additional mass on the pendulum will reduce the absolute value of the measured mass center offset,  $\delta$ . Additionally, due to the asymmetric loading of the pendulum, it is expected that the rotation center will have shifted from the designed location. By placing a counterbalance mass symmetric to the rotation center, the shift in the rotation center due to wire loading can be minimized. Yet this pendulum platform design did not incorporate the ability to locate a counterbalance mass in the direction opposite to the vertical wire. The actual rotation center and torsion pendulum radius of gyration with the measurement object in place can be determined by performing an additional calibration routine with the sphere located in the mass center

measurement configuration. Since the intent of this work is only to demonstrate the feasibility of mass center measurements using the torsion pendulum, the lengthy calibration routine with the sphere in the mass center measurement configuration was not performed.

In addition, recall that the measurements assumed the approximate location of the mass center was known, such that multiple measurements for various orientation of the sphere were not necessary. The overall accuracy of the measured offset will therefore be slightly affected. It is expected that the results presented here would be an underestimate of the actual mass center offset magnitude obtained from a more rigorous measurement procedure. This stems from the fact that the maximum and minimum separation distance for the mass center location relative to the pendulum rotation center was approximately known. An error in the assumed rotation angle,  $\phi$ , will result in an equivalently reduced mass center offset value.

### 6.3 Preferred Principal Axis of Inertia Sphere

For gravitational reference sensors, a rotating spherical proof mass may be used. For such a design it is beneficial to separate the polhode rate from the spin frequency. It is possible to spectrally separate the spin frequency from the polhode rate by creating a proof mass with one principal moment of inertia which is at least 10% greater than the other two [9]. To demonstrate the feasibility of manufacturing a spherical proof mass with such a moment of inertia difference ratio, a set of spheres were fabricated as part of a student project in the Precision Engineering course taught at Stanford University by Professors Dan DeBra and Dave Beach [8]. These preferred principal axis of inertia spheres were constructed of either two or three brass parts and then brazed together to create a complete sphere. Figure 6.3 shows a simplified cross-sectional view of the two designs and the theoretical design parameters for the preferred principal axis of inertia sphere are shown in Table 6.4. Note that the ideal simplified geometry depicted does not match exactly the fabricated version. The internal geometry was modified by adding features to simplify the machining process. The two-part sphere was machined using a computer numerical control (CNC) mill

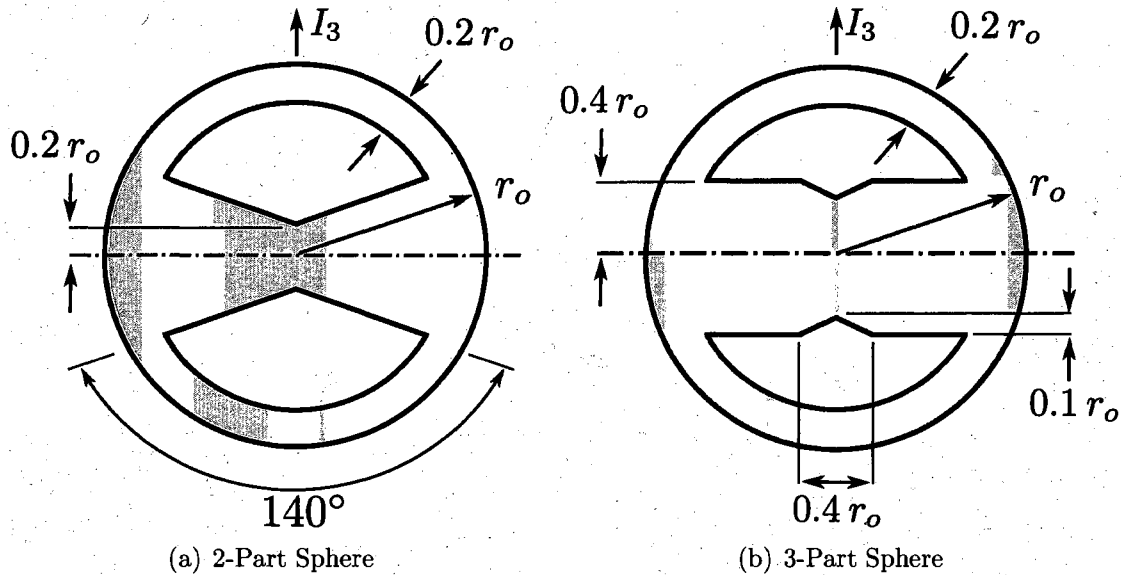


Figure 6.3: Preferred principal axis of inertia sphere simplified cross-section. The cross section view for the 2-part sphere is in the plane of the seam between the two hemispherical shells. The cross section view for the 3-part sphere is in a plane perpendicular to the plane of the two seams for each hemispherical shell.

and contains a number of features such as rounds in order to simplify the machining process. In addition, the two-part sphere contains features necessary for mating the two pieces together properly. The three-part sphere was machined using a lathe and does not contain the same machining or mating features. As a result, the two-part sphere deviates further from the ideal cross-sectional geometry than the three-part sphere.

Since, the moment of inertia difference ratio was designed to be on the order of 10% for preferred principal axis of inertia spheres, the five-wire pendulum is well-suited to measure the moment of inertia difference ratio. It should be noted that the moment of inertia tensor for a spinning spherical drag-free reference is important for two reasons:

1. Mass Attraction Calculations.
2. Characterization of the Spinning Sphere Dynamics.

Design Parameter	2-Part Sphere	3-Part Sphere
Radius, $r_o$	25.4 mm	25.4 mm
Inertia Ratio $(I_{p33} - I_{p22})/I_{p11}$	0.110	0.103
Material	Brass	Brass

Table 6.4: Preferred principal axis of inertia sphere design parameters.

To begin the measurement process, the preferred principal axis of inertia spheres must be marked. Two perpendicular great circles are drawn onto the surface of the spheres to be used as a coordinate reference. However, the intersection of the two great circles can not be placed at the center of the polhode paths as described in Section 5.4.2. Generating the polhode paths using the air bearing process as previously described is not possible with the current fabrication state of the spheres. Unlike commercially fabricated spheres, the two and three part spheres have not yet undergone a lapping and polishing procedure. As a result, the sphericity and surface finish of the spheres is not adequate for generating the torque free motion required for generating the polhode paths. Without the polhode path markings, the moment of inertia principal axis directions for the sphere are unknown. The full inertia tensor can therefore only be determined by measuring the instantaneous moment of inertia about a minimum of six different rotation directions as described in Section 4.3.2.

The torsion pendulum is designed to rotate about a single axis. As such the measurement object, i.e. the sphere, must be rotated to different orientations with respect to the rotation axis. The choice of these orientations must adequately map out the inertia ellipsoid. In order to select the orientations, recall Equation 4.2. Matrix  $A$  consists of the instantaneous directions of rotation associated with the inertia measurements. From Equation 4.2 it is seen that the selected rotation directions for the measurements must produce a well conditioned  $A$  matrix. In addition, for simplicity it is desired to rotate the sphere relative to the pendulum platform by simple angles. After calculating the condition number of the  $A$  matrix for different

rotation angles such as  $\pi/3$ ,  $\pi/4$ ,  $\pi/6$ , it is determined that the rotation angle of  $\pi/4$  should be used.

To position the sphere relative to the pendulum platform, a set of body axes are first established for the sphere, Figure 6.4, and the pendulum platform, Figure 6.5. On each of the fabricated preferred principal axis of inertia spheres, the seam is faintly visible as silver line resulting from the brazing material. One great circle is drawn in a plane parallel to the brazed seam. The origin for the sphere coordinate system is placed at the geometric center of the sphere. The  $\hat{x}$  axis is perpendicular to the surface of the sphere at the intersection of the two great circles. The  $\hat{y}$  axis is along the great circle drawn parallel to the seam. The  $\hat{z}$  axis completes the right-handed coordinate system. For the pendulum platform, the origin is located coincident with the designed mass center and rotation center. The  $\hat{i} - \hat{j}$  plane is located within the platform plane, with the  $\hat{i}$  axis pointing toward the vertical wire. The  $\hat{k}$  axis is vertical along the rotation axis, completing the right handed coordinate system.

Using the coordinate frames fixed to the body frame of the sphere, a set of Euler rotations are used to denote any orientation of the sphere relative to the pendulum platform. Denoting  $c$  and  $s$  for cosine and sine respectively, the Euler transformation matrices for the sphere frame,  $S$ , with respect to the five-wire pendulum frame,  $F$ , are:

$$T_{\phi}^{S/F} = \begin{bmatrix} 1 & 0 & 0 \\ 0 & c\phi & s\phi \\ 0 & -s\phi & c\phi \end{bmatrix}, \quad T_{\theta}^{S/F} = \begin{bmatrix} c\theta & 0 & -s\theta \\ 0 & 1 & 0 \\ s\theta & 0 & c\theta \end{bmatrix}, \quad T_{\psi}^{S/F} = \begin{bmatrix} c\psi & s\psi & 0 \\ -s\psi & c\psi & 0 \\ 0 & 0 & 1 \end{bmatrix} \quad (6.5)$$

where  $\phi$ ,  $\theta$ ,  $\psi$  denote a rotation about the sphere body fixed axes of  $\hat{x}$ ,  $\hat{y}$ ,  $\hat{z}$  respectively. Using the relations given in Equation 6.5, a  $\hat{z}, \hat{y}, \hat{x}$  transformation for example is given by:

$$\begin{bmatrix} \hat{x} \\ \hat{y} \\ \hat{z} \end{bmatrix} = T_{\phi}^{S/F} T_{\theta}^{S/F} T_{\psi}^{S/F} \begin{bmatrix} \hat{i} \\ \hat{j} \\ \hat{k} \end{bmatrix} = T_{\phi\theta\psi}^{S/F} \begin{bmatrix} \hat{i} \\ \hat{j} \\ \hat{k} \end{bmatrix} \quad (6.6)$$

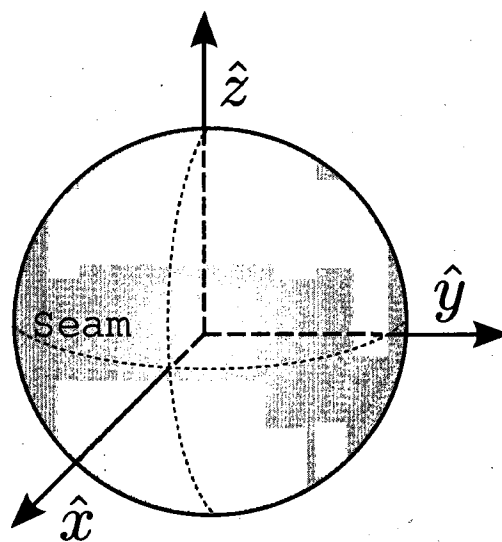


Figure 6.4: Sphere body coordinates.

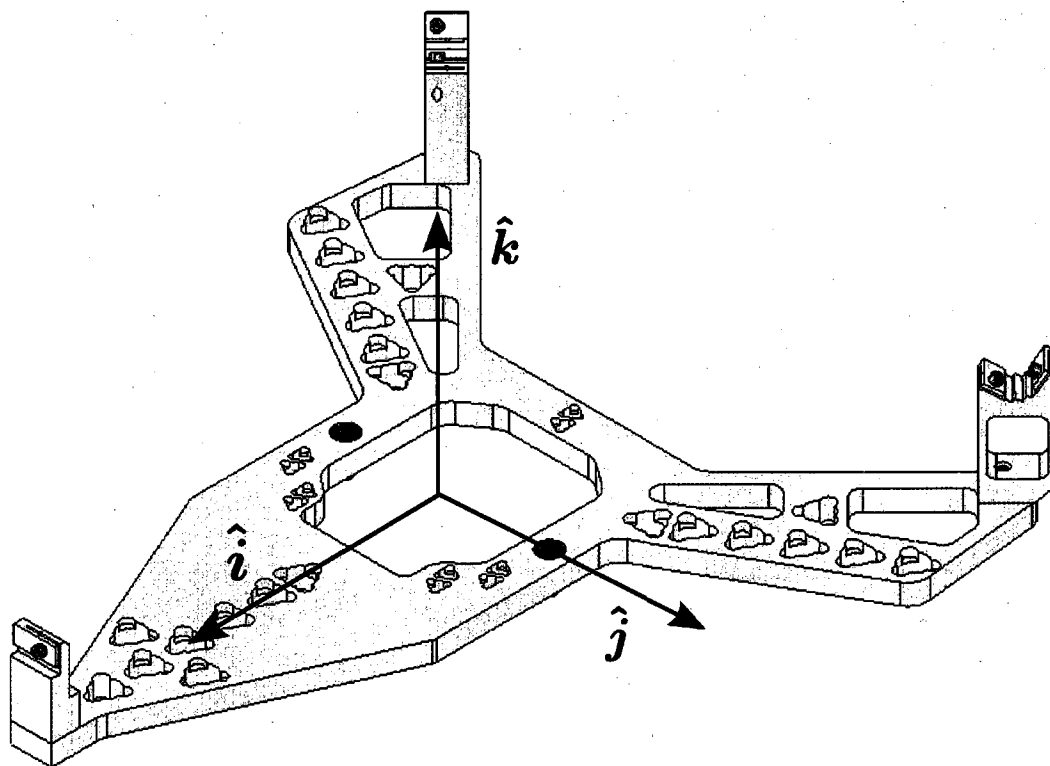


Figure 6.5: Pendulum platform coordinate system.



Yet, in order to determine the moment of inertia tensor for the sphere using Equation 4.2, the pendulum axis of rotation,  $\hat{k}$ , must be represented within the body frame of the sphere. Thus, for the  $\hat{z}, \hat{y}, \hat{x}$  transformation example one finds the representation of the  $\hat{k}$  axis within frame  $S$ :

$$\begin{bmatrix} \hat{i} \\ \hat{j} \\ \hat{k} \end{bmatrix} = \begin{bmatrix} T_{\phi\theta\psi}^{S/F} \end{bmatrix}^T \begin{bmatrix} \hat{x} \\ \hat{y} \\ \hat{z} \end{bmatrix} \quad (6.7)$$

For the preferred principal axis of inertia spheres, a set of nine measurement configurations was performed. The Euler rotation sequence for each configuration and the resulting  $\hat{k}$  measurement axis is presented in Table 6.5. Figure 6.6 shows a completed sphere with the great circles and markings for each of the nine orientation configurations. A two part sphere as positioned in orientation configuration 1 with the body frame of the sphere aligned with the pendulum frame is shown in Figure 6.7. For each of the measurement configurations, the natural frequency of oscillation is determined by applying the damped sinusoid curve fit routine described in Section 5.7 to the pendulum time response. The measurement data for the preferred principal axis of inertia spheres are listed in Appendix E, Table E.3 through Table E.7. By applying the least squares fit of the measured data, as outlined in Section 4.3.2, the inertia tensor in the body fixed coordinate system and the principal moments of inertia are determined. Table 6.6 lists the measured results for the preferred principal axis of inertia spheres.

As part of the measurement process, the eigenvectors of the measured inertia matrix are determined to produce the directions for the principal moments of inertia relative to the body-fixed coordinate system. Although the body frame may be somewhat arbitrarily defined, the information contained within the eigenvectors is quite valuable and additionally provides a cross-check on the measurement results. Recall the cross-sectional view of the preferred principal axis of inertia spheres in Figure 6.3. Clearly the spheres contain planes of geometric symmetry where the mass distribution is equally symmetric. Due to the symmetric mass distribution about the symmetry planes, the ellipsoid of inertia must possess the same plane of symmetry.

Config	Rotation Sequence				Measurement Axis				
1	No Rotation				$0\hat{x}$	+	$0\hat{y}$	+	$1\hat{z}$
2	$\phi =$	$\pi/2$			$0\hat{x}$	+	$1\hat{y}$	+	$0\hat{z}$
3	$\phi =$	$\pi/2$	$\psi =$	$\pi/2$	$1\hat{x}$	+	$0\hat{y}$	+	$0\hat{z}$
4	$\theta =$	$\pi/4$			$\frac{1}{\sqrt{2}}\hat{x}$	+	$0\hat{y}$	+	$\frac{1}{\sqrt{2}}\hat{z}$
5	$\theta =$	$-\pi/4$			$\frac{-1}{\sqrt{2}}\hat{x}$	+	$0\hat{y}$	+	$\frac{1}{\sqrt{2}}\hat{z}$
6	$\phi =$	$\pi/2$	$\psi =$	$\pi/4$	$\frac{1}{\sqrt{2}}\hat{x}$	+	$\frac{1}{\sqrt{2}}\hat{y}$	+	$0\hat{z}$
7	$\phi =$	$\pi/2$	$\psi =$	$-\pi/4$	$\frac{-1}{\sqrt{2}}\hat{x}$	+	$\frac{1}{\sqrt{2}}\hat{y}$	+	$0\hat{z}$
8	$\psi =$	$-\pi/2$	$\phi =$	$\pi/4$	$0\hat{x}$	+	$\frac{1}{\sqrt{2}}\hat{y}$	+	$\frac{1}{\sqrt{2}}\hat{z}$
9	$\psi =$	$-\pi/2$	$\phi =$	$-\pi/4$	$0\hat{x}$	+	$\frac{-1}{\sqrt{2}}\hat{y}$	+	$\frac{1}{\sqrt{2}}\hat{z}$

Table 6.5: Orientation configurations for sphere measurements.

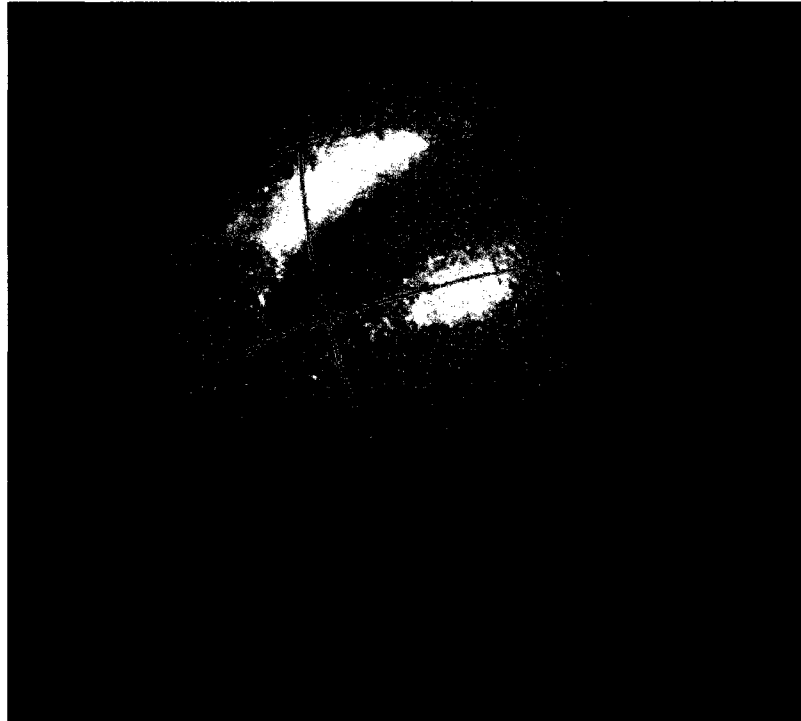


Figure 6.6: Preferred principal axis of inertia sphere marked with nine orientation configurations.

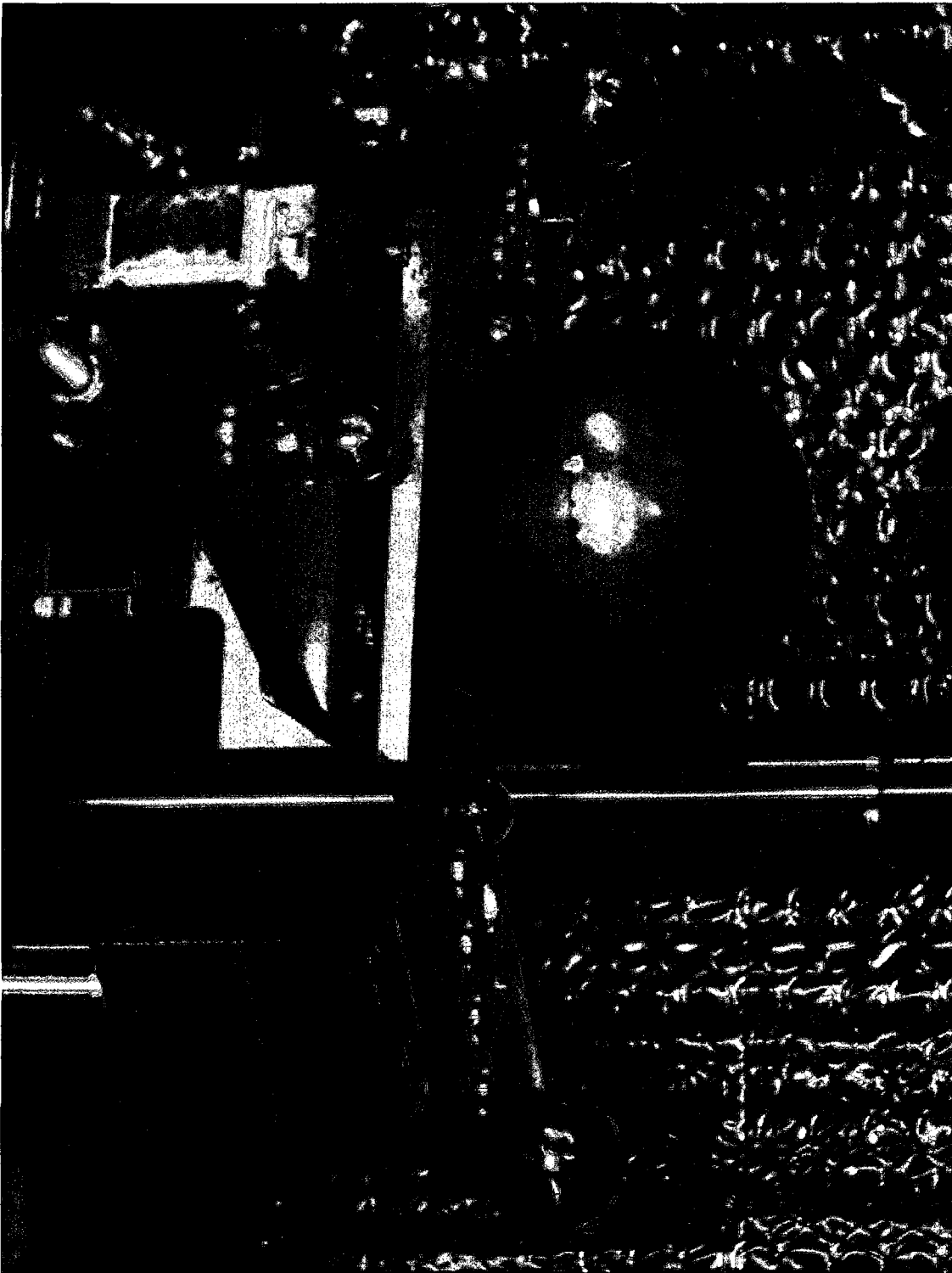


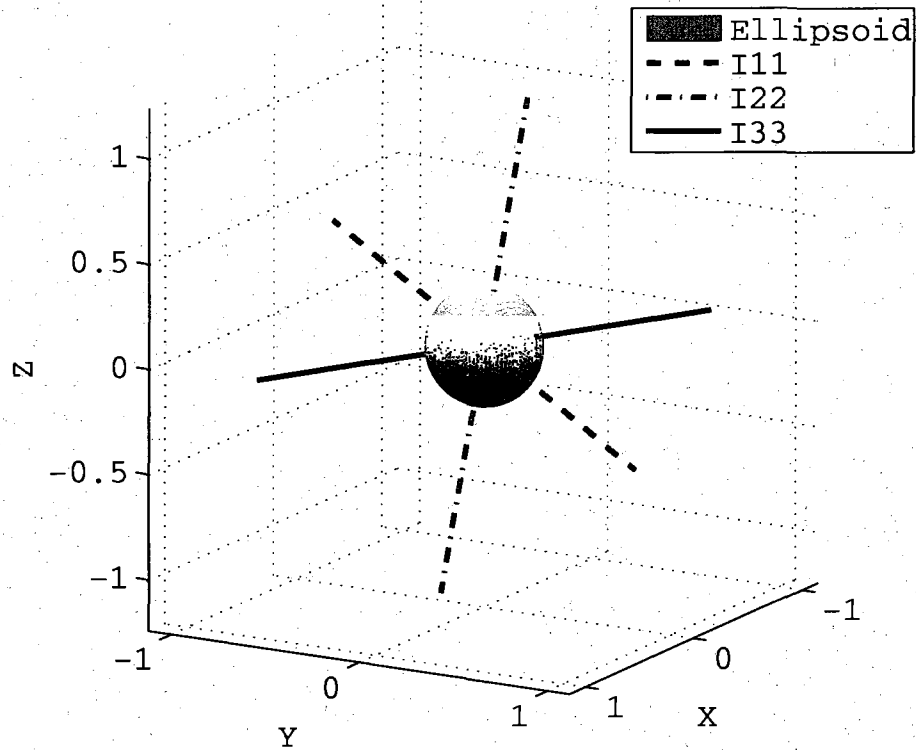
Figure 6.7: Preferred principal axis of inertia sphere on platform.

Sphere	$m_o$ kg	$[I_p]$ kg·mm <sup>2</sup>	$[\Sigma p]$ kg·mm <sup>2</sup> × 10 <sup>-2</sup>	$\sigma_{p_i}/I_{p_i}$ × 10 <sup>-4</sup>	$\frac{I_{p33} - I_{p22}}{I_{p11}}$
2-Part #1	0.4496	[111.45 113.53 124.87]	[5.2 6.6 1.0]	[4.69 5.82 0.79]	0.1018
2-Part #3	0.4443	[109.47 109.86 123.72]	[0.1 2.6 3.6]	[0.05 2.35 2.90]	0.1265
2-Part #4	0.4446	[109.59 110.17 123.03]	[2.9 0.6 4.1]	[2.68 0.53 3.31]	0.1174
2-Part #6	0.4489	[112.67 112.98 126.41]	[1.1 0.2 0.1]	[0.94 0.19 0.05]	0.1192
3-Part #8	0.4551	[113.15 113.60 126.50]	[1.7 0.1 1.1]	[1.50 0.12 0.89]	0.1141

Table 6.6: Measurement results for preferred principal axis of inertia spheres.

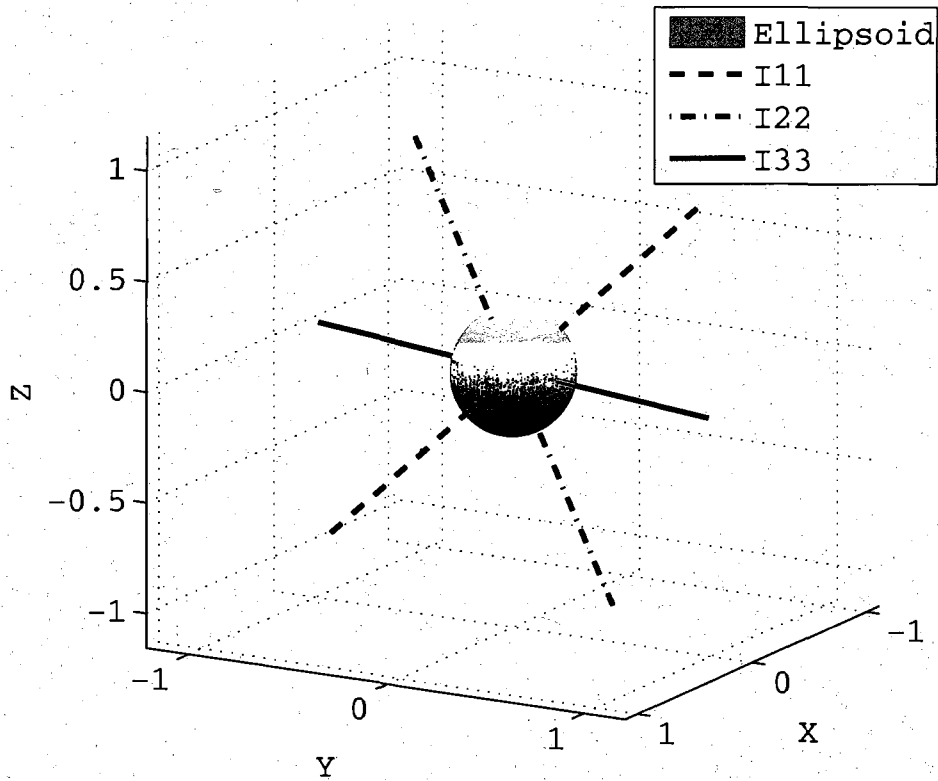
For the 2-part sphere, it is known that the direction of the maximum principal moment of inertia must be in the plane of the seam if the sphere was perfectly manufactured and of homogeneous density. Since the body fixed  $\hat{y}$  axis is drawn on top of the seam, the direction of the principal moment of inertia must be within the body  $x-y$  plane. The resulting eigenvectors for each of the 2-part sphere measurement data are shown in Figure 6.8 and Figure 6.11. As expected, the maximum moment of inertia direction has a nearly zero component along the body  $\hat{z}$  direction and thus is within the body  $x-y$  plane.

For a 3-part sphere of ideal geometry and of homogeneous density, it is known that the direction of the maximum principal moment of inertia must be in a plane that is perpendicular to the seams, or rather perpendicular to the  $x-y$  body frame. Figure 6.12, shows the results for the 3-part sphere principal axis directions. As expected, the direction for the maximum principal moment of inertia is primarily along the body  $\hat{z}$  axis.



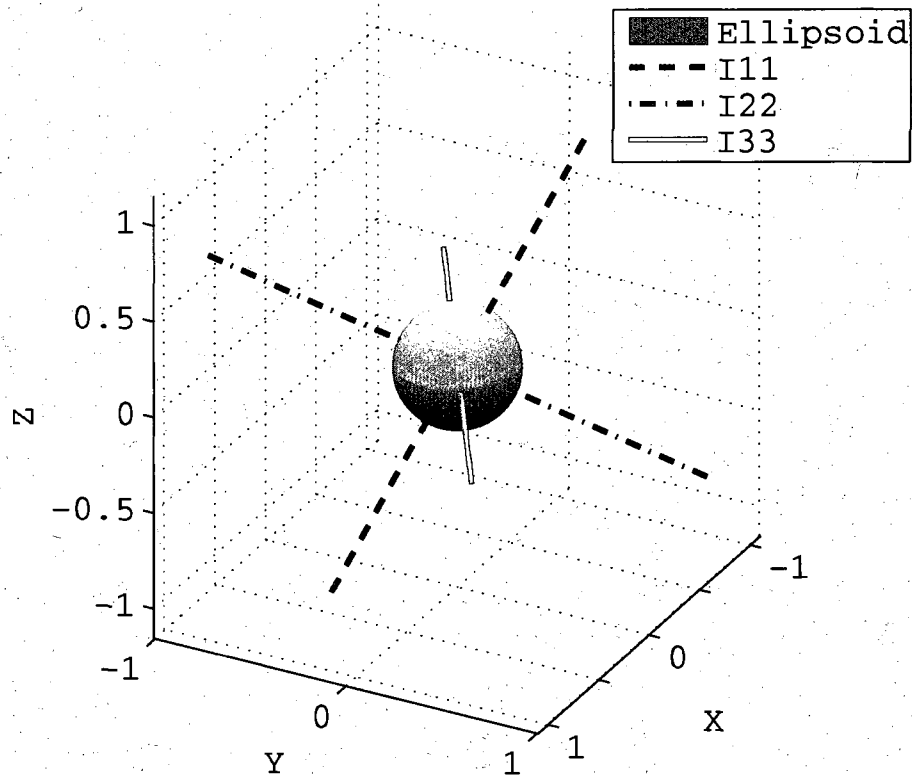
Sphere	$T^{P/B} = [\hat{e}_1, \hat{e}_2, \hat{e}_3]$ (Dimensionless)
2-Part #1	$\begin{bmatrix} 0.423 & 0.089 & -0.901 \\ 0.872 & 0.230 & 0.433 \\ -0.246 & 0.969 & -0.020 \end{bmatrix}$

Figure 6.8: Principal axis measurement data for 2-Part Sphere Number 1. The measured rotation matrix from the principal axis frame to the body fixed frame,  $T^{P/B}$ . The axis labels correspond to the directions of the body fixed frame and the axis values correspond to the eigenvectors.



Sphere	$T^{P/B} = [\hat{e}_1, \hat{e}_2, \hat{e}_3]$ (Dimensionless)
2-Part #3	$\begin{bmatrix} 0.861 & 0.408 & 0.304 \\ -0.262 & -0.156 & 0.952 \\ -0.436 & 0.900 & 0.028 \end{bmatrix}$

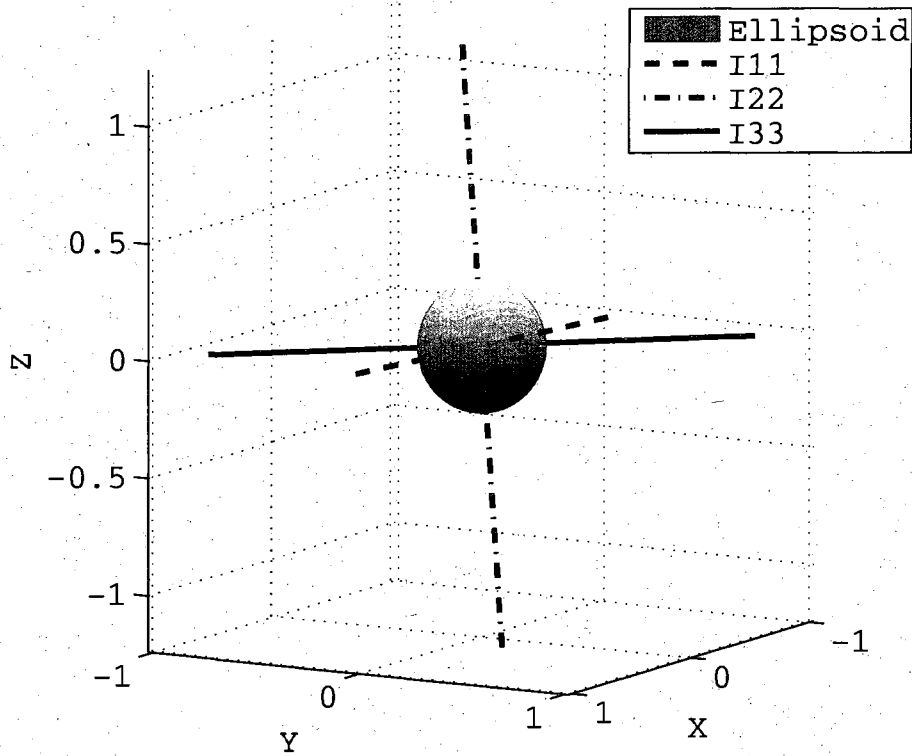
Figure 6.9: Principal axis measurement data for 2-Part Sphere Number 3. The measured rotation matrix from the principal axis frame to the body fixed frame,  $T^{P/B}$ . The axis labels correspond to the directions of the body fixed frame and the axis values correspond to the eigenvectors.



Sphere	$T^{P/B} = [\hat{e}_1, \hat{e}_2, \hat{e}_3]$ (Dimensionless)
2-Part #4	$\begin{bmatrix} -0.273 & 0.437 & 0.857 \\ 0.372 & -0.774 & 0.513 \\ 0.887 & 0.459 & 0.048 \end{bmatrix}$

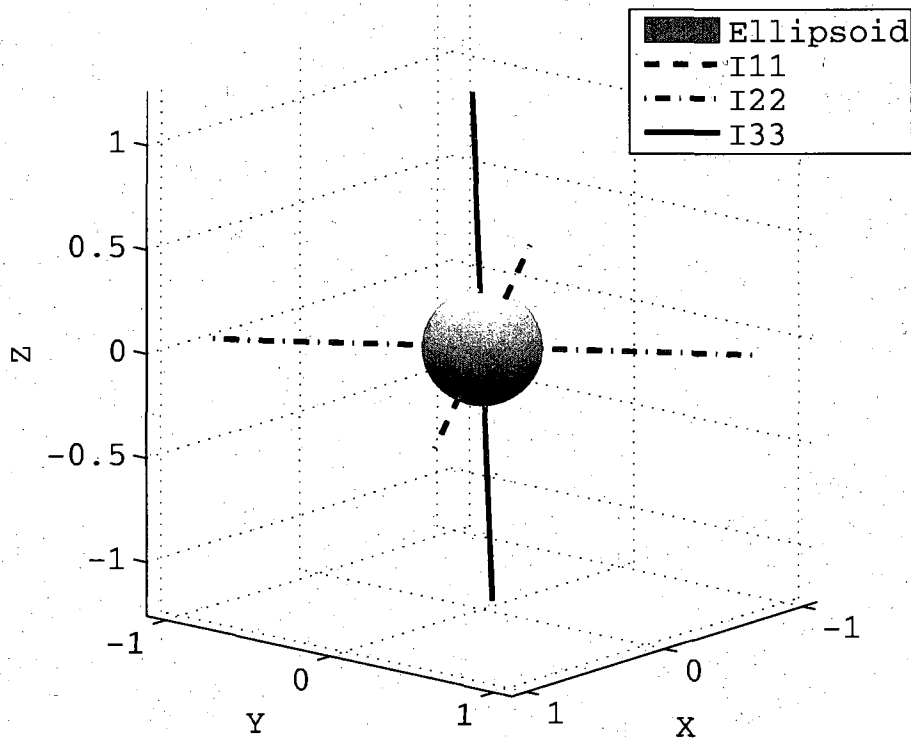
Figure 6.10: Principal axis measurement data for 2-Part Sphere Number 4. The measured rotation matrix from the principal axis frame to the body fixed frame,  $T^{P/B}$ . The axis labels correspond to the directions of the body fixed frame and the axis values correspond to the eigenvectors.





Sphere	$T^{P/B} = [\hat{e}_1, \hat{e}_2, \hat{e}_3]$ (Dimensionless)
2-Part #6	$\begin{bmatrix} 0.552 & -0.177 & 0.814 \\ 0.796 & -0.180 & -0.579 \\ 0.249 & 0.967 & 0.042 \end{bmatrix}$

Figure 6.11: Principal axis measurement data for 2-Part Sphere Number 6. The measured rotation matrix from the principal axis frame to the body fixed frame,  $T^{P/B}$ . The axis labels correspond to the directions of the body fixed frame and the axis values correspond to the eigenvectors.



Sphere	$T^{P/B} = [\hat{e}_1, \hat{e}_2, \hat{e}_3]$ (Dimensionless)
3-Part #8	$\begin{bmatrix} 0.861 & 0.497 & 0.111 \\ 0.496 & -0.867 & 0.044 \\ -0.118 & -0.017 & 0.993 \end{bmatrix}$

Figure 6.12: Principal axis measurement data for 3-Part Sphere Number 8. The measured rotation matrix from the principal axis frame to the body fixed frame,  $T^{P/B}$ . The axis labels correspond to the directions of the body fixed frame and the axis values correspond to the eigenvectors.

# Chapter 7

## Measurement Error

No measurement value is complete without a discussion on the associated measurement errors. Although the results discussed in Chapter 6 are for physical mass properties, the actual parameter measured is that of the pendulum oscillation frequency. The desired mass properties are then calculated from the frequency measurements. In practice it has been observed that the standard deviation on the inertia tensor components is typically a factor of three to five times worse than the observed standard deviation of the frequency measurements. As a result, this chapter will focus primarily on the error associated with a frequency measurement and the change in frequency as the fundamental error metric.

It is important to recognize that the error sources for a measurement or observation may be either systematic or random. The systematic errors cause the measurement value to differ from the true value by a fixed amount. The measurement value may be biased, for example due to the measurement method or due to improper calibration. A systematic error will affect the accuracy of a measurement. An improper calibration of the five-wire torsion pendulum will therefore affect the accuracy of the measurement. Random error affects the actual precision of a measurement result and is reflected in the standard deviation of the measurements. Random vibration of the five-wire torsion pendulum is an example of a random error, generating a deviation between sequential measurements. In the end, the repeatability of a measurement apparatus is the true indication of the precision.

For the five-wire torsion pendulum, the ability to calibrate the five-wire pendulum is the primary limitation to the absolute accuracy of the measurements performed. For the spherical measurement objects, the ability to mark the object with accurate orientation marks will also contribute to the final accuracy of the mass property measurements. Still, the calibration of the apparatus is the key limiting factor. Since it is assumed that systematic offsets such as calibration can be reduced with additional measurements or by using calibration measurement objects, this chapter will focus on the errors associated with the precision of repeated measurements. That is, the repeatability and corresponding effects to the standard deviation of the frequency measurements are of interest. A few of the error sources associated with the five-wire torsion pendulum as related to measurement of the torsional frequency are discussed in the following sections. A summary of the primary error sources and the approximate impact on the measured pendulum natural frequency is listed in Table 7.1.

## 7.1 Temperature

In order to establish the change in pendulum oscillation frequency due to temperature changes, we return to Equation 4.16 for the pendulum natural frequency:

$$\omega^2 = \frac{m_p}{I_p} \frac{gr^2}{L}$$

where  $m_p$  and  $I_p$  is the mass and instantaneous moment of inertia about the rotation axis for the pendulum respectively. The frequency of oscillation is therefore a function of the wire length,  $L$ , and the distance from the pendulum rotation center to the wire attach point,  $r$ . A reference natural frequency,  $\omega_o$ , is defined to be the natural frequency with the nominal wire length,  $L_o$ :

$$\omega_o^2 = \frac{m_p}{I_p} \frac{gr^2}{L_o} \tag{7.1}$$

Error Source	Without Countermeasures	Estimate with Countermeasures
Temperature (Theoretical)	$6 \times 10^{-6}$ Hz per 1 K	PID Provides 15 mK Stability
Temperature (Observed)	$1 \times 10^{-4}$ Hz per 1 K	$7.5 \times 10^{-5}$ Hz per 1 K PID Provides 15 mK Stability
Temperature & Platform Tilt	$6 \times 10^{-5}$ Hz per 5 mK	PID Provides 15 mK Stability
Vibration	$> 5 \times 10^{-5}$ Hz	1 to $0.5 \times 10^{-5}$ Hz
Foundation Tilt From Temperature	$4 \times 10^{-6}$ Hz	Not Observable
Air Currents	$> 1 \times 10^{-4}$ Hz	Not Observable
Nonlinearity (Theoretical)	$1 \times 10^{-4}$ Hz per 1 deg	Not Observable

Table 7.1: Estimated noise source contributions based on experimental observations.

Parameter	Value	Notes
$L_o$	11.43 cm	Design value: 4.5 inches
$r$	10.16 cm	Design value: 4.0 inches
$m_p$	124.08 g	Measured
$I_p$	398.3 kg·mm <sup>2</sup>	SolidWorks Estimate
$\alpha_L$	4.5e-6 K <sup>-1</sup>	Tungsten

Table 7.2: Pendulum properties.

The wire length will change due to fluctuations in temperature, resulting in a change in the oscillation frequency. The frequency due to a change in the nominal reference wire length  $\Delta L$  is therefore:

$$\omega_T^2 = \frac{m_p}{I_p} \frac{gr^2}{L_o + \Delta L} \quad (7.2)$$

Assuming a linear thermal expansion for the wires, the change in the original wire length,  $L_o$ , due to a temperature change  $\Delta T$  is related by:

$$\Delta L = \alpha_L \Delta T L_o \quad (7.3)$$

where  $\alpha_L$  is the linear thermal expansion coefficient for the material. Substituting the relationship for the change in wire length due to material thermal expansion into Equation 7.2, the resulting frequency due to a change in temperature becomes:

$$\omega_T^2 = \frac{m_p}{I_p} \frac{gr^2}{L_o(1 + \alpha_L \Delta T)} \quad (7.4)$$

Using Equation 7.4 and the values in Table 7.2 for the pendulum parameters, a 1 K change in temperature results in a theoretical frequency change  $|\omega_o - \omega_T|$  on the order of  $6 \times 10^{-6}$  Hz. In practice however, the variation in frequency for a change in temperature is larger than the theoretical calculation. Figure 7.1 shows the correlation between the pendulum natural frequency and temperature over a range of 0.55°C at 25°C. Although the simplified theoretical model for the pendulum frequency dependency on temperature was linear, the measured results indicate a clear nonlinear dependency. The deviation from the observed temperature dependency and

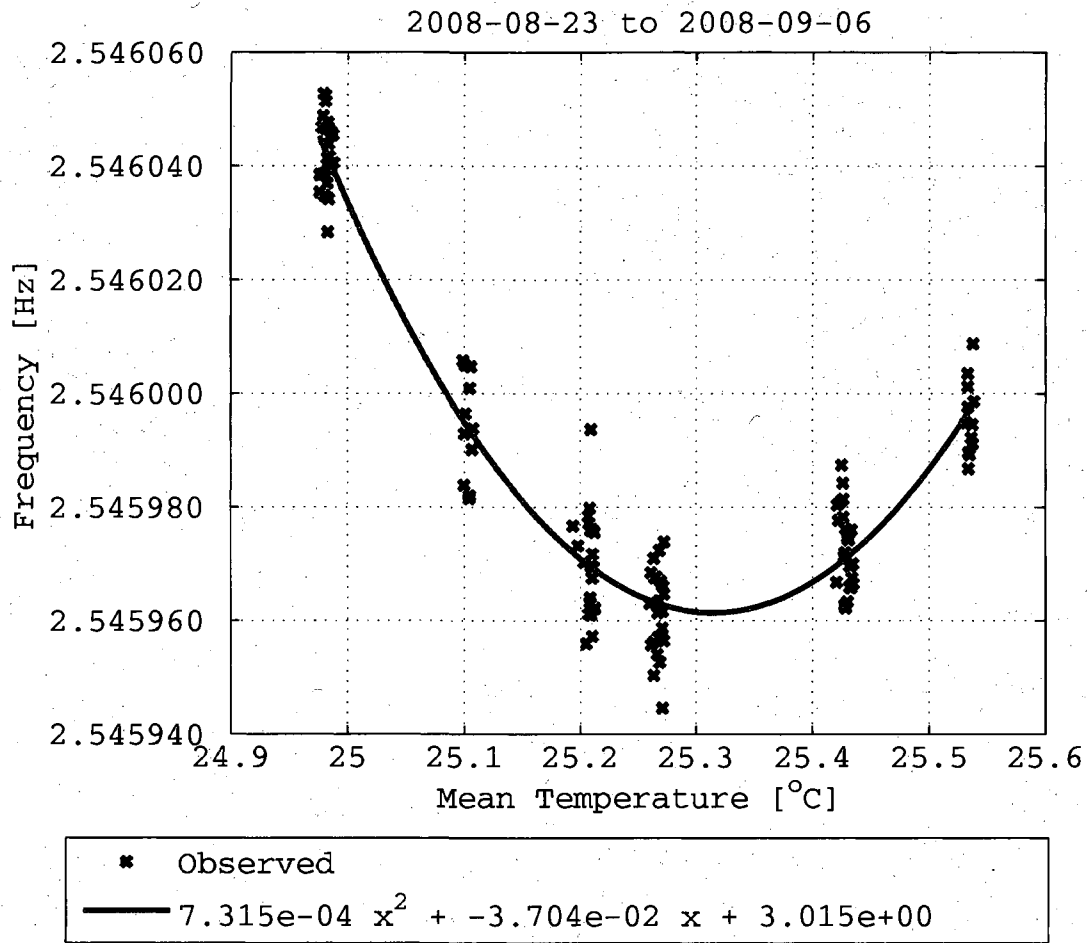


Figure 7.1: Pendulum temperature calibration prior to compensation.

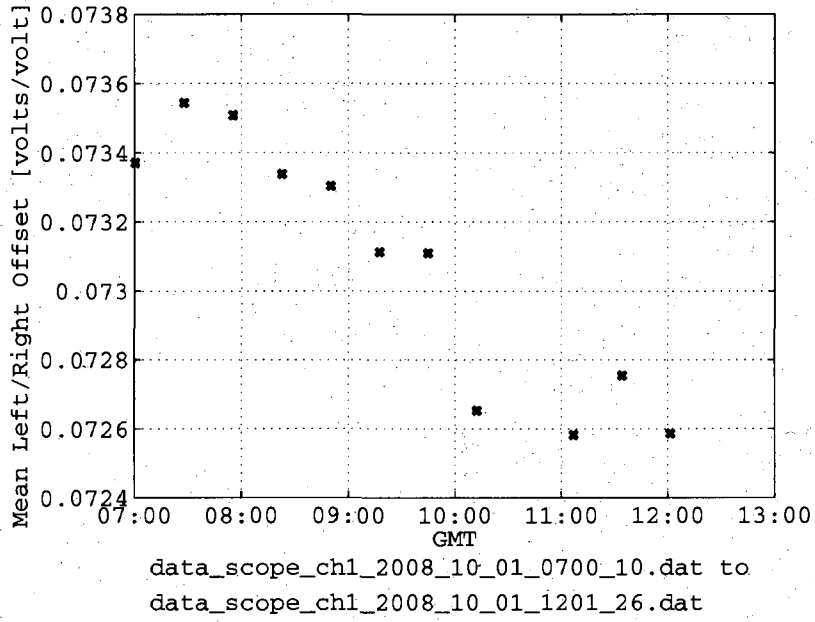
the theoretical calculation is a result of two primary factors:

- Pendulum wire geometry.
- Pendulum foundation stability.

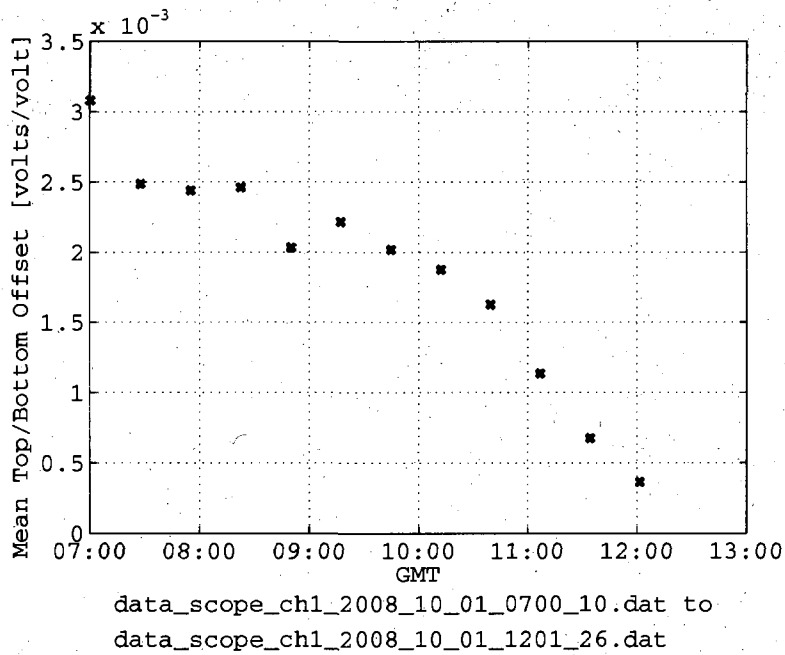
The expected frequency change was calculated due to a wire elongation from a change in temperature. The five-wire pendulum has different length wires. As such, there will be a different change in wire length for each wire due to a temperature change. Thus, not only is there a change in frequency due to a change in wire length from temperature effects, but there will also be a change in frequency associated with a change in the orientation of the pendulum rotation axis. Since the wire configuration is symmetric about one axis, the platform will tend to tilt around the pendulum  $\hat{j}$  axis (Figure 6.5). In addition, fluctuations in the other directions will exist as thermal equilibrium of each wire is achieved with the ambient air.

The change in orientation of the pendulum due to temperature is easily verified by monitoring the vertical and horizontal position signal produced by the quad photo diode sensor. Figure 7.2 for example shows the variation in the null position of the pendulum platform as measured by the quad photo sensor over the course of five hours. The air temperature surrounding the apparatus for the course of the five hour measurement is depicted in Figure 7.3 and shows about a 6 mK drift in temperature over the five-hour measurement period. As expected, a change in temperature results in an observed change in the vertical and horizontal null position on the quad photo diode sensor. In fact, the null top/bottom signal on the quad photo detector provides a more sensitive temperature measurement than the PtRTD used for temperature measurement. Figure 7.4 shows the temperature and quad photo sensor drift over a five-hour measurement. Both the left/right and top/bottom null position measurements from the quad sensor are related to temperature fluctuations. The top/bottom signal is also a true representation of the pendulum rise in the direction of the vertical wire and the left/right signal is a representation of a pendulum rotation due to the mismatch in the wire elongation between the symmetric angled wire pairs. Thus the relationship between the pendulum frequency and the quad sensor top/bottom signal is used to gain an estimate of the systematic change in pendulum





(a) Left/Right



(b) Top/Bottom

Figure 7.2: Pendulum platform null position change due to temperature.

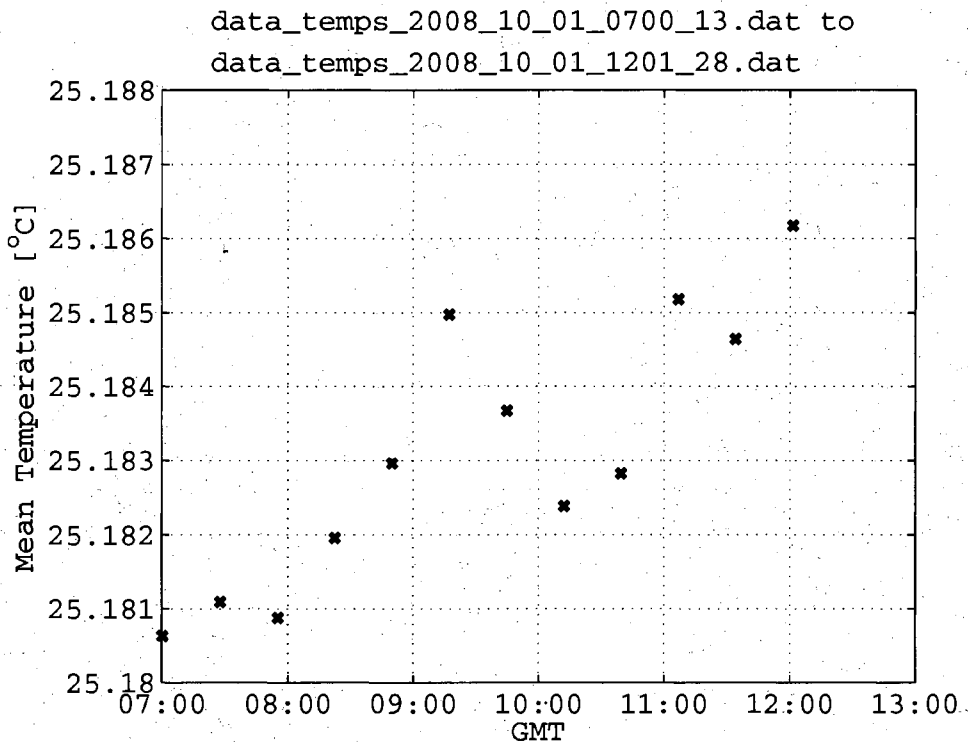


Figure 7.3: Temperature drift for Figure 7.2

rotation frequency due to a combined temperature change and a change in pendulum tilt. The correlation between frequency and the quad sensor top/bottom signal is depicted in Figure 7.5 and Figure 7.6. The actual relationship depends on the loading configuration of the pendulum platform and the temperature stability. Figure 7.5 shows the relationship over a five hour run for a symmetrically loaded pendulum using the calibration spheres in the fourth hole set from the center. The temperature for the measurement exhibited a steady drift over the range of 12 mK which equates to approximately  $2.6 \times 10^{-5}$  Hz for a 5 mK change. Figure 7.6 shows the relationship between three nightly runs and the top/bottom signal where the temperature was within a standard deviation of 3 mK over each of the five-hour measurement runs. The variation in mean temperature between the three different runs was within 5 mK, which was within the limitations of the sensor. The same asymmetric loading configuration was used for each measurement. The results in Figure 7.6 indicate a

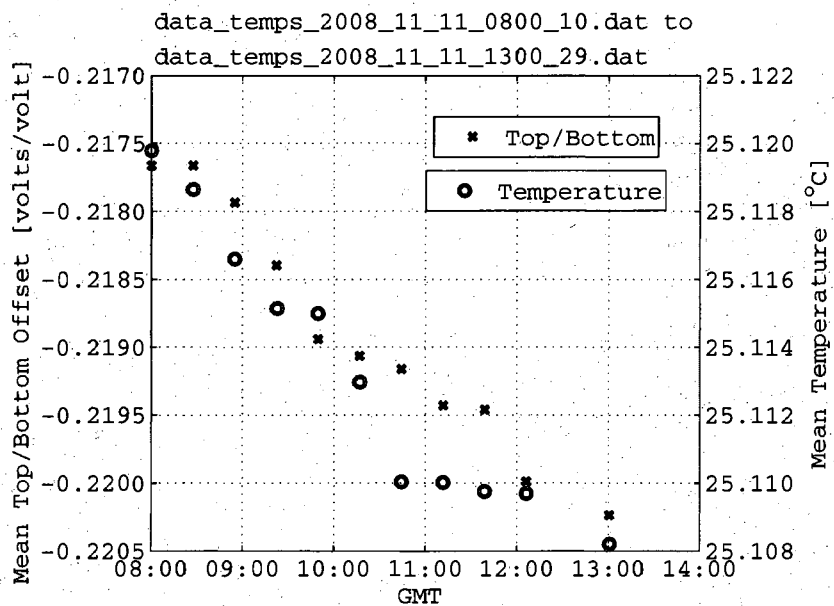


Figure 7.4: Quad sensor top/bottom null position change due to temperature.

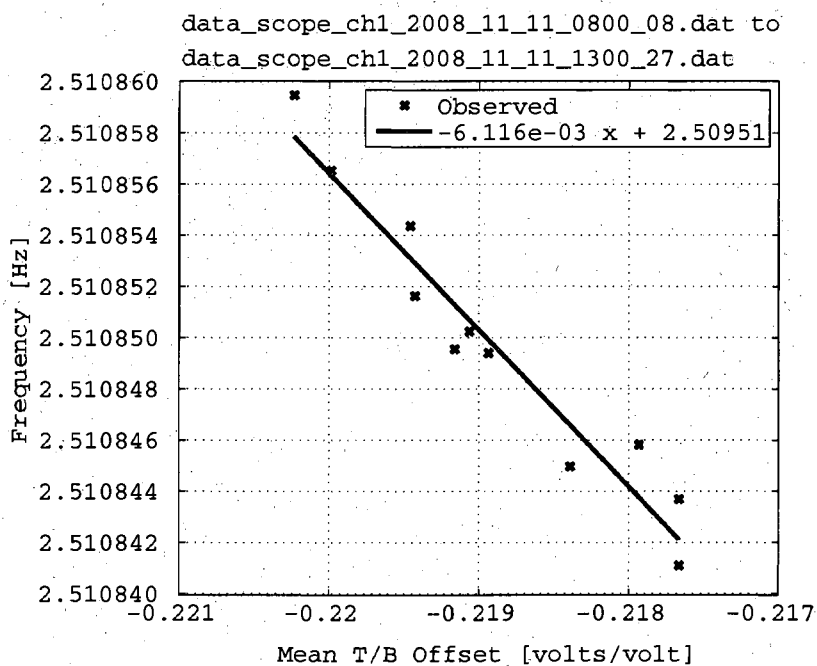


Figure 7.5: Pendulum frequency vs. null top/bottom position. Symmetric loading.

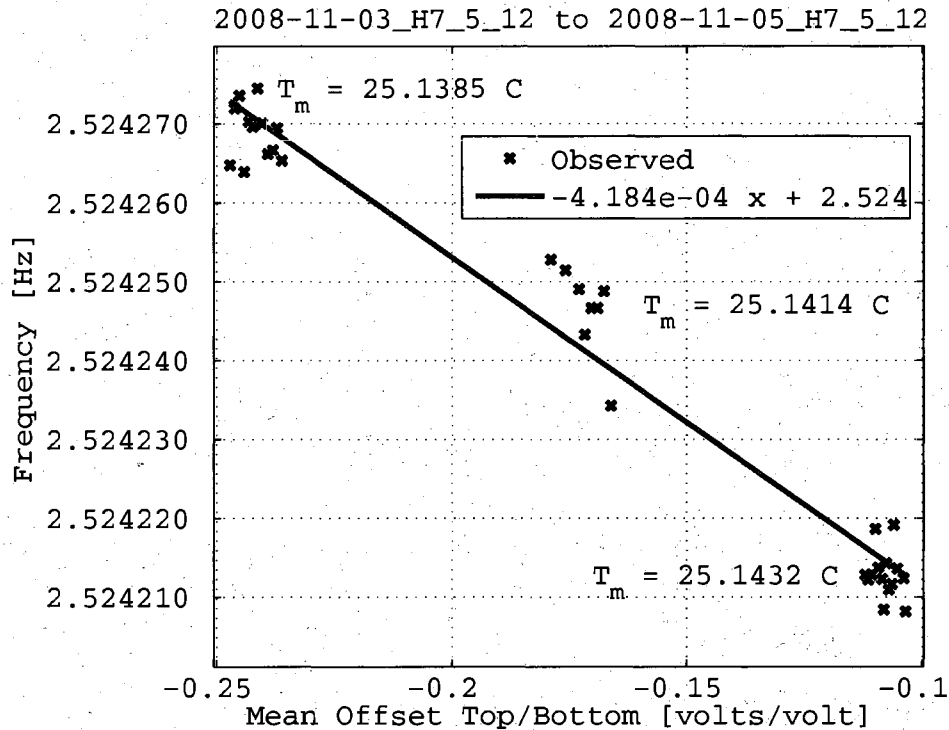


Figure 7.6: Pendulum frequency vs. null top/bottom position. Asymmetric pendulum loading.

$6 \times 10^{-5}$  Hz frequency change for a temperature change of approximately 5 mK.

In addition to the pendulum wire geometry, the stability of the pendulum foundation and the corresponding temperature dependency contributes to the pendulum frequency variation. The pendulum foundation stability depends on both the stability of the actual pendulum wire attach foundation as well as the optics table on which the pendulum is located. For example, a change in the laboratory temperature was observed to change the level of the optics table. In addition, the pendulum wire attach foundation optics plate is separated from the optics table through vibration isolation mounts, which are further described in Section 7.2. The temperature stability of the isolation mounts affects the stability of the platform level. In practice, it was found that by maintaining the temperature of the vibration mounts, the standard deviation in frequency measurements could be reduced by approximately  $4 \times 10^{-6}$  Hz.

Device	Model	Description
Power Supply	HP 6038A	Max Voltage Set to 60 V Max Current Set to 2 A
Heater Strips	HK5173R110L12	Polyimide Thermofoil™ 110 Ω, 12 inch x 2 inch
Temperature Sensor	Omega 747	Thermistor

Table 7.3: PID temperature controller hardware.

### Temperature Control

In order to reduce air temperature fluctuations at the pendulum, a simple insulated chamber is used to enclose the five-wire apparatus. The main outer chamber consists of 5 cm thick polystyrene. Within the outer chamber is the optics plate on which the five-wire apparatus is constructed. An inner chamber on top of the optics plate composed of Reflectix™, a reflective bubble wrap insulation, encloses the pendulum and optics.

To further reduce the platform oscillation frequency temperature dependency, a PID temperature controller was placed within the chamber containing the five-wire pendulum. The PID controller was implemented using a power supply and two Minco flexible heater strips attached to a 45 cm by 75 cm by 0.5 cm aluminum plate. The PID controller sends a current control signal to the power supply attached to the Minco heater strips. Additional details of the hardware implementation is found in Table 7.3. For the PID software implementation, the standard form of a PID controller output  $u(t)$  was used:

$$u(t) = K_p \left( e(t) + \frac{1}{T_i} \int_0^t e(\tau) d\tau + T_d \frac{de(t)}{dt} \right) \quad (7.5)$$

where  $e(t)$  is the error from the desired set value and the actual measured value. The proportional gain,  $K_p$ , derivative time,  $T_d$ , and integral time,  $T_i$ , PID controller parameters are found in Table 7.4. The PID controller was implemented using a sample and hold technique, with a cycle time much less than the system response time.

Parameter		Value	Units
Proportional Gain	$K_p$	5.0	dimensionless
Derivative Time	$T_d$	200.0	seconds
Integral Time	$T_i$	1250.0	seconds
Cycle time	dt	4.0	seconds

Table 7.4: PID temperature controller gains. See Eq. 7.5

The PID parameters were obtained using a manual tuning process. The proportional gain was first increased with the other parameters set to zero until instability was observed. The proportional gain was then reduced by at least a half. The derivative term was then adjusted until instability was observed and then reduced. Finally, the integral term was adjusted for a reasonable time response without excessive overshoot. The time response of the PID temperature controller using the determined control gains is depicted in Figure 7.7.

Before starting pendulum frequency measurements, the PID temperature controller is started. The system has a short temperature time constant on the order of minutes which is associated with the wires and a longer temperature time constant on the order of several hours, which is associated with the support foundation and measurement optics/fixtures. As a result, the system is maintained at a constant temperature for about 1 day prior to making measurements. Even though pendulum oscillation frequency measurements are not conducted during the PID preheat, the pendulum is pulsed at regular intervals at the same rate the pendulum would be pulsed during measurement runs. Through experimentation, it was found that starting the oscillation of the pendulum after an inactive period generates a disturbance to the stagnant air, causing a 15 mK or more change in temperature of the chamber. Thus, by continuously pulsing the pendulum, the conditions inside the chamber are consistent during measurements.

As shown previously in Figure 7.1 the temperature calibration for the pendulum indicated a quadratic dependency, which is contrary to the theoretical linear relationship. It was found through experimentation, that the exhibited quadratic relationship was due to motion of the pendulum support frame from temperature fluctuations.

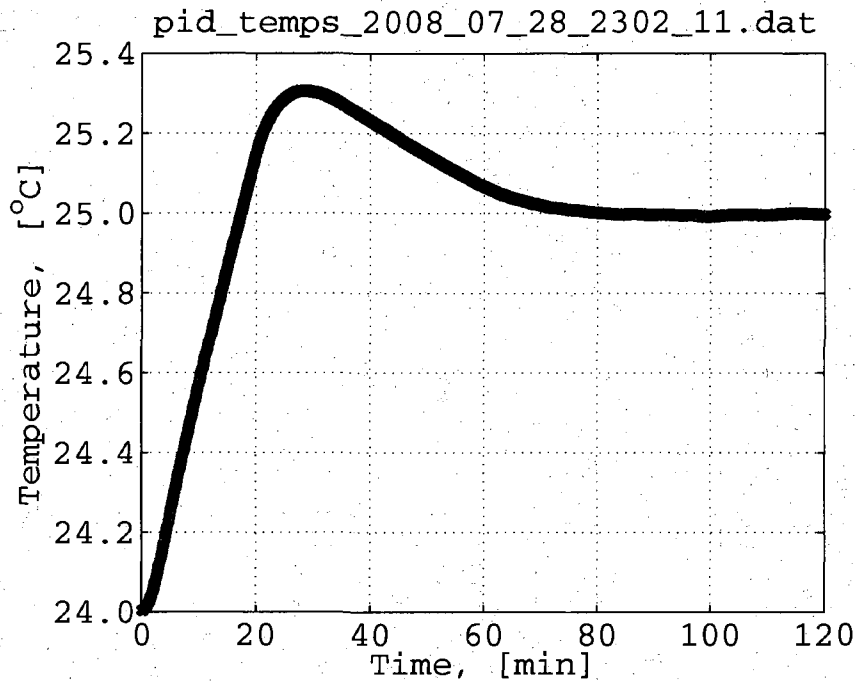
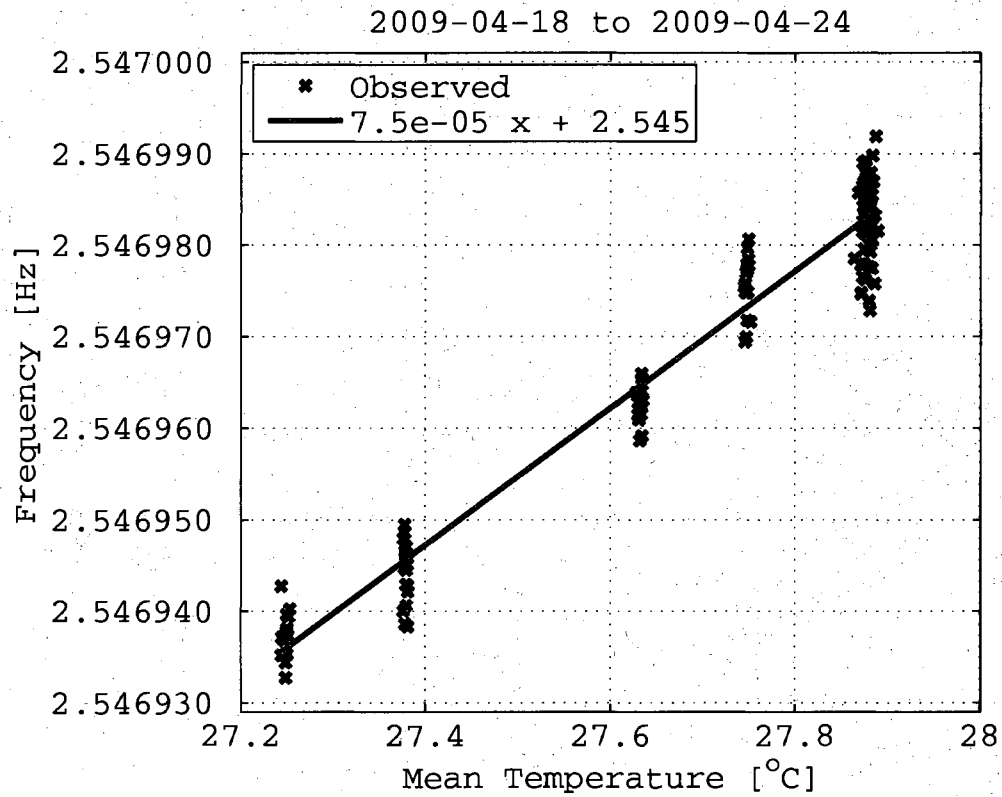


Figure 7.7: PID temperature controller step input time response.

Specifically, the optics plate and the rubber vibration isolation pads below the optics plate (described in Section 7.2), were the root cause. Thus, in addition to maintaining the temperature of the surrounding air with the PID controller, the temperature stability of the supporting foundation structure is also required. The heat input to the system via the PID controller must therefore be isolated from the optics plate containing the experiment and supporting structure. The aluminum plate with the heater strips is isolated from the optics plate by placing the heater plate onto a set of thermally non-conductive pads. Figure 7.8, shows the final temperature correlation for the pendulum after implementing the PID controller and taking care to reduce temperature fluctuations of the optics plate and supporting structure. The final correlation between the pendulum oscillation frequency and temperature results in the expected theoretical linear relationship. The expected linear relationship shown in Figure 7.8, is primarily a result of maintaining the temperature stability of the supporting structure.



Temperature [°C]	$\sigma$ $\times 10^{-3}$ [°C]	Frequency [Hz]	$\sigma$ $\times 10^{-6}$ [Hz]
27.248	2.9	2.546 937	2.6
27.378	1.5	2.546 944	3.3
27.632	2.2	2.546 962	2.2
27.748	1.7	2.546 976	3.3
27.878	4.6	2.546 983	4.0

Figure 7.8: Pendulum temperature calibration results using PID controller. The frequency measurements are for the combined pendulum platform with sphere fixture, 3/8 inch calibration sphere in hole set 1, and the 3/4 inch trim mass spheres in hole set 6.



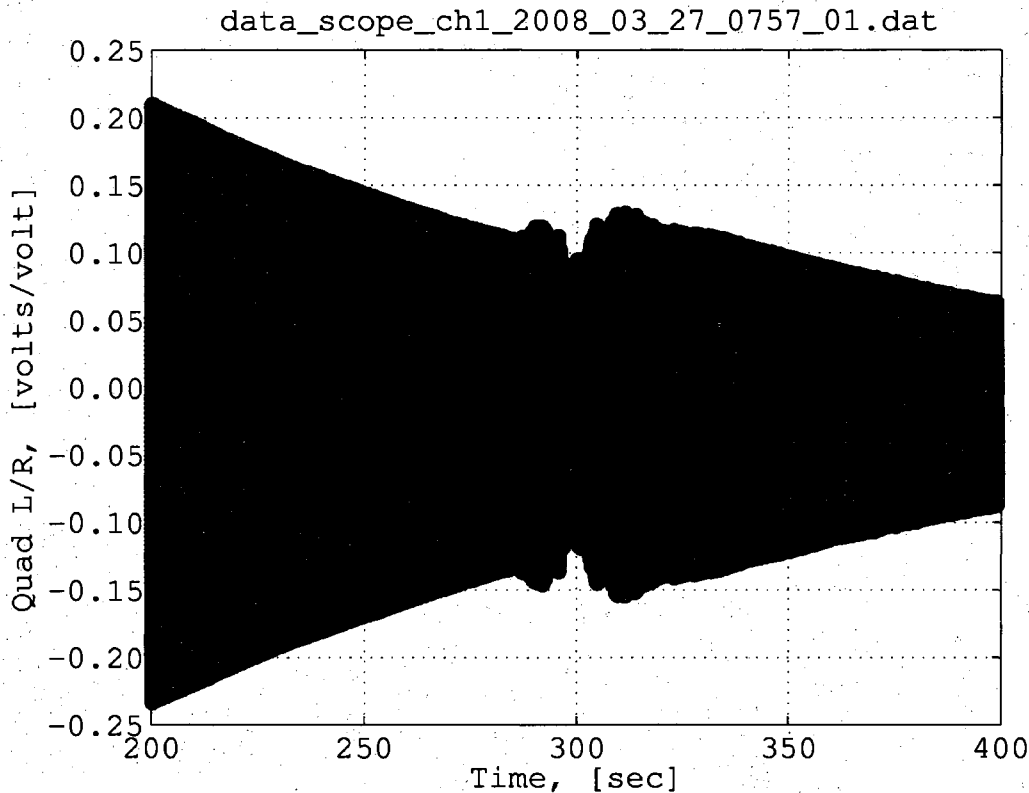


Figure 7.9: Observed earthquake in measurement data.

## 7.2 Vibrational Disturbances

Random vibrations at the pendulum foundation due to seismic disturbances and human activity cause the pendulum to oscillate. As described in Section 5.7, the pendulum frequency is measured by applying a nonlinear curve fit to the expected damped sinusoidal response. If the pendulum response does not match the expected damped sinusoidal response, due to a disturbance in the phase or amplitude of the signal, then the curve fitting procedure will be inconsistent. Disturbances to the pendulum response via random vibrations therefore limit the accuracy of the frequency measurement procedure. For a sense of the pendulum sensitivity to ground vibrations, consider the results from two lab measurements. Figure 7.9, shows for example the effect on the measurement data from a magnitude 3.2 earthquake near Antioch,

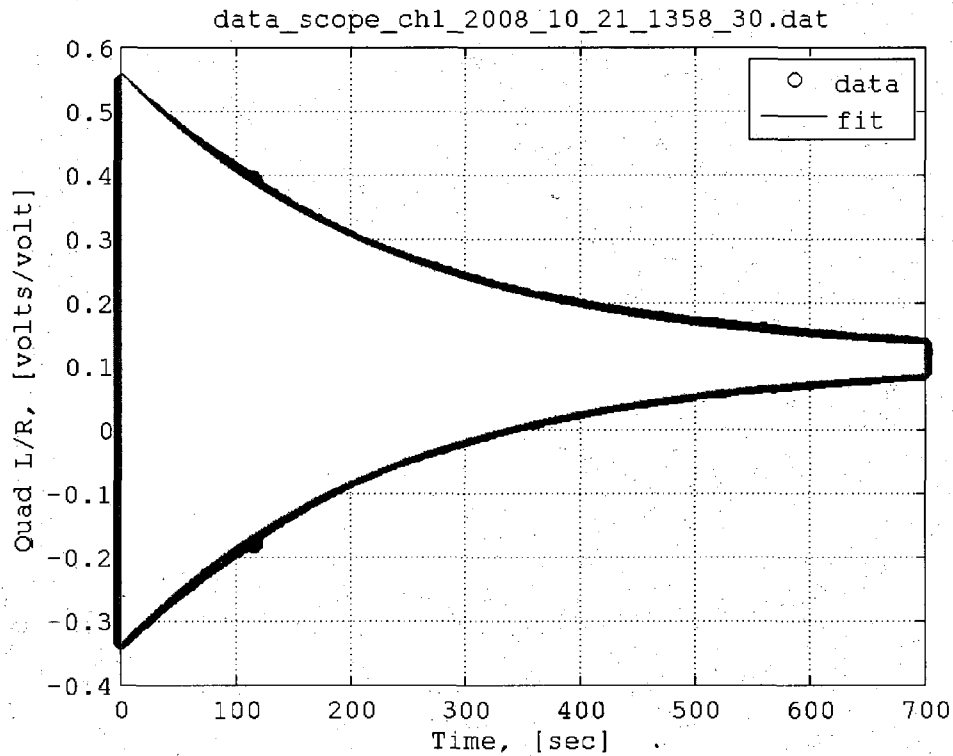


Figure 7.10: Observed disturbance in measurement data.

CA, USGS event nc51199149. The pendulum response clearly shows the presence of the earthquake induced ground vibrations for an epicenter about 100 km away from the Stanford laboratory. More frequent disturbances to the pendulum are impulsive shocks as a result of hallway lab doors slamming shut. Figure 7.10 shows a slight disturbance to the pendulum response about 120 seconds into a data run. The disturbance is thought to be the effect of a stairwell door down the hallway slamming shut. Processing of the raw data containing the disturbance generated a frequency measurement which was more than  $1 \times 10^{-4}$  Hz different than the other measurements from the same data acquisition run containing measurements with a standard deviation of  $1 \times 10^{-5}$  Hz.

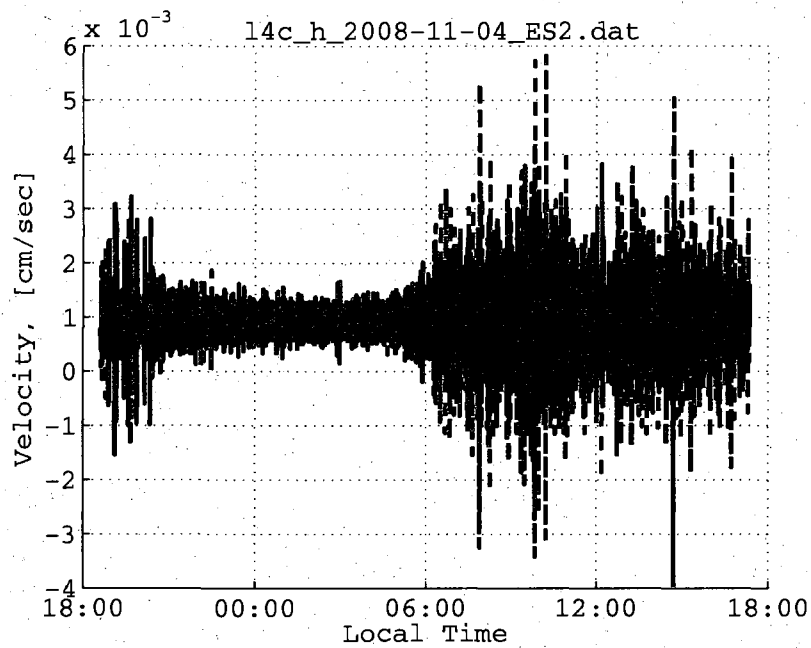
### **Pendulum Design for Vibration Environment**

Proper design is the key to minimizing the susceptibility to random vibration. During the initial design for the five-wire apparatus, the natural frequency of oscillation for the pendulum was selected to be below the existing vibrational noise sources. Before the five-wire pendulum was fabricated, the vibrational noise floor of the table to be used was recorded using a Mark Products L4C seismometer. Figure 7.11 and Figure 7.12 shows the seismic horizontal and vertical noise floor respectively of a granite table located within Stanford's End Station II lab space.

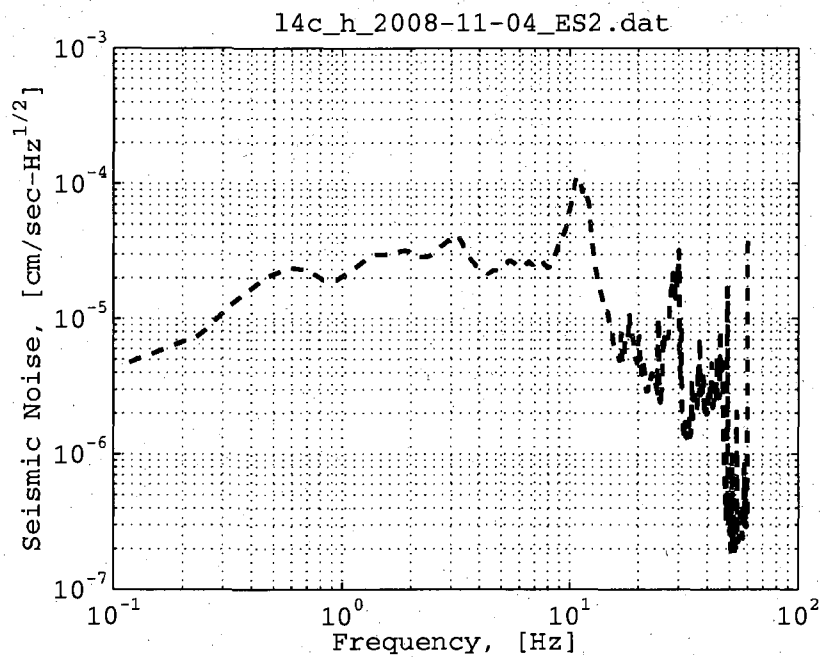
When selecting the natural frequency of oscillation for the pendulum, the highest frequency below the noise sources in the amplitude spectral density noise plot is selected for the pendulum natural frequency. The pendulum frequency is easily trimmed to a lower value after the platform fabrication by the addition of mass distant from the rotation center. From Figure 7.11 and Figure 7.12, it is seen that the vibrational noise source for the granite table has a peak around 10 Hz and 30 Hz in the horizontal and vertical directions respectively. As a result the target design natural frequency for the five-wire pendulum was chosen to be no greater than 3 Hz. Due to the required wire geometry for the five-wire pendulum, a higher pendulum natural frequency results in a more compact and smaller apparatus. As the equivalent pendulum wire length is increased, the long wires on the five-wire pendulum can become very long. For example, with an equivalent pendulum wire length of 11.4 cm for a pendulum natural frequency of almost 3 Hz, the long wires on the five-wire pendulum are nearly 30.5 cm long. As a result, the targeted pendulum natural frequency for the five-wire pendulum was designed to be on the order of 3 Hz.

### **Challenges with Vibrational Disturbances**

A granite table in Stanford's End Station II was originally planned as a work surface for the five-wire pendulum. Unfortunately, due to lab space availability and limited budget constraints, the experiment had to be moved to an alternate location, consisting of an optics table with standard non-vibration isolation legs. This alternate optics table is located within the newly constructed Astrophysics building at Stanford.

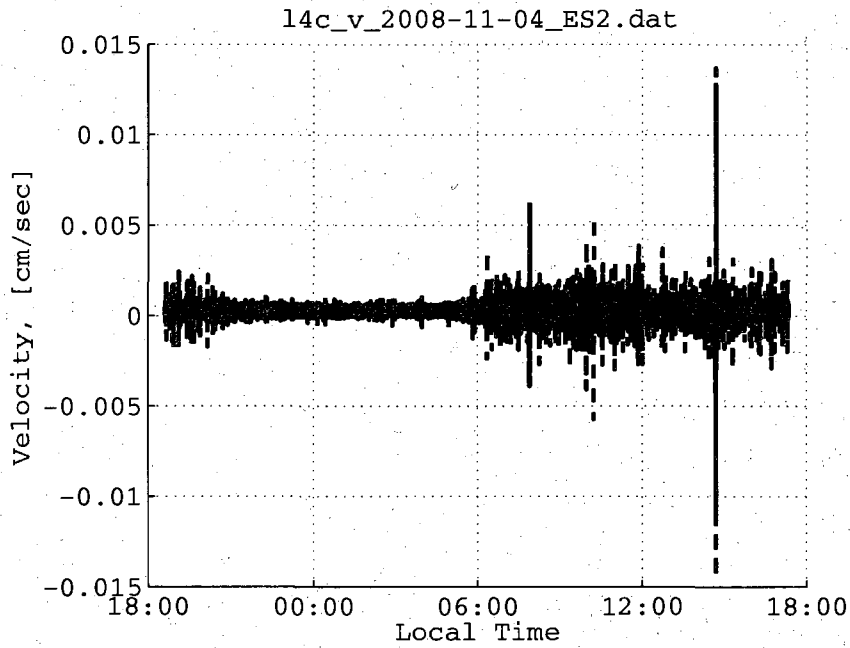


(a) Time history

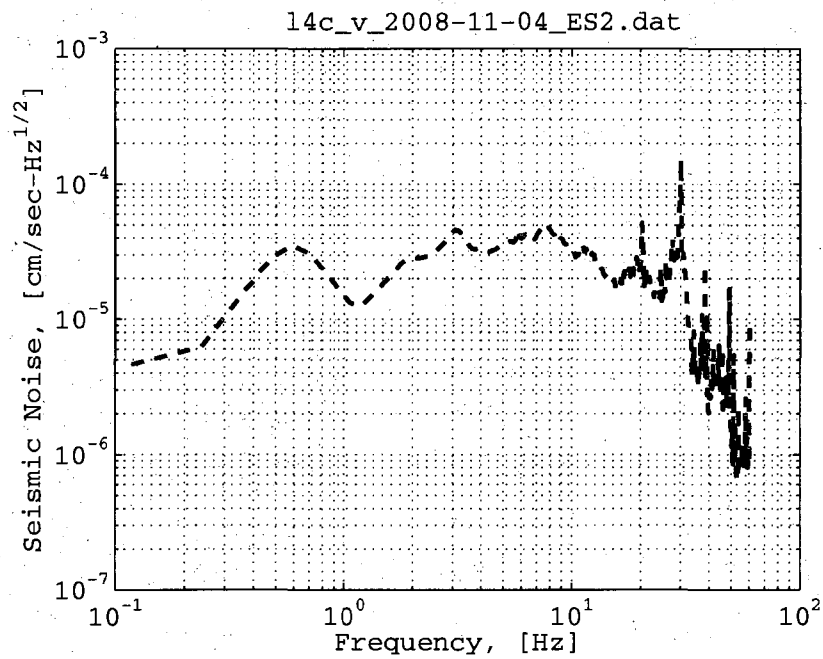


(b) Root mean square spectral density

Figure 7.11: Vibration noise floor of granite table, horizontal direction.



(a) Time history



(b) Root mean square spectral density

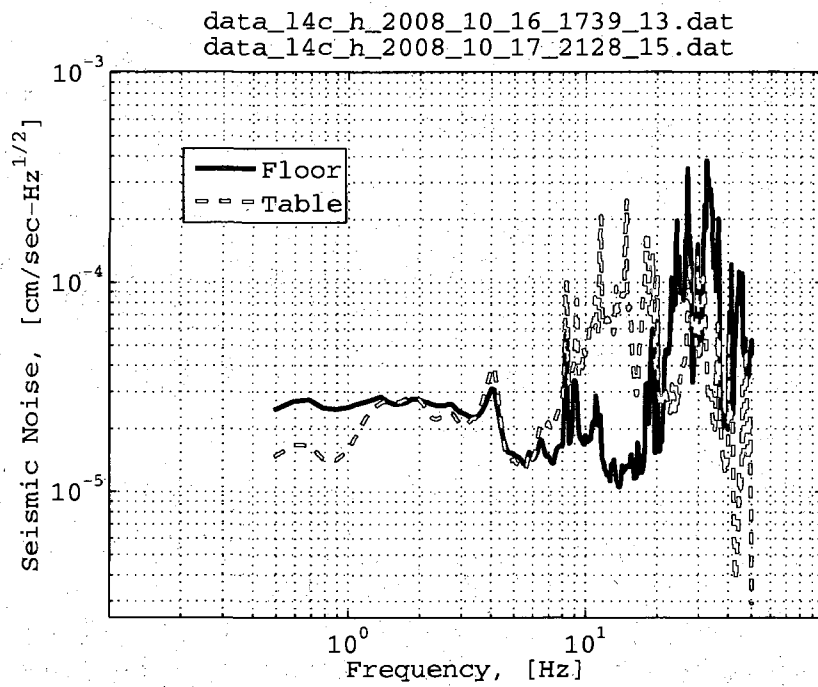
Figure 7.12: Vibration noise floor of granite table, vertical direction.

The vibration noise floor of the Astrophysics building and the optics table were found to be significantly different than the originally planned location. Figure 7.13 shows for example the vibrational characteristics of the lab floor and the optics table in the newly constructed Astrophysics building basement. The vibrational spectrum for the floor and optics table in the Astrophysics building indicates a much higher vibration level above approximately 6 Hz. These high frequency vibrations in the building are produced by the building air handler system and are slightly reduced when the outside air temperature does not exceed approximately 18°C over the course of a day. The lab in which the measurements were taken is located on the basement level of the Astrophysics building and below this level is the sub-basement. In the building the air handler system is attached directly to the cement ceiling, which is effectively the floor to the level directly above. As a result, vibrations from the air handler system of the lab below are transferred to the floor of the lab above. For comparison, refer to Figure 7.14, for the vibration characteristics of the floor in an Astrophysics building lab located on the bottom level. The spectrum in Figure 7.14 exhibits the expected high frequency roll-off characteristics.

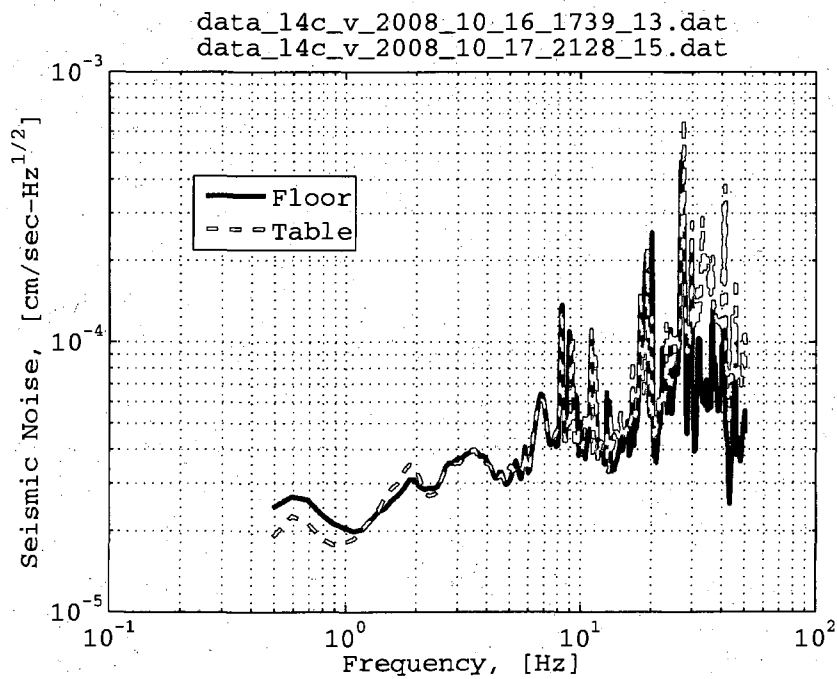
After the actual construction and assembly of the five-wire pendulum on the optics table in the Astrophysics building, it was found that the vibration noise level was too high for running the pendulum. First, the 3.1 Hz pendulum natural frequency was too high to avoid interference from the vibrational disturbance peak at 4 Hz. In addition, the translational modes of the pendulum, which are much higher than the pendulum torsional natural frequency, are magnified by the high frequency noise observed in the spectrum. As a result, the pendulum response was not a clean damped sinusoid. Due to the presence of the high vibration levels in the laboratory, a passive isolation system had to be designed.

### **Passive Vibration Isolation**

With any signal measurement, it is desired to have a large signal to noise ratio. For vibrational disturbances to the pendulum, the signal to noise ratio can be easily increased by pulsing the pendulum at larger amplitudes. Yet, for the five-wire pendulum a trade off is made between the initial induced amplitude of rotation and

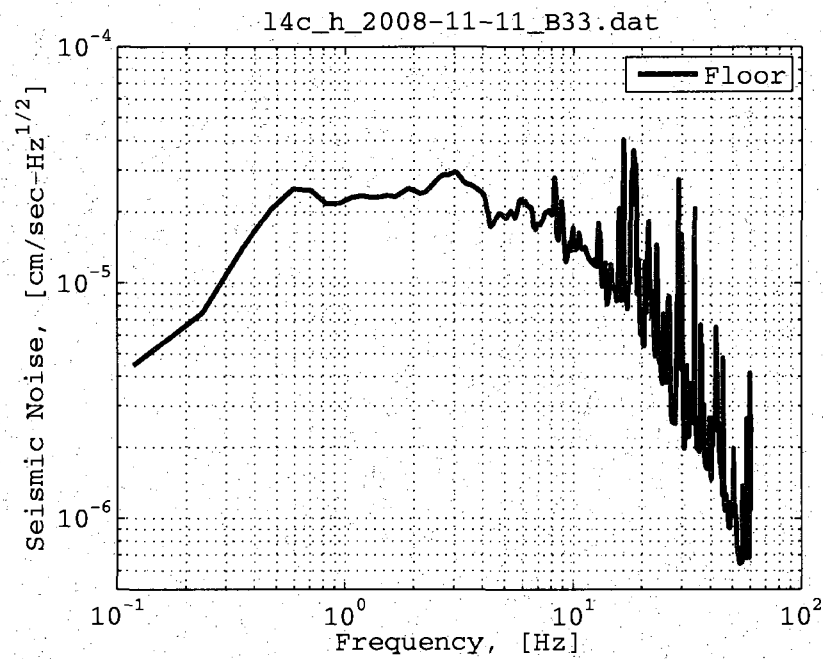


(a) Horizontal

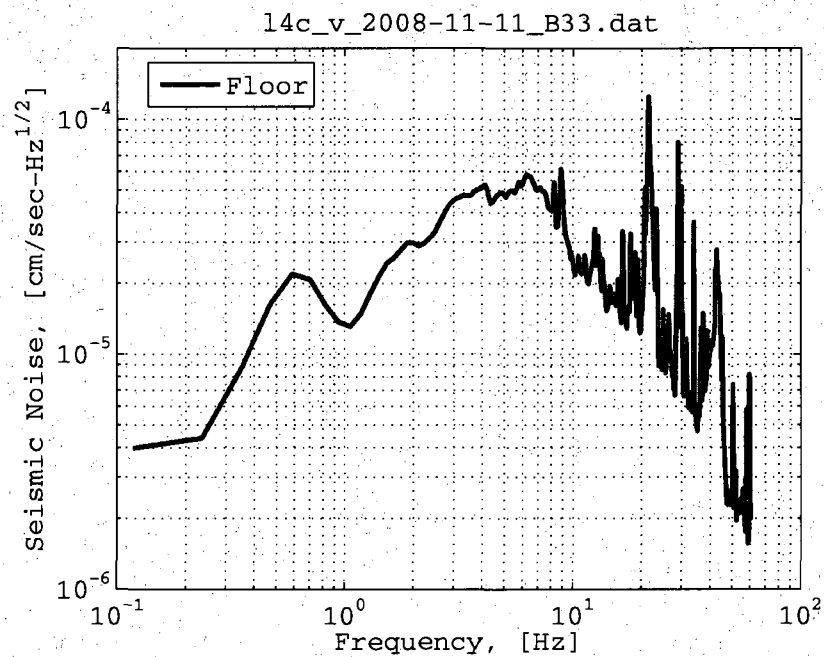


(b) Vertical

Figure 7.13: Vibration noise spectrum in Astrophysics building, Lab B11.



(a) Horizontal



(b) Vertical

Figure 7.14: Vibration noise spectrum in Astrophysics building, Lab B33.



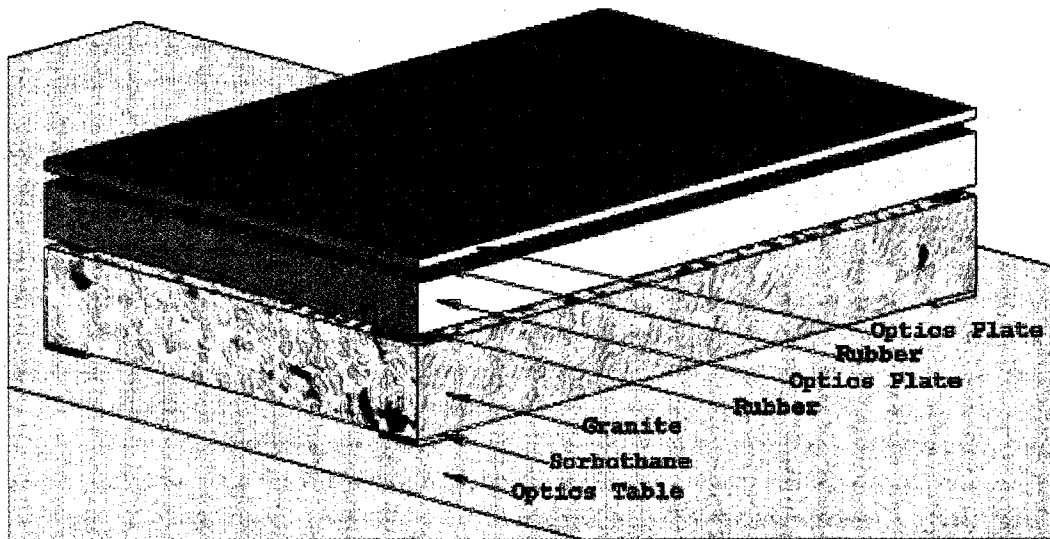


Figure 7.15: Vibration isolation stack.

the error associated with the small angle assumption. The pendulum oscillation amplitude is set to be greater than the noise signal, trading the error due to random vibrations with a systematic error of known magnitude due to nonlinearities. The errors associated with the small angle assumption can later be corrected if necessary. As a result, some degree of vibration isolation is necessary in order to allow small rotation angles and a low vibration noise floor. For the five-wire pendulum, passive vibration isolation was implemented to reduce the excitation from floor vibration due to seismic and human activity.

A tiered vibration isolation system was designed, Figure 7.15, consisting of an optics table, a 2 ft by 3 ft by 4.5 inch thick granite slab, a 2 ft by 3 ft by 2 inch thick aluminum optics plate, and a 2 ft by 3 ft by 1/2 inch thick aluminum optics plate. The five-wire pendulum foundation and required optics are attached directly to the final thin optics plate, such that the entire optics and pendulum assembly move as a single entity. A passive vibration isolator is then placed between each tier. At the lowest interface between the optics table surface and the granite slab, four 1/4 inch thick Sorbothane sheet pads are used for vibration isolation. The Sorbothane material

is an excellent isolator for a wide range of frequencies and for the heavy load of the granite slab. At the next interface between the granite slab and the thick optics plate, four hemispherical rubber isolators are used. The hemispherical isolators provide additional low frequency isolation and are chosen to accommodate the mass of the supported optics plate and pendulum structure.

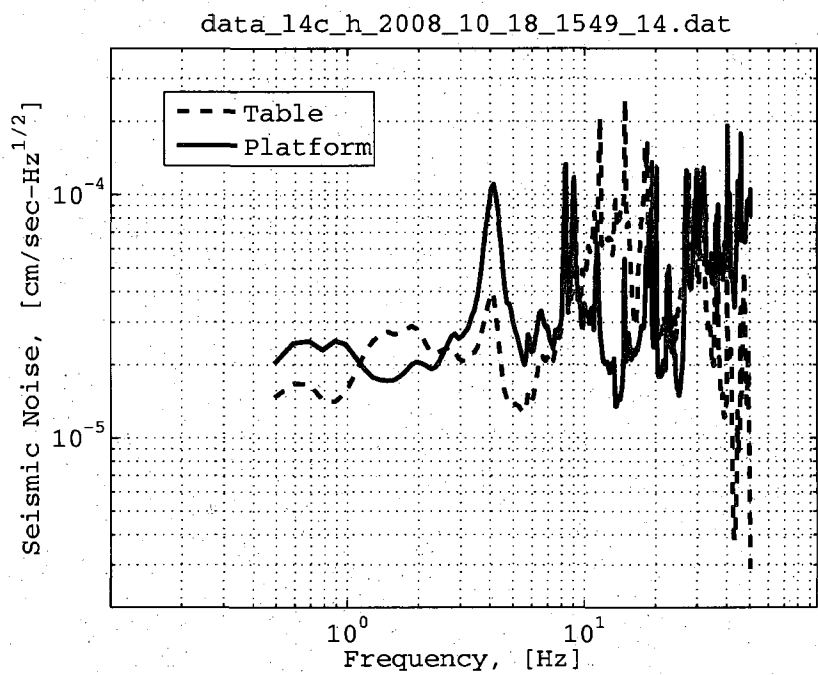
At the final interface between the thick optics plate and the 1/2 inch optics plate with the five-wire pendulum, there are several simple hard rubber disks. The disks provide little vibration isolation and were used only for additional clearance between the layers. The Mounts are kept at the same temperature to allow the use of rubber-like mounts, which tend to have better low frequency vibration suppression. The temperature of the isolation mounts is maintained through the use of the PID temperature controller on the thick optics plate as discussed in Section 7.1.

The vibrational noise spectrum at the pendulum platform foundation is shown in Figure 7.16. Although the spectrum now indicates an increased level of the peak due to human activity at 4 Hz, the high frequency noise content was reduced.

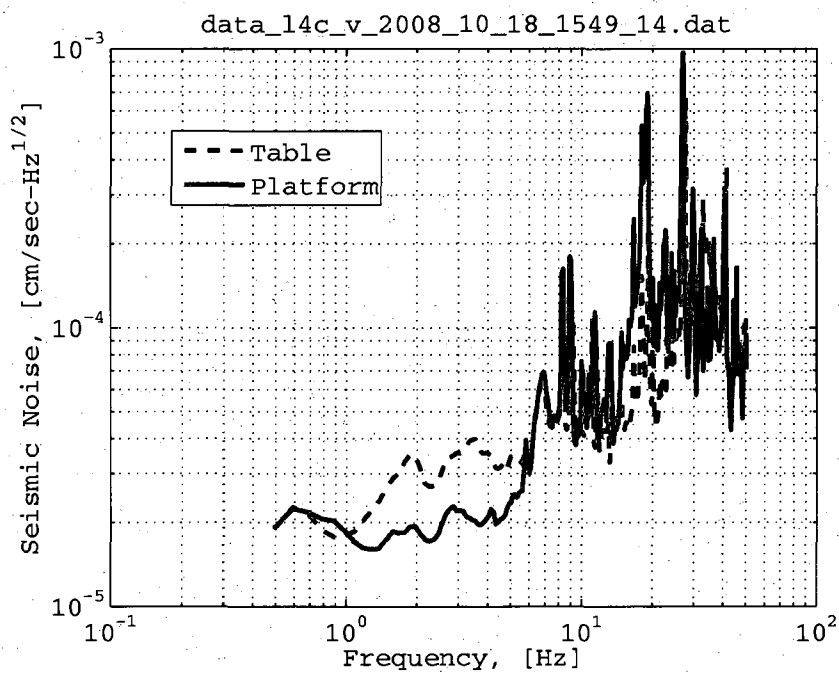
### **Additional Vibration Countermeasures**

In addition to passive vibration isolation, the pendulum response was improved by trimming the natural frequency. The oscillation frequency was trimmed by the addition of three 3/4 inch diameter 316 stainless steel spherical trim masses, Table B.3, in the outermost calibration holes. The trim masses were added in a symmetric fashion about the pendulum mass center and reduced the natural frequency from 3.1 Hz to approximately 2.5 Hz near a local minimum in the vibration spectrum depicted in Figure 7.16. The frequency reduction was enough to allow a clean damped sinusoidal response for 1000 seconds with an initial amplitude 0.5 mrad or less. Relocation of the experiment to a laboratory space on the ground floor is expected to provide a more effective solution in reducing the influence of vibrational disturbances. A relocation of the experiment to the ground floor is therefore recommended.

In addition to the passive vibration isolation countermeasures, improved results were obtained by simply taking measurements when human activity was at a minimum. Measurements are primarily performed at night and on the weekends to help



(a) Horizontal



(b) Vertical

Figure 7.16: Pendulum platform vibration noise spectrum.

reduce the random vibrations associated with human activity. Human activity causes a vibration interaction with the pendulum around the range of 3 Hz to 6 Hz and is the source of the peak at 4 Hz seen in the spectrum measurements. The 1 AM to 5 AM time frame proved to be the best time for running the experiment in order to avoid vibrations due to human activity. As a result, software was written to fully automate the acquisition procedure.

The root mean square spectral density of the pendulum response is shown in Figure 7.17. The spectrum is the final result after the application of passive vibration isolation, addition of trim masses, and temperature control via the PID controller. For comparison, Figure 7.18, shows the spectrum with the pendulum placed on the assembly mounts (as described in Section 5.3) to restrict the pendulum motion.

## 7.3 Air Currents

Air currents from air conditioning systems or simply from a person walking past the apparatus disturb the pendulum and induce oscillation. Disturbances due to air currents are reduced by placing the apparatus within an enclosure. The thermal enclosure described in Section 7.1 provides adequate isolation from the surrounding environment. In addition to air currents disturbing the pendulum, fluctuations in the surrounding air affect the grating angular sensor described in Section 5.5.2. As air passes through the laser beam path, density variations cause a change in the index of refraction, which generates an artificial signal at the sensor. The variation due to air currents is observed in the FFT data plots as a wide peak and the exact frequency depends on the air velocity. To reduce the affect of air currents, originally a small enclosure was placed around the path of the laser beam. Later, when the internal thermal chamber described in Section 7.1 was constructed, the laser beam enclosure was removed as the internal thermal chamber was found to be adequate for eliminating the air currents.

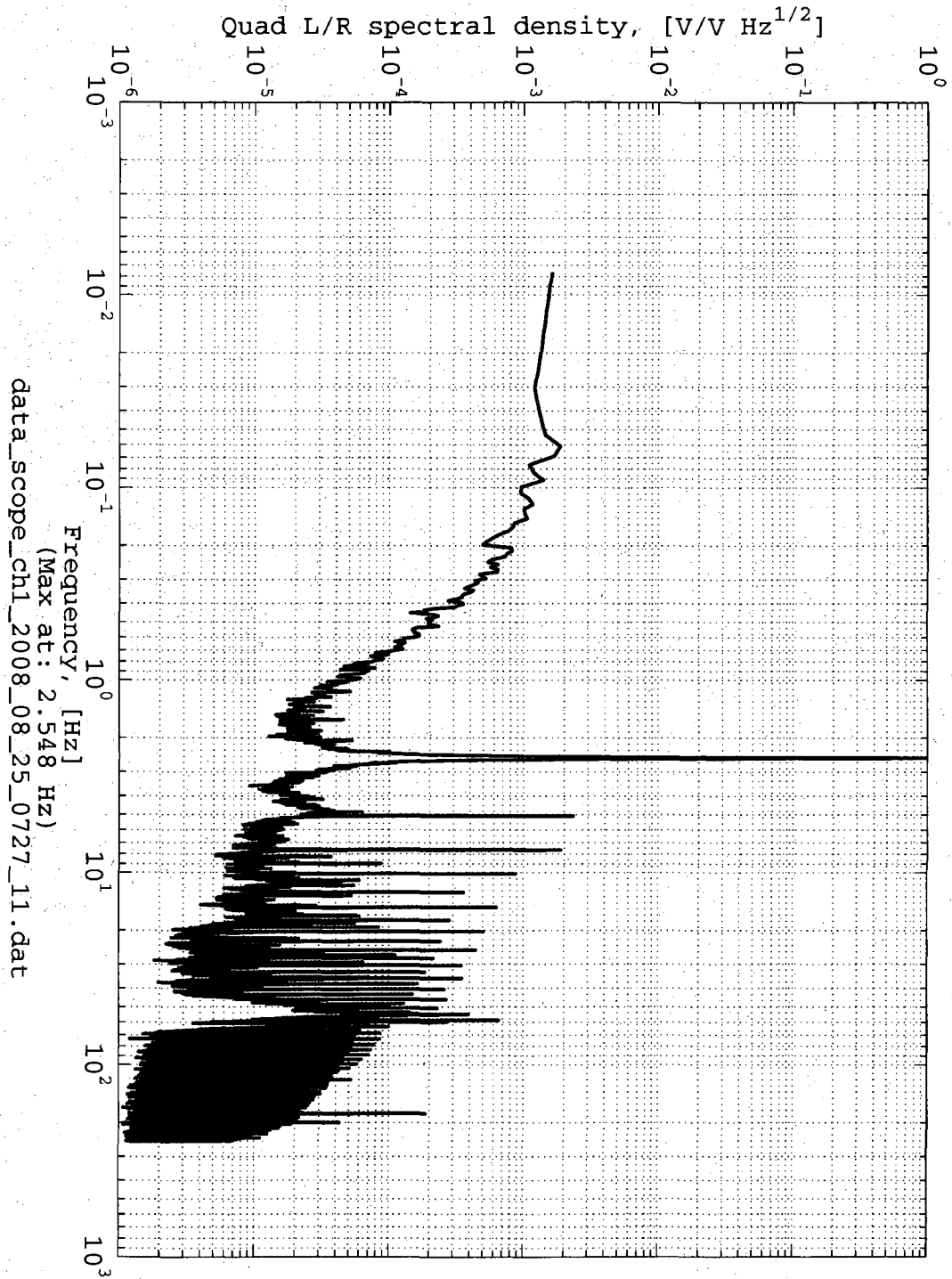


Figure 7.17: Pendulum response root mean square spectral density.

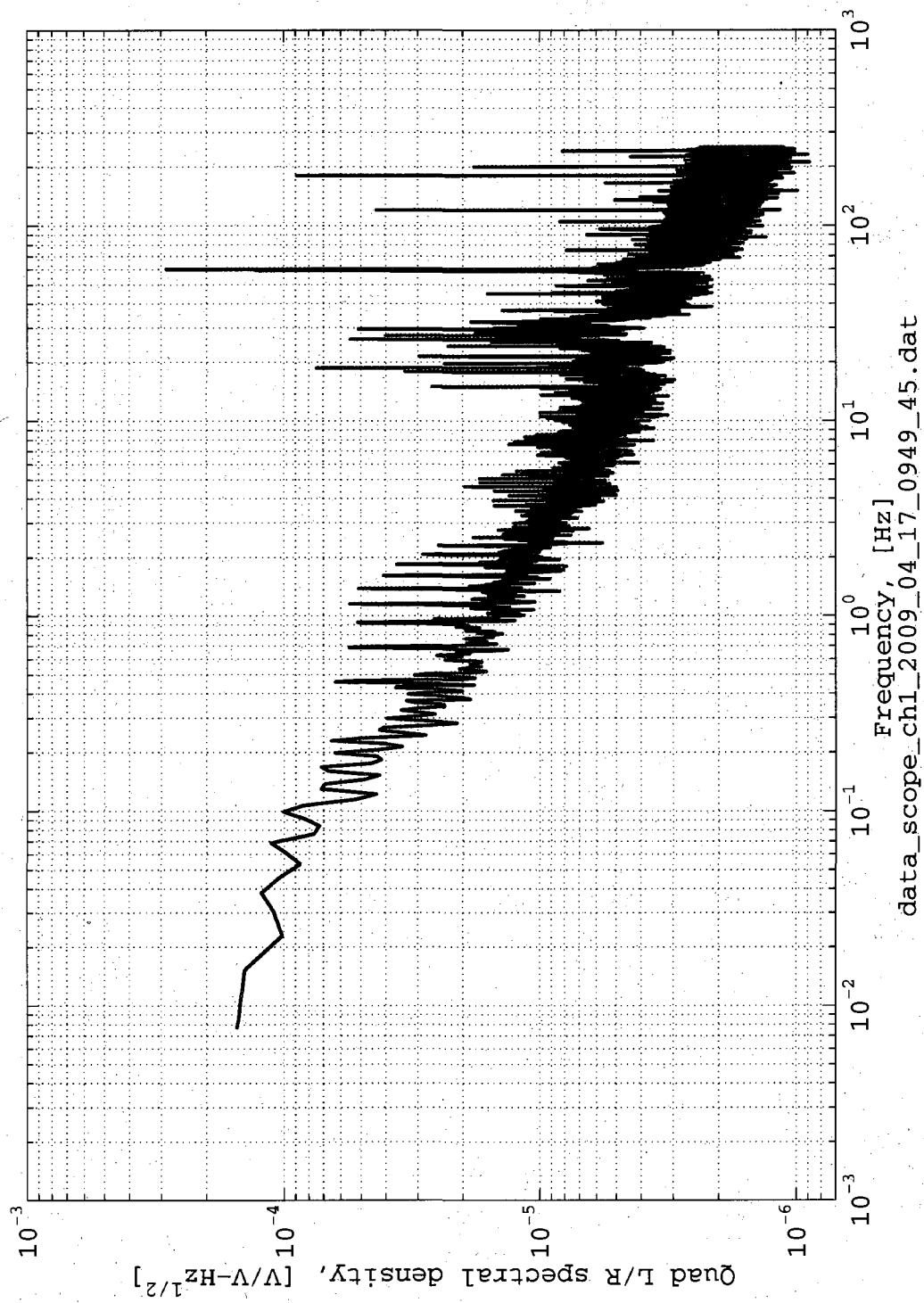


Figure 7.18: Root mean square spectral density with pendulum on assembly mounts.

## 7.4 Dynamical Nonlinearity

For a simple pendulum with length  $l$ , it is known that the pendulum period is given by  $T_l = 2\pi\sqrt{l/g}$ , where small motion,  $|\theta| \ll 1$ , is assumed to linearize the equations of motion. The subscript  $l$  on the period  $T$  is used to denote the period of the linearized solution. From Greenwood [25], the pendulum period for the general case where the amplitude,  $\theta$ , is not necessarily small is given by:

$$T_{nl} = 4\sqrt{\frac{l}{g}}K(\kappa) \quad (7.6)$$

The subscript  $nl$  on the period  $T$  is used to denote the period of the nonlinearized solution.  $K(\kappa)$  is the complete elliptic integral of the first kind with  $\kappa$  defined as:

$$\kappa = \sin \frac{\theta_o}{2} \quad (7.7)$$

where  $\theta_o$  is the maximum amplitude. By comparing the period for the linear and nonlinearized solutions one finds a simple ratio for establishing the error in the frequency associated with assuming small amplitude motion.

$$\frac{T_{nl}}{T_l} = \frac{\omega_l}{\omega_{nl}} = \frac{2}{\pi}K(\kappa) \quad (7.8)$$

Using Equation 7.8, one finds the associated change in frequency between the linear and nonlinear solution:

$$\begin{aligned} \Delta\omega &= |\omega_{nl} - \omega_l| \\ &= \left| \omega_l \left( \frac{\omega_{nl}}{\omega_l} - 1 \right) \right| \\ &= \left| \omega_l \left( \frac{\pi}{2} \frac{1}{K(\kappa)} - 1 \right) \right| \end{aligned} \quad (7.9)$$

For a maximum amplitude of one degree, the resulting change in frequency is  $\Delta\omega = \omega_l \times 1.9 \times 10^{-5}$ . Thus, for a linearized natural frequency,  $\omega_l/2\pi$ , on the order of 5 Hz or less, the error is on the order of  $10^{-4}$  Hz. It is therefore important to ensure the small

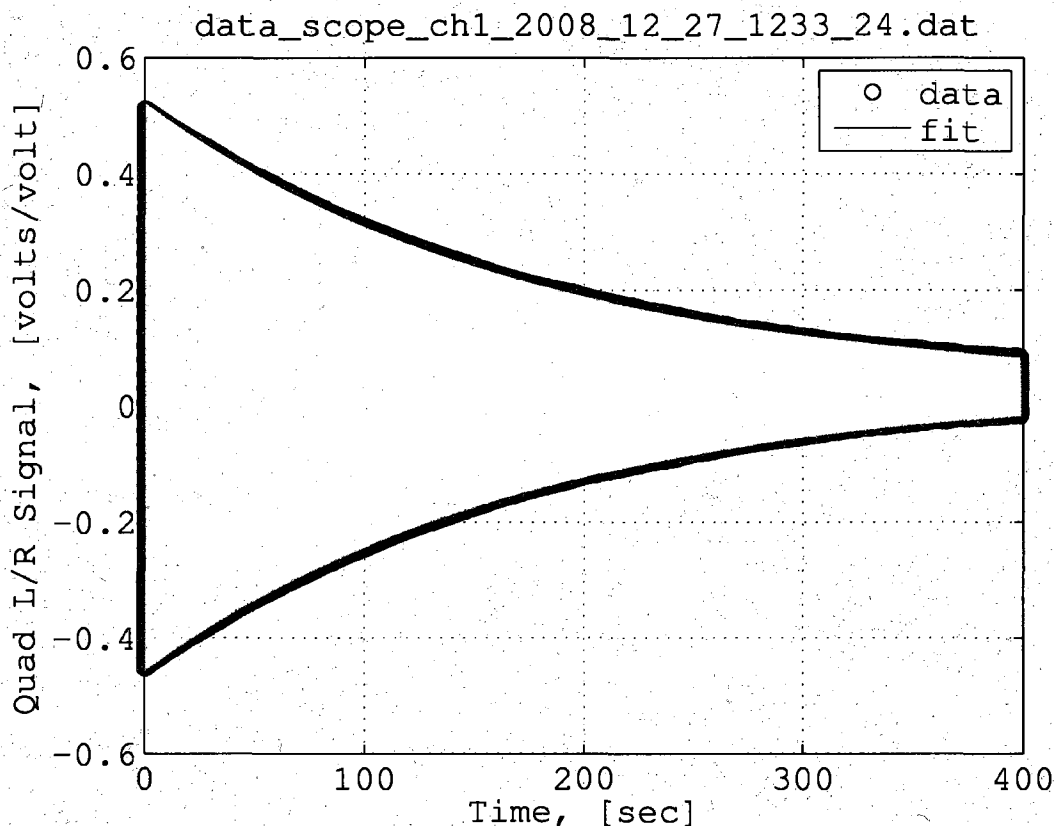


Figure 7.19: Pendulum response, Quad sensor signal.

angle assumption has not been violated. Since the amplitude of the motion is recorded in the measurement process, it is easy to verify that the small angle assumption is satisfied to the first order. A representative pendulum response as recorded by the quad photo-diode sensor and normalized by the total laser intensity on the sensor is shown in Figure 7.19. Section A.2 provides the calibration between the normalized sensor voltage signal and pendulum rotation angle. For the pendulum response shown in Figure 7.19, the initial signal amplitude of approximately 0.5 volts/volt indicates the pendulum rotation amplitude does not exceed 0.25 mrad for a typical measurement run. The corresponding difference in the linear and nonlinear solution is therefore less than  $10^{-7}$  Hz for a linearized natural frequency,  $\omega_1/2\pi$ , on the order of 5 Hz or less.



Since the system natural frequency is a slight function of the oscillation amplitude, it is also important to ensure a consistent initial amplitude for the five-wire torsion pendulum. By generating a repeatable pendulum response, a consistent measured oscillation frequency will result. As discussed in Section 5.7, a repeatable pendulum response is achieved by sending a small electromagnetic disturbance to the pendulum platform. The initial oscillation amplitude of the five-wire pendulum for a series of measurements as recorded by the quad photo-diode sensor is shown in Figure 7.20. The results indicate a mean value of 0.2435 mrad for the pendulum oscillation amplitude, with a standard deviation of  $\sigma = 2.0 \mu\text{rad}$  over 50 measurements during a 24 hour period. The limitation on the repeatability of the initial oscillation amplitude is dominated by the initial steady state condition of the pendulum prior to sending the actuation signal. Using the mean oscillation amplitude of  $0.2435 \text{ mrad} \pm 2\sigma$  for the range in initial oscillation amplitude, the difference in frequency for Figure 7.20 is less than  $10^{-9}$  Hz. Therefore, due to the repeatable actuation system, the variation in the measured frequency between measurements is negligible compared to the other error sources.

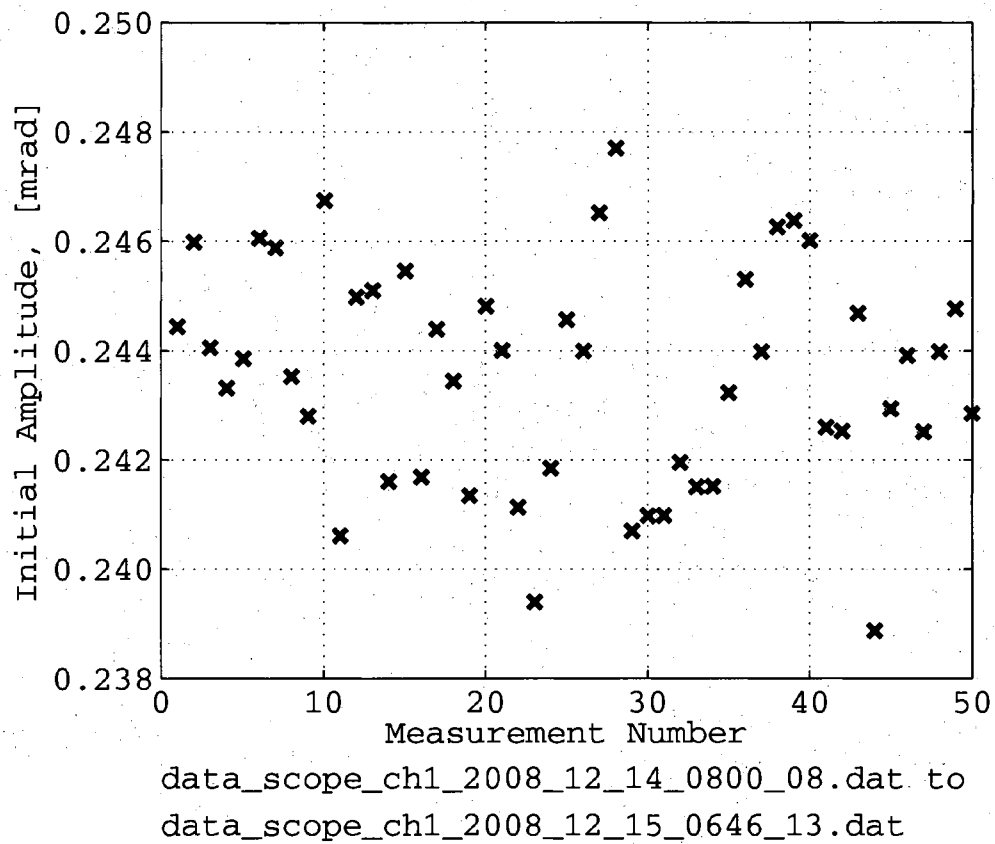


Figure 7.20: Variation in pendulum initial oscillation amplitude. The plot shows a mean amplitude of 0.2435 mrad with a standard deviation of  $\sigma = 2.0 \mu\text{rad}$ . The results were recorded using the quad photo sensor. The preferred principal axis of inertia sphere number six was positioned on the platform during the measurements.

# Chapter 8

## Future Work

### 8.1 Measurement Apparatus Modifications

As with any design revision, issues arise from which the designer gains insight into the system. During the integration and testing phase, a few issues came to attention which should be implemented in future revisions of the five-wire apparatus. The following sections describe the issues encountered and suggest possible modifications on future apparatus revisions. Table 8.1 summarizes the changes described in the following sections and indicates the importance of implementation for future designs. It is believed that with the addition of a simple vibration isolation system and a vacuum chamber, that the standard deviation on the frequency measurements for the five-wire torsion pendulum could easily surpass the level of  $2e-6$  Hz.

#### 8.1.1 Vacuum Chamber and Temperature Isolation

There are a number of observed characteristics which indicate that a vacuum chamber at a modest vacuum level would improve the performance of the five-wire pendulum. The most prominent being the local air stability and temperature variations. For example, as the pendulum is pulsed after a having been at rest since the previous night data acquisition run, an immediate drop in temperature is observed. The stagnate air within the chamber is disturbed by the motion of the pendulum.

Nice to Have	Essential
	Lab. Relocation
	Vibration Isolation
	Vacuum Chamber
	Temperature Control
	Grating Orientation
	Wire Angle
Tilt Reduction	
Object Fixtures	

Table 8.1: Importance of future modifications.

With the current setup, it is therefore essential to pulse the pendulum at the same rate the measurements are to be made to ensure proper stability of the surrounding air and temperature. In fact, if the pendulum is pulsed at every 25 minutes during the nightly data acquisition runs, but the pendulum is pulsed at a different rate during the day at every 15 minutes, a change in the temperature will be observed during the nightly runs, resulting in a frequency standard deviation change of up to  $1e-5$  Hz. This temperature stability induced by the motion of the pendulum would be eliminated by placing the entire apparatus within a vacuum chamber, resulting in a more consistent frequency measurement. In addition, better temperature stability can be obtained as the vacuum chamber container temperature can be controlled to maintain a consistent thermal input to the system..

An additional benefit of using a vacuum chamber is the elimination of air currents. It is difficult to completely eliminate all air currents in a large sealed volume. Even with a proper container to shield the apparatus from air currents induced by human activity and air conditioning systems, there will be air currents within the container from thermal convection and pendulum motion.

Lastly, the systematic error from the buoyancy force induced on the pendulum platform from the presence of the surrounding atmosphere would be eliminated by placing the five-wire pendulum inside a vacuum chamber. Maintaining a constant air pressure around the apparatus will aid in producing consistent frequency measurements from day to day.

### 8.1.2 Vibration Isolation

Although the tiered vibration system described in Section 7.2 was adequate for initial results, it is highly recommended that the apparatus be constructed in a location with lower vibration noise than the current laboratory. Alternatively, an expensive commercial vibration isolation system or the use of a granite table should be reconsidered for future precision measurements. As mentioned in Section 7.2, the apparatus was moved from the granite table to an alternate optics table in a newly constructed building due to lab space availability. The isolation provided by the alternate solution was marginally adequate for the operation of the pendulum. A location on the bottom floor of the building or a granite table will provide a far superior vibration noise level. Compare for example the seismic measurements for the optics table used in the experiment, Figure 7.13, with the seismic measurements for the granite table on which the apparatus was originally constructed, Figure 7.11 and Figure 7.12. From Figure 7.11 it is seen that the granite table provides about an order of magnitude better vibration isolation for the frequencies above approximately 6 Hz. Although the higher frequencies are above the natural frequency of the pendulum, the harmonics of the natural frequency corresponded with the higher undamped frequencies. In addition, the translational frequencies of the pendulum are excited by these vibrational frequencies. Use of the granite table for vibration isolation would also eliminate the need for the tiered vibration isolation system described in Section 7.2. As mentioned in Section 7.1, there is a coupling between the temperature stability of the vibration isolation mounts and the stability of the platform level. By removing the isolation mounts, the temperature stability effects on the measurements would be reduced considerably. In addition, the need to shift the frequency of the pendulum to a lower frequency in order to avoid peaks in the vibration spectrum is eliminated and the added trim masses may no longer be necessary.

The natural frequency of the pendulum can be trimmed by the addition of inertia, yet the frequency can only be easily reduced, not raised. In addition, when the measurement object is placed on the pendulum platform, the oscillation frequency is reduced. The pendulum frequency was chosen to be as high as possible in order to reduce the wire length and hence the size of the apparatus. When the apparatus was

moved to the standard optics table, the lowest frequency noise floor from vibration became 6 Hz, which is too close to the pendulum natural frequency for a consistently clean response. Therefore, for future revisions, it is recommended that the natural frequency be reduced in order to further spectrally separate the pendulum signal from the vibrational noise sources. Alternatively, if the high frequency noise is adequately suppressed and no prominent low frequency peaks exist, the natural frequency of the pendulum can be increased substantially, thereby taking advantage of the 1/f roll off for a higher signal to noise ratio.

### 8.1.3 Platform Tilt Reduction and Wire Angle

The orientation of the rotation axis is affected by the level of the pendulum platform. By using the pendulum platform assembly mounts described in Section 5.3, the pendulum platform is positioned level to the optics plate containing the entire five-wire pendulum apparatus. Yet, since the platform hangs from the support structure, the pendulum platform will obtain a level position relative to the gravitational vector. The system is leveled by making sure the optics platform is level. The initial static level condition is achieved by the use of a simple bubble level.

The level condition of the optics plate will however change due to a number of error sources, including thermal variations and floor/building motion. Due to the five-wire design, the pendulum is the least stiff along the positive  $\hat{i}$ -axis, in the direction from the rotation center to the vertical wire support. Refer to Figure 6.5, for a coordinate system of the pendulum platform. If the pendulum support structure is rotated in a positive sense about the  $\hat{j}$ -axis using the right hand rule, the pendulum platform will translate along the positive  $\hat{i}$ -direction. In the five-wire design, the pendulum platform is stiff along the negative  $\hat{i}$ -axis and in both the positive and negative  $\hat{j}$ -axis. An attempt to rotate the platform support structure about the  $\hat{i}$ -axis results primarily in a rotation of the pendulum platform about the vertical  $\hat{k}$ -axis. Therefore, in future pendulum versions, it is suggested to angle the vertical wire slightly inward toward the rotation center in order to increase the stiffness along the positive  $\hat{i}$ -axis. In addition, since it is known that the direction along the positive  $\hat{i}$ -axis is sensitive

to a tilt, the pendulum should be oriented on the support structure accordingly. For example, it was found that the optics table on which the pendulum structure was built tends to tilt along the short direction of the table. At the time the pendulum was constructed, the tilting nature of the optics table was unknown and the  $\hat{i}$ -axis of the pendulum platform was oriented along the short direction of the table. In hindsight, the pendulum should have been oriented 90 degrees from the current position such that the sensitive direction to tilt was not aligned with the short direction of the table.

In general, the actual wire geometry deserves reconsideration for any future five-wire design. The wire geometry utilized for this work was selected based primarily from the promising characteristics exhibited by the original student project design. The five-wire geometry produced a pure rotational motion with the translational modes shifted to frequencies well above the pendulum rotation frequency. During the course of this work, it was found that the asymmetries associated with the wire geometry lead to other challenges, such as tilt or differential wire stretch due to loading or temperature variations. During the course of this work, an alternative wire design was considered, where all the wires were of the same length and oriented symmetrically about the pendulum platform. This was Design 3, which was briefly noted in Section 5.1. The symmetric wire length reduces differential tension in the wires or changes in orientation due to differential wire elongation. Yet during analysis, the design proved to inadequately constrain the pendulum translational modes. The symmetrical pendulum design exhibited low frequency rocking modes, which were on the same order as the desired torsional frequency. Without the proper spectral separation, the desired pure rotation could not be achieved with the initial symmetric design. Thus, some work should be devoted to investigating other designs with a low friction method for producing the pure rotation. Future designs to be considered should also include low friction magnetic bearings or air bearings. Still, there are applications where the issues associated with the asymmetric wire geometry are not a limiting factor in the precision of the desired measurement. The issues associated with the asymmetric wire geometry translate primarily into the ability to calibrate the pendulum for moment of inertia measurements. Thus, the five-wire torsion pendulum

design may be useful for any application requiring a pure rotation about an axis. The mass center measurement application for the five-wire pendulum discussed in Section 4.4.2 and Section 6.2 is one such example.

#### 8.1.4 Grating Orientation

The grating angular sensor described in Section 5.5.2 is only sensitive to translations in the direction of the grating norm. For the assembled configuration of the five-wire pendulum, as depicted in Figure 5.26, the grating norm is aligned with the radial direction from the rotation center to the vertical support wire. Consistent with the coordinate system depicted in Figure 6.5, the grating norm is aligned with the  $\hat{i}$ -axis. As mentioned in Section 5.3, the positive  $\hat{i}$ -axis is the direction of the pendulum that is least stiff and most susceptible to translations due to pendulum tilt. In addition to the translational motion generated by a tilt of the pendulum support structure, a similar tilt/translation effect is observed due to temperature changes as described in Section 7.1. Thus, in order to reduce sensor error due to pendulum translation along the grating norm, the grating should simply be rotated by  $90^\circ$ , such that the grating is aligned with a stiff translational direction of the pendulum. It should be noted however, that the current grating orientation allows for monitoring of the temperature fluctuations by measuring the drift in the quad photo-detector. Re-orientation of the grating will no longer allow for this feature. As such, the proposed grating re-orientation should be implemented after the addition of improved temperature stability or the addition of a vacuum chamber.

Should a redesign of the grating holder occur, a design which allows two gratings to be oriented simultaneously with their respective norms at perpendicular directions should also be considered. By using two signals, any noise sources due to the translation of the pendulum could be subtracted out of the science signal. In addition, the translation of the pendulum rotation center due to an applied load could then also be monitored.



### 8.1.5 Trim Masses

Trim masses were added to the pendulum platform near the wire attach points. The trim masses have the following functions:

1. Shift the natural frequency of the pendulum to a desired frequency away from vibration noise sources.
2. Pre-stress the wires at the attach points to prevent a change in signal due to asymmetric loading of the calibration spheres.
3. Shift mass center to the rotation center.

The trim masses were added primarily to shift the pendulum natural frequency and to avoid a change in signal due to asymmetrically loading the platform with the calibration spheres. Prior to the machining of the pendulum platform, it was not known that large trim masses would be necessary. Only a small trim mass was placed on the grating holder to assist in trimming the mass center of the final apparatus.

In future revisions, there should exist specific holes on the pendulum platform for the trim spheres. The trim masses must be added in a symmetric fashion to avoid shifting the mass center of the entire apparatus. Currently the trim spheres are placed in the outer calibration holes. The required amount of trim mass dictated a sphere diameter large enough to prevent the use of the adjacent calibration hole. By creating a set of holes devoted solely for the trim masses, it can be ensured that the trim masses will not conflict with the calibration procedure or the measurement object placement and still provide a symmetric loading of the platform.

### 8.1.6 Object Fixtures

The measurement object fixtures, discussed in Section 5.4, have the dual purpose of repeatable object positioning and placement with respect to the pendulum platform. For objects with distinguishing geometrical features, the fixtures can be designed to kinematically constrain the object's orientation. The fixtures designed for the cylindrical shaped object as described in Section 5.4.1 are such a design, where

each fixture is designed for a specific object orientation. The difficulty with the cylindrical fixtures in Section 5.4.1 is that in order to change the orientation of the object, the fixture needs to be changed. Even with a repeatable positioning method for the fixture to the platform, the configuration change results in an associated measurement uncertainty. As discussed in Section 6.1, it is essential to maintain a constant mass for the pendulum platform and associated fixtures. If the configuration of the platform changes, such as the total mass, or fixture location, the pendulum will require a re-calibration. For the cylindrical fixtures, each time the orientation of the object needs to be changed, a new fixture is placed on the pendulum. The configuration of the pendulum has therefore changed with the addition and removal of fixtures and the pendulum requires re-calibration. The process not only necessitates unnecessary measurements, but also introduced additional uncertainty into the final measurements. As a result, for kinematic orientation fixtures, it is desired to have one fixture for the object and various orientations.

For the spherical measurement object, with no geometrical distinguishing features, the object was marked to allow orientation positioning. As described in Section 5.4.2, the polhode paths were used to intelligently position a set of perpendicular great circles on the sphere to be used as a coordinate reference. The coordinate reference frame creates the basis for placing additional orientation marks onto the sphere for orientation. These additional marks however, need to be placed at well-determined angles relative to the coordinate system. For the spheres measured in this work, the great circle marking apparatus was used to generate the additional orientation marks at  $\pi/4$  increments. These angles have limited accuracy, as the great circle marking apparatus was only designed to create two perpendicular great circles. In order to generate the additional angle markings, a triangle fixed at  $\pi/4$  radians was placed onto the apparatus. The location of the  $\pi/4$  marks was adequate for this work, as the ability to position the spherical object with the visible laser beam has a larger error than the ability to place the  $\pi/4$  marks. For future measurements, it is suggested to design a more accurate method for marking spherical shaped objects at pre-determined angles relative to the great circle markings. More accurate markings on the sphere will increase the overall accuracy of the moment of inertia measurements.

### 8.1.7 Continuous Feedback Drive

Due to damping in the system, the pendulum will exhibit a damped sinusoidal response. The pendulum was specifically designed with a higher stiffness than typical single wire torsion pendulums, such that small disturbances such as local gravitational mass attraction effects do not affect the pendulum response. The result is however a limited data length from a single pendulum pulse. This in turn limits the precision on utilizing an FFT for data reduction, as the frequency determination will be bin width limited.

It may be useful to investigate the advantages of performing frequency extraction via an FFT of longer data acquisition runs. One way to increase the amount of time for a useful signal to noise ratio measurement is to overcome the damping effects by continuously providing additional energy to the pendulum via the excitation coils. The pendulum oscillation amplitude will thereby be maintained. Feedback from the pendulum position will be necessary, as a periodic pulse generated at regular intervals will cause a discontinuity in the response. A simple analog controller implemented using op-amp circuitry is sufficient for a continuous feedback driven system. In fact, only a proportional controller is necessary to utilize the position feedback signal from either the PSD or quad sensor.

With a continuous feedback analog controller in place, a little consideration must be given to the actual phase of the pendulum response at which the proportional controller provides the signal. If only a proportional controller is used from the pendulum position response, the result would be a sinusoid matching the pendulum response, with the maximum signal applied at the maximum rotational displacement of the pendulum. This configuration however is not ideal, as the direction of the current in the excitation coils would need to be switched at the maximum rotation position of the pendulum. Issues with timing on the transition could disturb the pendulum response. This intuitively is similar to pre-ignition or detonation within four cycle combustion engines where an excitation to the system occurs prior to the reversal of the piston direction.

A better solution is therefore to shift the phase of the feedback signal by  $\pi/2$ , such that the excitation signal is zero at maximum rotation amplitude and a max at

the zero crossing of the pendulum. A proportional signal applied near the maximum velocity should also have a minimal affect on the pendulum response. Although a phase shifting circuit could be implemented in analog hardware, a more appropriate solution is to use the pendulum velocity as the signal for a continuous feedback controller. The pendulum velocity signal is simply the position signal shifted by  $\pi/2$ . Without the pendulum velocity directly available, the derivative of the pendulum position is necessary, which again is easily obtained via analog op-amp circuitry. The signal can then be fed into the proportional feedback controller.

## 8.2 Recommended Future Research

### 8.2.1 Mass Center Measurement

In Section 4.4.2 it was shown that a torsion pendulum can be used for determining the mass center offset from the geometric center. Section 6.2 further showed initial proof of concept measurement results for the mass center offset. There were two issues with the initial mass center measurement results:

1. Measurements should be performed for multiple configurations.
2. Pendulum calibration in mass center measurement configuration is required.

The first item is easily solved by simply repeating the frequency measurements for different orientations of the measurement object within the rotation plane as described in Figure 4.2. There are no distinguishing features for orienting the spherical shaped measurement object. Thus, in order to orient the measurement object at specified orientations, an apparatus for accurately marking the desired orientations is necessary. This is the same issue as described in Section 8.1.6 and should be a simple task.

The second item deals with the pendulum calibration routine. Clearly, the absolute accuracy of the measurements are limited by the calibration routine. For a proper measurement, the calibration routine should be repeated for the measurement object in place on the pendulum platform. In so doing, any shift in the pendulum

rotation center location, or any change in the direction of the rotation axis is accounted for. In addition, in order to reduce any shift of the rotation center from the nominal location, the pendulum requires a counter balance for measurement object. Since the pendulum was not initially designed for mass center measurements, there is no symmetric location about the rotation center for adding a counter balance. A future pendulum platform for use in mass center measurements should contain two mounting locations for mass center measurements, located symmetrically about the rotation center. A sphere of similar mass can then be placed in the other mounting location, with a fixed orientation throughout the measurements. For the current wire configuration, it is suggested that the additional mass center mounting holes be a mirror of the current configuration, to ensure proper loading of the wires.

### 8.2.2 Satellite Design for Mass Attraction

In order to meet challenging drag-free satellite design requirements for a minimized contribution to the drag-free performance from mass attraction effects, it is important to begin early with the initial satellite design. During the layout of satellite components and early satellite design, it is essential to have an engineer present with basic knowledge of gravitational mass attraction effects. Although this work does not go into detail of the actual satellite design process for minimizing the gravitational attraction force and gradient, there are a number of points which are beneficial to understand.

First it is clear that separation distance is the simplest method for reducing gravitational attraction effects. The first drag-free satellite Triad-1/DISCOS reduced the influence of gravitational mass attraction effects by moving the disturbance compensation system to the center of a long boom, thereby increasing the separation distance from the drag-free proof mass and the majority of the satellite components, while retaining a gravity gradient stabilization for the spacecraft. Where the use of a boom is not practical or feasible, the same concept still holds. It is beneficial to move those components which are expected to have a large contribution to the mass attraction uncertainty to locations far from the drag-free proof mass.

In addition, symmetry is the friend of an engineer working with gravitational mass attraction. Clearly, the symmetrical placement of similar components relative to the drag-free reference will help to reduce the overall static gravitational attraction force on the test mass and reduce the amount of mass required in the form of trim masses. In addition, on a component level it is beneficial to produce components which exhibit symmetry with respect to the mass distribution. Recall for instance the observations made in Section 3.6 and in Section 3.10. In Section 3.10 it was shown that a cube and a sphere exhibit similar gravitational attraction effects through a third order expansion. The similar characteristics were a result of the cube having identical principal moments of inertia similar to that of a perfect sphere. In Section 3.6 it was also shown that higher order expansion terms equate to zero for objects with identical principal moments of inertia. Thus, in order to approximate the attraction effects of a distributed body with a point mass, the error associated with such an idealized assumption is reduced when the distributed body is symmetrical. In addition, if the object exhibits a plane of symmetry such that only two of the principal moments of inertia are similar, then the gravitational attraction effects may be reduced by intelligently choosing the orientation of the component.

The use of regular geometric shapes was also used for the gravitational mass attraction analysis of Triad-1/DISCOS [22]. Although the mass attraction analysis for DISCOS utilized geometric shapes simply for the theoretical calculation of the attraction force and gradient, it should be noted that certain geometrical shapes also exhibit gravitational attraction properties which are beneficial to the satellite designer. As shown by Fleming et. al [22], there are a number of geometries which have in specific directions either zero force or gradient contributions to the gravitational attraction analysis. These objects include for example spherical shells, plano-convex spherical sections and cylinders. Of special note is a toroid geometry or a homogeneous spherical shell. Such geometries are quite useful for time varying mass quantities, such as propellant tanks. There exists a location at the center of the toroid where the gradient of the attraction force is identically zero. For a perfectly homogeneous spherical shell, any location within the shell has a zero contribution to the force and gradient. A toroidal shape is a more practical solution, but achieving an even distribution of

the propellant within the tank is another challenging task. Indeed, Triad-1/DISCOS utilized toroidal shaped propellant tanks, which were placed symmetrically about the proof mass [15], [22].

# Chapter 9

## Final Remarks

Gravitational mass attraction property prediction for drag-free satellite design has historically utilized theoretical calculations based on ideal mass properties. Typically the attraction calculation additionally assumes the drag-free reference mass can be represented by a single point mass. Such assumptions are unacceptable for future precision drag-free satellite missions. Chapter 3 therefore provided the equations for determining the gravitational mass attraction between two general distributed bodies. The developed equations also generate a foundation for including mass property measurements into the mass attraction calculation. This work for the first time provides a complete procedure for incorporating physical measurements into the mass attraction calculations, such that the assumed ideal geometry and density distribution for components are included in the mass attraction computations.

Precision mass property measurements are clearly essential in drag-free satellite design for a number of reasons. Chapter 5 therefore provided the design for a five-wire torsion pendulum. The apparatus was primarily designed for measuring the moments of inertia and was also shown to provide mass center measurements. As shown by the experimental results in Chapter 6, the designed torsion pendulum is capable of precision mass property measurements. Measurement results from the prototype torsion pendulum apparatus matched state of the art moment of inertia measurements. For the mass center measurements, the results were better than typical mass center



measurement devices. Section 6.3 provided precision moment of inertia measurements of prospective drag-free reference mass geometries. These measurements not only verify the mass properties to ensure proper shifting of the polhode frequency out of the science band as needed for missions such as LISA, but are also essential to the gravitational mass attraction disturbance budget calculation. In order to aid in improving on the five-wire pendulum design for future applications, measurement error sources for the five-wire pendulum were presented in Chapter 7. In addition, insight into current limitations and future proposed modifications to the pendulum design is described in Chapter 8. Future work to suppress laboratory environmental disturbances are expected to make the measurement apparatus capable of exceeding state of the art moment of inertia measurements by approximately an order of magnitude. The prototype five-wire pendulum apparatus was not primarily designed for mass center measurements. Still, application of the pendulum to mass center measurements exhibited promising potential. With minor modifications to the pendulum platform or with a similar five-wire design, the five-wire torsion pendulum may be capable of achieving state of the art mass center measurement levels. Some insight into the necessary steps for improving the five-wire pendulum design for mass center measurements was presented in Chapter 8.

By combining the methods developed in this work for gravitational mass attraction calculations, Part I, and the precision mass property measurements using the five-wire torsion pendulum, Part II, a complete solution for analyzing the mass attraction properties of high-performance drag-free satellites is established. Although a detailed computation of the gravitational mass attraction properties for an entire satellite were out of the scope of this work, the methods presented in this work will enable the detailed analyses required for high-performance drag-free satellites. The techniques presented in this work provide a solution to one of the challenges associated with achieving the demanding drag-free performance levels necessary for gravitational wave observatories such as LISA. First, the incorporation of measured mass properties into the mass attraction calculations will provide a result which incorporates unknown density inhomogeneities and variations in geometry. The analysis is no longer a purely theoretical model requiring additional verification by measurements,

but rather the analysis is an indirect measurement of the mass attraction forces and gradients. Secondly, provided the mass properties of satellite components have not changed, the described method allows for repeated analyses of the attraction properties for the entire satellite as component locations or orientations are altered during the design process. Once the mass properties of a satellite component are established and tabulated, the mass attraction properties may be simply updated for satellite configuration changes. Finally, by reducing the overall uncertainty associated with the satellite mass attraction properties, the contribution to the overall satellite drag-free performance budget may be reduced further. The total drag-free performance level is a combination of all the disturbances acting on the drag-free reference mass. Thus, by reducing the uncertainty in the mass attraction contribution to the overall drag-free performance, other challenging disturbance requirements may be relaxed, which otherwise may not have been reduced to required levels in order to satisfy mission requirements.

# Appendix A

## Additional Information

### A.1 Tetrahedron Volume Moments

For completeness, the volume moments through the second order of a tetrahedron are stated here. Refer to Sheynin [49] and Tuzikov [66] for a full derivation of the tetrahedron volume moment calculation formula, Equation 3.13. A tetrahedron is defined with one vertex at the origin. Each of the other three vertexes are defined by coordinate points  $\bar{a}$ ,  $\bar{b}$ ,  $\bar{c}$ , and the matrix  $A$  is defined to be the coordinates of the vertexes such that  $A = [\bar{a}, \bar{b}, \bar{c}]$ . The volume moments for the tetrahedron are given by [49]:

$$\begin{aligned}M_{0,0,0} &= \frac{1}{6} \det A \\M_{1,0,0} &= \frac{1}{24} \det A (a_1 + b_1 + c_1) \\M_{0,1,0} &= \frac{1}{24} \det A (a_2 + b_2 + c_2) \\M_{0,0,1} &= \frac{1}{24} \det A (a_3 + b_3 + c_3)\end{aligned}$$

$$M_{2,0,0} = \frac{1}{60} \det A (a_1^2 + b_1^2 + c_1^2 + a_1b_1 + a_1c_1 + b_1c_1)$$

$$M_{0,2,0} = \frac{1}{60} \det A (a_2^2 + b_2^2 + c_2^2 + a_2b_2 + a_2c_2 + b_2c_2)$$

$$M_{0,0,2} = \frac{1}{60} \det A (a_3^2 + b_3^2 + c_3^2 + a_3b_3 + a_3c_3 + b_3c_3)$$

$$M_{1,1,0} = \frac{1}{60} \det A \left( a_1a_2 + b_1b_2 + c_1c_2 + \frac{a_1b_2 + a_1c_2 + b_1c_2 + a_2b_1 + a_2c_1 + b_2c_1}{2} \right)$$

$$M_{1,0,1} = \frac{1}{60} \det A \left( a_1a_3 + b_1b_3 + c_1c_3 + \frac{a_1b_3 + a_1c_3 + b_1c_3 + a_3b_1 + a_3c_1 + b_3c_1}{2} \right)$$

$$M_{1,0,1} = \frac{1}{60} \det A \left( a_2a_3 + b_2b_3 + c_2c_3 + \frac{a_2b_3 + a_2c_3 + b_2c_3 + a_3b_2 + a_3c_2 + b_3c_2}{2} \right)$$

## A.2 Grating Angular Sensor Calibration

In order to extract the time history of oscillation for the five-wire pendulum, it is not necessary to know the exact translation between the sensor signal and a rotation angle. Yet for the five-wire pendulum, a small angle assumption is made to simplify the dynamics. As such, a calibration of the sensor voltage signal to the rotation angle is desired to ensure the assumption of a small rotation angle has not been violated.

The grating angular sensor described in Section 5.5.2 is composed of a quad photo detector and a position sensitive diode. Both of the sensors are calibrated using the same procedure. The sensors are calibrated by using an optics micrometer stage. Contact between the micrometer stage and the pendulum platform is established at the vertical wire attachment by a simple round Allen head fastener as depicted in Figure A.1. As the micrometer stage is translated, a corresponding rotation of the pendulum platform is achieved. Using a small angle assumption, the translation distance of the micrometer stage is related by  $\Delta x = r\Delta\theta$ , where  $r$  is the distance from the rotation center to the point of contact,  $x$ , the amount of translation produced by the micrometer stage, and  $\theta$  the amount of pendulum rotation in radians. The resulting sensor signal is recorded for the quad photo detector and the position sensitive diode. A value of  $r = 96$  mm was used for the distance to the point of contact from

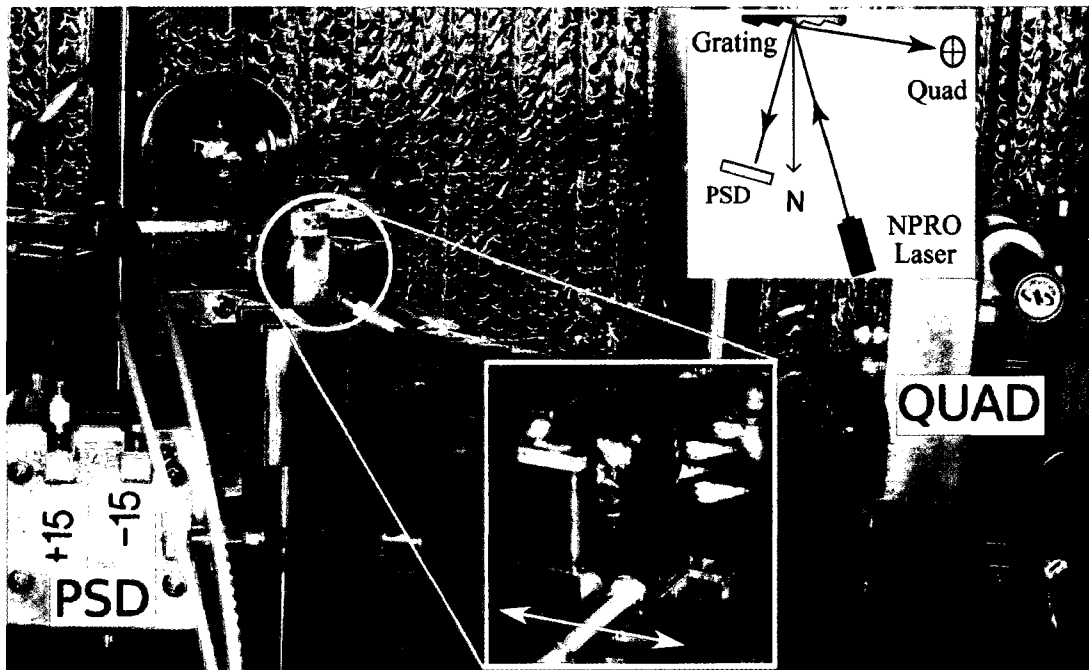
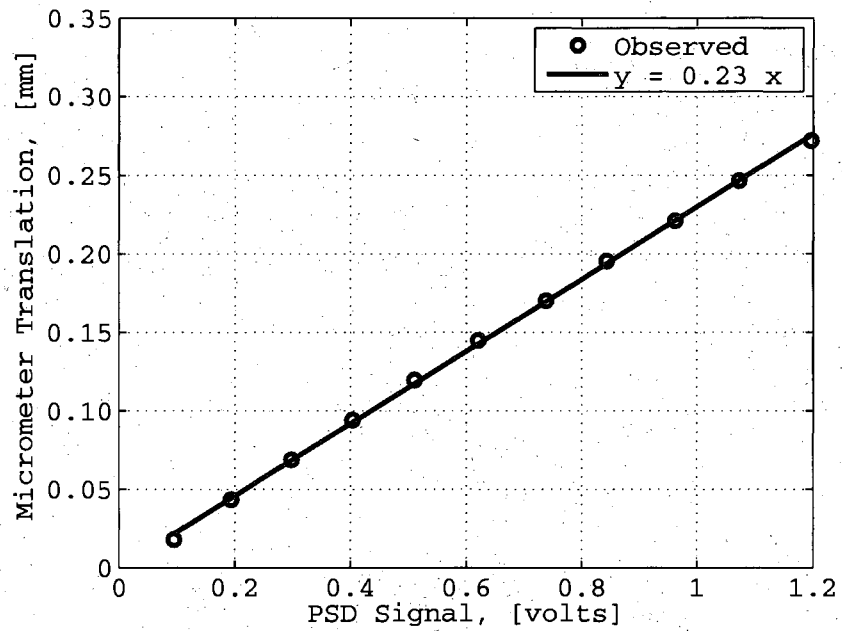


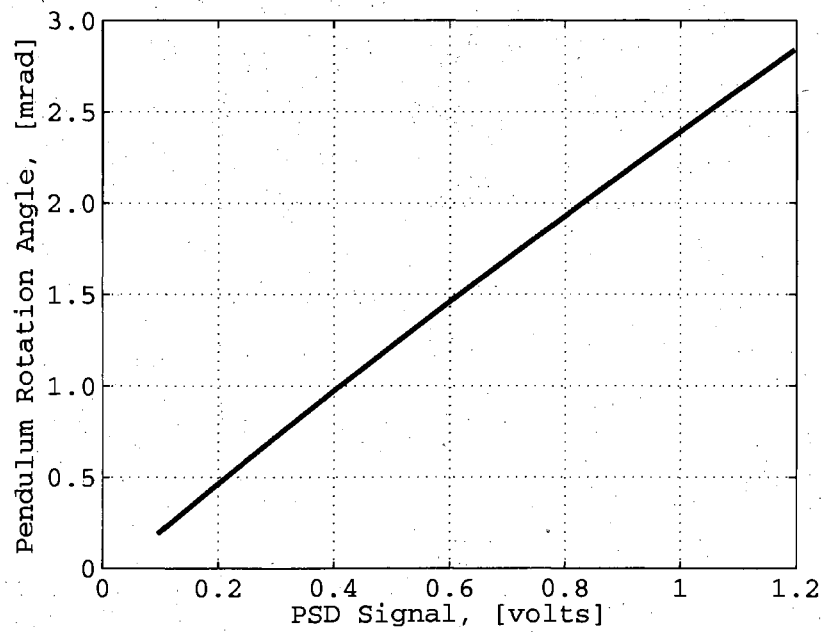
Figure A.1: Pendulum platform setup for sensor calibration.

the rotation center. For the quad photo detector, the resulting left/right position is also normalized by the detector total intensity in order to reduce errors due to laser fluctuations or from the laser beam leaving the detector surface area. Since the PSD was only a secondary sensor, the signal was not normalized by the total intensity during the measurement runs. Refer to Figure A.2 and Figure A.3 for the position sensitive diode and quad photo detector calibration curves respectively.

Each sensor is mounted on a micrometer stage for proper alignment with the incoming laser beam. The position sensitive diode is located on a single axis micrometer stage for translation along the length of the sensor. The quad photo detector is positioned on a two-axis micrometer stage for adjustment both in the horizontal and vertical directions. Note that the null position of each sensor is controlled through the positioning of the micrometer stage. As such, only the slope of the calibration curves is of interest.

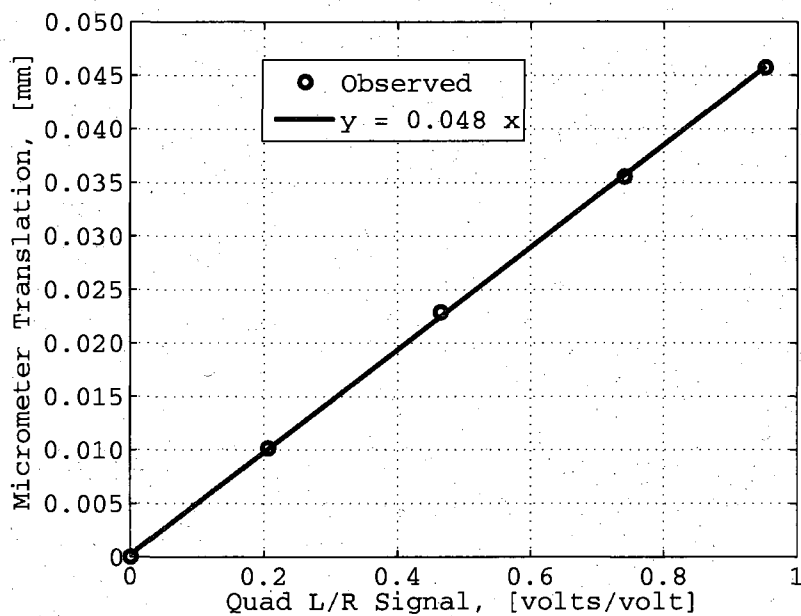


(a) Micrometer Translation vs. Sensor Voltage.

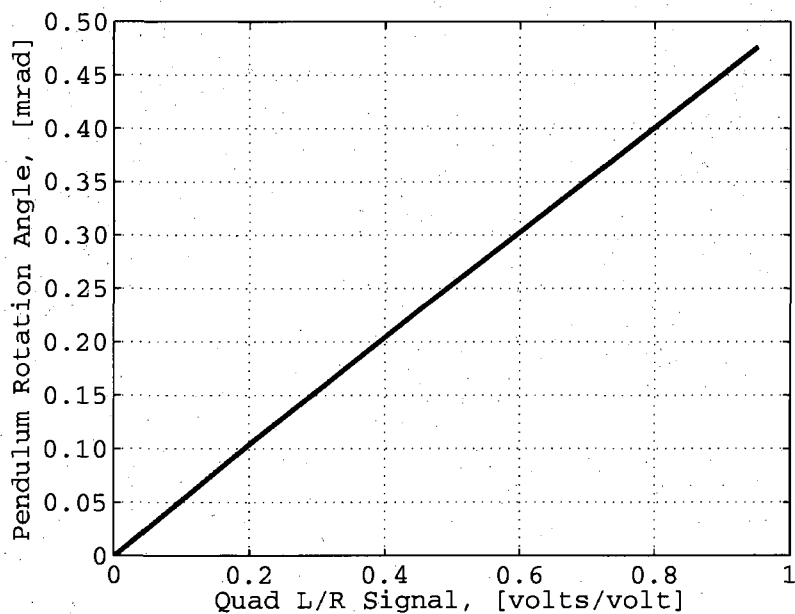


(b) Rotation Angle vs. Sensor Voltage. Slope: 2.39 mrad/volt

Figure A.2: PSD sensor calibration curves.



(a) Micrometer Translation vs. Sensor Signal



(b) Rotation Angle vs. Sensor Signal. Slope: 0.5 mrad/signal

Figure A.3: Quad sensor calibration curves.

# Appendix B

## Mechanical

### B.1 Mechanical Drawings

The mechanical drawings presented here are not intended to be fully complete for a machinist to manufacture the parts. These drawings rather present a number of the important features and dimensions associated with the parts. The majority of the parts were produced on a computer numerical control (CNC) mill and were generated by an expert (one of the best you can find) research and development model maker. The parts were produced using either a Lagun 310 CNC 3-Axis Mill or a Tree 310 CNC 3-Axis Mill. Each CNC was coupled with a Heidenhain Control. A Handsvedt Sinker EDM was used to cut the 0.015 inch (0.381 mm) slot in each wire mount to create the wire clamp feature (Figures 5.10, B.4 and B.5 ). Simple parts such as the pendulum platform assembly mounts or the first generation proof of concept grating angular sensor parts (not pictured here) were created by hand on a Bridgeport Series 1 milling machine. The estimated machining time for each of the components is listed in Table B.1.

Special thanks to Emmett Quigley, Evan Jackson, Dave Mayer and Stevan Spremo for their help in making the designed parts a reality. In addition, their valued comments had an influence on some of the final design details, especially for making the final product into one which could be machined and still function as originally intended.



<b>Component</b>	<b>Hours</b>	<b>Figure</b>
Pendulum Platform	25	B.1, B.2, B.3
Angled Wire Mount (Pair)		B.4
Part	20	
EDM of Wire Clamp Slot	8	
Vertical Wire Mount		B.5
Part	10	
EDM of Wire Clamp Slot	5	
Grating Mount Top	6	B.6
Grating Mount Bottom	10	B.7
Sphere Mount Fixture	10	B.8
Platform Assembly Mount (Three)	12	B.9

Table B.1: Estimated machining time for pendulum components.

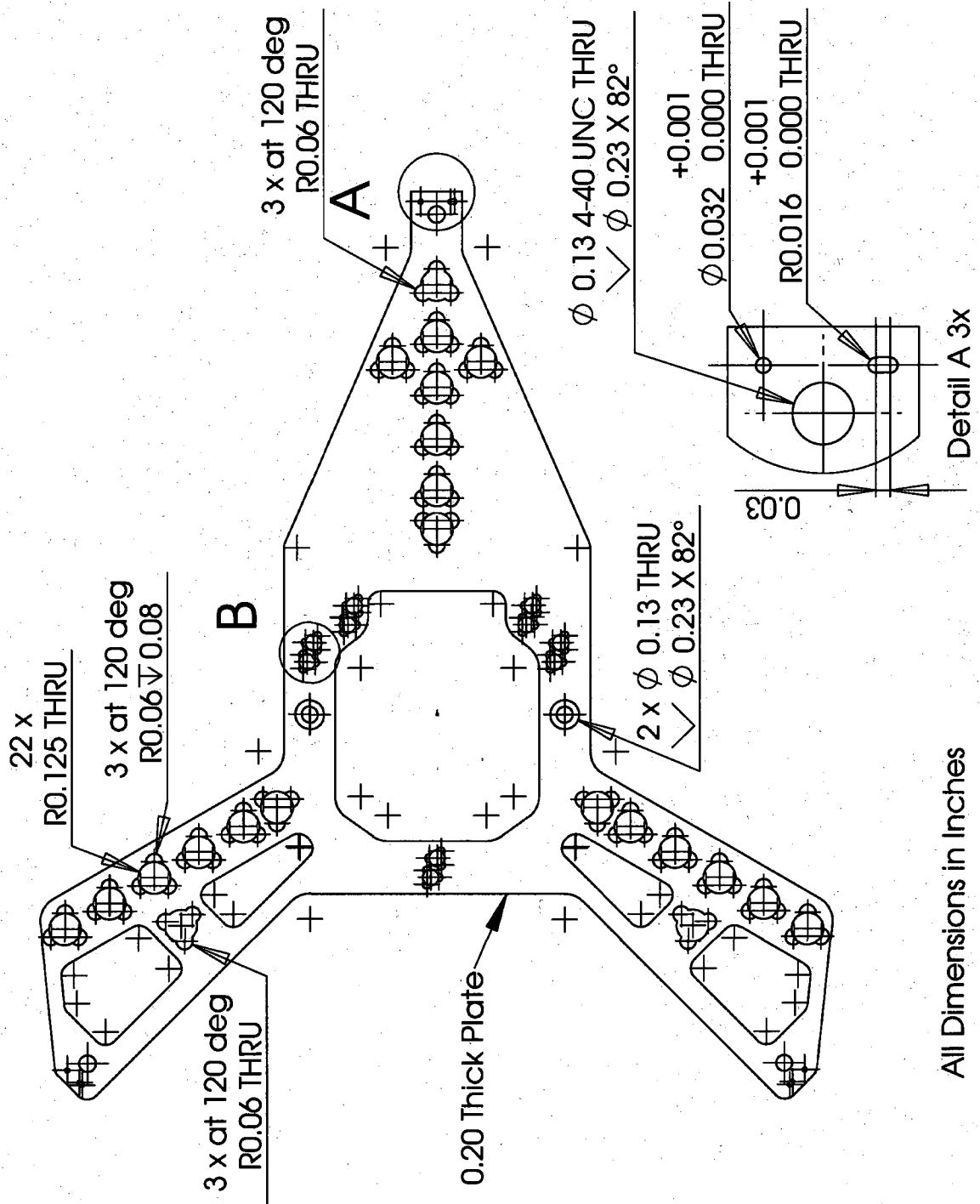


Figure B.1: Mechanical Drawing: Pendulum platform.

All Dimensions in Inches

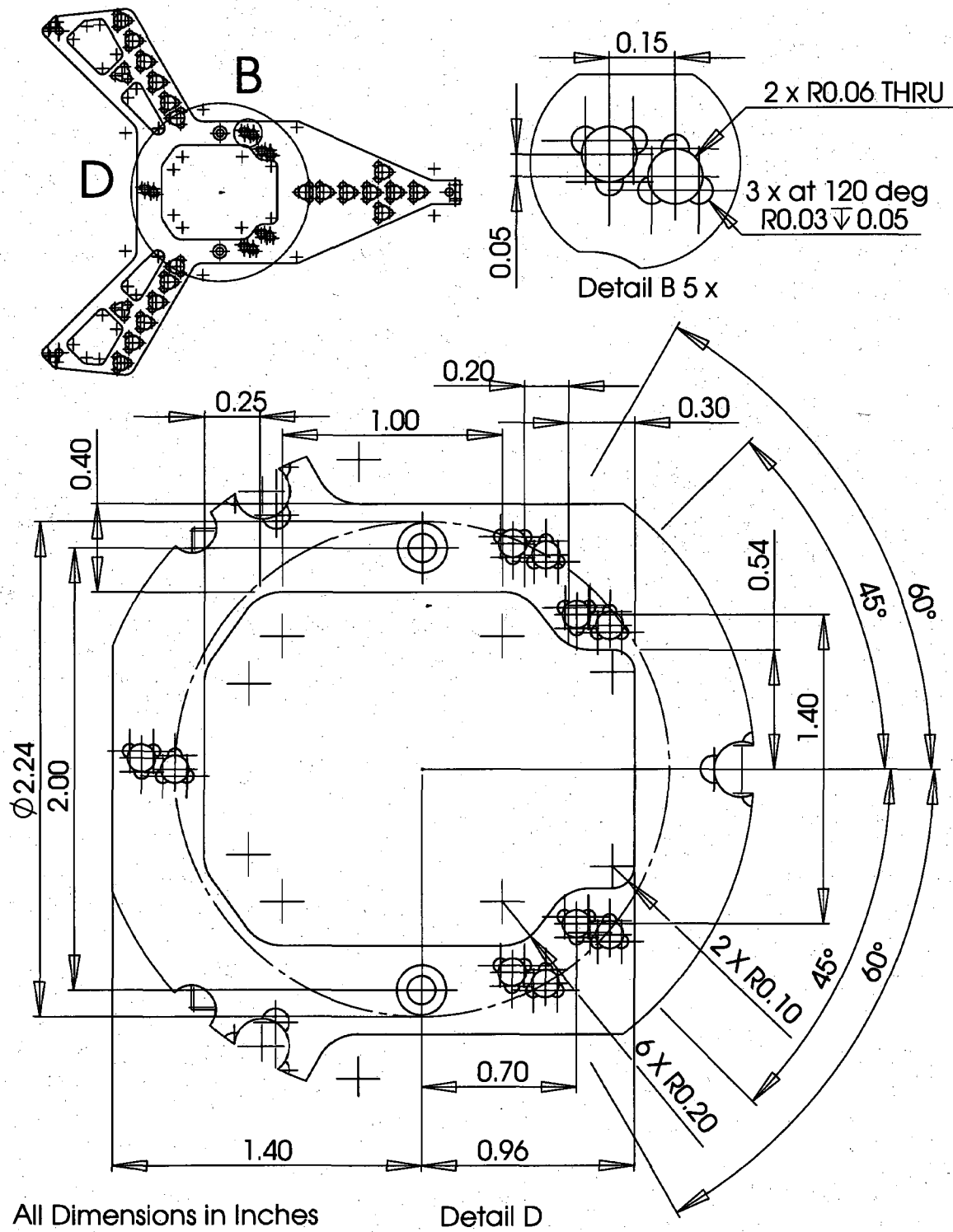


Figure B.2: Mechanical Drawing: Pendulum platform, mounting fixture holes.

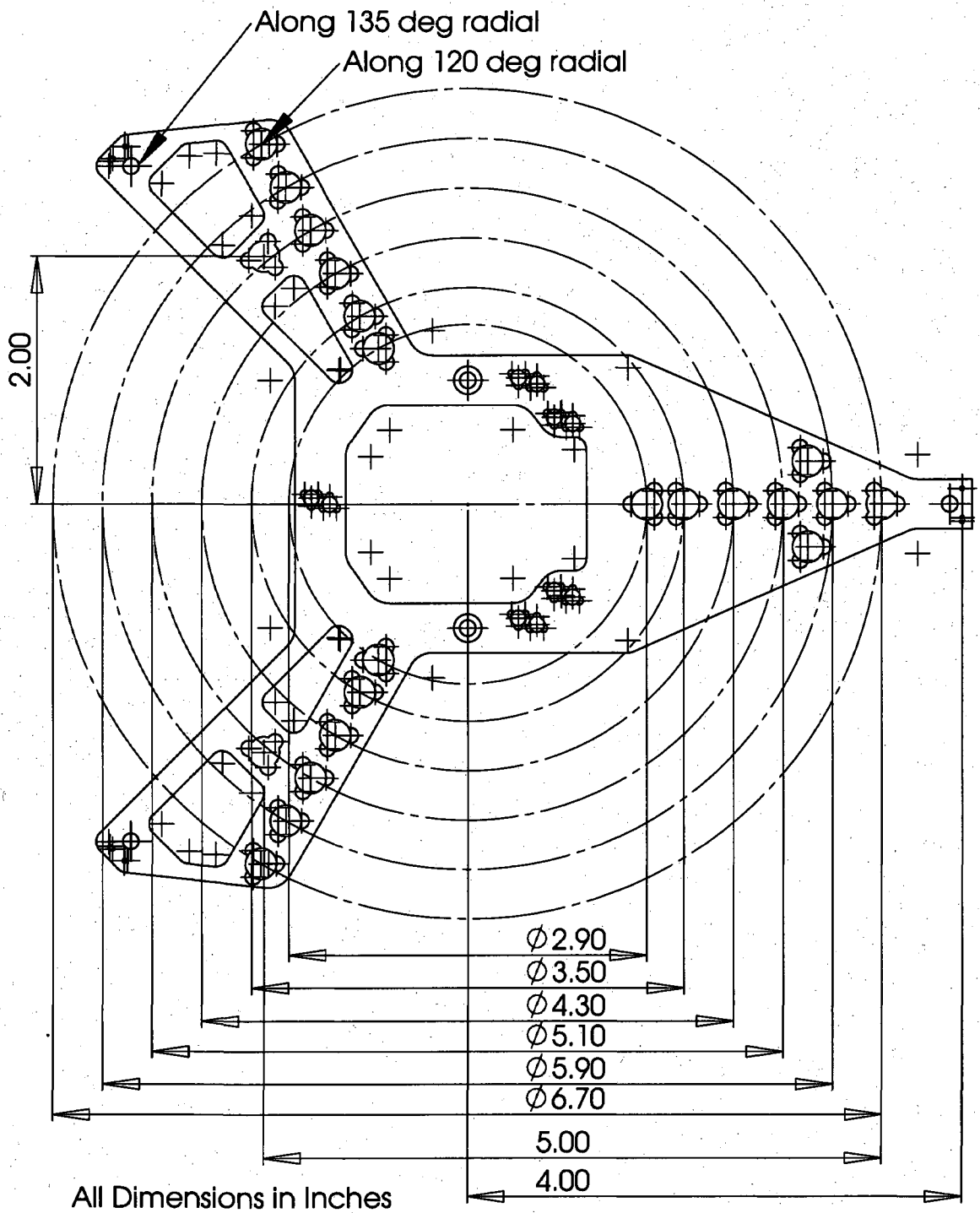


Figure B.3: Mechanical Drawing: Pendulum platform, calibration holes.

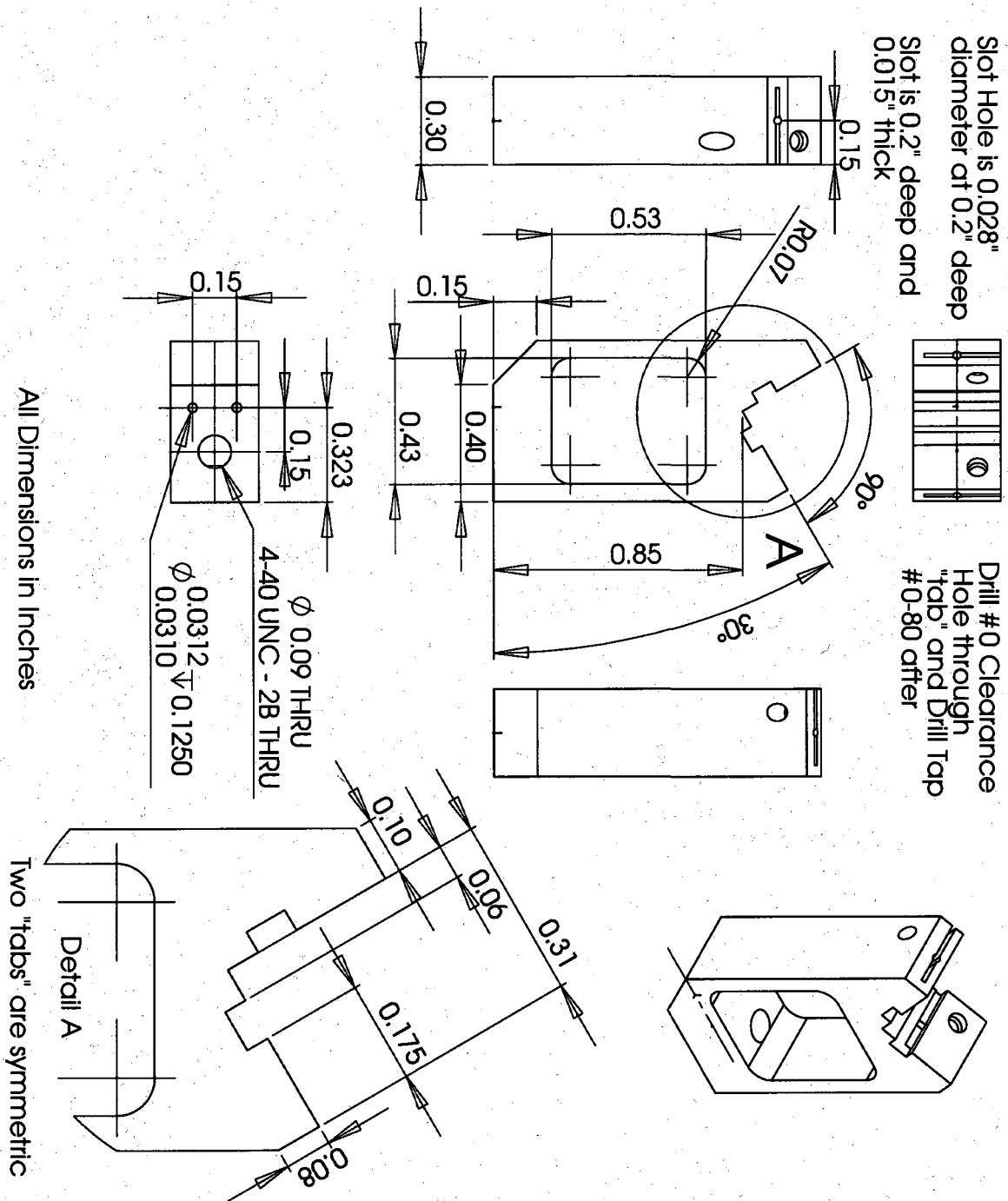


Figure B.4: Mechanical Drawing: Pendulum angled wire mount.

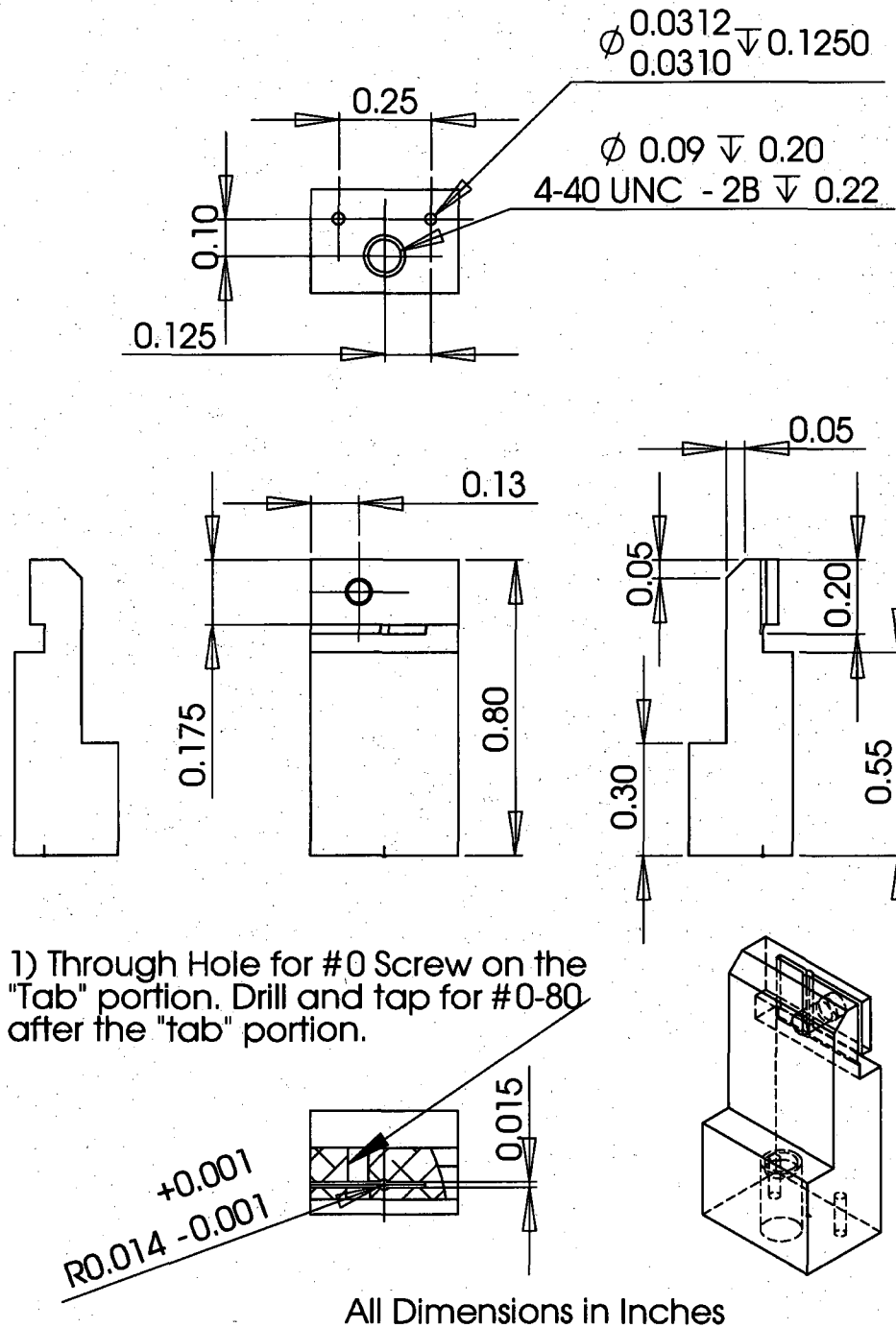


Figure B.5: Mechanical Drawing: Pendulum vertical wire mount.

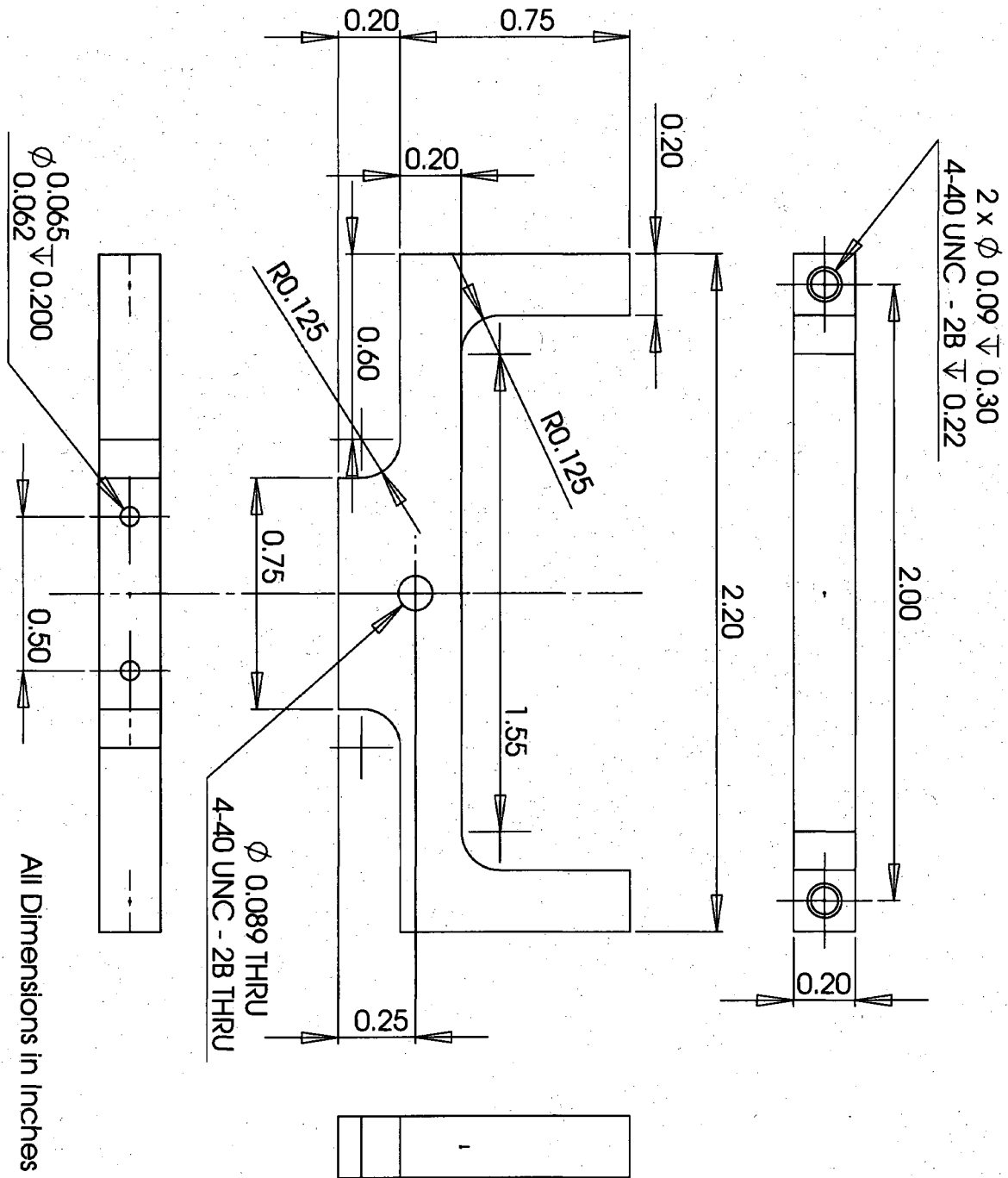


Figure B.6: Mechanical Drawing: Grating mount top portion.

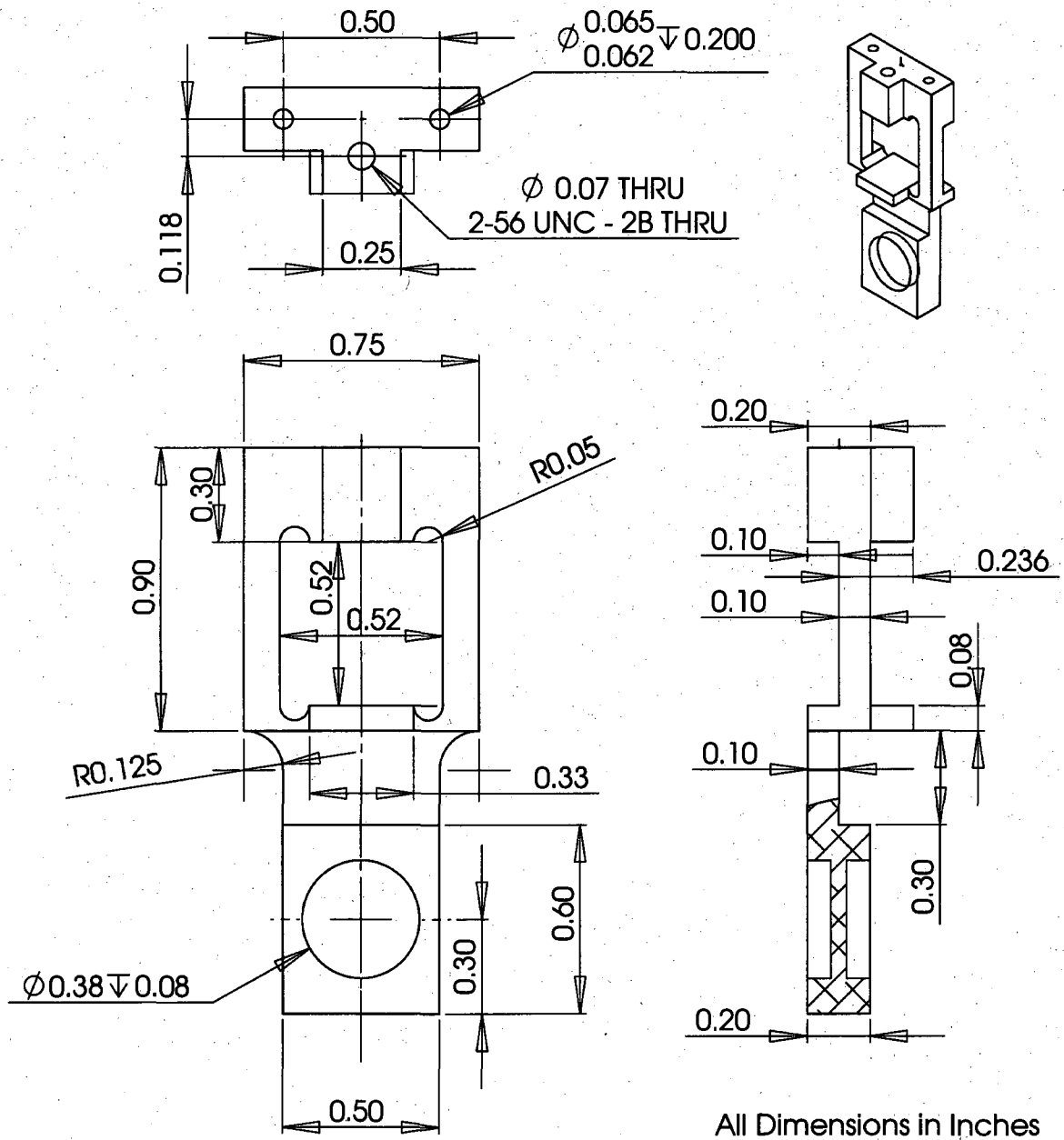


Figure B.7: Mechanical Drawing: Grating and magnet mount bottom part.



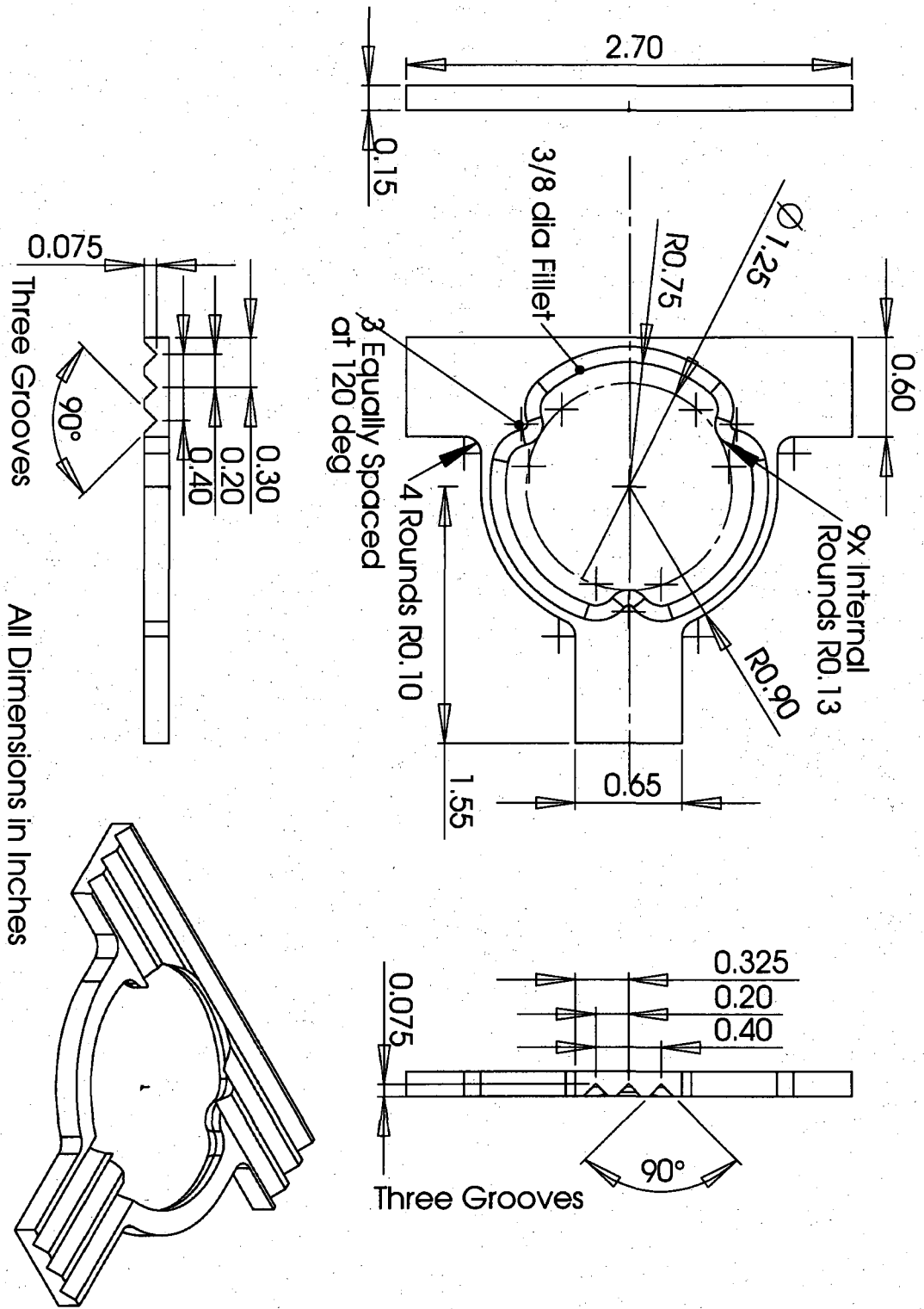


Figure B.8: Mechanical Drawing: Sphere mounting fixture.

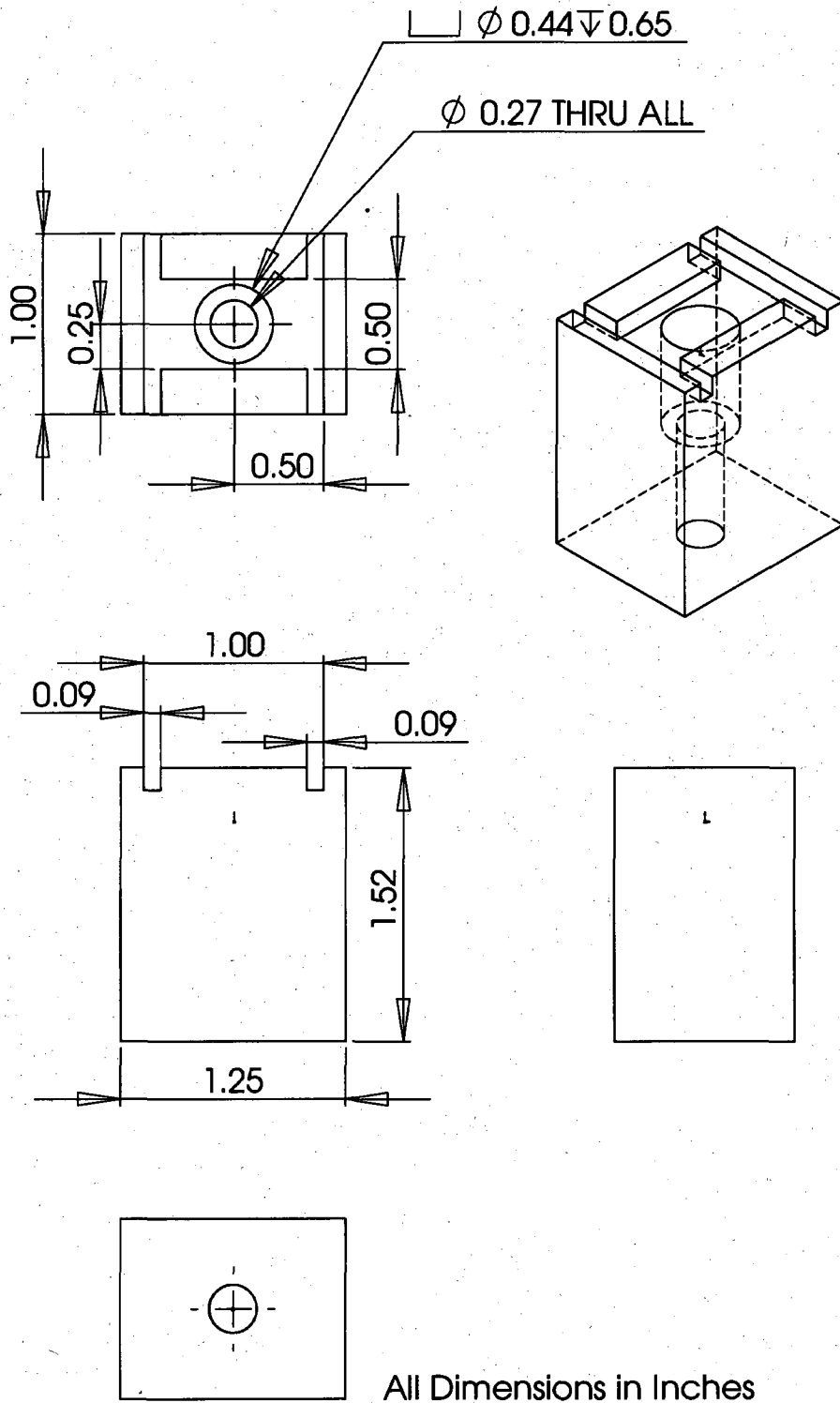


Figure B.9: Mechanical Drawing: Pendulum platform assembly mount.

## B.2 Measurement Apparatus Parameters

Parameter		Value	Notes
Pendulum Inertia	$I_p$	398.3 kg·mm <sup>2</sup>	SolidWorks Estimate
Pendulum Mass	$m_p$	124.08 g	Measured, Assembled
Sphere Mount Mass	$m_s$	11.73 g	Measured
Characteristic Wire Length	$L_o$	114.3 mm	Design value: 4.5 inches
Vertical Wire Length	$L_1$	114.3 mm	Design value: 4.5 inches
Short Wire Length	$L_2$	76.2 mm	Design value: 3.0 inches
Long Wire Length	$L_3$	304.8 mm	Design value: 12.0 inches
Wire Attach Point Radius	$r$	101.6 mm	Design value: 4.0 inches
Radius to Mass Center Mount	$R$	74.9 mm	Design value: 2.95 inches
Hole Set 1 Radius	HS1	36.8 mm	Design value: 1.45 inches
Hole Set 2 Radius	HS2	44.5 mm	Design value: 1.75 inches
Hole Set 3 Radius	HS3	54.6 mm	Design value: 2.15 inches
Hole Set 4 Radius	HS4	64.8 mm	Design value: 2.55 inches
Hole Set 5 Radius	HS5	74.9 mm	Design value: 2.95 inches
Hole Set 6 Radius	HS6	85.1 mm	Design value: 3.35 inches
3/8 inch Cal. Sphere Mass	$m_b$	3.61 g	Measured
7/16 inch Cal. Sphere Mass	$m_b$	5.63 g	Measured
1/2 inch Cal. Sphere Mass	$m_b$	8.39 g	Measured
3/4 inch Cal. Sphere Mass	$m_b$	28.19 g	Measured

Table B.2: Measurement apparatus parameters.

**B.3 Bill of Materials**

Item	Description	Qty	Part Number
Ball Bearing	Diameter 3/8 in. Sphericity 0.0001 in. 316 Stainless	3	McMaster: 96415K77
Ball Bearing	Diameter 7/16 in. Sphericity 0.0001 in. 316 Stainless	3	McMaster: 96415K78
Ball Bearing	Diameter 1/2 in. Sphericity 0.0001 in. 316 Stainless	3	McMaster: 96415K79
Ball Bearing	Diameter 3/4 in. Sphericity 0.0001 in. 316 Stainless	3	McMaster: 96415K81

Table B.3: Bill of Materials: Calibration and Trim Mass Spheres.

Item	Description	Qty	Part Number
Straightened Wire	Diameter: 0.005 in. 304 Stainless Tungsten	1	SmallParts: GWX-0050-30-05
		5	SmallParts: TW-005-30
Straightened Wire	Diameter: 0.010 in. 304 Stainless Tungsten	1	SmallParts: GWX-0100-30-05
		5	SmallParts: TW-010-30
Straightened Wire	Diameter: 0.013 in. 304 Stainless Tungsten	1	SmallParts: GWX-0130-30-05
		5	SmallParts: TW-013-30
Hypodermic Tubing	I.D. 0.00625 in. O.D. 0.01225 in. 304 Stainless	5	SmallParts: HTX-30R-06-05
Hypodermic Tubing	I.D. 0.00725 in. O.D. 0.01425 in. 304 Stainless	5	SmallParts: HTX-28R-06-05
Hypodermic Tubing	I.D. 0.01225 in. O.D. 0.02225 in. 304 Stainless	5	SmallParts: HTX-24R-06-05
Hypodermic Tubing	I.D. 0.013 in. O.D. 0.025 in. 304 Stainless	5	SmallParts: HTX-23R-06-05
Hypodermic Tubing	I.D. 0.01625 in. O.D. 0.02825 in. 304 Stainless	5	SmallParts: HTX-22R-06-05

Table B.4: Bill of Materials: Support Wires.

Item	Description	Qty	Part Number
Dowel Pin	1/32 in. Diameter Length 1/4 in. 18-8 Stainless	6	McMaster: 90145A312
Spring Pin	1/16 in. Diameter 3/8 in. Length 18-8 Stainless	2	McMaster: 92373A107
Cap Screw	#4-40 Flat Head Hex Socket Length 3/8 in. 316 Stainless	5	McMaster: 90585A202
Hex Screw	#0-80 Length 1/8 in. 316 Stainless	5	McMaster: 92200A052
Hex Screw	#4-40 Length 3/8 in. 316 Stainless	1	McMaster: 92185A108
Set Screw	#2-56, Length 1/4 in. 316 Stainless	1	McMaster: 92313A022
Round Spacer	1/4 in. O.D. I.D. for #4 Screw 7/32 in. Length 18-8 Stainless	1	McMaster: 92320A034
Pin Vise	Single End 0 in. to 0.055 in. 5/16 in. Diameter	5	McMaster: 8455A16

Table B.5: Bill of Materials: Fasteners.

Item	Description	Qty	Part Number
NPRO Laser	1064 nm wavelength	1	Lightwave Electronics: 120-03A
Grating	1200 lines/mm 1000 nm wavelength 12.7 mm square	1	Edmund Optics: NT43-851
Optics Post	7 in., Stainless Steel 1/4-20 Thread	6	Newport: P-7
Optics Post	3 in., Stainless Steel 1/4-20 Thread	3	Newport: P-3
Optics Mount	2 in. Pedestal	2	New Focus: RS2P
Optics Mount	Clamping Fork	3	ThorLabs: CF125
Optics Mount	Sliding Base Clamp	2	Newport: SB-TPS
Mirror	Silver Coated Mirror	2	New Focus: 5103
Mirror Mount	Corner Mount	2	New Focus: 9809
Riser Plate	4 in. x 4 in. x 0.25 in.	3	Newport: MRP4-0.25
Riser Plate	4 in. x 4 in. x 0.5 in.	1	Newport: MRP4-0.5
Riser Plate	10 in. x 6 in. x 0.5 in.	1	Newport: 290-TP
Riser Plate	10 in. x 6 in. x 0.5 in.	2	Newport: 290-BP
Position Sensitive Diode	One-Dimensional PSD	1	On-Trak: 1L10
Quadrant Photodiode	Large Area Silicon Detector, 3/8 in. Diam.	1	Pacific Sensor
Translation Stage		1	Newport: 423 Series
90-deg Mount		1	Newport: 360-90

Table B.6: Bill of Materials: Optics

# Appendix C

## Electrical

### C.1 Instrumentation

<b>Instrumentation</b>	<b>Model Number</b>
GPIB PCI Card	Agilent 82350B
Oscilloscope	Texktronix TDS5054B
Function Generator	Agilent 3320A
Digital Multimeter	Agilent 34401A
Triple Output Power Supply	Agilent E3631
DC Power Supply	HP 6038A
Digital Temperature Monitor	Omega 747
Universal Frequency Counter	HP 53132A
Dynamic Signal Analyzer	HP 3562A

Table C.1: Experimental apparatus instrumentation.



## C.2 Schematics

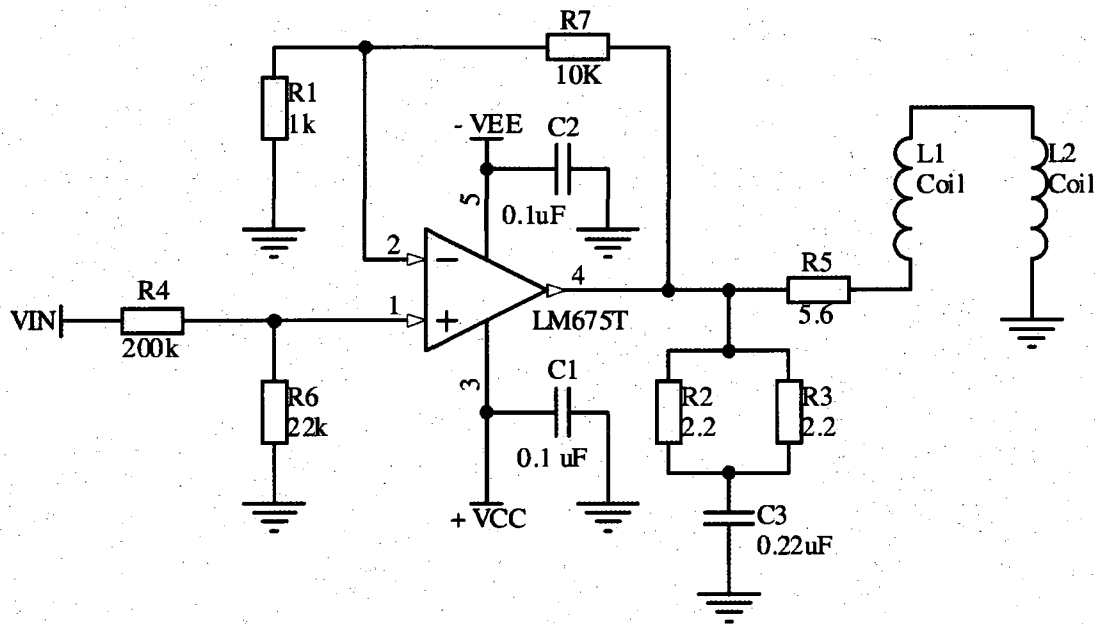


Figure C.1: Schematic: Pendulum coil driver.

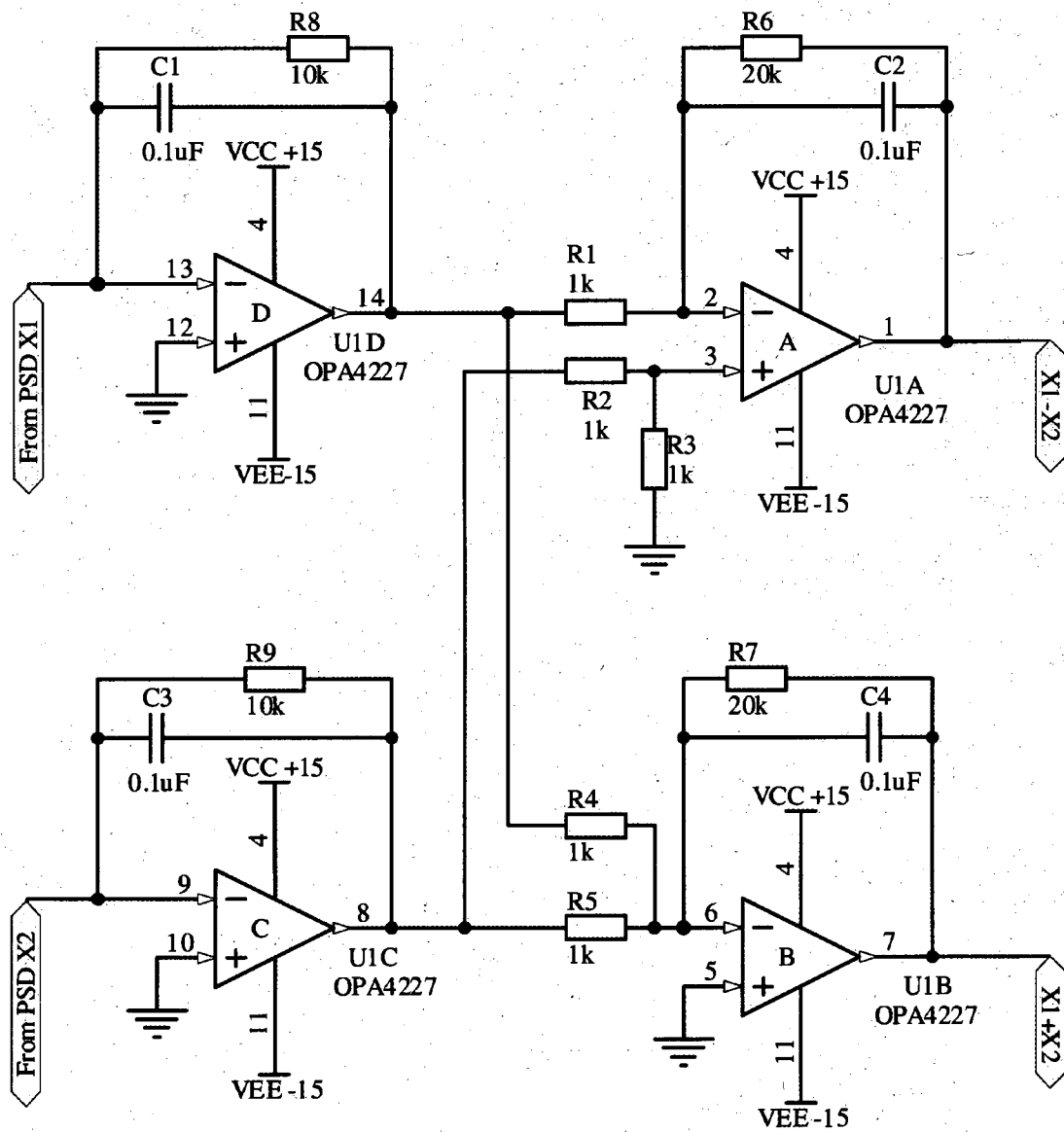


Figure C.2: Schematic: Position sensitive diode.

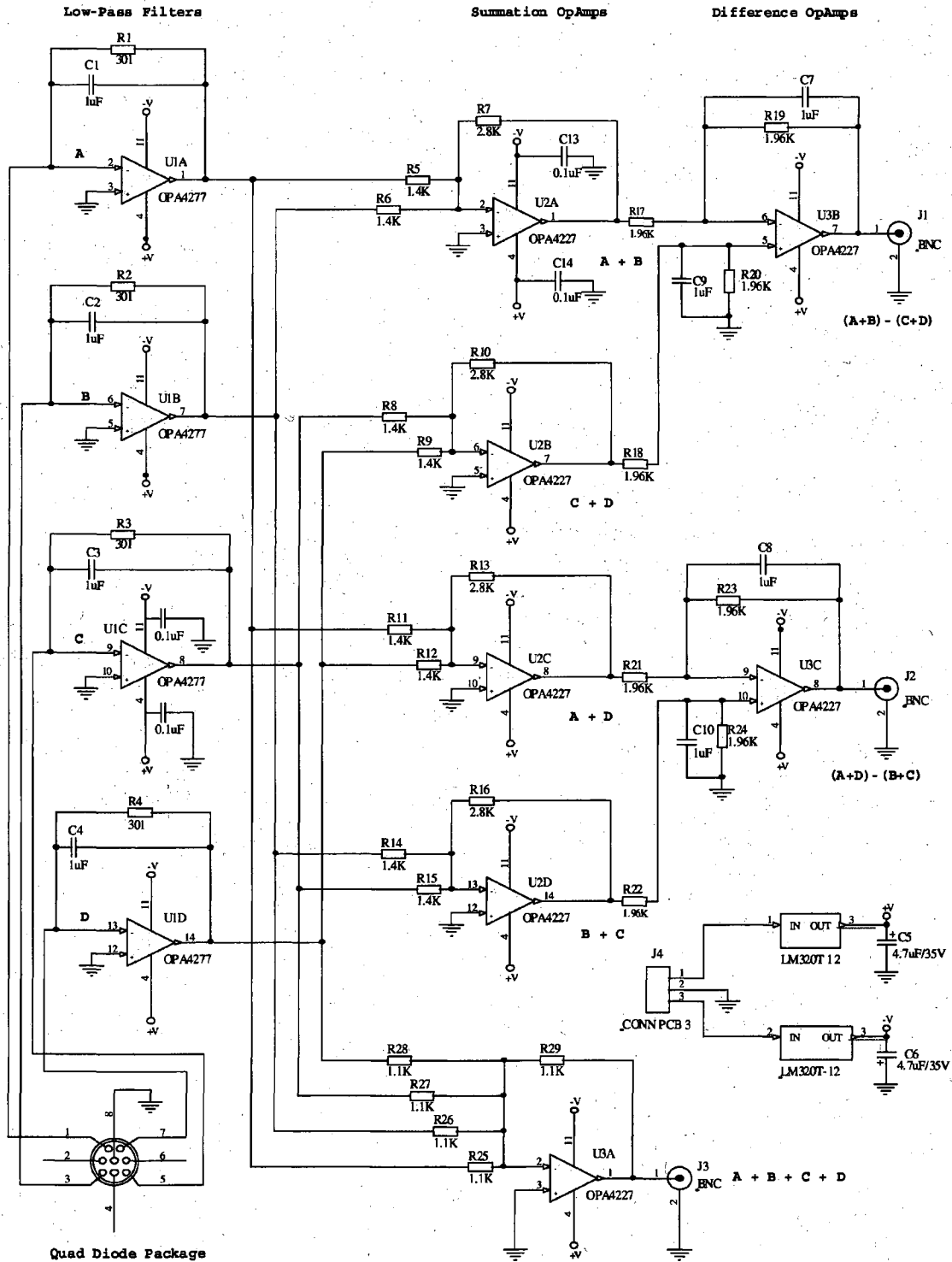


Figure C.3: Schematic: Quadrant photodiode, autocollimator.

# Appendix D

## Software

The software used for this project falls into two categories:

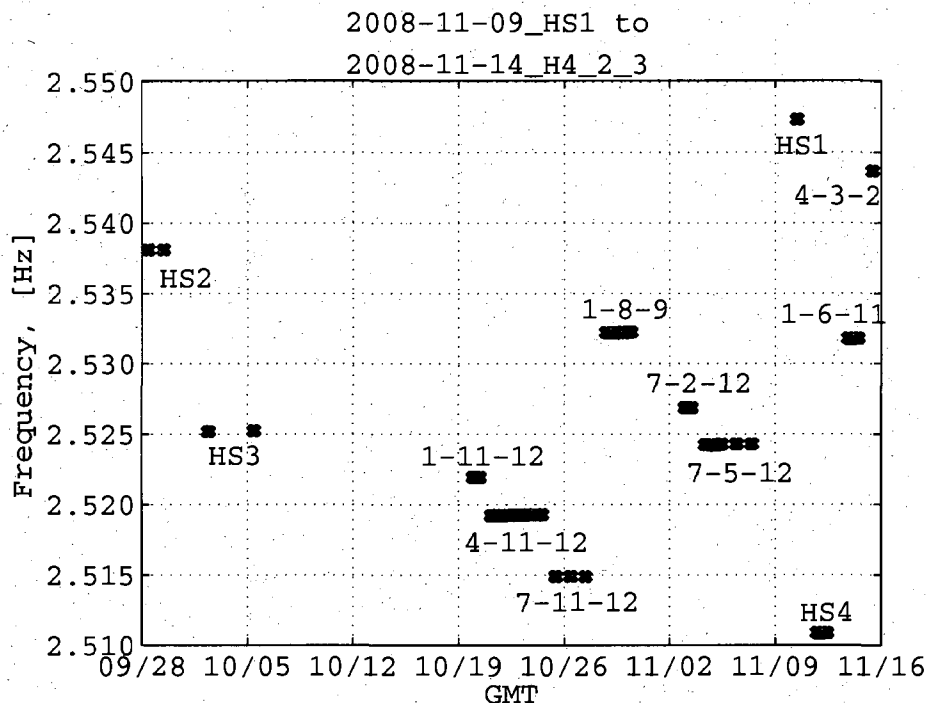
1. Software to perform the double Taylor method for gravitational mass attraction.
2. Software to automate the five-wire pendulum and measurements.

The software for the double Taylor method was written using Fortran 90. Early versions utilized both MPI and OpenMP for parallel computing methods. The final version utilized only OpenMP calls. The software was primarily used to verify the double Taylor method and to investigate the contribution due to higher order terms in the expansion.

The software created for the five-wire pendulum operation was written in python and was designed to have a modular fashion. For each GPIB device used in the instrumentation setup as listed in Table C.1, a python module was created to perform common GPIB commands to the instrument. The modules could then be used to operate each device. These building blocks were used to automate the measurement procedure and data acquisition. Automated measurements could then be performed remotely or by using a time-based job scheduler, allowing middle of the night measurements to avoid disturbances due to human activity. The software modules are available from the author and are released by the author under the GNU Public License. The modules were designed to use the gpib-linux package.

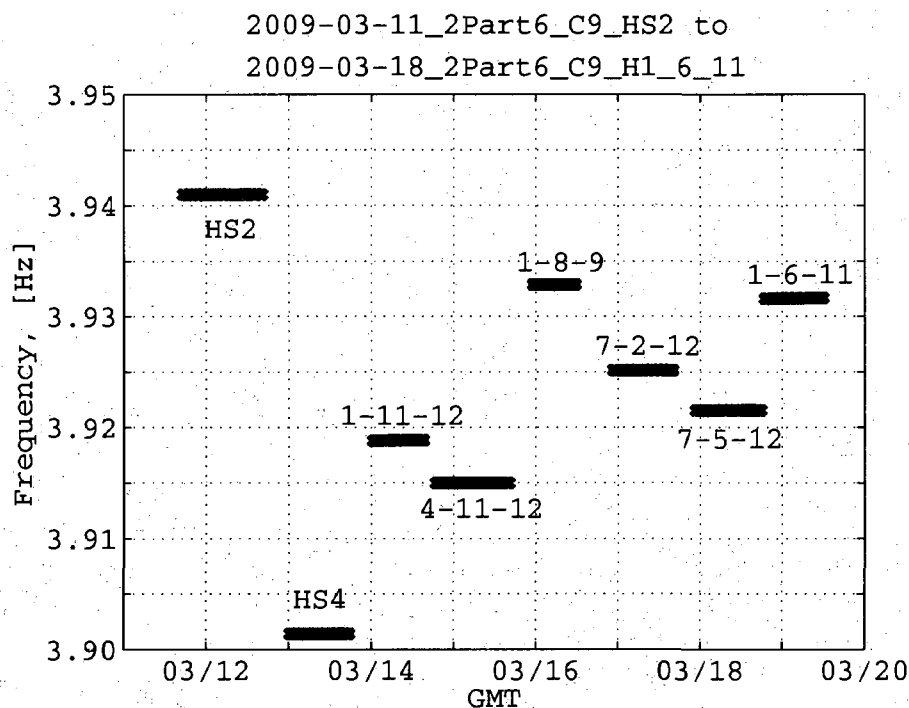
# Appendix E

## Measurement Data



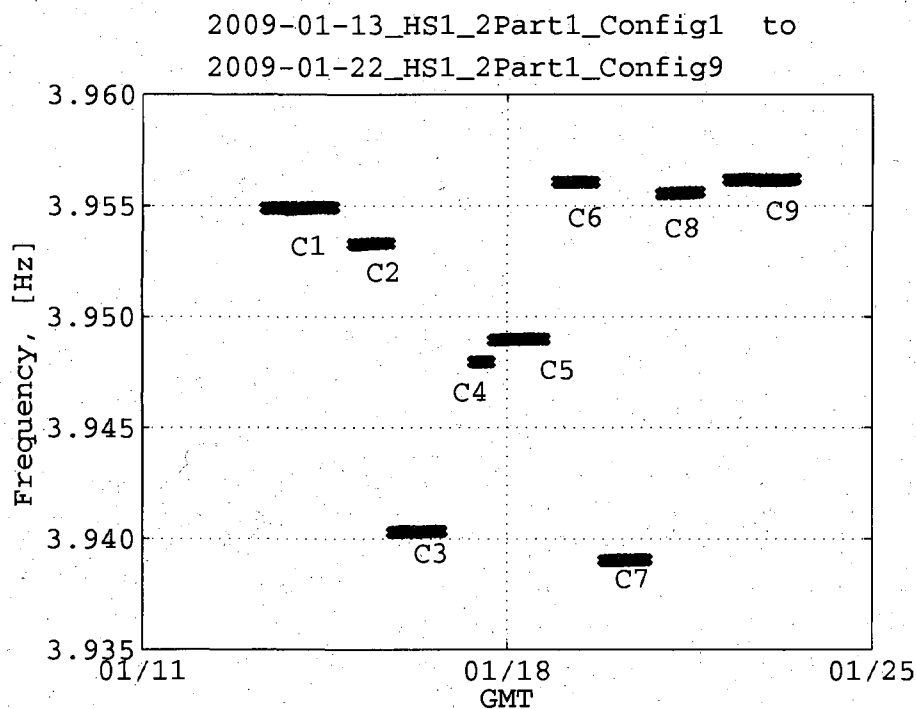
Config	Frequency [Hz]	$\sigma$ $\times 10^{-5}$ [Hz]	# Measurements
HS1	2.547 314	0.4	12
HS2	2.538 104	0.7	22
HS3	2.525 208	2.3	23
HS4	2.510 835	3.7	42
1-11-12	2.521 920	1.0	44
4-11-12	2.519 232	2.8	155
7-11-12	2.514 887	0.5	31
1-8-9	2.532 219	2.3	88
7-2-12	2.526 860	0.7	32
7-5-12	2.524 237	3.2	77
1-6-11	2.531 761	2.1	42
4-3-2	2.543 671	0.5	12

Table E.1: Measurement Data for Pendulum Calibration with Sphere Mount. The measurements were performed with the sphere mount in the nominal center location and with the 3/4 inch trim mass spheres in hole set 6.



Config	Frequency [Hz]	$\sigma$ $\times 10^{-5}$ [Hz]	# Measurements
HS2	3.940 983	2.04	48
HS4	3.901 397	1.67	38
1-11-12	3.918 799	1.40	33
4-11-12	3.914 960	1.10	45
1-8-9	3.932 824	1.13	28
7-2-12	3.925 108	1.76	37
7-5-12	3.921 516	2.06	41
1-6-11	3.931 587	2.38	34

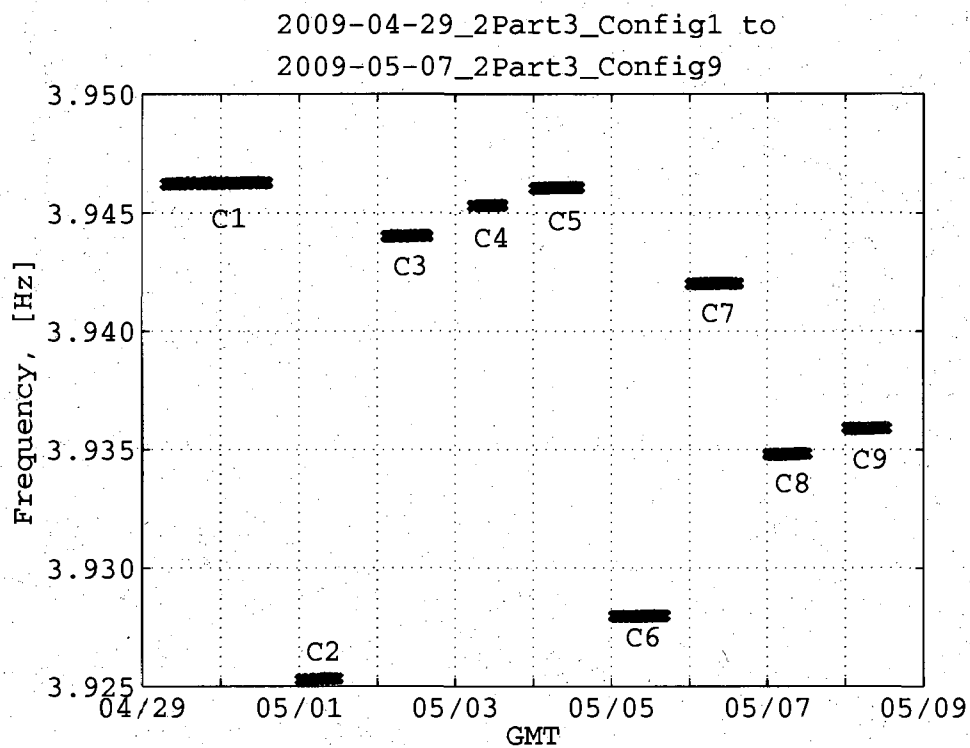
Table E.2: Measurement Data for Pendulum Calibration with Measurement Object. The preferred principal axis of inertia sphere number six was on the pendulum platform in orientation configuration nine. The measurements were performed with the sphere mount in the nominal center location and with the 3/4 inch trim mass spheres in hole set 6.



Config	Frequency [Hz]	$\sigma$ $\times 10^{-5}$ [Hz]	# Measurements
1	3.954 899	3.08	68
2	3.953 273	2.82	30
3	3.940 309	2.36	49
4	3.947 950	1.39	18
5	3.948 968	1.71	50
6	3.956 053	0.96	30
7	3.939 028	2.14	39
8	3.955 566	2.43	30
9	3.956 146	2.54	62

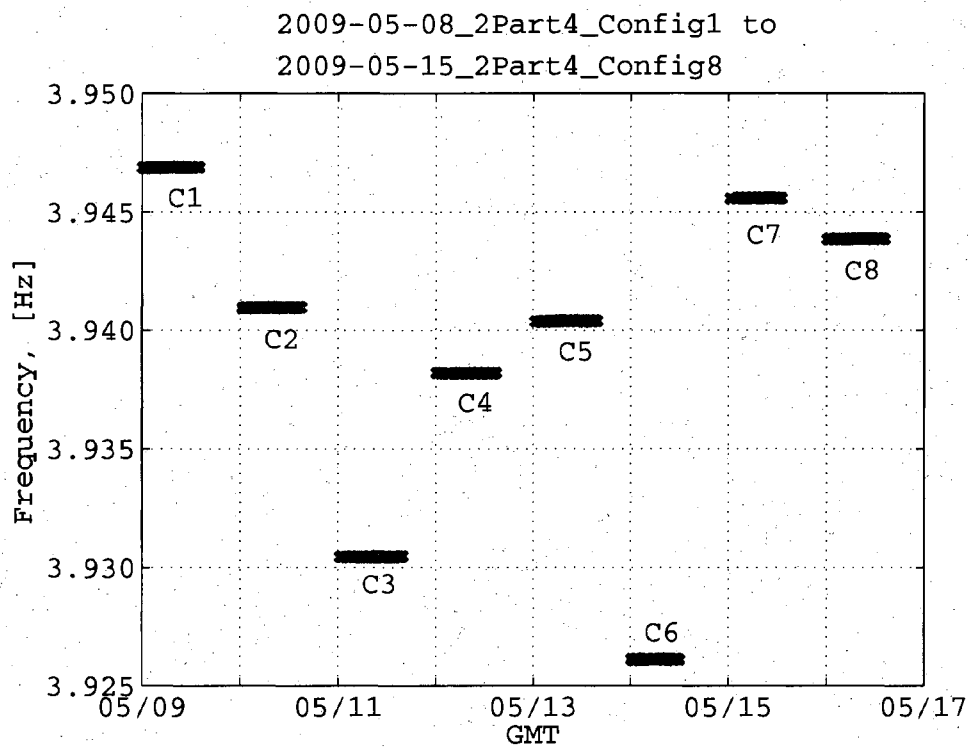
Table E.3: Measurement Data for 2-Part Sphere Number 1. The frequency measurements are for the combined pendulum platform with sphere fixture, 3/8 inch calibration sphere in hole set 1, and the 3/4 inch trim mass spheres in hole set 6.





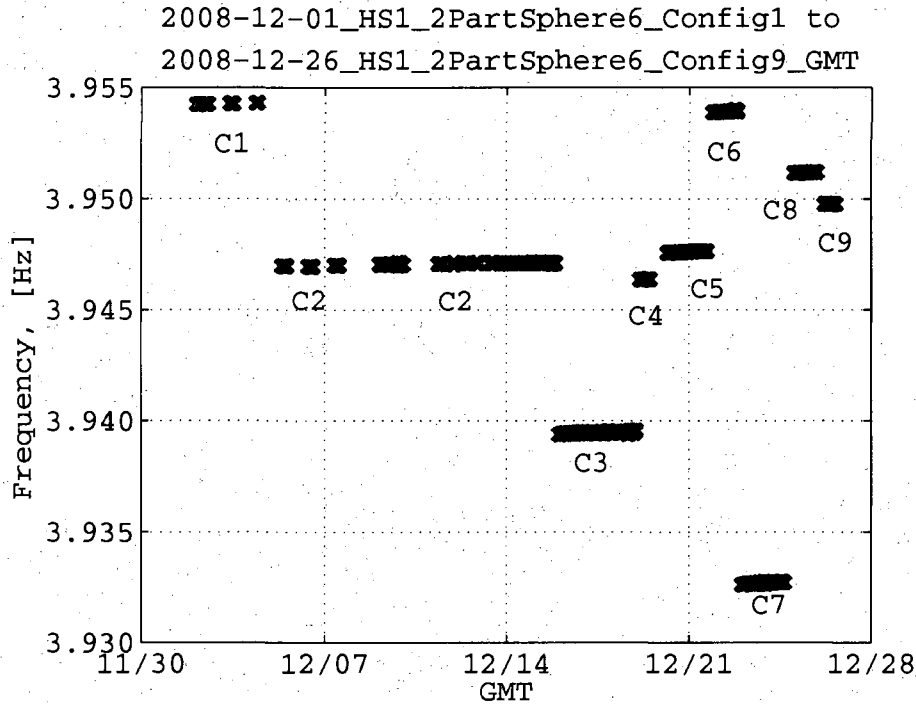
Config	Frequency [Hz]	$\sigma$ $\times 10^{-5}$ [Hz]	# Measurements
1	3.946 251	2.37	62
2	3.925 280	3.43	23
3	3.944 020	1.49	28
4	3.945 304	0.98	19
5	3.946 053	1.36	30
6	3.927 950	1.36	33
7	3.942 009	1.11	29
8	3.934 799	1.29	24
9	3.935 871	1.77	25

Table E.4: Measurement Data for 2-Part Sphere Number 3. The frequency measurements are for the combined pendulum platform with sphere fixture, 3/8 inch calibration sphere in hole set 1, and the 3/4 inch trim mass spheres in hole set 6.



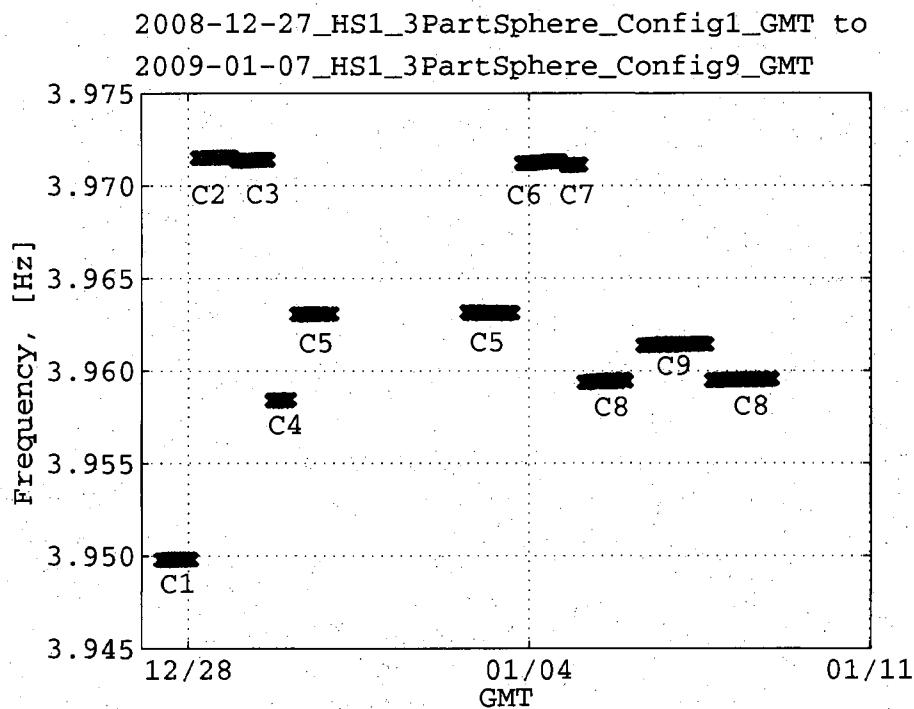
Config	Frequency [Hz]	$\sigma$ $\times 10^{-5}$ [Hz]	# Measurements
1	3.946 877	1.24	29
2	3.940 950	1.22	30
3	3.930 441	1.40	31
4	3.938 174	0.96	28
5	3.940 376	1.87	33
6	3.926 106	1.74	26
7	3.945 572	1.41	25
8	3.943 858	1.34	30

Table E.5: Measurement Data for 2-Part Sphere Number 4. The frequency measurements are for the combined pendulum platform with sphere fixture, 3/8 inch calibration sphere in hole set 1, and the 3/4 inch trim mass spheres in hole set 6.



Config	Frequency [Hz]	$\sigma$ $\times 10^{-5}$ [Hz]	# Measurements
1	3.954 257	2.58	36
2	3.947 062	4.64	237
3	3.939 457	3.97	150
4	3.946 357	1.81	26
5	3.947 610	3.18	80
6	3.953 920	3.34	51
7	3.932 671	3.83	85
8	3.951 166	1.65	46
9	3.949 759	1.73	25

Table E.6: Measurement Data for 2-Part Sphere Number 6. The frequency measurements are for the combined pendulum platform with sphere fixture, 3/8 inch calibration sphere in hole set 1, and the 3/4 inch trim mass spheres in hole set 6.



Config	Frequency [Hz]	$\sigma$ $\times 10^{-5}$ [Hz]	# Measurements
1	3.949 831	1.86	34
2	3.971 542	1.74	37
3	3.971 397	2.37	33
4	3.958 421	2.74	17
5	3.963 067	1.10	28
6	3.971 301	2.81	27
7	3.971 121	1.86	14
8	3.959 518	2.75	57
9	3.961 444	1.77	28

Table E.7: Measurement Data for 3-Part Sphere Number 8. The frequency measurements are for the combined pendulum platform with sphere fixture, 3/8 inch calibration sphere in hole set 1, and the 3/4 inch trim mass spheres in hole set 6.

# References

- [1] ABRAMOWITZ, M. and STEGUN, I. A., eds., *Handbook of Mathematical Functions With Formulas, Graphs, and Mathematical Tables*, Dover Publications, New York, 1974.
- [2] BANERJEE, B. and GUPTA, S. P. D., “Short note, gravitational attraction of a rectangular parallelepiped,” *Geophysics*, vol. 42, no. 5, pp. 1053–1055, August 1977.
- [3] BATTIN, R. H., *An Introduction to the Mathematics and Methods of Astrodynamics*, AIAA Education Series, American Institute of Aeronautics and Astronautics, Washington, D. C., 1987, ISBN 1563473429.
- [4] BLAKELY, R. J., *Potential Theory in Gravity & Magnetic Applications*, Cambridge University Press, Cambridge, 1995, ISBN 0521575478.
- [5] BOWER, J., NELSON, E., and THIELVOLDT, M., “Sphere with adjustable mass center for the LISA project,” ME 324 precision engineering course, final report, Stanford University, 2005.
- [6] CAVALLERI, A., CIANI, G., DOLESI, R., HEPTONSTALL, A., HUELLER, M., NICOLODI, D., ROWAN, S., TOMBOLATO, D., VITALE, S., WASS, P. J., and WEBER, W. J., “A new torsion pendulum for testing the limits of free-fall for LISA test masses,” *Classical and Quantum Gravity*, vol. 26, no. 9, 2009.
- [7] CHEN, Y. T. and COOK, A., *Gravitational Experiments in the Laboratory*, Cambridge University Press, Cambridge, April 1993, ISBN 0521391717.

- [8] CLARK, D., DOLPHIN, M., DREISSIGACKER, M., TRITTLER, M., and ULMEN, J., "Preferred principal axis of inertia spheres," ME 324 precision engineering course, final report, Stanford University, 2007.
- [9] CONKLIN, J. W., *Estimation of the mass center and dynamics of a spherical test mass for gravitational reference sensors*, Ph.D. thesis, Stanford University, Dec. 2008.
- [10] CONKLIN, J. W., SUN, K.-X., and DEBRA, D. B., "Gravitational reference center of mass determination by velocity modulation," *Proceedings of the 21st Annual Meeting*, October 2006. Monterey, California.
- [11] CONKLIN, J. W., SUN, K.-X., and DEBRA, D. B., "Mass center determination by optical sensing of velocity modulation," *Laser Interferometer Space Antenna: 6th International LISA Symposium*, vol. 873, no. 1, pp. 566–570, 2006.
- [12] CONKLIN, J. W., SWANK, A. J., SUN, K.-X., and DEBRA, D. B., "Mass properties measurement for drag-free test masses," *Journal of Physics: Conference Series*, vol. 154, 2009.
- [13] DASSOULAS, J., "The TRIAD spacecraft," *The APL Technical Digest*, vol. 12, no. 2, 1973.
- [14] DAVIS, R. S., "NIST measurement services: mass calibrations," NIST Special Publication 250-31, U.S. Department of Commerce, National Institute of Standards and Technology, January 1989.
- [15] DEBRA, D. B., "Disturbance compensation system design," *The APL Technical Digest*, vol. 12, no. 2, 1973.
- [16] DEBRA, D. B., "Drag-free spacecraft as platforms for space missions and fundamental physics," *Classical and Quantum Gravity*, vol. 14, no. 6, pp. 1549–1555, 1997.
- [17] DEBRA, D. B., Personal correspondence, March 2009.

- [18] DEDE, E., GLASSMAN, J., HARDHAM, C., KALCIC, D., and RICHMOND, K., "Inertia pendulum for the STEP project," ME 324 precision engineering course, final report, Stanford University, 2001.
- [19] DOLPHIN, M. D., *Polhode dynamics and gyroscope asymmetry analysis on gravity Probe B using gyroscope position data*, Ph.D. thesis, Stanford University, Sept. 2007.
- [20] EVANS, J. P., "Plan for compensation of self-gravity on ST-7/DRS," *Classical and Quantum Gravity*, vol. 22, no. 10, pp. 177–183, 2005.
- [21] EVANS, J. P., "Engineering the LISA project: systems engineering challenges," *Aerospace Conference, 2006 IEEE*, 2006.
- [22] FLEMING, A. W., TASHKER, M. G., and DEBRA, D. B., "Mass attraction of Triad-1/DISCOS," Tech. rep., Stanford University, Center for Systems Research, Guidance and Control Laboratory, September 1972.
- [23] FOLKNER, W. M., HECHLER, F., SWEETSER, T. H., VINCENT, M. A., and BENDER, P. L., "LISA orbit selection and stability," *Classical and Quantum Gravity*, vol. 14, pp. 1405–1410, 1997.
- [24] FRYKMAN, P. and VANG, R., "Drawing great circles on a spherical test mass," ME 324 precision engineering course, final report, Stanford University, 2006.
- [25] GREENWOOD, D. T., *Principles of Dynamics*, Prentice-Hall, New Jersey, 2nd ed., 1988, ISBN 0137099819.
- [26] GÜNTER, N. M., *Potential theory, and Its Applications to Basic Problems of Mathematical Physics*, Frederick Ungar Publishing, New York, 1967. Translated from Russian by John R. Schulenberger.
- [27] HANSON, J., BUCHMAN, S., GILL, D., LAUBEN, D., and WILLIAMS, S., "ST-7 gravitational reference sensor technology development program," *Aerospace Conference, 2004. Proceedings. 2004 IEEE*, vol. Vol. 1, March 2004.

- [28] HANSON, J., KEISER, G., BUCHMAN, S., BYER, R. L., LAUBEN, D., SHELEF, B., SHELEF, G., HRUBY, V., and GAMERO-CASTANO, M., "Disturbance reduction system: testing technology for drag-free operation," in CRUISE, M. and SAULSON, P., eds., "Gravitational-Wave Detection. Proceedings of the SPIE," vol. 4856, pp. 9–18, Mar 2003.
- [29] HANSON, J., KEISER, G. M., BUCHMAN, S., BYER, R., LAUBEN, D., DEBRA, D., WILLIAMS, S., GILL, D., SHELEF, B., and SHELEF, G., "ST-7 gravitational reference sensor: analysis of magnetic noise sources," *Classical and Quantum Gravity*, vol. 20, no. 10, pp. S109–S116, 2003.
- [30] HELTINGS, R. W., "Gravitational wave detectors in space," *Contemporary Physics*, vol. 37, no. 6, pp. 457–469, 1996.
- [31] JELLETT, J. H. and HAUGHTON, S., eds., *The Collected Works of James MacCullagh*, Longmans, Green, and Co., London, 1880.
- [32] JENKINS, R. E., "Performance in orbit of the TRIAD disturbance compensation system," *The APL Technical Digest*, vol. 12, no. 2, 1973.
- [33] KEISER, G., BUCHMAN, S., DEBRA, D., GUSTAFSON, E., GODDARD, L., HANSON, J., and ROUTE, R., "Advantages and disadvantages of a spherical proof mass for LISA," Presented at COSPAR 2000, July 2000. Warsaw, Poland.
- [34] KELLOGG, O. D., *Foundations of Potential Theory*, Dover Publications, June 1969, ISBN 0486601447.
- [35] LANDKOF, N. S., *Foundations of Modern Potential Theory*, Die Grundlehren der mathematischen Wissenschaften in Einzeldarstellungen mit besonderer Berücksichtigung der Anwendungsgebiete, Bd. 180, Springer-Verlag, Berlin, New York, 1972, ISBN 3387053948. Translated from Russian by A. P. Doohovskoy.
- [36] LISA STUDY TEAM, "LISA: Laser Interferometer Space Antenna for the detection and observation of gravitational waves," Pre-Phase A Report MPQ 233 2nd ed., Max-Planck-Institut für Quantenoptik, Garching, Germany, July 1998.



- [37] LOCKERBIE, N. A., “Dynamical measurements of the gravitational quadrupole coupling to experimental test masses,” *Classical and Quantum Gravity*, vol. 18, pp. 2521–2531, 2001.
- [38] LOCKERBIE, N. A., “A dynamical technique for measuring the gravitational quadrupole coupling of the STEP and  $\mu$ SCOPE experimental test masses,” *Classical and Quantum Gravity*, vol. 18, pp. 2521–2531, 2001.
- [39] LOCKERBIE, N. A., “Gravitational quadrupolar coupling to equivalence principle test masses: the general case,” *Classical and Quantum Gravity*, vol. 19, pp. 2063–2077, 2002.
- [40] MACMILLAN, W. D., *Theory of the Potential*, Dover Publications Inc, January 1958, ISBN 0486604861.
- [41] MERKOWITZ, S. M., CONKEY, S., HAILE, W. B., KELLY, W. R., PEABODY, H., and DUMONT, P. J., “Structural, thermal, optical and gravitational modelling for LISA,” *Classical and Quantum Gravity*, vol. 21, pp. 603–610, 2004.
- [42] MERKOWITZ, S. M., HAILE, W. B., CONKEY, S., KELLY, W. R., and PEABODY, H., “Self-gravity modelling for LISA,” *Classical and Quantum Gravity*, vol. 22, pp. 395–402, 2005.
- [43] NAGY, D., “The gravitational attraction of a right rectangular prism,” *Geophysics*, vol. 31, no. 2, pp. 362–371, April 1966.
- [44] NATIONAL RESEARCH COUNCIL, *Gravitational Physics, Exploring the Structure of Space and Time*, National Academy Press, Washington, D. C., 1999.
- [45] NIST, “Mechanical measurements, mass standards,” January 2009, URL <http://ts.nist.gov/MeasurementServices/Calibrations/mass.cfm>. [Online; accessed 08-March-2009].
- [46] POISSON, S.-D., *A Treatise of Mechanics*, vol. 1, Longman and Co., London, 1842. Translated from the French, and elucidated with explanatory notes by the Rev. Henry Hickman Harte.

- [47] SCHUMAKER, B. L., "Disturbance reduction requirements for LISA," *Classical and Quantum Gravity*, vol. 20, no. 10, pp. S239–S253, 2003.
- [48] SCHUTZ, B. E., "The mutual potential and gravitational torques of two bodies to fourth order," *Celestial Mechanics and Dynamical Astronomy*, vol. 24, no. 2, pp. 173–181, 1979.
- [49] SHEYNIN, S. A. and TUZIKOV, A. V., "Explicit formulae for polyhedra moments," *Pattern Recognition Letters*, vol. 22, pp. 1103–1109, 2001.
- [50] SHIOMI, S., *Test Mass Metrology for Tests of the Equivalence Principle*, Ph.D. thesis, The University of Birmingham, 2002. Birmingham Gravitations Group School of Physics and Astronomy.
- [51] SOKOLNIKOFF, I. S., ed., *Tensor Analysis Theory and Applications to Geometry and Mechanics of Continua*, Applied Mathematics Series, John Wiley & Sons, Inc., 2nd ed., 1964.
- [52] SOLER, T. and CHIN, M., "On transformation of covariance matrices between local cartesian coordinate systems and commutative diagrams," Tech. rep., NOAA, Cockville, MD, 1985.
- [53] SPACE DEPARTMENT OF JOHNS HOPKINS UNIVERSITY APPLIED PHYSICS LAB AND GUIDANCE & CONTROL LAB OF STANFORD UNIVERSITY, "A satellite freed of all but gravitational forces: TRIAD I," *Journal of Spacecraft*, vol. 11, pp. 637–644, 1974.
- [54] SPACE ELECTRONICS LLC, "High precision mass properties measurement," 2008, URL <http://www.space-electronics.com>. [Online; accessed June-2008].
- [55] STAFF OF RESEARCH AND EDUCATION, *Handbook of Mathematical, Scientific, and Engineering Formulas, Tables, Functions, Graphs, Transforms*, Research and Education Association, New Jersey, 1997.

- [56] STEBBINS, R. T., BENDER, P. L., HANSON, J., HOYLE, C. D., SCHUMAKER, B. L., and VITALE, S., "Current error estimates for LISA spurious accelerations," *Classical and Quantum Gravity*, vol. 21, pp. 653–660, 2004.
- [57] STRANG, G., *Introduction to Applied Mathematics*, Wellesley-Cambridge Press, 1986, ISBN 9780961408800.
- [58] SUN, K.-X., ALLEN, G., BUCHMAN, S., BYER, R. L., CONKLIN, J. W., DEBRA, D. B., GILL, D., GOH, A., HIGUCHI, S., LU, P., ROBERTSON, N., and SWANK, A. J., "Modular Gravitational Reference Sensor for High Precision Astronomical Space Missions," in "Bulletin of the American Astronomical Society," vol. 38, Dec. 2006.
- [59] SUN, K.-X., ALLEN, G., BUCHMAN, S., BYER, R. L., CONKLIN, J. W., DEBRA, D. B., GILL, D., GOH, A., HIGUCHI, S., LU, P., ROBERTSON, N. A., and SWANK, A. J., "Progress in developing the modular gravitational reference sensor," *Laser Interferometer Space Antenna: 6th International LISA Symposium*, vol. 873, no. 1, pp. 515–521, 2006.
- [60] SUN, K.-X., ALLEN, G., WILLIAMS, S., BUCHMAN, S., DEBRA, D. B., and BYER, R., "Modular gravitational reference sensor: Simplified architecture to future LISA and BBO," *Journal of Physics: Conference Series*, vol. 32, pp. 137–146, 2006.
- [61] SUN, K.-X., BUCHMAN, S., BYER, R., DEBRA, D. B., GOEBEL, J., ALLEN, G., CONKLIN, J. W., GERARDI, D., HIGUCHI, S., LEINDECKER, N., LU, P., SWANK, A. J., TORRES, E., and TRITTLER, M., "Modular gravitational reference sensor development," *Journal of Physics: Conference Series*, vol. 154, 2009.
- [62] SUN, K.-X., BUCHMAN, S., and BYER, R. L., "Grating angle magnification enhanced angular and integrated sensors for LISA applications," *Journal of Physics: Conference Series*, vol. 32, pp. 167–179, 2006.

- [63] SUN, K.-X., BUCHMAN, S., BYER, R. L., DEBRA, D., GOEBEL, J., ALLEN, G., CONKLIN, J., GERARDI, D., HIGUCHI, S., LEINDECKER, N., LU, P., SWANK, A. J., TORRES, E., TRITTLER, M., and ZOELLNER, A., "Modular Gravitational Reference Sensor (MGRS) For Astrophysics and Astronomy," in "American Astronomical Society Meeting Abstracts," vol. 213 of *American Astronomical Society Meeting Abstracts*, Jan. 2009.
- [64] SWANK, A. J., HARDHAM, C., SUN, K.-X., and DEBRA, D. B., "Moment of inertia measurement using a five wire torsion pendulum and optical sensing," *Proceedings of the 21st Annual Meeting*, October 2006. Monterey, California.
- [65] SWANK, A. J., SUN, K.-X., and DEBRA, D. B., "Determining gravitational attraction by mass property measurements," *Laser Interferometer Space Antenna: 6th International LISA Symposium*, vol. 873, no. 1, pp. 588–592, 2006.
- [66] TUZIKOV, A. V., SHEYNIN, S. A., and VASILIEV, P. V., "Efficient computation of body moments," in SKARBEK, W., ed., "Proceedings of 9th International Conference, CAIP 2001, Warsaw, Poland, September 5-7, 2001," vol. 2124, pp. 201–208, *Computer Analysis of Images and Patterns*, Springer, 2001.
- [67] VALLADO, D. A., *Fundamentals of Astrodynamics and Applications, 2nd Ed.*, Microcosm Press, El Segundo, 2001.